DESY 95-225

On the Preservation of Single- and Multi-Bunch Emittance in Linear Accelerators

Vom Fachbereich Elektrische Nachrichtentechnik
der Technischen Hochschule Darmstadt
zur Erlangung der Würde eines Doktor-Ingenieurs (Dr.-Ing.)
genehmigte

Dissertation

von
Dipl.-Ing. Michael Drevlak
geb. am 23. Februar 1967
in Leoben

Referent:	Prof. Dr.-Ing. Th. Weiland
Korreferenten:	Dr. rer. nat. R. Brinkmann
	Prof. Dr. rer. nat. Dr. h. c. A. Richter

Tag der Einreichung:	5.7.1995
Tag der mündlichen Prüfung:	2.11.1995

D17
Darmstädter Dissertation

Contents

1 Introduction **3**

2 Single-Bunch Dynamics **11**
2.1 Fundamental Concepts 11
2.1.1 Bunch Model and Transport 11
2.1.2 Emittance 15
2.1.3 Longitudinal Wake Fields 18
2.1.4 Deflection by Dipole and Quadrupole Wakes 22
2.2 BNS Damping 26
2.3 Quadrupole Misalignment 33
2.3.1 Emittance Growth without Correction and Vibration Tolerance 33
2.3.2 Emittance Growth with Orbit Correction 34
2.4 Structure Misalignment 41
2.4.1 Emittance Growth without Correction 41
2.4.2 Emittance Correction with Trajectory Bumps 41
2.5 Minor Effects 45
2.5.1 Longitudinal Dipole Wake 45
2.5.2 Quadrupole Wake 45

3 Multi-Bunch Dynamics **47**
3.1 Introduction 47
3.1.1 Modeling the Bunch Train 47
3.1.2 Wake Fields and Modes 48
3.2 Beam Loading and Staggered Timing 52
3.3 Interaction with Dipole Modes 60
3.3.1 Interaction with TM-like Modes 60
3.3.2 Detuning the Dipole Modes 66
3.3.3 Influence of the Dipole Mode Quality Factors 69
3.3.4 Simulations Using the Displacement Parameters 70
3.3.5 Longitudinal Dipole Wakes 75
3.3.6 Orbit Correction 76
3.3.7 Transverse Dynamics with Beam Loading 77
3.3.8 Deflection by TE-like Modes 80
3.4 Deflection by the Accelerating Mode 83
3.5 Perturbing Effects 86
3.5.1 Longitudinal Jitter 88
3.5.2 Charge Fluctuation 90
3.5.3 RF Phase Errors 92

4 Combined Single- and Multi-Bunch Effects **95**
4.1 Impact of Multi-Bunch Effects on Single-Bunch Dynamics . . . 95
4.1.1 Machine Tuning and Staggered Timing . . . 95
4.1.2 Kicks from the Accelerating Mode . . . 96
4.1.3 Transverse Long Range Wake and Finite Bunch Length . . . 96
4.1.4 Transverse Long Range Wake and Filamentation . . . 98
4.2 Complete Machine Tuning Procedure . . . 100
4.3 Dependence on Machine and Beam Parameters . . . 108
4.3.1 Quality Factor of the Deflecting Modes . . . 109
4.3.2 BPM Resolution . . . 110
4.3.3 Charge Fluctuation . . . 113
4.3.4 Longitudinal Jitter . . . 115
4.3.5 RF Phase Errors . . . 119

5 Summary **121**

A Formula Symbols **124**

B The Parameter Panel **127**

C Particle Optics **129**

D SBLC: Fundamental Design and Layout Properties **137**
D.1 Machine Lattice . . . 137
D.2 Accelerating Structure . . . 138
D.3 Short Range Wakes . . . 140

Bibliography **144**

Acknowledgements **148**

Chapter 1

Introduction

Today, the properties and interaction of particles at high energies have been probed by $p\overline{p}$-colliders up to an energy range of $\approx$ 2TeV center of mass ("c-o-m") and by (circular and linear) e^+e^--colliders to a range of $\approx$ 100GeV, confirming the Standard Model with outstanding accuracy. For e^+e^--colliders the energy is going to be extended to $\approx$ 200GeV (at LEP). Collisions of protons and electrons at high energies are being explored at HERA [1].

Despite the previous success of the Standard Model, there are several issues requiring more thorough examination [2]. For example, the mass of the recently discovered top-quark [3] needs to be determined with greater accuracy. In $p\overline{p}$-colliders this accuracy is limited to $\approx$ 4GeV, whereas an e^+e^--collider, with its cleaner experimental environment, could achieve an accuracy of $\approx$ 0.5GeV. Similarly, the properties of the electroweak gauge bosons could be measured with good precision. In addition, an e^+e^--collider with an energy of $300 - 500$GeV c-o-m has the potential of discovering the Higgs boson. Particularly, if the mass of the Higgs is in the range of $140 - 250$GeV, an e^+e^--collider would probably be the only machine capable of detecting it [2]. Finally, extensions of the Standard Model are conceivable, with supersymmetric theories being prominently attractive among them. These theories predict the existence of so-called supersymmetric partners to the known particles. Supersymmetric partners of the leptons might be found with an e^+e^--collider.

Circular e^+e^--colliders have played a crucial role in high energy physics research for several decades and will continue to do so for many years. However, as the desired collision energies are being pushed to higher values, these machines suffer from a decisive drawback. Highly relativistic charged particles loose energy by synchrotron radiation if they are subjected to an acceleration. This energy loss increases with the 4-th power of the relativistic factor γ^{rel} and determines the amount of power that must be replenished to an electron beam kept on a circular trajectory of a given radius or, conversely, puts a limit on the minimal trajectory radius of an electron beam for a given available drive power. For particle energies of 250GeV, circular e^+e^--colliders are therefore not considered feasible. The alternative approach is then to build a linear collider, which has been pioneered at SLAC.

The processes under investigation in colliding machines are very rare. This holds especially for high energy machines, since the reaction cross sections decrease inversely proportional to the square of the energy. Therefore, in order to produce a reasonable number of events, it is a fundamental requirement for any colliding machine to provide a high luminosity

$$\mathcal{L} = \frac{N_+ N_- N_b f_{rep}}{4\pi\sigma_x\sigma_y} \cdot H_D, \tag{1.1}$$

where N_+ and N_- are the number of particles per bunch, N_b the number of bunches in the bunch train, f_{rep} the repetition frequency, σ_x and σ_y the horizontal and vertical cross sections

of the beam at the interaction region and H_D the pinch factor. H_D describes the enhancement of the luminosity by the mutual focusing of the interacting particle bunches and is usually in the range of $1-5$. For a 500GeV c-o-m e^+e^--collider the luminosity must be in the order of $\mathcal{L} \approx 10^{33} \ldots 10^{34}\mathrm{cm}^{-2}\mathrm{s}^{-1}$. This can essentially be achieved by increasing the number of particles per bunch, the number of bunches in the bunch train and the repetition frequency, or by making the horizontal and vertical cross sections σ_x, σ_y small. Either way to increase the luminosity has drawbacks on the other parameters. The most unattractive parameter to increase is the repetition frequency f_{rep}: the power consumption of a machine is directly proportional to this parameter. On the other hand, as we will outline in greater detail later, there is a conflict between raising the number of particles ($N_+ \cdot N_b$, $N_- \cdot N_b$), and decreasing the beam cross section (σ_x, σ_y).

The particles of the beam are generally scattered over different transverse offsets (x, y) and different trajectory slopes (x', y'). The areas occupied by the particles in the transverse degrees of freedom are described by the projected emittances ϵ_x and ϵ_y (see section 2.1.2). The cross section of the beam at the interaction point (I.P.) depends from the beam emittance as

$$\sigma_x = \sqrt{\beta_x \epsilon_x},$$

where β_x is a property of the focusing lattice (see appendix C). For this reason, expression 1.1 for the luminosity can be rewritten as

$$\mathcal{L} = \frac{N_+ N_- N_b f_{rep}}{4\pi\sqrt{\beta_x \beta_y \epsilon_x \epsilon_y}} \cdot H_D. \tag{1.2}$$

It follows that a small projected emittance of the beam is required for producing a high luminosity according to formula 1.2.

In recent years, several studies have been started investigating possible machine designs for a 500GeV e^+e^--collider that would meet the above requirements. From this effort, two strategies have evolved for producing the necessary high luminosity. On one side, we have the studies CLIC, JLC-X and NLC, which can be characterized as "low beam power" machines. These machines, having a rather small efficiency, produce small beam powers but at the same time provide small emittances. On the other side, there are the studies SBLC and TESLA, which are characterized as "high beam power" machines. Having a higher conversion efficiency, these machines generate beams with high current, but also higher emittances. A summary of the machine parameters envisaged by the various studies is given in table 1.1. The figures have been taken from [4].

In this document we want to deal especially with the problems associated with the beam dynamics for the case of the SBLC study. This study envisions the construction of a linear collider operating at a rather low frequency of 2.998GHz with relatively conventional "off-the-shelf" technology. It is intended as a 2×250GeV e^+e^--collider. A schematic view of this linear collider is shown in Fig. 1.1. In order to clarify the macroscopic principles of operation for this collider, we will briefly go through the most important machine components and explain their purpose in the framework of the overall machine operation.

The electron beam is first generated in an electron gun, where short pulses of electron current are emitted from a cathode over a period of $2\mu s$. These current pulses emerging from the electron gun are bunched longitudinally and accelerated to an energy of $\sim$ 5MeV in the injector system. Upon leaving the injector system, the beam enters a pre-accelerator, which accelerates the beam further to an energy of 3.15GeV.

The beam emerging from this pre-accelerator still has an emittance that is too large for producing the required luminosity. In addition to occupying a large volume in the transverse

	CLIC	JLC-X	NLC	SBLC	TESLA
C-O-M Energy / GeV	500	500	500	500	500
Luminosity / (10^{33}cm^{-2}s^{-1})	2.2-8.9	6.3	8.2	3.6	6.5
Particles per bunch / 10^{10}	0.6	0.63	0.65	2.9	5.0
Normalized vert. emittance / (10^{-7}radm)	2	0.45	0.5	5	10
Normalized hor. emittance / (10^{-7}radm)	18	33	50	100	200
Repetition rate / Hz	1700	150	180	50	10
Bunches per pulse	1-4	90	90	125	800
Bunch separation / ns	0.33	1.4	1.4	16	1000
Beam loaded gradient / (MV/m)	78-73	30.6	37.6	17.0	25.0
RF frequency / GHz	30	11.4	11.4	2.998	1.3
Damping ring energy / GeV	3.0	1.98	1.8	3.15	4.5
Beam power per beam / MW	0.4-1.6	3.4	4.2	7.3	16.5
AC-to-beam efficiency / %	2	9	6	13	24

Table 1.1 Machine parameters envisioned by the different linear collider studies.

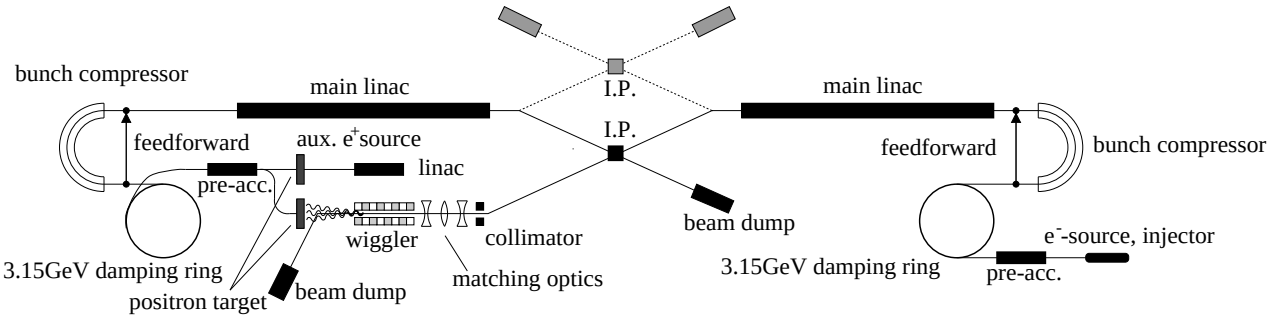

Fig. 1.1 Global layout of the SBLC, showing the macroscopic components of the entire collider.

phase space, the bunches of this beam will have a rather large length ($\sim$ 4mm). Since the different longitudinal regions of the bunches are accelerated at different RF phases of the accelerating voltage in the pre-accelerator, the bunch will also have a large energy spread. From the pre-accelerator, the bunches of the beam are injected into a damping ring, where the emittances of the beam are reduced to the values that are desired at the beginning of the main linear accelerator (linac).

The positron beam will be generated in a rather different fashion. For this purpose, the spent electron beam will be guided through a large wiggler where it generates very strong synchrotron radiation. This synchrotron radiation will strike a metal target and produce pairs of electron and positrons. The positrons are captured and then, as in the case of the electrons, accelerated to an energy of 3.15GeV in a pre-accelerator [5]. Again, this positron beam will be injected into a damping ring, from where on it will undergo the same procedure as the electron beam.

The bunches of the beams emerging from the damping rings are still very long ($\sim$ 4mm): therefore, the particle bunches are led through a bunch compressor ([6], [7]). In the bunch compressor, the particles travel on curved trajectories that are non-isochronous for particles of different energy. As a result, one can achieve a reduction of the bunch length by inducing an appropriate longitudinal energy profile on the bunch prior to injection into the bunch com-

pressor. The bunches emerging from the compressor will have a length of $\sigma_z = 0.5$mm. At the same time, the systematic energy profile induced on the bunch prior to injection into the bunch compressor will convert into an uncorrelated energy spread of $\sim 1\%$, which is no longer correlated with the longitudinal position in the bunch.

The particle bunches emerging from the damping ring may exhibit a random error of their transverse positions and trajectory slopes, which would lead to an undesired transverse injection error for the beam at the main linac. It is therefore conceivable that a feedforward system is used to measure the beam trajectory between the damping ring and the bunch compressor and carry out the appropriate trajectory corrections between the bunch compressor and the main linac. In this scheme, the offset and trajectory slope of each bunch could be corrected according to the measurement of its own trajectory after the damping ring, since the measurement signal can shortcut the longer path of the particles through the bunch compressor.

In the main linac the beam is accelerated to an energy of 250GeV in order to be delivered to the final focus system and the interaction region. This main linac is the part of the linear collider that is the subject of this treatise. From the beam dynamics viewpoint, the linac envisioned in the scope of the SBLC study essentially consists of a chain of accelerating structures, between which quadrupole magnets are inserted in order to provide focusing for the particles of the beam. These machine elements are separated by empty drift spaces. The elements of an accelerator may be equipped with dipole (correction) magnets that can be used to deliberately impart a deflection on the beam.

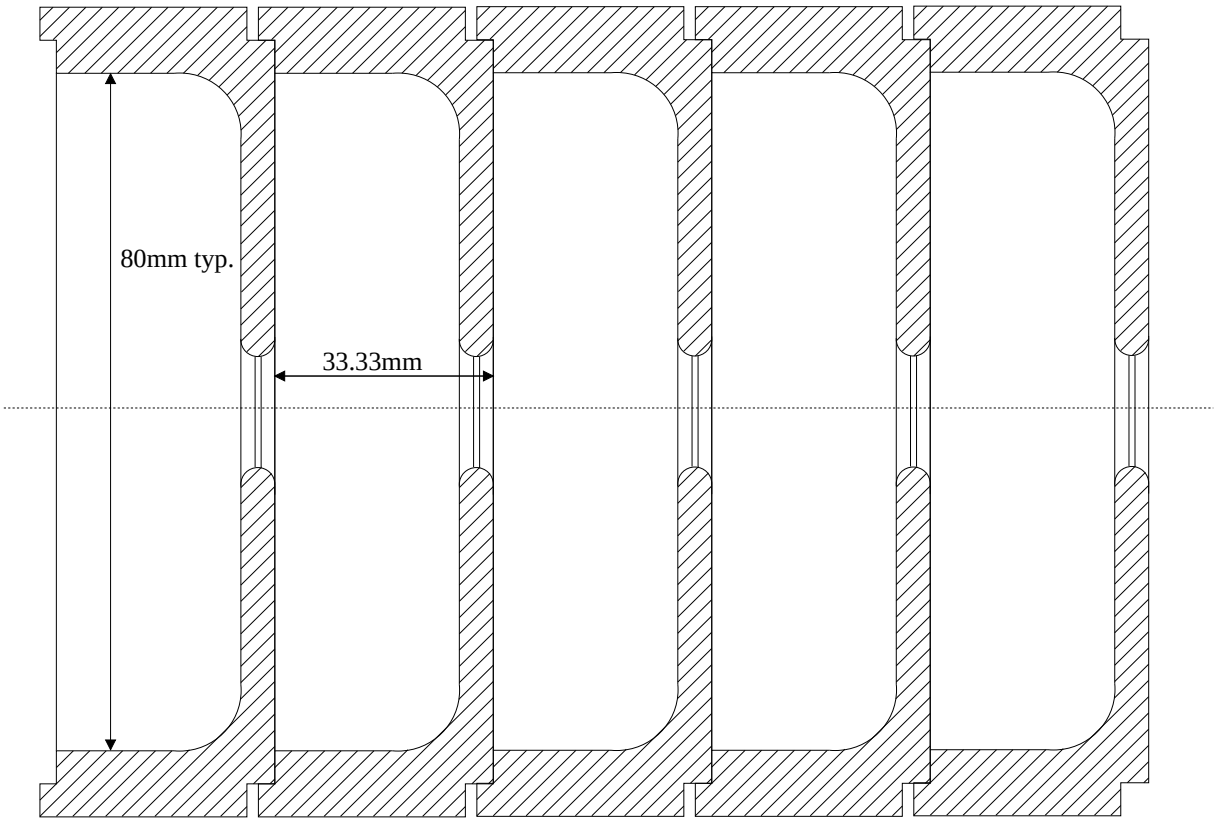

Fig. 1.2 Schematic view of a segment of the accelerating structure. It is a traveling wave structure. The full structure has a length of 6m and consists of a total of 180 coupled cells.

Accelerating structures are devices for increasing the particle energies. In the case of the SBLC it is foreseen to use traveling wave structures operating at a frequency of 2.998GHz. A schematic view of a short segment of this structure is shown in Fig. 1.2. It is a so-called

slow wave structure consisting of a series of coupled resonators. Along this structure a traveling wave, the "accelerating mode", can propagate with a phase velocity equal to the velocity of light in vacuum c_0 and a group velocity of a few percent of c_0. The individual cells of this structure generally have a cylindrical symmetry and are coupled to the adjacent cells by comparatively small apertures (the irises). The full accelerating structure has a length of 6m and consists of 180 cells. The RF power required by the structures for the accelerating mode is provided by klystrons, which must be able to produce a power of 150MW over a pulse length of 3μs. A klystron meeting these requirements has been designed and constructed successfully at SLAC [8]. A schematic view of the assembly of the machine elements as envisioned in the SBLC

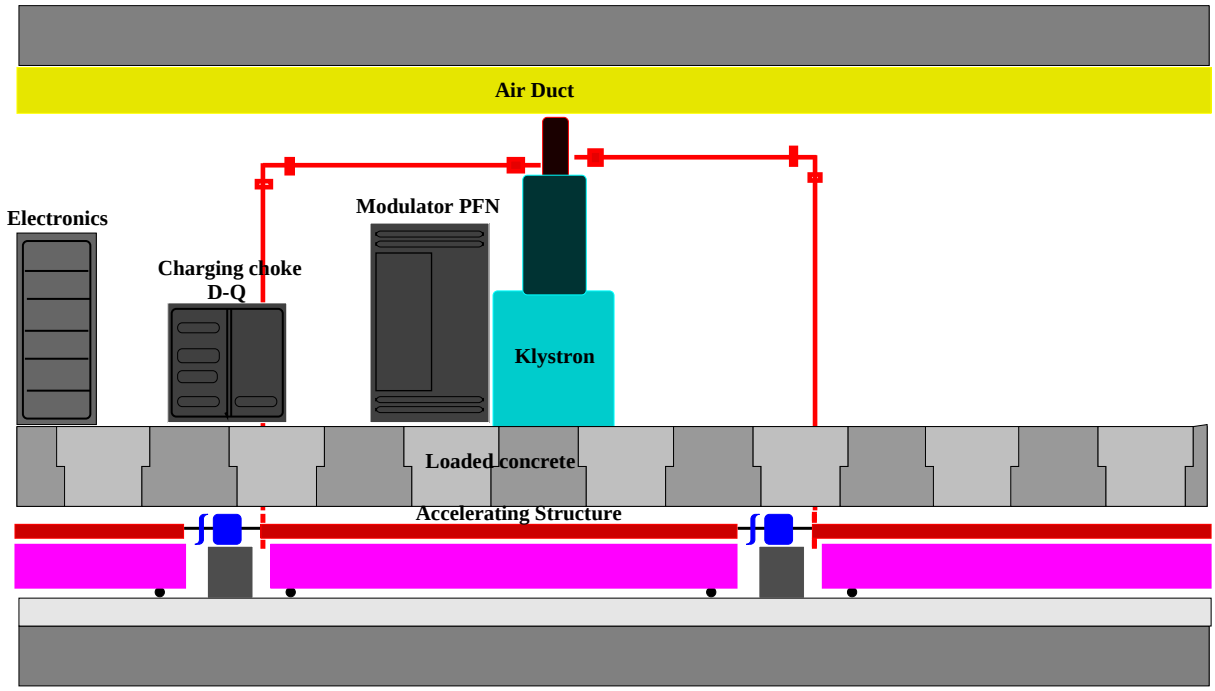

Fig. 1.3 Longitudinal cross-section of the SBLC tunnel, showing the schematic arrangement of the elements of the main accelerator [9]. The beamline consisting of accelerating structures and quadrupoles is installed at the bottom of the tunnel under a concrete shielding. The klystrons generating the RF power for the accelerating structures and the modulators providing the klystron power are installed above the shielding.

study is shown in Figs. 1.3 and 1.4. The beamline consisting of the accelerating structures and quadrupoles is mounted under a heavy concrete shield. The remaining tunnel volume is accessible and holds the klystrons and the modulators, which feed pulses of electric power to the klystrons.

Ideally, the accelerating structures and focusing elements of the linac would be aligned perfectly along an ideal axis, onto which the beam would be injected without transverse offset or angle. Furthermore, the particles in the beam would have a vanishing energy spread at injection and experience the same acceleration. Finally, the accelerating structures would not interact with the particles of the beam in any other way than to increase their momentum in the direction of the machine axis. In such an ideal accelerator, particles being injected into the machine would emerge from the machine exactly on axis. In addition, the normalized emittance, defined as the product $\epsilon_N = \epsilon\beta^{rel}\gamma^{rel}$ of the emittance and the relativistic factors, would be conserved during acceleration of the beam along the linac. In that case the accelerator could deliver a beam with arbitrarily small emittance to the final focus system, as long as this small emittance could be provided by the damping ring and the bunch compressor.

However, in a real accelerator matters are different. To begin with, the particles in the beam have an initial uncorrelated energy spread due to the bunch compressor. In addition, even more important contributions to the energy spread are generated in the accelerating structures, which interact with the particle beam in a much more complex fashion than outlined previously. Finally, the elements of the accelerator are never aligned perfectly along some ideal axis. Likewise, the beam will not be injected exactly along the machine axis but with non-vanishing offset and angle. These circumstances cause an intricate interplay of processes influencing both the particle energies and particle trajectories of the beam traversing the machine. We briefly enumerate some of the most important of these processes. More elaborate discussions of these effects are given in later parts of this document.

- The non-uniformity of the inner cross section of the accelerating structure along the axis gives rise to an excitation of electromagnetic fields in the structure by the beam current. These electromagnetic fields are called wake fields. This process goes along with a loss of energy of the beam to the excited fields. Moreover, the excited fields affect the energies of trailing particles. This effect generates an additional contribution to the energy spread in the beam.

- Particles traversing an accelerating structure off axis excite wake fields that will deflect trailing particles transversely. As the deflection imparted on a trailing particle by these wake fields is a function of its delay with respect to the leading particle, different particles are deflected at different angles and hence a divergence is imparted to the particles of the beam. The additional excitation of electromagnetic fields also affects the particle energies.

- The particle bunches have a finite longitudinal extent, which means that different particles of the beam enter the accelerating structures at different times. As a consequence, these particles are accelerated at different phases of the accelerating wave and experience different energy gains. This process affects the profile of particle energies along the bunch.

- Particles traversing a transversely misaligned quadrupole magnet experience an additional transverse deflection. The deflection angle is inversely proportional to the particle momentum. As the particles of the beam have an energy spread, they will be deflected at different angles. Upon deflection, the particles will perform a transverse oscillation in the restoring force exerted by the quadrupole magnets. Due to this oscillation, other elements of the machine will be traversed with non-vanishing offset.

- Accelerating structures may be misaligned with an angle with respect to the machine axis. As a consequence, the accelerating field has a component in the transverse plane and the beam will be deflected accordingly. Since the energy gain in a structure is different for all particles, the particles will be deflected at different angles. Again, an additional contribution to the divergence of the beam is generated. This effect is particularly severe with respect to the different bunches of a bunch train, since the energy gains of the individual bunches can deviate very strongly from their mean value.

- Particles that have been injected into the machine with non-zero offset or angle or that have been deflected transversely at some location in the accelerator will perform a transverse oscillation in the restoring force exerted by the quadrupole magnets. As the strength of this focusing is inversely proportional to the particle momentum, the particles will oscillate with different frequencies. It follows that particles of different energy starting out with an initially coherent oscillation will decohere and assume transverse offsets and trajectory slopes that are scattered over a range of different values.

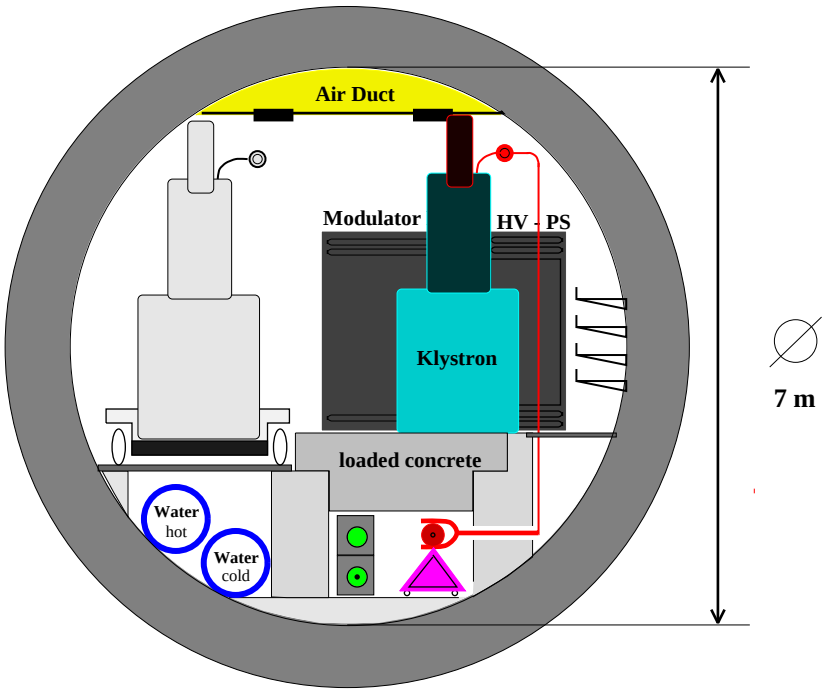

Fig. 1.4 Transverse cross section of the SBLC tunnel (see also Fig. 1.3) [9]. The tunnel is accessible to allow for maintenance of the accelerator components, especially the modulator-klystron units.

These processes disturb the distribution of the particles of the beam in the transverse degrees of freedom. More specifically, the particles will become scattered over a wider range of transverse offsets and momenta, corresponding to an increase of the projected emittance. In addition, there may be a considerable spread in the final particle energies. Both effects are undesirable for reasons that arise from the requirements of the final focus system and the intended collision experiments.

Several of the effects listed above become more severe as the number of particles in the beam is increased. Specifically, the excitation of wake fields in the accelerating structures increases directly proportional to the charges involved. It follows that the contributions to the energy spread and the transverse emittance from these processes increase with the beam current. Therefore, the acceleration of a large beam current and the preservation of a small normalized emittance are opposed to each other.

The effects involving particle deflections generally grow with the particle offsets and misalignments of the accelerator elements. The additional deflections from misaligned quadrupoles are proportional to the quadrupole offsets. The excitation of transversely deflecting wake fields grows at least linearly with the particle displacement from the structure axes. It follows that the effects causing the transverse particle deflections, leading to an increase of the projected emittance, will make diligent alignment of the machine elements and precise injection of the beam along the machine axis necessary.

After this account of effects relating to the transverse particle motion in a linear accelerator, we finally arrive at a description of the function and requirements of the final focus system. The final focus system essentially is a system of quadrupole and sextupole magnets that focuses the beam to a very small cross section (670nm $\times$ 28nm in the case of the SBLC). In the interaction region, this tightly focused bunch of electrons will then collide with a bunch of positrons of the same energy emerging from the opposing linac. Owing to the strong focusing requirements, the final focus system can only focus particles within a certain momentum bandwidth to a small

spot. This interval of particle energies has a width of $\Delta W/W < \pm 1.8\%$ [10]. At the final focus test beam (FFTB) at SLAC, the demagnification of a beam with an emittance of $2 \cdot 10^{-6}$radm by a factor of 320 to a vertical height of $\sigma_y = 70$nm was demonstrated successfully [11].

As mentioned earlier, this document will be concentrated on the investigation of the dynamics of a particle beam in a linear accelerator. We will numerically simulate a number of effects and evaluate the severity of their impact on the beam. Furthermore, we will examine the applicability of several correction techniques aiming at the suppression or correction of the effects diluting the beam emittance. First, there is the issue of single-bunch dynamics: we will see that wake field effects and dispersive errors (appendix C) can cause a significant emittance growth. Secondly, long range dipole wakes and dispersive effects arising from the energy spread between different bunches will cause relative offsets between the individual bunches and likewise result in emittance growth. Finally, we will observe interactions between the single-bunch and multi-bunch dynamics in a bunch train, which will further aggravate these effects. The corrective measures against emittance growth will first be tested with respect to individual effects relating to issues of single- or multi-bunch dynamics. Later, these different correction techniques will be joined to one machine tuning procedure that will be applied in order to achieve good emittance preservation for operation of the accelerator with a full beam consisting of the full number of bunches. The performance of this procedure will be tested in simulations of the combined single- and multi-bunch dynamics. Finally, tolerances on the machine alignment as well as machine and beam parameters will be established.

Chapter 2

Single-Bunch Dynamics

In this chapter we will treat the behavior of a single bunch of particles during its motion through a linear accelerator. In the first section we will describe the model that will be used to represent such a bunch and its transformation through the accelerator. Furthermore, we will give a brief account of the wake fields acting on such a bunch, which are a major cause of emittance growth. The definitions concerning the concept of the emittance will be clarified for the context of our investigations.

After this introductory section we will turn to the issues relating to the machine operation for the case of the SBLC study. First, we will look at the emittance growth caused by betatron motion of a bunch in the machine. In order to minimize this emittance growth we will make use of a technique called BNS damping, which will define the operating point of the machine also for subsequent investigations. Then we will simulate the emittance growth caused by misalignment of quadrupoles and accelerating structures and demonstrate the effectiveness of several orbit and emittance correction schemes. Finally, we will consider the effect of longitudinal dipole wakes and from quadrupole wakes, which will both turn out to be of secondary importance.

The preservation of small beam emittances and the subsequent requirements imposed on the machine will be one of the most important objectives of our investigation. We will therefore establish limits on the machine design, machine tolerances or methods of machine operation. These limits will be set in order to keep the emittance contributions from individual effects smaller than 6% of the injection emittance.

2.1 Fundamental Concepts

In this section, we will describe how a bunch of particles is modeled in order to simulate its behavior in a linear accelerator. Then, we will give a brief review of the wake fields in an accelerating structure and show how their effect on particle motion will be calculated. In addition, we will give a definition of the emittance which will serve as the most important criterion for beam quality throughout the entire scope of this document.

2.1.1 Bunch Model and Transport

The current design studies for an e^+e^- collider envision to accomplish the acceleration of electrons to very high energies with electromagnetic waves in slow wave or standing wave structures. Here, the phase velocity of the accelerating wave is made identical with the particle velocity, which at the particle energies of interest for our investigation is virtually equal to the velocity of light c_0. In order to allow acceleration with a wave, the particle beam must

be divided into discrete bunches which will be longitudinally located near the crests of the accelerating wave.

Bunch Model

The bunches, containing a large number of particles ($2.9 \cdot 10^{10}$ in the case of the SBLC), are of finite extent both in the longitudinal and transverse directions. For their description we will use an approach that is in part deterministic, in part statistical.

While the bunch propagates through the machine, the particles of the bunch generally have different transverse offsets x and y with respect to the machine axis, trajectory slopes x' and y' and energies W. Furthermore, they are scattered over different longitudinal positions s with respect to the center of the bunch. We define that particles with $s < 0$ are ahead of the bunch center while particles with $s > 0$ are trailing. The particles constituting the bunch are said to be distributed in the 6-dimensional coordinate space $\{x, x', y, y', s, W\}$.

As the number of particles in a bunch is very large, it is not possible to simulate the motion of every single particle of that bunch. In our tracking calculations, we will therefore confine ourselves to simulating the collective behavior of particles contained in short longitudinal regions of the bunch. For this reason, we divide the bunch longitudinally into "slices" distributed equidistantly over the range over which we choose to model the bunch. Each of these slices represents a fraction of all particles in the bunch and must reflect the distribution of its particles in the 5-dimensional coordinate space $\{x, x', y, y', W\}$ (see Fig. 2.1). It follows that a slice ν is

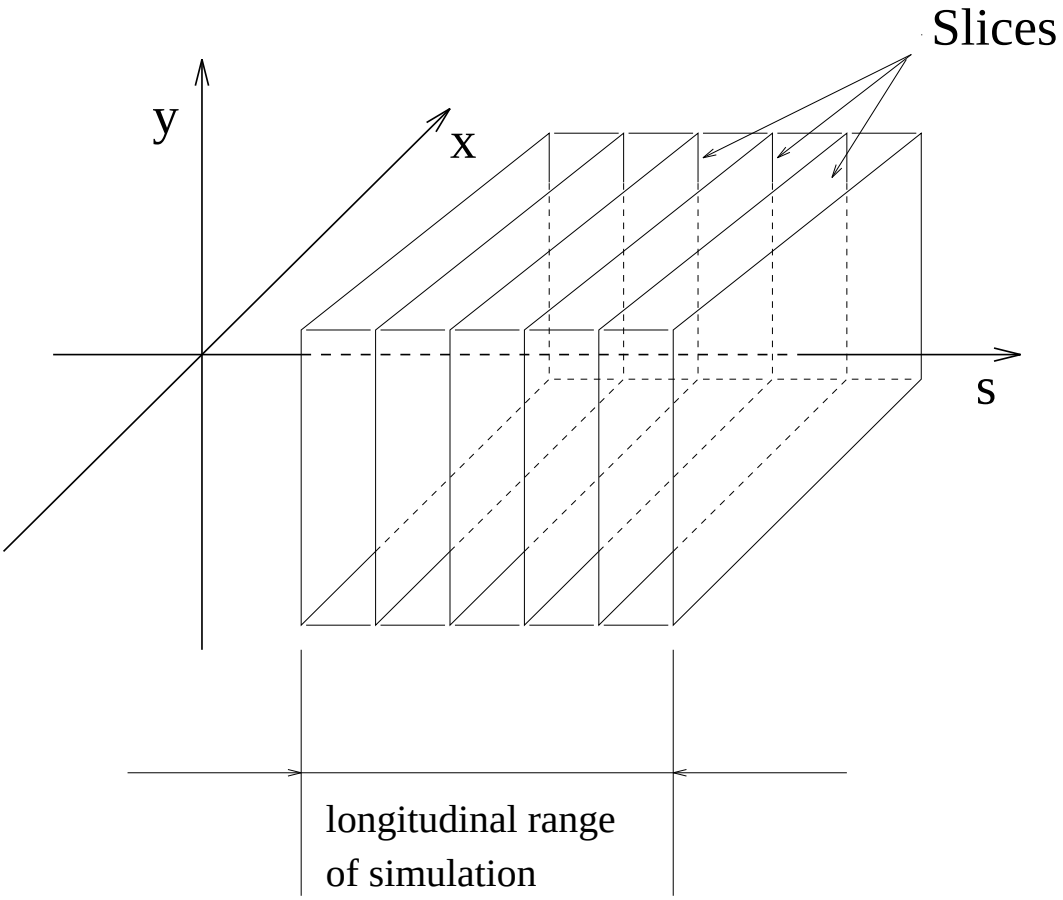

Fig. 2.1 Longitudinal division of a bunch in slices. Each slice represents the particles within a certain longitudinal interval.

characterized by its transverse coordinates $\vec{\mathcal{X}}_\nu = (x_\nu, x'_\nu, y_\nu, y'_\nu)^t$, the mean energy of its particles

W_ν and its longitudinal position within the bunch s_ν. In addition, a slice has a total charge q_ν. The coordinates of a slice are the mean value of the particle coordinates represented by the slice. Obviously, every bunch must consist of at least 1 slice.

The individual particles of a slice are bound to have transverse positions and slopes that deviate from the mean values attributed to the slice coordinates, giving each slice a finite transverse extent. This transverse extent of the particle distribution is described conveniently by its central second-order moments. These moments are defined as the variance of the particle coordinates $x \ldots y'$ from their center $x_\nu \ldots y'_\nu$ and read for instance:

$$m_{xx'\,\nu} = \overline{(x - x_\nu)\,(x' - x'_\nu)}, \tag{2.1}$$

the bar indicating the mean value over all particles in the slice. In order to get a complete characterization of the variances of the transverse particle distribution within a slice one needs the 10 central moments $m_{xx\,\nu}$, $m_{xx'\,\nu}$, $m_{x'x'\,\nu}$, $m_{yy\,\nu}$, $m_{yy'\,\nu}$, $m_{y'y'\,\nu}$, $m_{xy\,\nu}$, $m_{xy'\,\nu}$, $m_{x'y\,\nu}$, $m_{x'y'\,\nu}$ (see A. Chao, [12]). For the purposes of the bunch transformation it will turn out to be convenient to write the central moments in a matrix form:

$$\mathbf{M}_\nu = \begin{pmatrix} m_{xx\,\nu} & m_{xx'\,\nu} & m_{xy\,\nu} & m_{xy'\,\nu} \\ m_{x'x\,\nu} & m_{x'x'\,\nu} & m_{x'y\,\nu} & m_{x'y'\,\nu} \\ m_{yx\,\nu} & m_{yx'\,\nu} & m_{yy\,\nu} & m_{yy'\,\nu} \\ m_{y'x\,\nu} & m_{y'x'\,\nu} & m_{y'y\,\nu} & m_{y'y'\,\nu} \end{pmatrix}. \tag{2.2}$$

From the definition 2.1 it follows that the matrix $\mathbf{M}_\nu$ is symmetric.

Throughout all our tracking calculations we will assume that the particles are ultrarelativistic and hence approximate the longitudinal velocity of the particles to be equal to the speed of light c_0. As a consequence, the relative longitudinal position of a particle within the bunch remains practically fixed. The charge exchange between adjacent slices can therefore be neglected and the charges attributed to the individual slices remain constant. In order to justify this approximation we will carry out an estimation of the relative motion of particles caused by a spread of the injection energies and by a spread of the accelerating gradients acting on different particles.

The transit time required by a particle to traverse the entire accelerating machine can be written as

$$T = \int_0^{L_{tot}} \frac{\mathrm{d}z}{v(z)} = \frac{1}{c_0} \int_0^{L_{tot}} \frac{\mathrm{d}z}{\beta(z)}, \tag{2.3}$$

where $\beta(z) = v(z)/c_0$ is the relativistic factor and L_{tot} denotes the machine length. We will assume now that the particles are accelerated uniformly along the machine, which means that the relativistic factors $\gamma(z)$ of the particles vary as $\gamma(z) = \gamma_0 + z\gamma'$. Integration of 2.3 then gives us

$$\begin{aligned} T &= \frac{1}{c_0} \int_0^{L_{tot}} \frac{\gamma(z)}{\sqrt{\gamma^2(z) - 1}} \mathrm{d}z \\ &= \frac{1}{c_0 \gamma'} \left(\sqrt{(\gamma_0 + L_{tot}\gamma')^2 - 1} - \sqrt{\gamma_0^2 - 1} \right), \end{aligned} \tag{2.4}$$

where γ_0 denotes the relativistic factor at the beginning of the machine and γ' the derivative of the relativistic factor or, in other words, the relative energy gain per machine length.

Using the nominal values $\gamma_0 = 6164$ and $\gamma' = 33.3\mathrm{m}^{-1}$ for the SBLC design in formula 2.4, we find that a 1% deviation of the initial value for γ_0 and a 1% deviation of γ' each result in a lead or a lag of a particle of 0.024μm. For a bunch length of 0.5mm this corresponds to

$4.8 \cdot 10^{-5}$ units of the bunch length. We conclude therefore that our approximation of fixing the longitudinal positions of the particles within the bunch is justified.

For practical simulations concerning the SBLC, we will assume that the longitudinal distribution of the charge in the bunch has a Gaussian shape with the standard deviation σ_z. σ_z will also be referred to as the bunch length. The particles of a bunch will be simulated over a longitudinal range of $s = -N_\sigma\sigma_z \ldots + N_\sigma\sigma_z$. N_σ thus defines the longitudinal simulation range over a bunch in units of the bunch length. If not stated otherwise, N_σ will be chosen to be $N_\sigma = 4$. The centers of the slices s_ν will be placed equidistantly in the interval $-N_\sigma\sigma_z \ldots + N_\sigma\sigma_z$ at the positions

$$s_\nu = \frac{2\nu - (N_s + 1)}{N_s} N_\sigma \sigma_z, \qquad \nu = 1 \ldots N_s, \tag{2.5}$$

where N_s is the number of slices in the bunch. The charge attributed to a slice then becomes:

$$q_\nu = q_{bunch} \frac{\exp\left(-\frac{s_\nu^2}{2\sigma_z^2}\right)}{\sum_{\mu=1}^{N_s} \exp\left(-\frac{s_\mu^2}{2\sigma_z^2}\right)}. \tag{2.6}$$

In its current state our bunch model will simulate all particles of a slice as having the same energy, since the equations of motion will be solved using the uniform particle energy W_ν for all particles of one slice. In reality, however, particles located in the same region of a bunch will have energies that deviate from the mean particle energy in that region. These energy deviations are referred to as the uncorrelated energy spread. The most important source of uncorrelated energy spread in a linear collider are the bunch compressors. Into these bunch compressors the beams are injected from the damping rings in order to reduce the bunch length. (See [6] as an example.) In the case of the SBLC, the reduction of the bunch length is roughly one order of magnitude and the bunches will emerge from the compressor with an uncorrelated energy spread of $\approx 1\%$ rms (root mean square).

In some cases it may be desirable to include the uncorrelated energy spread in the simulations [13]. If inclusion of the uncorrelated energy spread seems necessary, we will simulate each slice as a superposition of a number of subslices. Each of these subslices will be modeled in the same way as was outlined previously for a slice. Thus, every subslice has its individual transverse coordinate vector $\vec{\mathcal{X}}_{\nu\lambda} = (x_{\nu\lambda}, x'_{\nu\lambda}, y_{\nu\lambda}, y'_{\nu\lambda})^t$, a mean energy $W_{\nu\lambda}$ and a charge $q_{\nu\lambda}$. Again, the transverse extent of each subslice is described by the distribution moments $m_{xx\,\nu\lambda} \ldots m_{y'y'\,\nu\lambda}$. All subslices constituting a slice will share the same longitudinal position that was already attributed to the slice. However, the subslices will differ in their initial energies. We will assume that at injection the initial particle energies within a slice of the bunch are distributed with a Gaussian density profile around the mean value W_ν. This density distribution will be characterized by its standard deviation σ_W. σ_W is also referred to as the uncorrelated energy spread at injection. For the simulations we will consider all particles with initial energies ranging within $W = W_\nu - N_W\sigma_W \ldots W_\nu + N_W\sigma_W$. N_W thus describes the simulation range for the initial energy in units of σ_W. In our simulations that include the uncorrelated energy spread we will use $N_W = 3$. The subslices are assigned values of the initial energy that are distributed equidistantly in the interval $W_\nu - N_W\sigma_W \ldots W_\nu + N_W\sigma_W$:

$$W_{\nu\lambda} = W_\nu + \frac{2\lambda - (N_{ss} + 1)}{N_{ss}} N_W \sigma_W, \qquad \lambda = 1 \ldots N_{ss}, \tag{2.7}$$

where, N_{ss} is the number of subslices per bunch. As the beam travels along the accelerator, the energies of the subslices may evolve independently. As we assume a Gaussian density profile

for the energy distribution within a slice, the charge attributed to a subslice becomes:

$$q_{\nu\lambda} = q_\nu \frac{\exp\left(-\frac{(W_{\nu\lambda} - W_\nu)^2}{2\sigma_W^2}\right)}{\sum_{\mu=1}^{N_{ss}} \exp\left(-\frac{(W_{\nu\mu} - W_\nu)^2}{2\sigma_W^2}\right)}. \tag{2.8}$$

Bunch Transport

A particle passing through an element of the linac with an initial transverse position $\vec{\mathcal{X}} = (x, x', y, y')^t$ in the $\{x, x', y, y'\}$-space and an energy W will experience a transformation of its position vector and perhaps a change of energy ΔW. This transformation will be approximated as being linear and can be expressed with a transfer matrix $\mathbf{T}$ as:

$$\tilde{\vec{\mathcal{X}}} = \mathbf{T}\vec{\mathcal{X}}.$$

Let $\Delta\vec{\mathcal{X}} = \vec{\mathcal{X}} - \vec{\mathcal{X}}_\nu$ denote the deviation of the particle coordinates from the mean coordinates of the slice. Due to linearity we get immediately

$$\Delta\tilde{\vec{\mathcal{X}}} = \mathbf{T}\Delta\vec{\mathcal{X}}.$$

The transformation law for the central distribution moments becomes

$$\tilde{\mathbf{M}} \;=\; \mathbf{T}\mathbf{M}\mathbf{T}^{\mathbf{t}} \tag{2.9}$$

(see for instance [14]). As the matrix $\mathbf{M}$ is symmetric, we need not carry out the full matrix multiplications during the calculation. In addition, many of the elements of the transfer matrices $\mathbf{T}$ vanish, so exploiting the properties of these matrices will result in further simplification. Then, the transformation of the moments through a drift space of length L for instance becomes:

$$\begin{aligned} \tilde{m}_{xx} &= m_{xx} + 2Lm_{xx'} + L^2 m_{x'x'} \\ \tilde{m}_{xx'} &= m_{xx'} + Lm_{x'x'} \\ \tilde{m}_{x'x'} &= m_{x'x'} \\ &\dots \end{aligned} \tag{2.10}$$

and likewise for the other moments.

2.1.2 Emittance

It was mentioned in section 2.1.1 that the particles of a beam are distributed randomly in the coordinate space $\{x, x', y, y', s, W\}$ around the mean values of these parameters for the beam $(\bar{x}, \bar{x}', \bar{y}, \bar{y}', \bar{s}, \bar{W})$. This corresponds to a distribution of these particles in the phase space $\{x, p_x, y, p_y, s, W\}$ around their center $(\bar{x}, \bar{p_x}, \bar{y}, \bar{p_y}, \bar{s}, \bar{W})$, where p_x and p_y are the transverse momenta of the particles. For an ensemble of particles, the mean deviation of the particle coordinates in the phase space from their mean values can be parametrized by a phase space volume. According to Liouville's theorem, phase space volumes are invariant for a time invariant Hamiltonian system. Furthermore, if the various degrees of freedom are decoupled, conservation of the phase space volume holds for each degree of freedom [15]. A conservation of the volume V_p

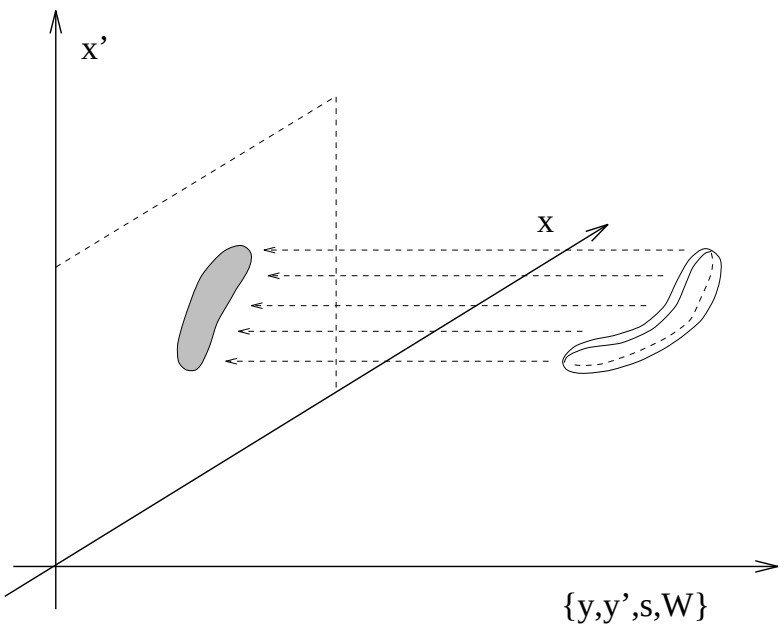

Fig. 2.2 Projection of the coordinate space on the $\{x, x'\}$-plane. The area occupied by the particles in the transverse planes will serve as a measure for the beam quality.

in the transverse coordinates $\{x, p_x\}$ (or equivalently $\{y, p_y\}$) is equivalent to a transformation of the volume V_c in the coordinate space $\{x, x'\}$ according to

$$V_p(t) = V_{p0} \qquad \rightarrow \qquad \gamma(t)\beta(t)V_c(t) = \gamma(t_0)\beta(t_0)V_{c0}, \tag{2.11}$$

where $\beta(t)$ and $\gamma(t)$ are the relativistic factors. For our applications we will assume $\beta \approx 1$. As a criterion for the beam quality we are particularly interested in the distribution of particles in the transverse degrees of freedom, i.e. in the coordinate spaces $\{x, x'\}$ and $\{y, y'\}$. To this end we introduce a quantity called emittance which denotes the volume of the projection of the full coordinate space of the particles in a bunch on the coordinate spaces $\{x, x'\}$ or $\{y, y'\}$ (Fig. 2.2).

With $\Delta x = x - \overline{x}$ denoting the deviation of the offset of a particle from the mean offset of the particles in the beam and $\Delta x' = x' - \overline{x'}$ likewise denoting the deviation of its slope, it is defined mathematically as

$$\epsilon_x = \sqrt{\overline{\Delta x^2}\;\overline{\Delta x'^2} - \overline{\Delta x \Delta x'}^2}. \tag{2.12}$$

The definition of the emittance for the y-coordinates is equivalent. In some references, this emittance is called projected emittance in order to distinguish it from the full 6-dimensional emittance. The geometrical significance as equivalent area in the coordinate space is illustrated in Fig. 2.3. Due to the conservation of phase space volume, the emittance decreases inversely proportional to $\gamma\beta$ as the beam is accelerated. This effect is called adiabatic damping and it contributes decisively to the realization of a small absolute beam emittance at the interaction region. The normalized emittance is defined by

$$\epsilon_{xN} = \gamma\beta\epsilon_x. \tag{2.13}$$

In an ideal accelerator without nonlinear forces and without interaction between the particles of the beam, barring dispersive effects, the normalized emittance is invariant. Imperfections in the machine leading to deformations of the bunch through wake field effects, dispersion etc. lead to emittance dilution, increasing the normalized emittance to a value greater than its value

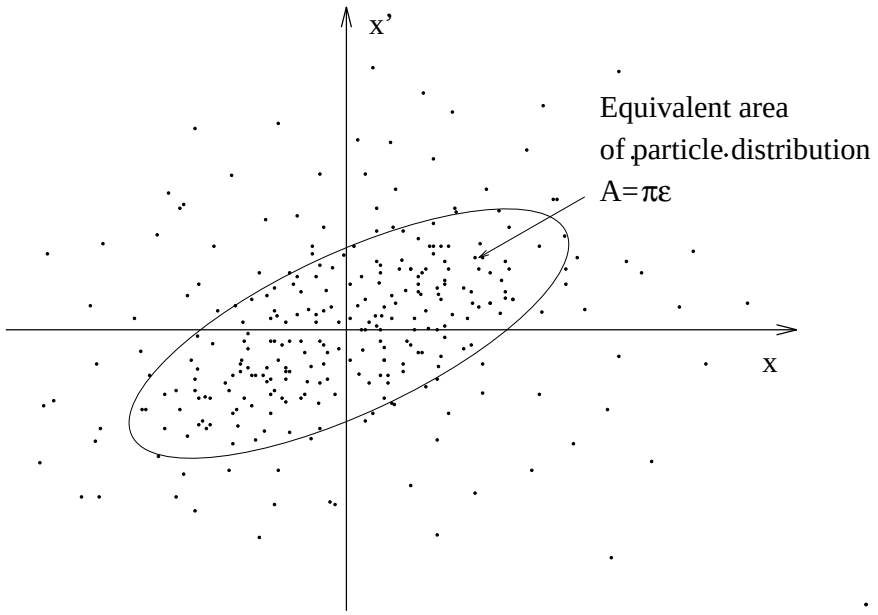

Fig. 2.3 Distribution of particles in the coordinate space. The area over which the particles are scattered will be described by the emittance.

at injection into the machine. This increase of the normalized emittance of the beam along the machine is therefore a suitable measure of the capacity of that machine to preserve a small phase space volume and hence produce a small beam spot at the interaction point.

In our simulations we will calculate the beam emittance explicitly as

$$\epsilon_x = \sqrt{\sigma_{xx}\sigma_{x'x'} - \sigma_{xx'}^2}, \tag{2.14}$$

where the variances are defined as

$$\begin{aligned}
\sigma_{xx} &= \frac{1}{\sum_\nu q_\nu} \sum_\nu q_\nu \left[(x_\nu - \bar{x})^2 + m_{xx\,\nu} \right], \\
\sigma_{x'x'} &= \frac{1}{\sum_\nu q_\nu} \sum_\nu q_\nu \left[(x'_\nu - \bar{x'})^2 + m_{x'x'\,\nu} \right], \\
\sigma_{xx'} &= \frac{1}{\sum_\nu q_\nu} \sum_\nu q_\nu \left[(x_\nu - \bar{x})\,(x'_\nu - \bar{x'}) + m_{xx'\,\nu} \right].
\end{aligned}$$

The summation extends over all bunches, slices and subslices used for modeling the beam. This definition of the emittance includes both the emittance contributions from the finite transverse extent of the slices, and the relative offsets and trajectory slopes of the bunches, slices and subslices representing the beam.

In our picture of the beam being decomposed into bunches, slices and subslices, the emittance can be thought of as being composed of two different contributions, namely the finite extent of the individual slices in the $\{x, x'\}$ or $\{y, y'\}$ space, which shall be referred to as self emittance, and second the relative offsets between the individual slices (or bunches) in that space, which we will call the centroid emittance. The centroid emittance is an emittance that gives us the area over which the centers of the slices or bunches of a beam are scattered as opposed to the full emittance, which gave the equivalent area occupied by all particles of the beam. Hence, the centroid emittance is the emittance that would be seen if all particles of a bunch or slice were concentrated at its center. The definition of the centroid emittance is

equivalent to expression 2.12 and reads

$$\epsilon_{xC} = \sqrt{\sigma_{xxC}\sigma_{x'x'C} - \sigma_{xx'C}^2}, \tag{2.15}$$

where the variances are defined as

$$\begin{aligned}
\sigma_{xxC} &= \frac{1}{\sum_\nu q_\nu} \sum_\nu q_\nu \left(x_\nu - \bar{x}\right)^2, \\
\sigma_{x'x'C} &= \frac{1}{\sum_\nu q_\nu} \sum_\nu q_\nu \left(x'_\nu - \bar{x'}\right)^2, \\
\sigma_{xx'C} &= \frac{1}{\sum_\nu q_\nu} \sum_\nu q_\nu \left(x_\nu - \bar{x}\right)\left(x'_\nu - \bar{x'}\right).
\end{aligned}$$

The sums in the variances extend over all bunches, slices and subslices in the bunch train. Again, the normalized centroid emittance is

$$\epsilon_{xCN} = \gamma\beta\epsilon_{xC}. \tag{2.16}$$

The self emittance, describing the extent of an individual slice or subslice, is defined as

$$\epsilon_{xs} = \sqrt{m_{xx}m_{x'x'} - m_{xx'}^2}.$$

In several applications, we will be interested only in the centroid emittance. This is especially the case in situations where the emittance contribution from a process is smaller than the self emittance. Then, the larger self emittance would obscure small changes of the centroid emittance and hence obstruct interpretation of the response of this process to parameter changes. During our investigation of multi-bunch effects we will exclusively deal with centroid emittances.

Both normalized emittance and normalized centroid emittance may be expressed in units of the initial normalized vertical emittance of the beam at injection. This leads to the definition of the relative emittance

$$\epsilon_r = \epsilon_N / \epsilon_{yN0}$$

($\epsilon_{yN0} = 5 \cdot 10^{-7}$radm) and the relative centroid emittance

$$\epsilon_{rC} = \epsilon_{CN} / \epsilon_{yN0}.$$

2.1.3 Longitudinal Wake Fields

A charged particle (q_1) traversing a cavity with a trajectory $\vec{r}_1(t)$ will excite electromagnetic modes that have a non-vanishing electric field component parallel to the particle trajectory, resulting in a loss of energy for that particle. In addition, the excited modes can influence the energies of trailing particles and their transverse motion. The electromagnetic fields associated with these modes are called the wake field. The excited fields obey the Maxwell equations for vacuum

$$\begin{aligned}
\text{curl } \vec{H} &= \dot{\vec{D}} + \vec{j} & \qquad \text{div } \vec{B} &= 0 \\
\text{curl } \vec{E} &= -\dot{\vec{B}} & \qquad \text{div } \vec{D} &= \rho
\end{aligned} \tag{2.17}$$

The equations

$$\vec{D} = \varepsilon_0 \vec{E} \qquad \vec{B} = \mu_0 \vec{H} \tag{2.18}$$

establish the relation between $\vec{E}$ and $\vec{D}$ and the relation between $\vec{B}$ and $\vec{H}$. The corresponding electromagnetic field exerts the force

$$\vec{F}(\vec{r},t) = q_2 \left[\vec{E}(\vec{r},t) + \vec{v} \times \vec{B}(\vec{r},t)\right] \tag{2.19}$$

on a trailing particle with the charge q_2. Extensive discussions of wake fields can be found for instance in [16], [17], [18], [19].

We now assume that we are dealing with a cavity that has perfect cylindrical symmetry. Moreover, we assume that the length of an accelerating structure is short in comparison with a betatron wavelength (see appendix C). In this case, the change of the transverse particle offsets with respect to the structure axes over a structure length will be small. This leads us to the

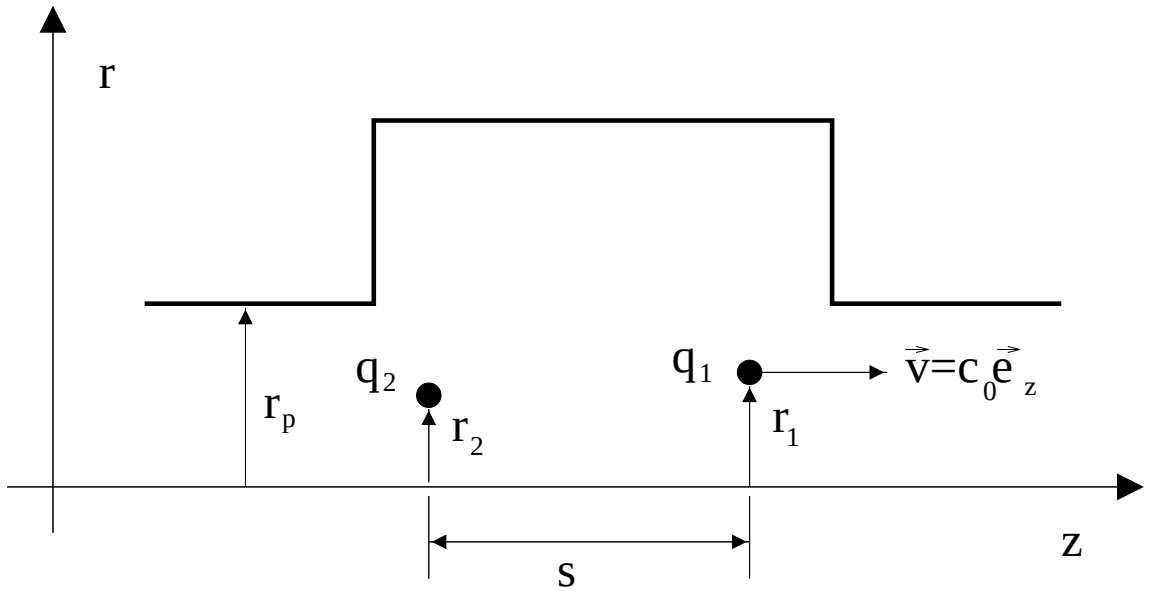

Fig. 2.4 Two charges q_1 and q_2 traversing a cavity at the constant radii r_1 and r_2. It is assumed that the longitudinal velocity is equal to the velocity of light c_0. r_p is the radius of the beam pipe.

approximation that the leading and the trailing particles traverse the structure with constant offsets from the structure axis r_1, r_2 at the constant azimuthal angles ϕ_1, ϕ_2. Moreover, we assume that the longitudinal velocity of the particles is equal to the velocity of light c_0. This situation is illustrated schematically in Fig. 2.4

With these assumptions one obtains the total momentum transfer on a particle trailing with the distance s as:

$$\Delta\vec{p} = \frac{q_2}{c_0}\int_{-\infty}^{\infty}\left[\vec{E}(r_2,\phi_2,z,t=\frac{z+s}{c_0}) + c_0\cdot\vec{e}_z \times \vec{B}(r_2,\phi_2,z,t=\frac{z+s}{c_0})\right]\mathrm{d}z. \tag{2.20}$$

To begin with, we are interested in the energy that is transferred from a leading to a trailing particle by the wake fields. We therefore define the "longitudinal wake potential" of a charge q_1 ([16], [18]) as

$$\mathcal{W}_{\|}(r_1,r_2,\phi_1,\phi_2,s) = \frac{1}{q_1}\int_{-\infty}^{\infty} E_z(r_2,\phi_2,z,t=\frac{z+s}{c_0})\mathrm{d}z. \tag{2.21}$$

This definition of the wake potential does not require the charge exciting the wake fields to be pointlike. With the wake potential, we express the energy transfer to the trailing particle q_2 as

$$\Delta W = q_1 q_2 \mathcal{W}_{\|}(r_1,r_2,\phi_1,\phi_2,s). \tag{2.22}$$

For a cylindrically symmetric structure, the wake potential can be decomposed into contributions of different azimuthal order m. If the beam path area includes the symmetry axis $r = 0$ and extends to the beam pipe radius r_p, it can be shown that for particle offsets r_1, r_2 smaller than r_p the wake potential of a point charge can be expressed as ([18], [20]):

$$\mathcal{W}_{\parallel}(r_1, r_2, \phi_1, \phi_2, s) = \sum_{m=0}^{\infty} r_1^m r_2^m w_{\parallel}^m(s) \cos\left(m\left(\phi_2 - \phi_1\right)\right). \tag{2.23}$$

The functions $w_{\parallel}^m(s)$ are referred to as the "longitudinal wake functions." We point out that the wake functions $w_{\parallel}^m(s)$ are causal, which means that they vanish for negative arguments. They are a geometrical property of the cavity and may be computed numerically. The contributions $m = 0$ to $m = 2$ to the wake potential are called the "monopole", "dipole" and "quadrupole wake."

For practical applications, we will be interested in the effect of the wake potential in a bunch of particles, which has a finite longitudinal extent. In order to obtain this wake potential, one could convolve the wake functions of the structure with the charge density and the particle offsets in the bunch. A very straight-forward way to accomplish this would be to simply divide the bunch into a large number N_P of macro particles with the coordinates r_ν, ϕ_ν and the longitudinal position s_ν within the bunch and evaluate the sum

$$\mathcal{W}_{\parallel}(r, \phi, s) = \frac{1}{q_{bunch}} \sum_{m=0}^{\infty} r^m \sum_{\nu=1}^{N_P} q_\nu r_\nu^m w_{\parallel}^m(s - s_\nu) \cos\left(m\left(\phi - \phi_\nu\right)\right), \tag{2.24}$$

where q_{bunch} denotes the entire bunch charge

$$q_{bunch} = \sum_{\nu=1}^{N_P} q_\nu.$$

A similar procedure has been proposed for instance in [21]. A drawback of this method is the comparatively great computing effort required for carrying out this convolution. The number of operations required for this task is proportional to the square of the number of macroparticles N_P used for the simulation of the bunch. For this reason, we will follow a different approach. This approach is justified by the fact that the convolution of two Gauss functions characterized by their variances σ_1^2, σ_2^2 will yield another Gauss function according to

$$\frac{1}{\sqrt{2\pi}\sigma_3} \exp\left(-\frac{s^2}{2\sigma_3^2}\right) = \int_{-\infty}^{\infty} \frac{1}{\sqrt{2\pi}\sigma_1} \exp\left(-\frac{\varsigma^2}{2\sigma_1^2}\right) \frac{1}{\sqrt{2\pi}\sigma_2} \exp\left(-\frac{(s-\varsigma)^2}{2\sigma_2^2}\right) \mathrm{d}\varsigma, \tag{2.25}$$

$$\sigma_3^2 = \sigma_1^2 + \sigma_2^2. \tag{2.26}$$

From this observation it follows that by convolving the wake potential of a short bunch with Gaussian charge distribution with another Gaussian charge distribution, one will again obtain the wake potential of a bunch with a Gaussian charge distribution according to 2.26. As already mentioned in section 2.1.1, it will be assumed throughout all our simulations that the bunches have a Gaussian longitudinal charge distribution. For this reason, we will carry out our calculations of the wake potentials by calculating the wake $\mathcal{W}_{0\parallel}(s)$ of a short bunch with a time domain field calculation program ([22], [23]) and convolving this wake with the charge distribution of our actual bunch. This process is depicted in Fig. 2.5.

We now apply this method to the computation of the monopole wake potential. In the algorithm used for our simulations, the wake seen by the slice ν is calculated as the sum of the wakes of all slices at the center of slice ν. As the wakes attributed to the different slices

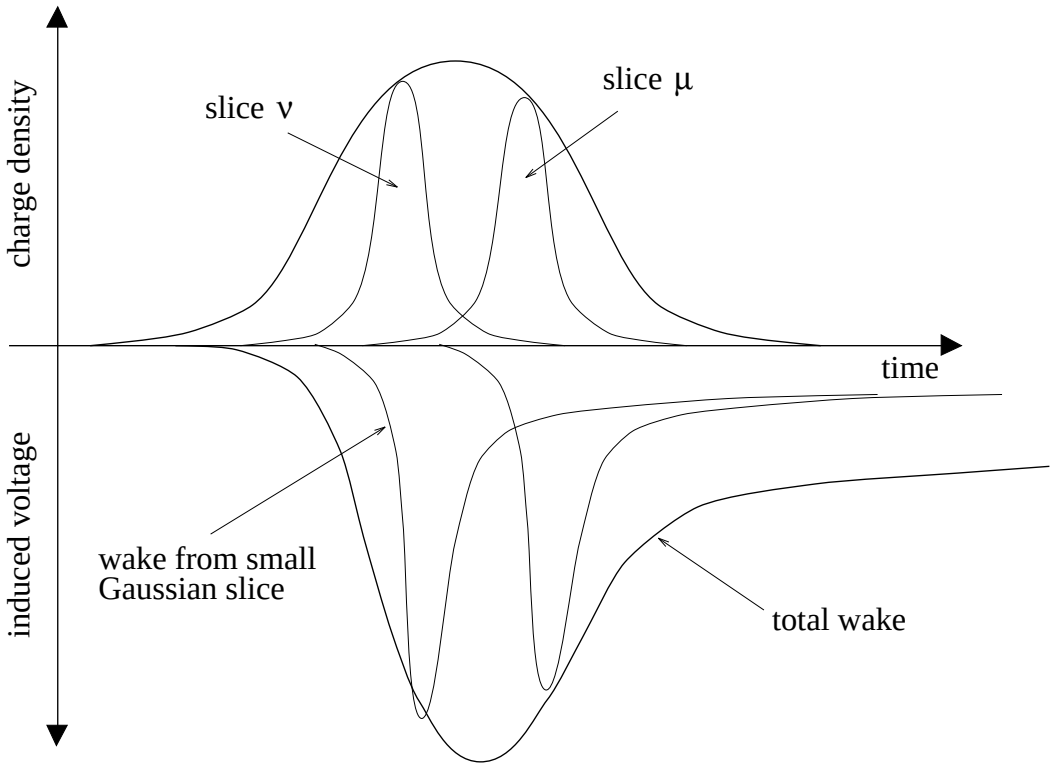

Fig. 2.5 Convolution of the wake potential from the wake of a short bunch. The wake of a short bunch is convolved with the charges contained in the slices of the actual bunch.

are associated with a Gaussian charge profile, there is an overlap of the charge distributions assigned to the various slices. Therefore, the wake of slice μ at slice ν is non-vanishing also if slice ν is earlier than slice μ, i.e. if $\nu < \mu$. The corresponding component of the wake at slice ν is included in the convolution of the wake [24].

For the case of the monopole wake, the radial and azimuthal dependence vanishes. The wake potential $\mathcal{W}_{\|\nu}^{monopole}$ for the ν-th slice in the bunch can thus be written in the following form:

$$\mathcal{W}_{\|\nu}^{monopole} = \frac{1}{q_{bunch}} \sum_{\mu} q_{\mu} \mathcal{W}_{0\|}^{monopole}(s_{\nu} - s_{\mu}). \tag{2.27}$$

The summation extends over all slices (or subslices) of the bunch. The voltage induced on a particle in the ν-th slice via the monopole wake can be expressed as

$$\Delta U_{\nu} = q_{bunch} \mathcal{W}_{\|\nu}^{monopole}. \tag{2.28}$$

A major advantage of this algorithm lies in the efficiency of the calculation. Instead of modeling the bunch as consisting of a large number of macro particles and carrying out a convolution according to 2.24, we confine ourselves to partitioning the bunch into comparatively few longitudinal regions, the slices, and calculate the influence of these entire slices on each other. As a consequence, the order of the computing effort reduces to the square of the number of slices, whereas in a calculation carrying out the convolution of the wake function with a large number of macro particles the computing effort would have been proportional to the square of the number of macro particles ([24], [25]).

The significance of the short range monopole wake lies in the fact that it generates an energy spread in the bunch train by inducing different voltages on different regions of the bunch. As a consequence, the different regions of the bunch will be subject to a different strong focusing in the quadrupoles, leading to different trajectories for the particles of the bunch. Particles

traversing the accelerator with an initially coherent transverse motion will decohere and emerge from the accelerator with different offsets and slopes, which corresponds to an increase of the projected emittance.

Secondly, we direct our attention to the case of the dipole wake (m=1). We proceed in a way that is very similar to our treatment of the monopole wake. We calculate numerically the dipole wake potential $\mathcal{W}_{0\|}^{dipole}(a,s)$ for a short bunch traversing the structure with the offset a. This wake potential will then be used as the Green's function for the convolution to the wake of the actual bunch.

Since for dipole wake the induced voltage is proportional both to the offset of the leading particle and the offset of the affected particle, the trajectory of the bunch through the cavity must be included in the calculation of the total wake. Because of the non-vanishing azimuthal dependence of the dipole wake, we get an excitation of the wake in two polarizations independently, namely in the x-direction and in the y-direction.

Continuing with the assumptions made already for 2.23, the offsets of the slices with respect to the structure axes are approximated as being constant. The convolution for the longitudinal dipole wake potential then reads:

$$\mathcal{W}_{\|\nu}^{dipole} = \frac{1}{q_{bunch}} \left[\bar{x}_\nu \sum_\mu q_\mu \bar{x}_\mu \frac{\mathcal{W}_{0\|}^{dipole}(a, s_\nu - s_\mu)}{a^2} + \bar{y}_\nu \sum_\mu q_\mu \bar{y}_\mu \frac{\mathcal{W}_{0\|}^{dipole}(a, s_\nu - s_\mu)}{a^2} \right] \tag{2.29}$$

where $\overline{x}_\nu$, $\overline{y}_\nu$ are the mean offsets of the ν-th slice from the cavity axis. The voltage induced on a particle in the $\nu - th$ slice by the dipole wake becomes

$$\Delta U_\nu = q_{bunch} \mathcal{W}_{\|\nu}^{dipole}. \tag{2.30}$$

Like the monopole wake, the longitudinal dipole wake will induce an energy spread in the bunch. However, the magnitude of the induced voltages is proportional both to the offset of the particles exciting the wake and the offset of the affected particles. The energy spread caused by the longitudinal dipole wake therefore tends to be considerably smaller than the effect of the monopole wake.

Finally, we remark that contributions to the longitudinal wake potential of orders higher than the dipole wake will not be considered.

2.1.4 Deflection by Dipole and Quadrupole Wakes

The momentum transfer on a trailing charge q_2 via the wake fields as described in equation 2.20 generally acts both in the longitudinal and in the transverse directions. The transverse momentum transfer is commonly expressed using the transverse wake potential as:

$$\Delta \vec{p}_\perp(s) = q_2 q_{bunch} \frac{1}{c_0} \vec{\mathcal{W}}_\perp(s). \tag{2.31}$$

As we will now show, this transverse momentum transfer is related to the transferred longitudinal momentum and hence to the transferred energy via the Panofsky-Wenzel theorem ([18], [26]). From the transverse electric and magnetic field, the transverse wake potential is derived as:

$$\vec{\mathcal{W}}_\perp(\vec{x}_\perp, s) = \frac{1}{q_{bunch}} \int_{-\infty}^{\infty} \left[\vec{E}_\perp(\vec{x}_\perp, z, t = \frac{z+s}{c_0}) + c_0 \vec{e}_z \times \vec{B}_\perp(\vec{x}_\perp, z, t = \frac{z+s}{c_0}) \right] \mathrm{d}z. \tag{2.32}$$

We write the derivative of the transverse wake potential with respect to s as

$$\frac{\partial}{\partial s}\vec{\mathcal{W}}_\perp(\vec{x}_\perp,s)=\frac{1}{q_{bunch}}\int_{-\infty}^{\infty}\left[\frac{1}{c_0}\frac{\partial}{\partial t}\vec{E}_\perp(\vec{x}_\perp,z,t=\frac{z+s}{c_0})+c_0\vec{e}_z\times\frac{1}{c_0}\frac{\partial}{\partial t}\vec{B}_\perp(\vec{x}_\perp,z,t=\frac{z+s}{c_0})\right]\mathrm{d}z. \tag{2.33}$$

From the Maxwell equations we get

$$\vec{e}_z\times\frac{\partial}{\partial t}\vec{B}_\perp=\frac{\partial}{\partial z}\vec{E}_\perp-\nabla_\perp E_z,$$

which allows us to rewrite 2.33 as

$$\begin{aligned}\frac{\partial}{\partial s}\vec{\mathcal{W}}_\perp(\vec{x}_\perp,s) &= \frac{1}{q_{bunch}}\int_{-\infty}^{\infty}\left[\left(\frac{\partial}{\partial z}+\frac{1}{c_0}\frac{\partial}{\partial t}\right)\vec{E}_\perp(\vec{x}_\perp,z,t=\frac{z+s}{c_0})\right.\\ &\qquad\left.-\nabla_\perp E_z(\vec{x}_\perp,z,t=\frac{z+s}{c_0})\right]\mathrm{d}z\\ &= \frac{1}{q_{bunch}}\int_{-\infty}^{\infty}\left[\frac{\mathrm{d}}{\mathrm{d}z}\vec{E}_\perp(\vec{x}_\perp,z,t=\frac{z+s}{c_0})-\nabla_\perp E_z(\vec{x}_\perp,z,t=\frac{z+s}{c_0})\right]\mathrm{d}z.\end{aligned}$$

If the transverse electric field $\vec{E}_\perp$ goes to zero for $z\to\pm\infty$, this reduces to

$$\frac{\partial}{\partial s}\vec{\mathcal{W}}_\perp(\vec{x}_\perp,s)=-\frac{1}{q_{bunch}}\int_{-\infty}^{\infty}\nabla_\perp E_z(\vec{x}_\perp,z,t=\frac{z+s}{c_0})\mathrm{d}z. \tag{2.34}$$

This relation is known as the Panofsky-Wenzel Theorem.

It follows from equation 2.34 that the transverse wake potential can be obtained from the longitudinal one by performing the integration

$$\vec{\mathcal{W}}_\perp(\vec{x}_\perp,s)=-\int_{-\infty}^{s}\nabla_\perp\mathcal{W}_\parallel(\vec{x}_\perp,\varsigma)\mathrm{d}\varsigma. \tag{2.35}$$

In the following, we will make use of relation 2.35 in order to derive the transverse wake potentials from the longitudinal ones and to show how the transverse kicks on the particles of the beam by the wake fields are obtained.

For the monopole wake the transverse derivative of the induced voltage vanishes. From 2.34 it follows immediately that the monopole wake does not impart any momentum transverse to the structure axis on the beam and we get for the transverse monopole wake potential:

$$\vec{\mathcal{W}}_\perp^{monopole}=0.$$

Thus, the monopole wake can only affect the particle energies by its longitudinal component.

For the dipole wake, the voltage goes linearly with the transverse offsets of the particles exciting the wake and of the influenced particles from the structure axis (see for instance [16], [17]). Integration of the longitudinal wake $\mathcal{W}_{0\parallel}^{dipole}(a,s)$ according to 2.34 and differentiation with respect to the offset of the kicked particle from the structure axis yields the transverse dipole wake:

$$\mathcal{W}_{0\perp}^{dipole}(a,s)=-\frac{1}{a}\int_{-\infty}^{s}\mathcal{W}_{0\parallel}^{dipole}(a,\varsigma)\mathrm{d}\varsigma. \tag{2.36}$$

Now we want to use $\mathcal{W}_{0\perp}^{dipole}(a,s)$ to calculate the transverse wake potential $\mathcal{W}_{\perp x\nu}^{dipole}$ in a bunch consisting of several slices with different offsets. This is achieved by performing the convolution

$$\mathcal{W}_{\perp x\nu}^{dipole}=\frac{1}{q_{bunch}}\sum_\mu q_\mu\overline{x}_\mu\frac{\mathcal{W}_{0\perp}^{dipole}(a,s_\nu-s_\mu)}{a} \tag{2.37}$$

from which the transverse momentum transfer is calculated according to 2.31. As equation 2.29 contains no terms coupling the wakes excited in the x-plane and in the y-plane, the convolution 2.37 must be carried out for both planes separately and also the resulting kicks will act independently in the two planes.

The significance of the transverse dipole wake lies in the fact that it imparts transverse kicks of different strength on different regions of the bunch. As a consequence of these differential kicks the particles of the beam acquire an additional divergence, leading to an increase in the projected emittance. As we will see later, the effect of the transverse dipole wake is very severe.

For the quadrupole wake, the voltage is proportional to the square of the distance of the leading and the trailing particles from the cavity axis. This complicates matters since both excitation of the wake as well as the involved transverse kicks depend not only on the centers of the charges q_1 and q_2, but also on the transverse charge distribution within the individual slices.

The energy transfer between two point charges by the quadrupole wake as expressed in equation 2.23 can be reformulated as

$$\Delta W^{quadrupole}(x_1, x_2, y_1, y_2, s) = q_1 q_2 w_{\parallel}^{quadrupole}(s) \left[(x_1^2 - y_1^2)(x_2^2 - y_2^2) + (2x_1 y_1)(2x_2 y_2)\right]. \tag{2.38}$$

Here, $w_{\parallel}^{quadrupole}(s)$ denotes the longitudinal quadrupole wake function and $x_1 \ldots y_2$ are the transverse particle offsets with respect to the structure axis.

We recognize that, in contrast to the case of the dipole wake, the two possible polarizations are not orthogonal but enclose an angle of 45°. The two polarizations will be referred to as the normal polarization with the extrema of its electric field lying in the direction of the vectors $\vec{e}_x$ and $\vec{e}_y$, and the skew polarization with the extrema of its electric field lying in the direction of the vectors $(\vec{e}_x + \vec{e}_y)/\sqrt{2}$ and $(\vec{e}_y - \vec{e}_y)/\sqrt{2}$. In equation 2.38 these polarizations correspond to the terms $x^2 - y^2$ and $2xy$ respectively. The indices $\oplus$ and $\otimes$ are used to indicate that a quantity pertains to the normal and the skew polarization of the wake fields respectively. As a consequence of the non-orthogonality of the two polarizations, the excitation of either polarization of the wake depends on the particle offsets in both planes. The transverse quadrupole wake in a short bunch traversing the structure at the transverse offset a is again obtained from the longitudinal one using theorem 2.35 as

$$\mathcal{W}_{0\perp}^{quadrupole}(a, s) = -\frac{2}{a}\int_{-\infty}^{s} \mathcal{W}_{0\parallel}^{quadrupole}(a, \varsigma)\mathrm{d}\varsigma \tag{2.39}$$

Assuming a constant particle offset in the cavity we can write the convolution sums for the excitation strengths as

$$\mathcal{C}_{\perp\oplus\nu}^{quadrupole} = \frac{1}{q_{bunch}} \sum_{\mu} q_\mu \left(\overline{x}_\mu^2 - \overline{y}_\mu^2 + \overline{m}_{xx\,\mu} - \overline{m}_{yy\,\mu}\right) \frac{\mathcal{W}_{0\perp}^{quadrupole}(a, s_\nu - s_\mu)}{a^3} \tag{2.40}$$

for the wake fields in the the normal polarization and

$$\mathcal{C}_{\perp\otimes\nu}^{quadrupole} = \frac{1}{q_{bunch}} \sum_{\mu} 2q_\mu \left(\overline{x}_\mu \overline{y}_\mu + \overline{m}_{xy\,\mu}\right) \frac{\mathcal{W}_{0\perp}^{quadrupole}(a, s_\nu - s_\mu)}{a^3} \tag{2.41}$$

for the skew polarization. From these sums we derive the transverse wake potentials as

$$\mathcal{W}_{\perp x\nu}^{quadrupole}(x, y) = x\mathcal{C}_{\perp\oplus\nu}^{quadrupole} + y\mathcal{C}_{\perp\otimes\nu}^{quadrupole}, \tag{2.42}$$

$$\mathcal{W}_{\perp y\nu}^{quadrupole}(x, y) = -y\mathcal{C}_{\perp\oplus\nu}^{quadrupole} + x\mathcal{C}_{\perp\otimes\nu}^{quadrupole}. \tag{2.43}$$

The transverse effect of the quadrupole wake is small, but as can be seen from equations 2.40 and 2.41, a quadrupole wake can be excited by a noncircular cross section of the beam even if the beam passes the cavity perfectly on axis. This is relevant for all current studies for a possible future linear collider, since they all envisage using a flat beam, where the horizontal emittance is considerably larger than the vertical emittance.

For brevity we introduce the parameters

$$\begin{aligned} S_{\oplus\nu} &= eq_{bunch}\frac{\mathcal{C}^{quadrupole}_{\perp\oplus\nu}}{W_\nu}, \\ S_{\otimes\nu} &= eq_{bunch}\frac{\mathcal{C}^{quadrupole}_{\perp\otimes\nu}}{W_\nu}, \end{aligned}$$

for the normal and the skew polarization of the wake at the slice under consideration. W_ν is the particle energy in the slice. The parameters $S_\oplus$ and $S_\otimes$ can be used to describe the deflection strength of the quadrupole wake potential. The transverse deflection imparted on a particle in the slice ν depends both on the deflection strength and its own transverse position and is expressed as:

$$\begin{aligned} \Delta x' &= S_{\oplus\nu}x + S_{\otimes\nu}y, \\ \Delta y' &= -S_{\oplus\nu}y + S_{\otimes\nu}x. \end{aligned} \tag{2.44}$$

The mean deflections of the entire slice are obtained directly from 2.44 by putting in its mean offsets $\overline{x}_\nu$, $\overline{x}_\nu$. Since for the quadrupole wake the strength of the deflecting field goes linearly with the distance from the axis, the quadrupole wake also has the effect of influencing the beam ellipse itself apart from imparting a transverse kick on its center. This is in contrast to the case of the transverse dipole wake: here, the transverse kick did not depend on the offset of the affected particle. Consequently, all particles in a subslice received the same transverse momentum transfer and hence the transverse distribution of the particles was not modified. Since in the case of the quadrupole wake the transverse kick depends on the offset of the affected particles, we get a modification of the divergence of the particles in a subslice. Modifying the transverse slopes of the particles by 2.44 transforms the central distribution moments as

$$\begin{aligned}
m_{xx\,\nu} &= m_{xx\,\nu 0} \\
m_{xx'\,\nu} &= m_{xx'\,\nu 0} + S_{\oplus\nu}m_{xx\,\nu 0} + S_{\otimes\nu}m_{xy\,\nu 0} \\
m_{x'x'\,\nu} &= m_{x'x'\,\nu 0} + S^2_{\oplus\nu}m_{xx\,\nu 0} + S^2_{\otimes\nu}m_{yy\,\nu 0} + 2\left(S_{\oplus\nu}m_{xx'\,\nu 0} + S_{\otimes\nu}m_{x'y\,\nu 0} + S_{\oplus\nu}S_{\otimes\nu}m_{xy\,\nu 0}\right) \\
m_{yy\,\nu} &= m_{yy\,\nu 0} \\
m_{yy'\,\nu} &= m_{yy'\,\nu 0} - S_{\oplus\nu}m_{yy\,\nu 0} + S_{\otimes\nu}m_{xy\,\nu 0} \\
m_{y'y'\,\nu} &= m_{y'y'\,\nu 0} + S^2_{\oplus\nu}m_{yy\,\nu 0} + S^2_{\otimes\nu}m_{xx\,\nu 0} + 2\left(S_{\otimes\nu}m_{xy'\,\nu 0} - S_{\oplus\nu}m_{yy'\,\nu 0} - S_{\oplus\nu}S_{\otimes\nu}m_{xy\,\nu 0}\right) \\
m_{xy\,\nu} &= m_{xy\,\nu 0} \\
m_{xy'\,\nu} &= m_{xy'\,\nu 0} - S_{\oplus\nu}m_{xy\,\nu 0} + S_{\otimes\nu}m_{xx\,\nu 0} \\
m_{x'y\,\nu} &= m_{x'y\,\nu 0} + S_{\oplus\nu}m_{xy\,\nu 0} + S_{\otimes\nu}m_{yy\,\nu 0} \\
m_{x'y'\,\nu} &= m_{x'y'\,\nu 0} + S_{\oplus\nu}\left(m_{xy'\,\nu 0} - m_{x'y\,\nu 0}\right) + S_{\otimes\nu}\left(m_{xx'\,\nu 0} + m_{yy'\,\nu 0}\right) + \\
&\quad \left(S^2_{\otimes\nu} - S^2_{\oplus\nu}\right)m_{xy\,\nu 0} + S_{\oplus\nu}S_{\otimes\nu}\left(m_{xx\,\nu 0} - m_{yy\,\nu 0}\right)
\end{aligned} \tag{2.45}$$

The distribution moments indexed as zero are the moments at the end of the cavity before inclusion of the effect from the quadrupole wakes. The modifications of these moments are thus applied as perturbations.

2.2 BNS Damping

After having discussed the impact of short range wake fields on the beam dynamics in the previous section, we will investigate the issues of actual machine operation. To this end we will first find a favorable operating point of the accelerating structures that will help minimize the emittance growth from dipole-like kicks. The obtained result will be relevant for all other simulations that include single-bunch effects.

One very important source of emittance dilution is betatron oscillation (see appendix C) of the beam around the machine axis. This emittance dilution is caused mainly by two effects.

1. Particles performing a betatron motion will traverse the accelerating structures with a non-vanishing offset from the structure axes. The dipole wake excited by leading particles of the bunch exerts a transverse force on trailing particles. As the magnitude of the transverse kick on the particles depends on their longitudinal position in the bunch, an additional spread of the particle coordinates in the transverse $\{x, x'\}$ and $\{y, y'\}$ planes is imparted. The effect of the wake fields is very severe, since the deflections in the individual structures add coherently.

2. If the bunch has a correlated energy spread, the various regions of the bunch move through the lattice with different betatron phase advance (appendix C), since the focusing strength of the quadrupoles is inversely proportional to the particle energies. As a result of this spread in the focusing strengths the transverse motion of the particles decoheres, i.e. it filaments, resulting in emittance dilution. The most important sources of the correlated energy spread are the monopole wake and the different phases of the accelerating wave for different longitudinal regions of the bunch.

A betatron oscillation of a bunch thus produces two effects that independently of each other have the potential of creating a large growth of the projected emittance. Betatron oscillations can be caused by a variety of effects, for instance injection error, dipole kicks from misaligned quadrupoles or ill-adjusted correction dipoles, long range dipole wakes or transverse kicks from the accelerating mode. A way to cope with this problem has been proposed in [27]. The idea here is to adjust the energy spread within the bunch in a fashion to get a mutual cancellation of the wake field and the chromatic effect. This is possible because the transverse force exerted by the quadrupoles and the force from the transverse dipole wakes display a similar behavior. The force from a quadrupole magnet on a particle is proportional to the offset of that particle, and the force from the dipole wake is proportional to the offset of the particles exciting this wake. If the bunch can be made to move coherently along the machine, both forces are proportional to the magnitude of the bunch offset in the quadrupoles and in the structures. Then an appropriate energy spread in the bunch can cause a variation of the focusing strength along the bunch that just cancels the force from the transverse dipole wake in the structures. A detailed discussion of this scheme, which is referred to as BNS damping (Balakin, Novokhatsky, Smirnov), can be found for example in [28].

In order to establish an analytical picture of how the chromatic and wake field effects act on a bunch one commonly utilizes a continuous approximation of the forces acting on a particle. In this approximation, the motion of the particles through the machine lattice is described by a differential equation for the transverse particle offset, using a smooth approximation for the forces caused by the quadrupoles and the wake fields in the structures. Specifically, we assume that the focusing of the particles is not confined to lumped quadrupole magnets but is distributed smoothly over the machine. This continuous focusing will be described by a focusing strength $k(z, s)$ for a particle at the position z in the machine and the position s

within the bunch. $k(z,s)$ is obtained from the betatron wavelength by $k(z,s) = (2\pi/\lambda_\beta(z,s))^2$. It is inversely proportional to the particle energy.

Furthermore, we assume a transverse dipole wake potential $\mathcal{W}'_\perp(a,s)$ that is distributed smoothly over the machine length. It is defined as the sum of the wake potentials of all accelerating structures in the machine divided by the machine length:

$$\mathcal{W}'_\perp(a,s) = \frac{1}{L_{tot}} \sum_{all\ structures} \mathcal{W}_\perp^{dipole}(a,s). \tag{2.46}$$

We generate the wake potential $\mathcal{W}_\perp^{dipole}(a,s)$ by convolution of the wake $\mathcal{W}_{0\perp}^{dipole}(a,s)$ of a short bunch with the charge density $\rho(s)$ of the actual bunch according to

$$\mathcal{W}_\perp^{dipole}(a,s) = \frac{1}{q_{bunch}} \int_{-\infty}^{\infty} \rho(\varsigma) \mathcal{W}_{0\perp}^{dipole}(a, s-\varsigma) \mathrm{d}\varsigma. \tag{2.47}$$

We assume now that the particles of the bunch have the uniform offset $x = x_0$ while the bunch is at the position $z = z_0$. The charge of the particles is q. The transverse motion the particles at this position is then characterized by the differential equation

$$\frac{\mathrm{d}^2}{\mathrm{d}z^2} x(z=z_0,s) = \left[-k(z=z_0,s) + \frac{q q_{bunch}}{\gamma(z=z_0,s) m_0 c_0^2} \frac{\mathcal{W}'_\perp(a,s)}{a} \right] x_0 = -K(s) x_0, \tag{2.48}$$

(see also [16], [28]). Here $\gamma(z,s)$ is the relativistic factor of a particle at the location z in the machine and the position s within the bunch and m_0 denotes the rest mass of the particle. As we will be interested in a local criterion for the energy spread to optimize the emittance growth, the influence from the acceleration has been neglected in equation 2.48. This is possible if the energy gain over one betatron wavelength is small.

We have introduced a new quantity $K(s)$, which is the total focusing strength, including both the focusing by the quadrupoles and the force from transverse dipole wake. In order to keep the emittance growth small it is desirable that the different longitudinal regions of the bunch perform a coherent motion and do not accumulate relative offsets due to different frequency or magnitude of their betatron motion. This demand can be expressed by requiring

$$K(s) = const. \tag{2.49}$$

This condition is called the autophasing condition. If this condition holds, then the particles of the bunch will oscillate transversely at identical amplitude and frequency, when they have been subjected to a uniform deflection. The different longitudinal regions of the bunch do not acquire relative offsets and the particle distribution in the transverse planes, while oscillating as a whole, remains compact. From equation 2.48 it can be seen that it is in principle possible to exactly fulfill the autophasing condition by choosing a suitable charge distribution $\rho(s)$ and an energy profile along the bunch.

Equation 2.48 also reveals a second interesting property. The deflections imparted by the dipole wake are inversely proportional to the particle energies. It follows that in order to cancel these deflections the absolute variation of the focusing strength $k(z,s)$, too, must go inversely with the particle energies. If we vary the focusing strength itself inversely with the particle energies along the machine, that is, if $k(z,s) \propto 1/\gamma(z,s)$, we can fulfill the autophasing condition with a constant relative energy spread. As the betatron wavelength λ_β goes inversely with the square root of the focusing strength, this implies $\lambda_\beta \propto 1/\sqrt{\gamma}$. Therefore it is convenient to scale the beta function (appendix C) of the lattice with the square root of γ. In this case, the autophasing condition, which is a local condition for minimizing the emittance growth, becomes

a global condition. If the beta function of the lattice does not scale like $\beta(z) \propto \sqrt{\gamma(z)}$, then the autophasing condition must be evaluated for a large number of positions along the machine independently and the energy spread in the bunch must be adjusted to different profiles for each of these positions.

In the following we will investigate the feasibility and effectiveness of the technique of BNS damping for the SBLC design. The most important beam and machine parameters in this case are:

- $2.9 \cdot 10^{10}$ particles per bunch,
- bunch length: 0.5mm with Gaussian charge distribution,
- accelerating gradient $E = 17\text{MV/m}$,
- injection energy: 3.15GeV.

The machine has a FODO lattice (see appendices C and D.1) in which the focusing strength has been scaled with the square root of the energy. The resulting beta function is shown in Fig. 2.6. The variation of the focusing strength was obtained by breaking the lattice into 8 sectors of uniform focusing strength. The betatron phase advance per FODO cell is always 90°. For the calculation of the wake potentials we used the wakes of a short bunch calculated with

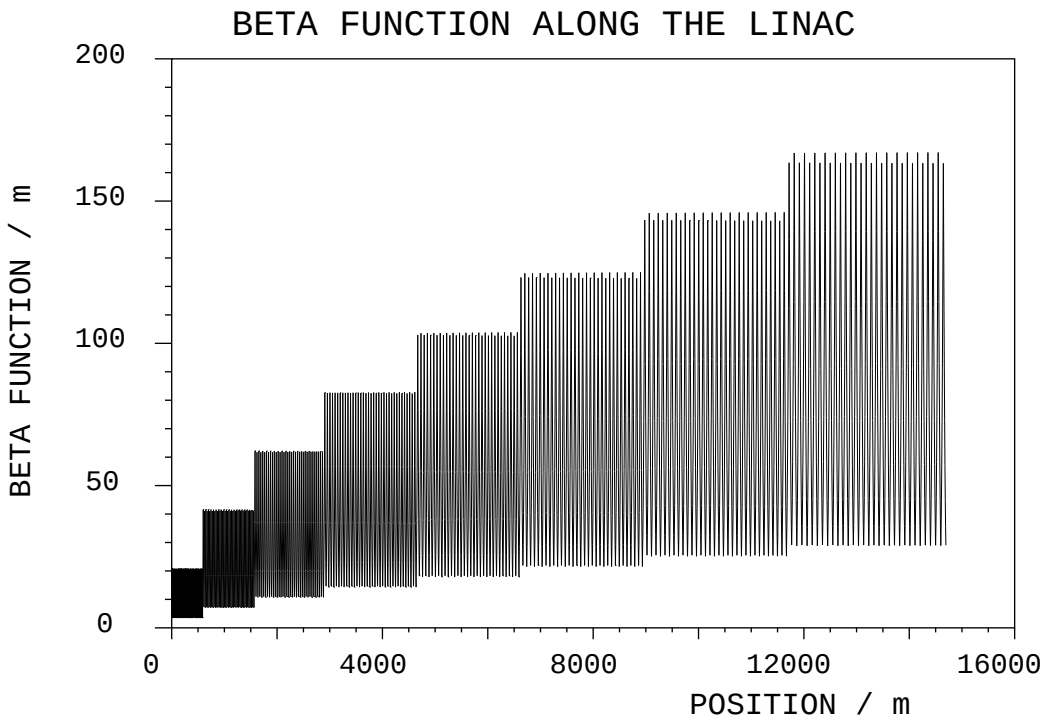

Fig. 2.6 Beta function along the linac. It can be seen that the lattice has been divided into 8 "sectors" of uniform focusing strength.

a time domain code ([22], [23]). They are shown in appendix D.3.

The correlated energy spread in a bunch is essentially caused by two effects, namely the longitudinal monopole wake and the finite bunch length, which leads to different RF phases for the different longitudinal regions of the bunch. This implies that by adjusting the phase φ_0 of

the accelerating wave relative to the bunch, the overall accelerating voltage $\Delta U(s)$ of a particle in the bunch seen in one structure with the length L_{struc} can be manipulated as:

$$\Delta U(s) = \Delta U_0 \cos\left(\varphi_0 + \frac{\omega_0 s}{c_0}\right) + q_{bunch}\mathcal{W}_{\parallel}(s), \qquad \Delta U_0 = E \cdot L_{struc}. \tag{2.50}$$

As we abstain from adjusting the charge density to achieve perfect autophasing we can only attempt to find an optimum approximation of the autophasing condition by optimizing the RF phase φ_0. As a measure for the local autophasing error we use the deviation of the total focusing strength K defined in equation 2.48 from its mean value $\overline{K}$

$$\Delta K(s) = K(s) - \overline{K}. \tag{2.51}$$

As a measure for the mean autophasing error we introduce

$$\delta K = \frac{\sqrt{\int \Delta K^2(s)\rho(s)/q_{bunch}\ \mathrm{d}s}}{\overline{K}}, \tag{2.52}$$

which is the normalized standard deviation of the total focusing strength.

In order to determine a suitable operating point for the SBLC we have investigated the autophasing condition at a point 3760m from the beginning of the linac, which is exactly in the middle of the fourth sector. The energy spread in the bunch was varied according to equation

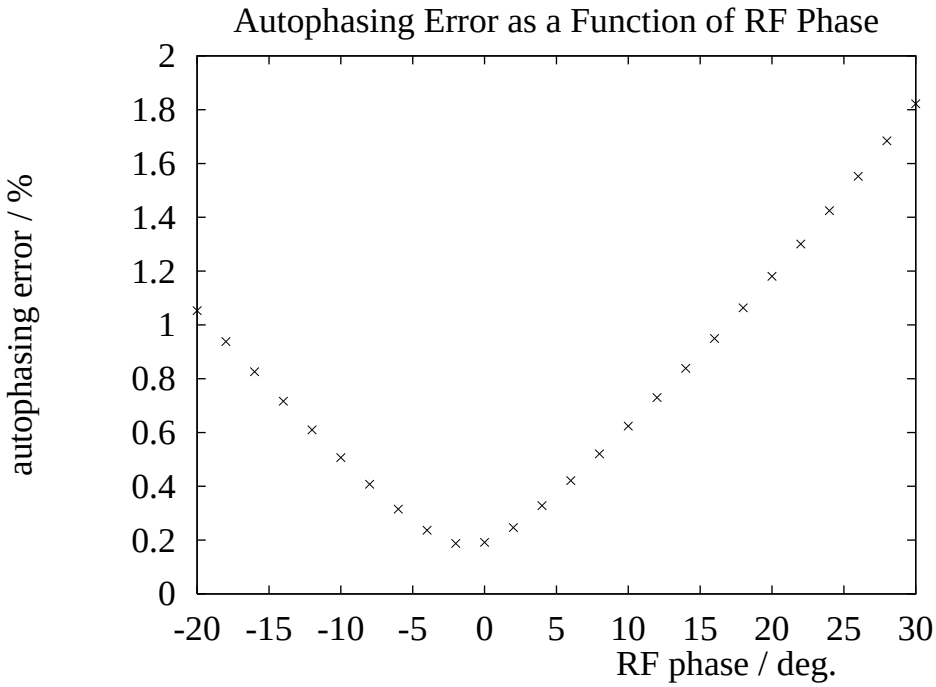

Fig. 2.7 Autophasing error δK as a function of the RF phase φ_0 in the middle of the fourth sector.

2.50 by setting the RF phases in all preceding accelerating structures to a uniform value φ_0 ranging from $-20°$ to $30°$. Fig. 2.7 shows the autophasing error δK (2.52) as a function of the RF phase φ_0. It is found that the RF phase for best approximation of the autophasing condition is in the range of $\varphi_0 = -2° \ldots 0°$, corresponding to a correlated energy spread of 0.65% rms. As the β-function of the lattice scales with $\beta \propto \sqrt{\gamma}$, this RF phase is optimal for the whole length of the machine (not accounting for the discontinuous reduction of the focusing strength). Fig. 2.8 shows the autophasing error ΔK along the bunch for RF phases

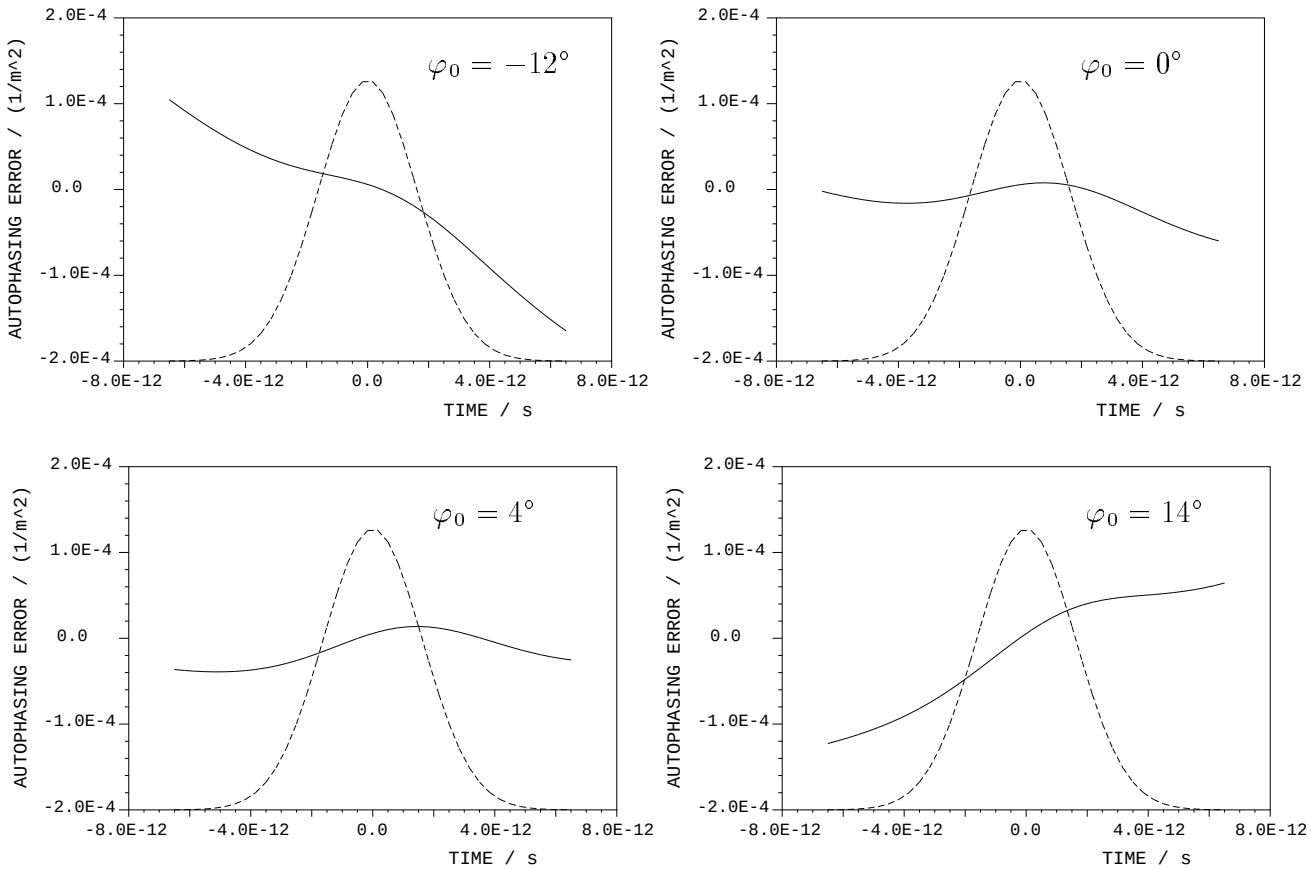

Fig. 2.8 The solid curves show the autophasing error ΔK over the bunch for RF phases $-12°$ (upper left), $0°$ (upper right) $4°$ (lower left) and $14°$ (lower right). Particles with negative times are ahead of the bunch center. The dashed curves indicate the profile of the charge density along the bunch.

$-12°$, $0°$, $4°$ and $14°$. The RF phase $-12°$ will be used later in this chapter to minimize the peak to peak energy spread in the bunch in the last part of the machine. However, we see that due to the wake fields the bunch tail is focused much less strongly than the head. As a consequence, emittance growth at this phase will be rather large. At an RF phase of $0°$ the the variation of the total focusing strength is at a minimum and we have best approximation of the autophasing condition. The third picture shows the autophasing error for $\varphi_0 = 4°$. The variation of the total focusing strength at this RF phase is still very small. At $14°$ finally we have a very large energy spread leading to a focusing strength that is larger in the tail than in the head of the bunch. The calculation was carried out with a division of the bunch into 40 slices. There was no division of the slices into subslices, since the uncorrelated energy spread has no relevance for the autophasing condition. It is important to note that even at the RF phase of $0°$ the variation of the total focusing strength does not vanish. This means that the autophasing condition cannot be fulfilled perfectly and hence the decoherence of an originally coherent betatron motion cannot be entirely avoided.

Our previous investigation of the autophasing condition contained two major simplifications which may restrict the applicability of the obtained result to a realistic machine. First, the focusing was assumed to be distributed smoothly over the whole machine length. In reality however, we use an alternating gradient focusing by quadrupoles confined to short discrete longitudinal regions of the machine. Second, the autophasing condition only holds strictly at locations close to the centers of the eight sectors, since the beta function is increased stepwise

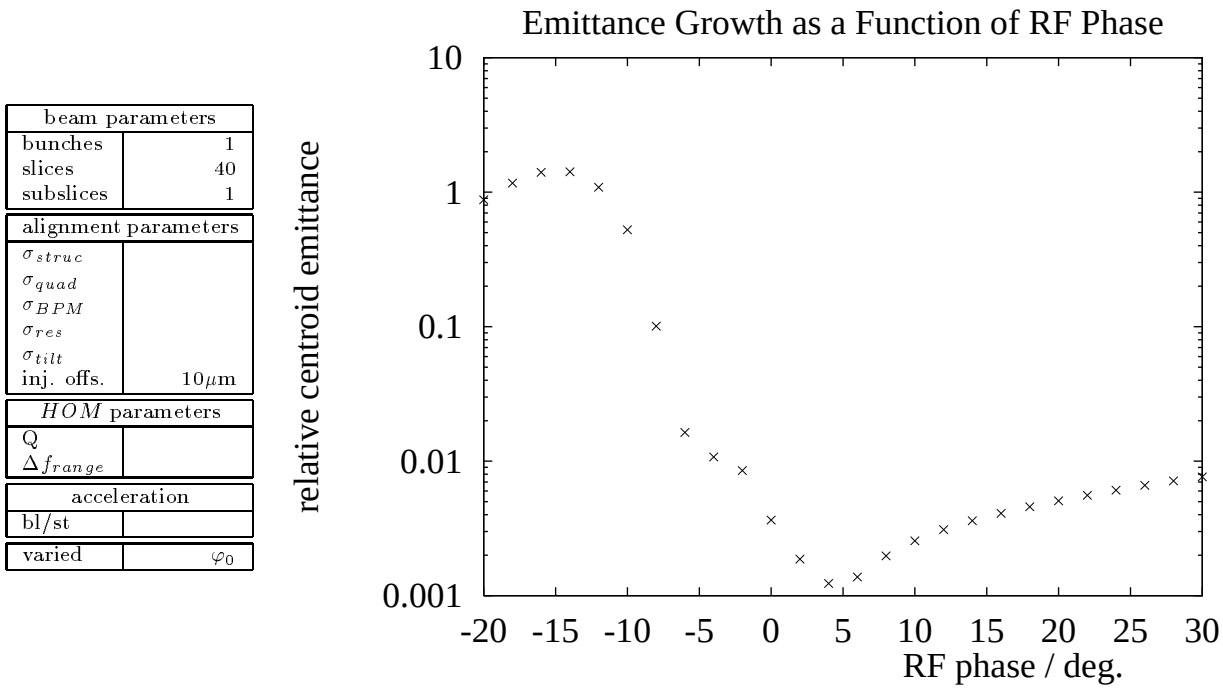

Fig. 2.9 Relative centroid emittance from injection offset as a function of the RF phase φ_0. The parameter panel on the left hand side of the plot is explained in appendix B.

along the linac instead of smoothly. Therefore, we want to complement our investigation by a look at the behavior of the emittance growth after a systematic injection offset of the beam with respect to the RF phase of the accelerating voltage. Specifically, we calculated the centroid emittance for a bunch that was injected with a systematic offset of 10μm at a beta function $\beta = 20.8$m (this offset corresponds to a quarter beam height σ_y) for different values of φ_0. The machine elements were assumed to be aligned ideally along a straight axis. The calculation was performed with 40 slices per bunch. The wake potentials were obtained by convolving the monopole and dipole wakes described in appendix D.3 with the bunch charge. The result of this calculation is shown in Fig. 2.9. The optimum RF phase is now found to be at $\varphi_0 = 4°$. This RF phase corresponds to a slightly higher correlated energy spread of 0.86% rms in the bunch. In addition, it is found that even at the optimum RF phase the emittance growth does not vanish completely. This result is analogous to the results from the analysis of the autophasing condition, where it was found that the variation of the total focusing strength could not be removed completely. Nevertheless, the suppression of the emittance growth compared with the emittances obtained at large negative phases is considerable. At the optimum energy spread of 0.86%, the emittance growth from the assumed injection offset is very small in comparison with the 6% growth that could have been tolerated.

We conclude that the two methods for determining the optimum correlated energy spread for BNS damping lead to similar results. However, the approximations contained in the autophasing condition, in particular the continuous approximation for the focusing lattice, lead to a certain discrepancy in the obtained values. For the subsequent investigations we therefore decide to use the RF phase of 4° obtained from the empirical investigation of the emittance growth in order to achieve BNS damping.

The energy spread required for effective BNS damping is fairly high and should be corrected before the end of the machine. On the other hand, we have seen that the emittance growth caused by injection offset is not a limiting factor. It should therefore be possible to operate only a few of the first sectors of the machine at an RF phase suitable for BNS damping and

beam parameters	
bunches	1
slices	40
subslices	1/30
alignment parameters	
σ_{struc}	
σ_{quad}	
σ_{BPM}	
σ_{res}	
σ_{tilt}	
inj. offs.	10μm
***HOM* parameters**	
Q	
Δf_{range}	
acceleration	
bl/st	
varied	sectors with BNS damping

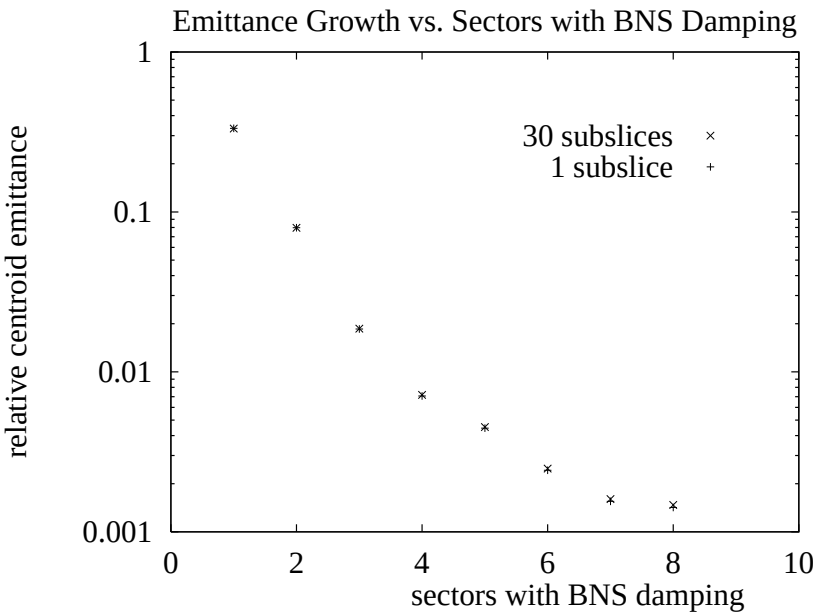

Fig. 2.10 Relative centroid emittance as a function of the number of sectors using BNS damping. Shown are the results of a computation with a division of the bunches into 30 subslices and an initial uncorrelated energy spread of 1% rms, and a computation without subdivision of the slices (1 subslice). The emittance values found in the two computations are practically identical.

set the remainder of the machine to a phase that minimizes the peak to peak energy spread in the bunch. Fig. 2.10 shows the relative centroid emittance at the end of the machine as a function of the number of sectors running with BNS damping. Here the first n sectors of the machine were operated at the optimum BNS phase of 4°, while the phases in the remaining $(8-n)$ machine sectors were set to $-12°$. The beam was again injected with an offset of 10μm at a beta function of $\beta = 20.8$m. The calculation was performed with a division of the bunch into 40 slices and 30 subslices per slice. The initial uncorrelated energy spread in the beam was 1% rms.

These results enable us to define an operation point for the machine. For the remainder of this chapter, especially in sections 2.3 and 2.4, we will choose to set the structures in the first four sectors to an RF phase of 4° for optimum BNS damping and the structures in the last four sectors to an RF phase of $-12°$ in order to minimize the peak to peak energy spread. The very first four structures are set to a phase of 90° in order to provide an initial energy spread. Fig. 2.11 shows the energy profile in the bunch at the end of the fourth sector and at the end of the entire linac. The energy profile at the end of the fourth sector has a relative spread of 0.86% rms. More importantly, the peak to peak energy spread (over a longitudinal range of $\pm 4\sigma_z$ of the charge distribution) is $\sim 3.9\%$. An energy spread of this magnitude would result in a loss of luminosity, since the final focus system can only accept particles with energy deviations smaller than $\pm 1.8\%$ [10]. In addition, the energy resolution available for the experiments would be degraded. For these reasons one is compelled to keep the energy spread at the linac end as small as possible.

As the structures in the last four sectors are set to a phase of $-12°$, the peak to peak energy spread reduces to 1% by the end of the linac, which is not only acceptable for the SBLC final focus system but even leaves room for a multi-bunch energy spread (see section 3.2). The rms energy spread (standard deviation) is reduced to 0.3%.

The calculation of the emittance growth from injection offset was also repeated without

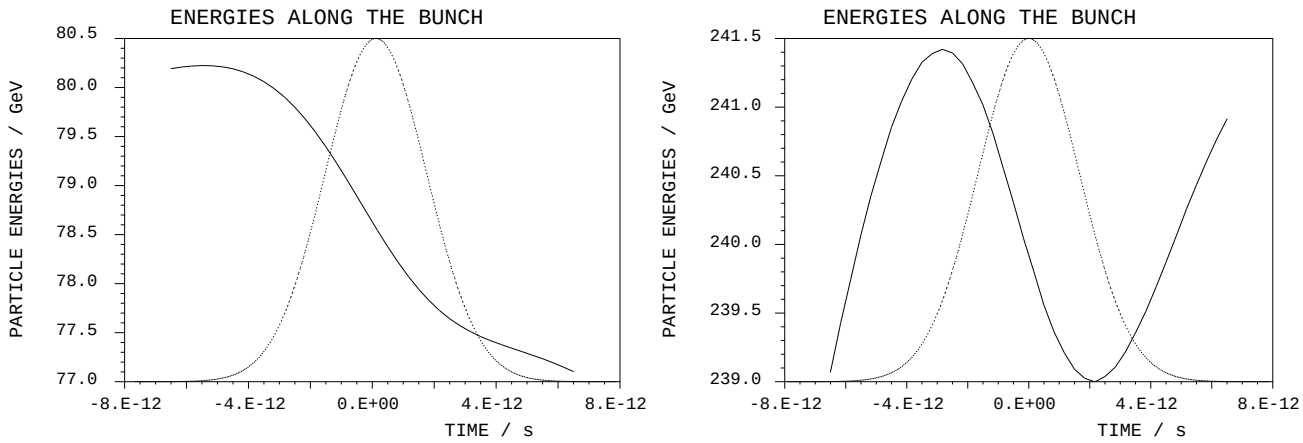

Fig. 2.11 The solid lines in these plots show the energy profile in the bunch after sectors 4 (left plot) and 8 (right plot). After the fourth sector, the rms energy spread is 0.86%, which reduces to 0.3% by the end of the machine. Particles with negative times are ahead of the bunch center. The dashed lines indicate the longitudinal charge density profile.

division of the slices into subslices, thus ignoring the initial uncorrelated energy spread. It was found that the effect of the uncorrelated energy spread is negligibly small and the final emittances differ little from the previous result. This is explained by the fact that due to the rapid energy gain, the beam energy quickly becomes very large in comparison with the initial uncorrelated energy spread.

2.3 Quadrupole Misalignment

In this section we will investigate the effect of quadrupole misalignments on the trajectory of particles through the linac and the associated emittance growth. It will become evident that corrective measures are imperative and we will examine the effectiveness of orbit corrections, especially those outlined in [29], for the SBLC machine design. These correction techniques will later also be of great relevance for multi-bunch issues.

2.3.1 Emittance Growth without Correction and Vibration Tolerance

A transverse misalignment of a quadrupole leads to a transverse kick on a bunch of particles traversing it and thus excites a coherent betatron motion. In a lattice consisting of a large number of quadrupoles these betatron motions accumulate to a very large amplitude. These kicks from the quadrupoles lead to a large emittance growth, due to both the dispersion caused by the energy spread in the beam (appendix C) and wake field effects arising from non-vanishing particle offsets with respect to the structures. Although the chromatic and wake field effects are compensated to some extent by the application of BNS damping, this compensation is not perfect since we only used the phase of the accelerating wave to adjust the energy spread in the bunches. As a consequence, the kicks from misaligned quadrupoles will be subject to a significant residual filamentation. We conclude that the very large orbits resulting from quadrupole misalignment will lead to a very strong emittance growth due to both wake fields and dispersive effects.

An example of this process is shown in Fig. 2.12, where the particle trajectory through an

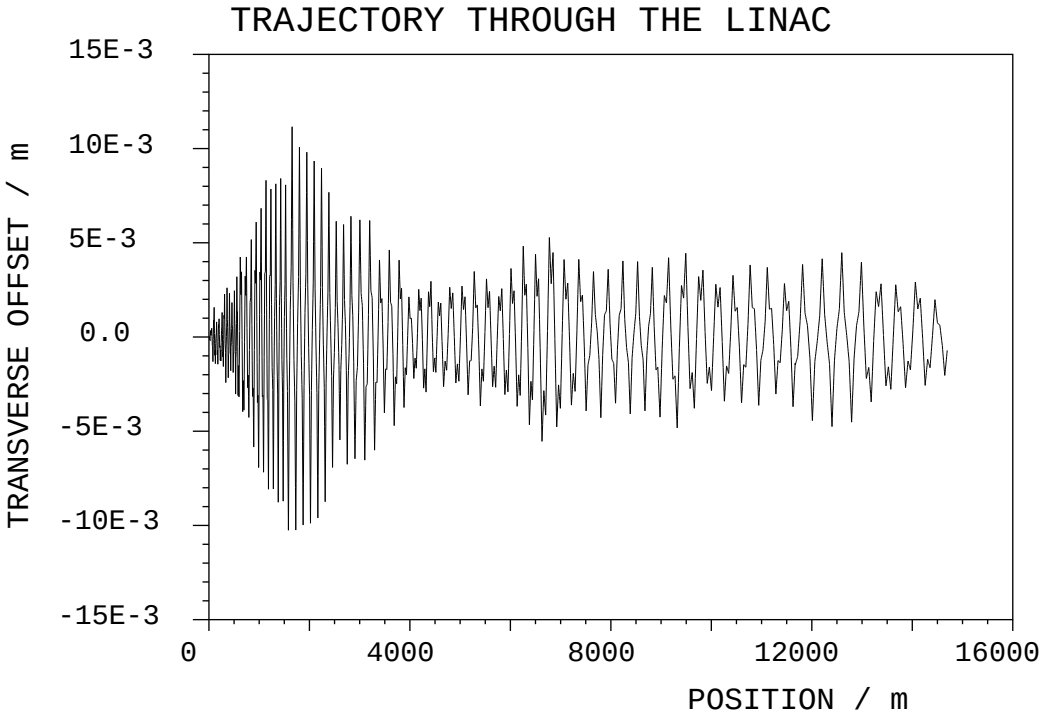

Fig. 2.12 Uncorrected trajectory through a machine with 100μm rms random quadrupole misalignment.

uncorrected machine can be seen. In this calculation, it was assumed that the quadrupoles were misaligned randomly with respect to an ideal machine axis with an rms of $\sigma_{quad} = 100\mu$m, which leads to offsets from the machine axis in the order of centimeters. At a bunch population of $2.9 \cdot 10^{10}$, the emittance in average increases by a factor $4.2 \cdot 10^4$ due to this process. During realistic machine operation, we will make use of orbit correction techniques that will prevent such an emittance growth. However, the time interval between subsequent orbit corrections will be finite and probably be in the order of seconds. Small uncorrelated vibrations of the quadrupole magnets during that interval will superimpose an error orbit of the type shown in Fig. 2.12 on the trajectory and generate an additional contribution to the emittance. This emittance contribution scales with the square of the vibration amplitude, which allows us to calculate the maximum tolerable quadrupole vibration between two orbit corrections. If the additional contribution to the emittance is to be smaller than 6% of the normalized vertical emittance ($5 \cdot 10^{-7}$radm), the tolerable quadrupole vibration evaluates to 120nm.

2.3.2 Emittance Growth with Orbit Correction

The accumulation of large orbits due to quadrupole misalignment and the resulting emittance growth must be prevented by appropriate corrective measures. This is commonly done by installing beam position monitors (BPM's) at several locations in the machine and using correcting dipole magnets to steer the beam to a desired trajectory. For our case we will assume that both a BPM and a correcting dipole are installed at each quadrupole.

Beam position monitors are devices that measure the transverse displacement of beams or individual bunches traversing them. The BPM's are characterized by the rms value σ_{BPM} of their transverse misalignment relative to the magnetic center of the quadrupole they are attached to and by their resolution σ_{res}, which gives the rms of the random measurement error

from shot to shot. The relative misalignment σ_{BPM} of the BPM's to the quadrupoles refers to the electronic center of the BPM and includes both the physical misalignment of the BPM as well as offsets between the physical and the electronic axis of the BPM.

The dipole magnets, also referred to as correcting dipoles or correctors, are dipole magnets creating a magnetic field that is oriented perpendicularly to the beam axis and thus can cause a transverse deflection of the beam. The correcting dipoles are characterized by the deflection angle θ they impart on particles having an energy equal to the mean energy of the beam. This deflection angle will also be referred to as the corrector strength. Obviously, particles having a larger or smaller energy will be deflected with a smaller or larger angle.

The simplest algorithm for correcting the trajectory is the so-called One-to-One algorithm. In this algorithm, the correcting dipoles of the focusing quadrupoles are used to steer the

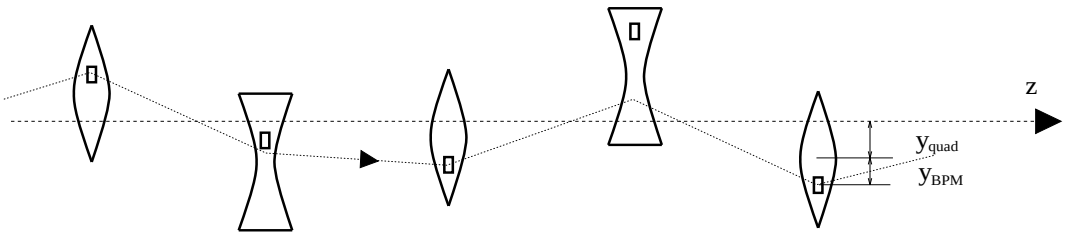

Fig. 2.13 Particle trajectory with One-to-One orbit correction. The rectangles in the quadrupoles symbolize the beam position monitors.

beam to the centers of the BPM's of the next focusing quadrupole [30]. The BPM's and dipoles of the defocusing quadrupoles are unused. This technique is depicted in Fig 2.13. After completion of a One-to-One correction, the particle trajectory essentially follows the total misalignments of the BPM's, which have a magnitude with respect to the machine axis of $\sigma_{BPMtot} = \sqrt{\sigma_{BPM}^2 + \sigma_{quad}^2}$. It follows that the magnitude of the trajectory with respect to the machine axis has a magnitude in the order of σ_{BPMtot}. We will see that this remaining orbit still leads to a substantial emittance growth due to both wake field and dispersive effects. The magnitude of this emittance growth is roughly proportional to σ_{BPMtot}^2, which would make diligent machine alignment the only handle for preventing emittance growth and hence lead to very tight alignment tolerances.

More sophisticated algorithms for orbit correction have been devised for instance in [29], [31], [32], [33], [34]. These correction methods exploit the fact that information on the transverse deflections of the beam along the linac is not only contained in the trajectory itself, but also in the dispersion. This dispersion could in principle be measured by changing the beam energy. However, a change of the beam energy can also be mimicked by changing the strength of the quadrupoles and their correction dipoles. Therefore, these schemes use not only the absolute readouts from the BPM's for orbit correction but also the response of the beam trajectory to changes of the focusing strength of quadrupoles in order to find a smooth orbit. Frequently, the process of correcting the orbit with these techniques is referred to as "beam based alignment". In our investigation we essentially follow the approach outlined in [29], [33] and [34].

Generally, the correction schemes of the types described in [29] incorporate the measurement of trajectories through the machine with the quadrupole strengths at their nominal values, and trajectories with a reduction of the strength of sets of quadrupoles and the strength of their dipoles. After completion of these trajectory measurements, the deflection angles of the dipoles are chosen to make the variation of the trajectory with variations of the lattice, the so-called difference orbits, minimal. This property of the correction scheme practically removes the emittance growth caused by dispersive errors. As the variation of the orbit with a change of

the lattice vanishes for any trajectory that is a straight line, it is necessary to include some information on the absolute BPM readouts in the correction scheme in order to prevent the corrected orbit from drifting away from the machine axis.

We can express correction schemes of the types described in [29] as an optimization problem:

$$\sum_j \left[\frac{(m_j + X_j)^2}{\sigma_{BPMtot}^2 + \sigma_{res}^2} + \sum_{k=1}^{K} \frac{\left(\Delta m_j^{(k)} + \Delta X_j^{(k)}\right)^2}{2\sigma_{res}^2} \right] \stackrel{!}{=} min. \tag{2.53}$$

Here, m_j is the orbit as measured by the j-th BPM with the nominal lattice and X_j the correction to be superimposed on the uncorrected orbit. $\Delta m_j^{(k)}$ is the difference between the orbit measured with the nominal lattice and the orbit measured with the k-th lattice, having a reduction of the focusing strengths of a set of quadrupoles and the strengths of their dipoles. It is called the difference orbit or dispersion orbit. Likewise, $\Delta X_j^{(k)}$ is the variation of the orbit correction for the k-th variation of the lattice. It follows that $(m_j + X_j)$ is the value of the orbit measurement expected after application of the correction and $(\Delta m_j^{(k)} + \Delta X_j^{(k)})$ the expected orbit variation after correction. K is the number of difference orbits to be included for the minimization.

We remark that m_j includes a measurement error that is composed of a systematic offset and a random shot to shot error of the measurement. The measurement offset is the sum of the offsets of the BPM with respect to the quadrupole and of the quadrupole with respect to the machine axis. The random measurement error is characterized by the BPM resolution σ_{res}. In $\Delta m_j^{(k)}$ the systematic offsets of the measurements cancel and only a random shot to shot measurement error remains.

The corrections X_j of the orbit at the j-th BPM are generated by setting the deflection angles created by the dipoles to appropriate values θ_i. The trajectory change caused at the j-th BPM by a deflection at the i-th dipole is calculated with the element T_{12}^{ji} of the optical transfer matrix between these elements as

$$X_j = T_{12}^{ji} \theta_i. \tag{2.54}$$

The corresponding elements of the transfer matrix for the k-th modified lattice is called $T_{12}^{ji(k)}$. The change of the corrector strengths for the k-th measurement can be expressed by a reduction parameter $R_i^{(k)}$ as:

$$\theta_i^{(k)} = R_i^{(k)} \theta_i.$$

We then can write the change of the orbit correction at the j-th BPM $\Delta X_j^{(k)}$ created by the i-th correction dipole (θ_i) as

$$\begin{aligned} \Delta X_j^{(k)} &= T_{12}^{ji}\theta_i - T_{12}^{ji(k)} R_i^{(k)} \theta_i & (2.55)\\ &= \left(T_{12}^{ji} - T_{12}^{ji(k)} R_i^{(k)}\right) \theta_i & (2.56)\\ &= \Delta T_{12}^{ji(k)} \theta_i, & (2.57) \end{aligned}$$

where we have introduced the effective change $\Delta T_{12}^{ji(k)}$ of the coefficient T_{12}^{ji} of the transfer matrix between the dipole i and the BPM j.

The optimization problem then can be recast in the form

$$\sum_j \left[\frac{\left(m_j + \sum_i T_{12}^{ji} \theta_i\right)^2}{\sigma_{BPMtot}^2 + \sigma_{res}^2} + \sum_{k=1}^{K} \frac{\left(\Delta m_j^{(k)} + \sum_i \Delta T_{12}^{ji(k)} \theta_i\right)^2}{2\sigma_{res}^2} \right] \stackrel{!}{=} min. \tag{2.58}$$

This expression finally can be solved for the deflection angles θ_i of the correcting dipoles.

The minimization gives a strong weight $\propto 1/2\sigma_{res}^2$ to the dispersive terms and a rather small one $\propto 1/\left(\sigma_{BPMtot}^2 + \sigma_{res}^2\right)$ to the absolute term. By assigning this large weight to the difference orbits and almost neglecting the information on the absolute trajectory one exploits the fact that a small BPM resolution in the lower μm-range is much easier to achieve than an alignment of the machine elements in the lower μm- to 10μm-range.

In our simulations we will make use of two cases of 2.53, namely the "Dispersion-Free" correction and the "Wake-Free" correction. The Dispersion-Free algorithm ("DF") makes use of one difference orbit that is obtained with a uniform reduction of the strength of all quadrupoles and correction dipoles. It can be written as:

$$\sum_j \left[\frac{\left(\Delta m_j + \Delta X_j\right)^2}{2\sigma_{res}^2} + \frac{\left(m_j + X_j\right)^2}{\sigma_{BPMtot}^2 + \sigma_{res}^2} \right] \stackrel{!}{=} min. \tag{2.59}$$

The Wake-Free algorithm ("WF") uses two difference orbits, one with a reduction of all focusing quadrupoles and their correction dipoles and one with reduction of all defocusing quadrupoles. The minimization problem then becomes:

$$\sum_j \left[\frac{\left(\Delta^{(F)} m_j + \Delta^{(F)} X_j\right)^2}{2\sigma_{res}^2} + \frac{\left(\Delta^{(D)} m_j + \Delta^{(D)} X_j\right)^2}{2\sigma_{res}^2} + \frac{\left(m_j + X_j\right)^2}{\sigma_{BPMtot}^2 + \sigma_{res}^2} \right] \stackrel{!}{=} min. \tag{2.60}$$

Here, $\Delta^{(F)} m_j$ denotes the difference orbit obtained from a reduction of the strength of the focusing quadrupoles and $\Delta^{(F)} X_j$ the change of the orbit correction that will occur when the strength of the focusing quadrupoles is reduced. $\Delta^{(D)} m_j$ and $\Delta^{(D)} X_j$ are the corresponding quantities at the reduced value of the defocusing quadrupoles. The designation "Wake-Free" of this algorithm is due to [29]. It expresses the tendency of the resulting orbit to reduce the effect from the transverse dipole wake, since the kicks at opposing betatron phases cancel.

Fig. 2.14 shows the orbits through the machine after trajectory correction with the One-to-One, Dispersion-Free and Wake-Free correction. For this simulation it was assumed that the quadrupoles were misaligned with an rms of $\sigma_{quad} = 100\mu$m relative to an ideal axis and the BPM's with an rms of $\sigma_{BPM} = 100\mu$m with respect to quadrupoles. The BPM resolution was assumed to be $\sigma_{res} = 5\mu$m. The reductions of the magnet strengths for the measurement of the difference orbits were 10%. The accelerating structures were aligned ideally along the machine axis. Furthermore, we assumed an accelerating gradient of 17MV/m and an injection energy of 3.15GeV. The monopole and dipole wake potentials were calculated using the wakes shown in appendix D.3. The accelerating structures were operated as suggested in section 2.2 with the structures in the first four sections running at 4° and those in the last 4 sectors at $-12°$. The beam was injected exactly on axis.

The deflections of the correcting dipoles were not calculated in one step, as it is not considered likely that such a procedure would work successfully on a real machine. There, small errors of the lattice parameters and errors in the calculated dipole strengths could accumulate to large orbits ([13], [29]). Instead, the corrector strengths were evaluated for each of the 8 lattice sectors consecutively.

It can be seen that after the Dispersion-Free correction and the Wake-Free correction the orbits are both smaller and, more importantly, smoother. The Dispersion-Free correction improves the emittance considerably, due to both a smaller orbit and a better smoothness of the trajectory. The Wake-Free correction gives another improvement of the emittance, and in addition leads to a further improvement of the orbit smoothness. It follows that the dispersive

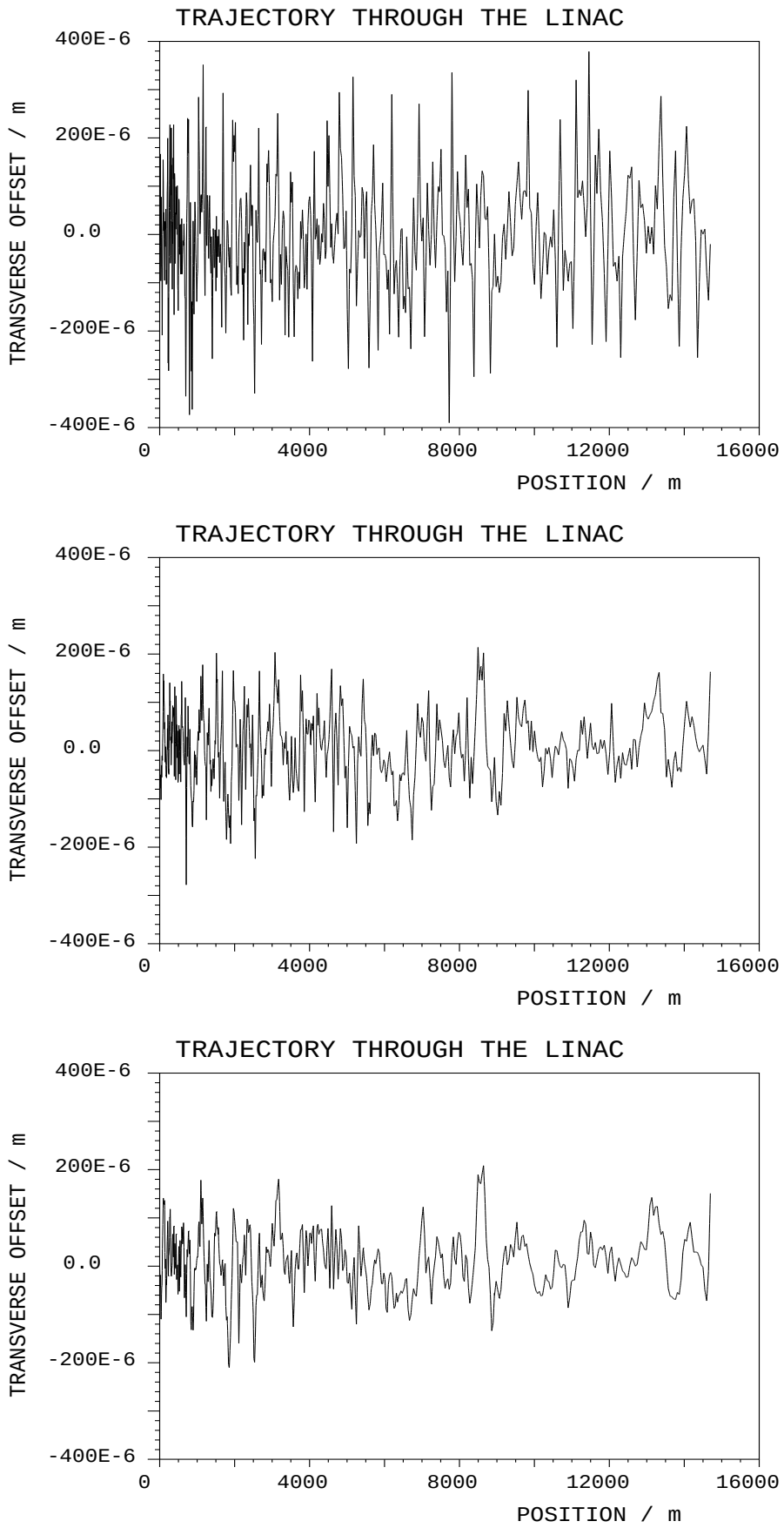

Fig. 2.14 Trajectories after One-to-One, Dispersion-Free and Wake-Free correction.

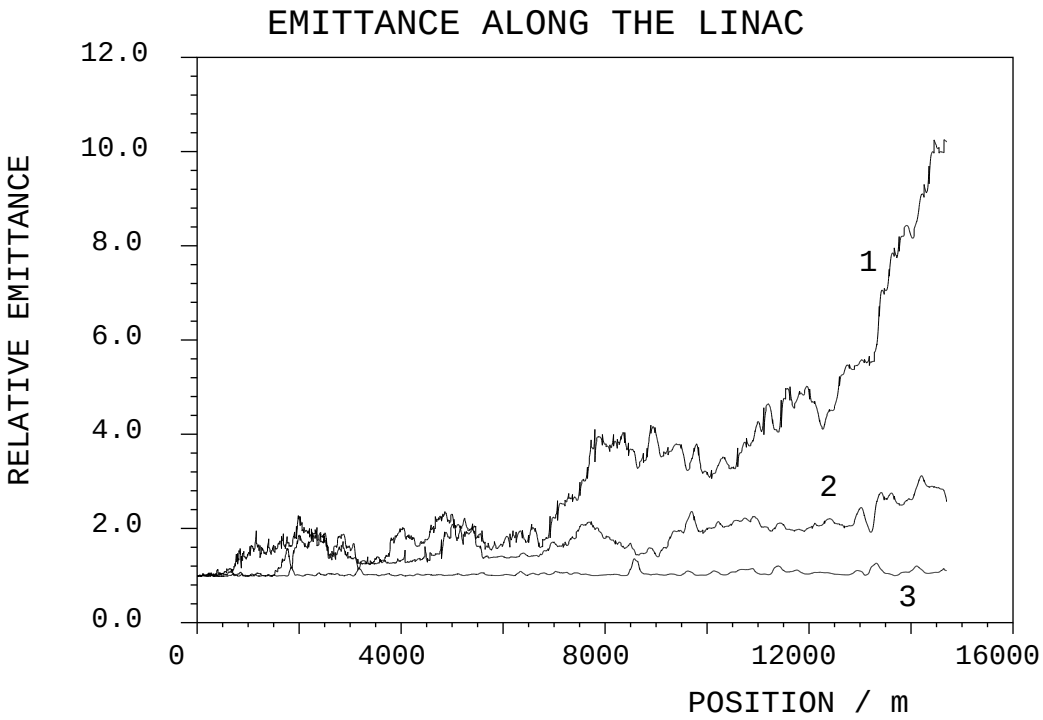

Fig. 2.15 Beam emittances in a linac with misaligned quadrupoles and BPM's after (1) One-to-One, (2) Dispersion-Free and (3) Wake-Free correction.

errors become very small. Fig. 2.15 gives an example of the beam emittances along the linac after correction with the three different algorithms.

As the emittance after correction fluctuates very substantially with the random misalignment of the elements, it is necessary to repeat the simulation for a large number of random seeds. We first carried out this calculation with bunches composed of 40 slices. Then, the same simulations were repeated with the slices of the bunches being partitioned into 30 subslices each and an initial uncorrelated energy spread of the beam of 1% rms. The mean values of the

	mean value of final emittances	
algorithm	1 slice	30 subslices
One-to-One	$(16.0 \pm 11.6)\epsilon_{yN0}$	$(16.0 \pm 11.6)\epsilon_{yN0}$
DF	$(3.3 \pm 1.0)\epsilon_{yN0}$	$(3.3 \pm 1.0)\epsilon_{yN0}$
WF	$(1.19 \pm 0.18)\epsilon_{yN0}$	$(1.19 \pm 0.18)\epsilon_{yN0}$

Table 2.1 Single-bunch emittances after One-to-One, Dispersion-Free and Wake-Free orbit correction. The calculation was carried out with and without division of the slices into subslices. Shown are the mean values of the emittances and their standard deviation found in 20 calculations using different random seeds for the misalignments.

emittances found in this procedure for the different correction schemes are given in table 2.1. The values in this table were obtained by averaging over 20 calculations with different random seeds for the machine misalignment and the BPM measurement errors. The emittances at the end of the machine are given in units of the normalized vertical emittance at injection, which is $\epsilon_{yN0} = 5 \cdot 10^{-7}$radm. It is found that the DF correction improves the emittance by almost

a factor 5 on average. The WF algorithm finally reduces the emittance growth to a value of 19%. In addition, we observe that the initial uncorrelated energy spread of 1% rms does not contribute in any significant manner to the final emittance of the beam. The emittance values found in the computation without division of the slices into subslices are practically identical with the emittances found in the computation with division of the slices into 30 subslices each.

Next, it is instructive to look at the dependence of the emittance growth after orbit correction on the BPM resolution. For this purpose, we simulated the orbit correction in a machine with 100μm rms random quadrupole misalignment and 100μm rms random BPM misalignment with respect to the quadrupoles. With these assumptions, we calculated the centroid emittances obtained with the One-to-One, Dispersion-Free and Wake-Free correction for different values of the BPM resolution ranging from 1μm to 32μm. These simulations were carried out with 10 different random seeds at each value of the BPM resolution.

beam parameters	
bunches	1
slices	30
subslices	1
alignment parameters	
σ_{struc}	
σ_{quad}	100μm
σ_{BPM}	100μm
σ_{res}	
σ_{tilt}	
inj. offs.	
HOM parameters	
Q	
Δf_{range}	
acceleration	
bl/st	
varied	σ_{res}

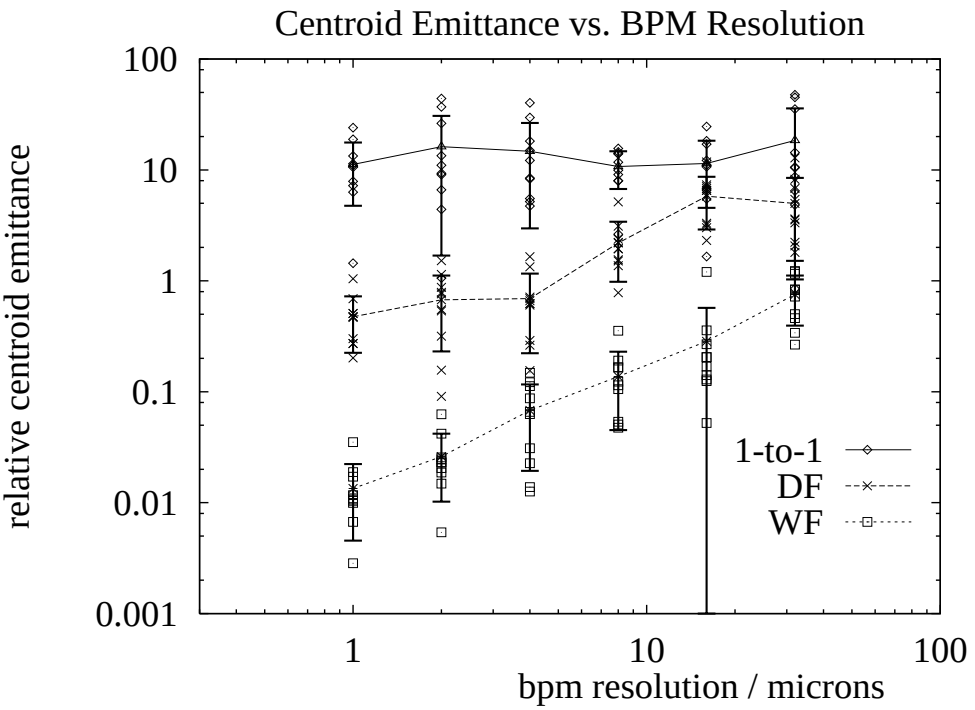

Fig. 2.16 Influence of the BPM resolution on the emittance. Shown are the relative centroid emittances found in calculations with 10 different random seeds for the misalignments after application of One-to-One, Dispersion-Free and Wake-Free correction. The error bars in this and all subsequent scatter plots extend over one standard deviation in each direction of the mean values. The large error bar at $\sigma_{res} = 16\mu$m for the WF algorithm is due to a standard deviation larger than the mean value of the emittances.

Fig. 2.16 shows the relative centroid emittances after One-to-One, DF and WF correction for the different values of the BPM resolution. It turns out that for the One-to-One algorithm the resulting emittances do not depend very strongly on the BPM resolution as long as this resolution is small in comparison to the total BPM misalignment σ_{BPMtot}. For the case of DF and WF correction matters are different. Here we see a strong dependence of the centroid emittance on the BPM resolution. In the case of the WF algorithm the emittance increases faster than linearly with the resolution. This means that emittance growth is decoupled to a large extent from the absolute element misalignments and is now almost dominated by the BPM resolution. For the One-to-One correction we find a mean relative centroid emittance of $(1120 \pm 650)\%$ (mean value $\pm$ standard deviation) at a BPM resolution of 1μm, which changes

to $(1840 \pm 1740)\%$ at a BPM resolution of 32μm. For the DF correction the dependence on the BPM resolution is already much more pronounced. The relative centroid emittances found with this correction technique rise from a value of $(47 \pm 25)\%$ at a BPM resolution of 1μm to a value of $(500 \pm 350)\%$ at a BPM resolution of 32μm. Finally, with the WF correction a mean relative centroid emittance of $(1.3 \pm 0.9)\%$ is achieved at a BPM resolution of 1μm, increasing by a factor 57 to a value of $(76 \pm 36)\%$ at a BPM resolution of 32μm.

We conclude that use of the Wake-Free orbit correction technique is preferred. This is still true if the wake field effects are largely eliminated by adjusting the accelerating structures with respect to the beam, since the WF correction achieves a good trajectory smoothness, thus giving best suppression of dispersive effects. In the context of active structure alignment, such a smooth orbit also is a good reference for achieving satisfactorily small tilt angles of the structures. Transverse kicks by the accelerating mode resulting from tilt misalignments of the accelerating structures will be shown to be an important source of emittance dilution in the scope of section 3.4. For the complete machine tuning procedure outlined in chapter 4, we will always make use of the Wake-Free orbit correction scheme.

2.4 Structure Misalignment

2.4.1 Emittance Growth without Correction

Misalignment of accelerating structures causes emittance growth due to the transverse dipole wake, which imparts different deflections on different fractions of the bunch. This growth is enhanced by the energy spread along the bunch, which leads to filamentation of the bunch motion, i.e. the different fractions of the bunch oscillate with different betatron frequencies and eventually decohere. Due to this effect, the transverse wakes of two misaligned structures located at opposing betatron phases can never cancel exactly.

We performed a calculation of the emittance growth from structure misalignment with the assumption that the quadrupoles were aligned perfectly on an ideal axis and the structures were misaligned randomly with an offset of 100μm rms with respect to that axis. For the beam we assumed a bunch population of $2.9 \cdot 10^{10}$ particles per bunch and a bunch length of 0.5mm with Gaussian charge distribution. The beam was injected into the machine exactly on axis. For the machine we assumed a lattice in which the β-function scales with $\sqrt{\gamma}$ as shown in Fig. 2.6. Further assumptions were:

- accelerating gradient $E = 17$MV/m,
- injection energy: 3.15GeV,
- monopole and dipole wake as shown in D.3.

The accelerating structures were operated as suggested in section 2.2 with the structures in the first 4 sectors running at an RF phase of $4°$ and the structures in the remaining 4 sectors operating at $-12°$. With these assumptions we found an average emittance growth of 120%. If we wanted to reduce this emittance growth to 6% of the vertical emittance ϵ_{yN0} $(5.0 \cdot 10^{-7}\text{radm})$ without utilizing correction techniques, this result would limit the tolerable alignment precision of the structures to 22μm.

2.4.2 Emittance Correction with Trajectory Bumps

Fortunately, this tolerance can be eased with the application of empirical correction techniques ([29], [35]). These correction schemes envision a manipulation of the beam trajectory or the

position of the accelerating structures with simultaneous measurement of the beam emittance.

The idea behind the method pursued in our investigation is to deliberately introduce a distortion, so-called bumps, on the trajectory with the correction dipoles (or alternatively by moving the quadrupoles). At some location downstream of the bump the emittance is measured and the magnitude of the bump adjusted until the emittance reaches a minimum. Such a procedure was suggested in [29]. In this section we will investigate the applicability of two different types of trajectory bumps, namely dispersive bumps ("D-bumps") and non-dispersive bumps ("ND-bumps").

A dispersive bump, in our context, is simply a betatron motion extending over some limited fraction of the lattice. The necessary deflections in the correction dipoles are defined by

1. the bump magnitude, yielding the strength of the first dipole and
2. the requirement that after the bump
   (a) the trajectory and
   (b) the trajectory slope

   are zero. Hence, in general two dipoles are required to close the bump.

In order to ease the impact of the bumps on multi-bunch issues to be discussed in a later chapter, it is advisable to use long bumps of small amplitude instead of short bumps with large amplitude.

One individual ND-bump [29] extends over 5 quadrupole/dipole sets, starting at a focusing quadrupole. The necessary deflections in the correction dipoles are defined by

1. the bump magnitude, yielding the strength of the first dipole and
2. the requirement that after the bump
   (a) the trajectory
   (b) the trajectory slope
   (c) the trajectory of a particle with a slightly different energy (we use a 10% lower energy) and finally
   (d) the trajectory slope of a particle with slightly different energy

   are zero, which gives us the condition for the last four dipoles.

For the assumptions made on the SBLC lattice (FODO lattice, 90° betatron phase advance per cell) one individual ND-bump looks roughly like an "M" (or like a "W"). For practical application, it is preferable to use an array of many small bumps instead of a single or few bumps with large amplitude, as this eases the impact of the bumps on the multi-bunch emittance growth. As one bump extends over two FODO cells or 180° betatron phase advance, subsequent bumps are given opposite sign, leading to a coherent accumulation of the effect of the individual bumps. Such an array of consecutive bumps of uniform magnitude will be called a bump-set. Fig. 2.17 shows the two kinds of bumps in question. There, we first see an array of 8 non-dispersive bumps and then a dispersive extending over 16 FODO cells.

In either case, the emittance correction requires two sets of bumps, since the emittance dilution in the bunch is distributed over different betatron phases. For the 90° FODO lattice that is being assumed for our simulations it is convenient to use a pair of bump-sets that are separated by a betatron phase shift of 90°. Fig. 2.18 shows as an example the emittance

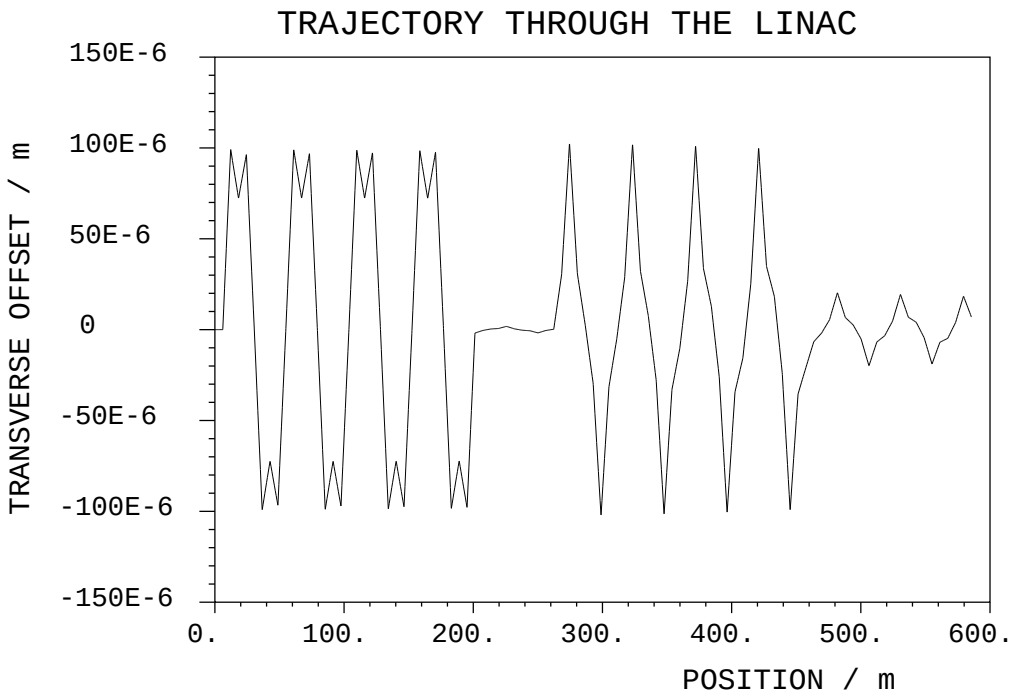

Fig. 2.17 An array of 8 non-dispersive bumps (left) and a dispersive bumps stretching over 16 FODO cells (right).

before and after correction with ND-bumps. The emittance was assumed to be measured at four stations in the machine, namely at the boundaries between the 2nd and the 3rd, the 4-th and the 5-th, the 6-th and the 7-th and after the 8-th sector. As it is desired to keep the emittance growth smaller than 6%, we assumed a resolution of the emittance measurement of 3%. Note that this resolution refers only to the relative precision of the emittance measurement. An absolute measurement of the emittance with this precision is not required. The emittance at one station was measured for 6 different magnitudes of one bump-set upstream of the station. The minimum of the emittance was determined using a parabolic fit and the magnitude of the bump-set was adjusted accordingly. This procedure was carried out for both bump-sets of a pair and then repeated for the next station with the next pair of bump-sets. Fig. 2.19 shows the trajectory with the bumps that minimized the emittance in Fig. 2.18. Each bump-set contains 14 bumps, thus extending over 28 FODO cells. The two bump-sets of a pair essentially occupy the same region on the lattice, with merely one bump-set being shifted by one FODO cell.

The results of an emittance correction with ND-bumps was studied with the assumptions stated above for different numbers of bump-set pairs. In these simulations, we assumed a random misalignment of the accelerating structures of 100μm rms. The quadrupoles were located exactly on the machine axis. The bunch population was $2.9 \cdot 10^{10}$ particles per bunch and the bunch length was $\sigma_z = 0.5$mm. The calculation was performed with a division of the bunch into 30 slices. Table 2.2 gives the mean emittance growth versus the number of measurement stations obtained from a calculation with 10 different random seeds for the structure misalignment. With dispersive bumps an improvement, though modest, could only be achieved with 8 bumps. Using 4 or even 2 bumps, no improvement of the emittance was found. Using non-dispersive bumps, the mean emittance growth could be improved to values from 77% with 2 pairs of bump-sets down to 2% for 8 pairs of bump-sets.

The results show clearly how a larger number of measurement stations improves the efficiency of the emittance correction. The reason for this behavior lies in the filamentation process

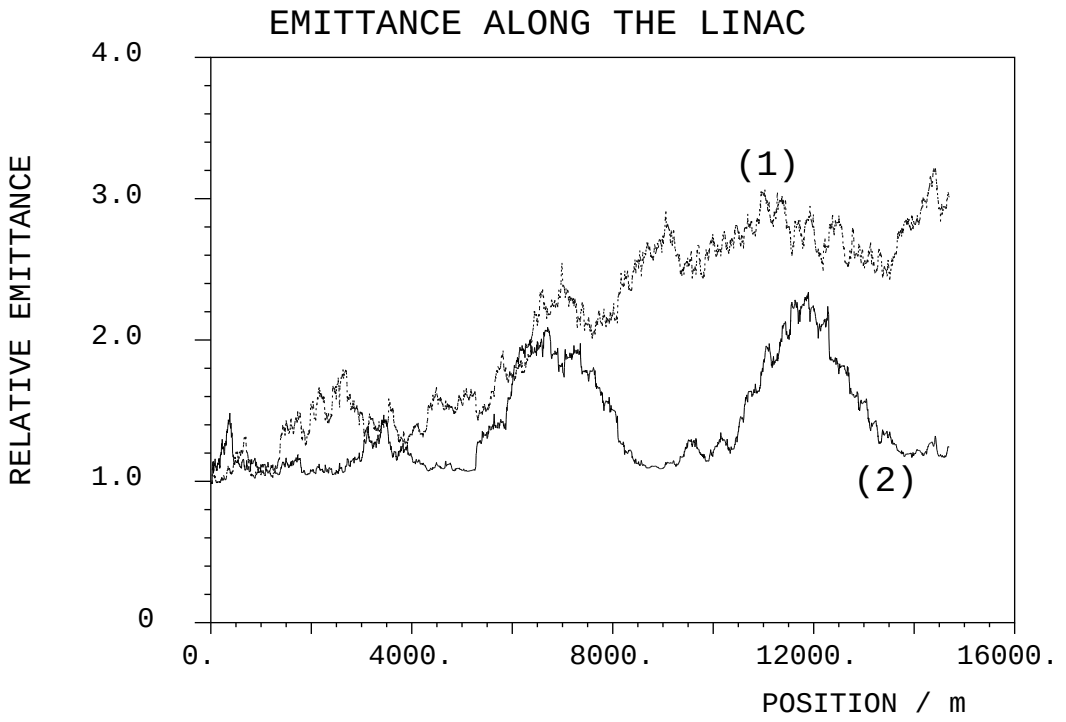

Fig. 2.18 Single-bunch emittance with 100μm rms random structure misalignment before (1) and after correction with non-dispersive bumps (2).

described earlier. As the ND-bumps create no dispersion, they only impose a wake field effect on the bunch, which is used to cancel the wake field effect from structure misalignments. If one attempts to achieve this cancellation at a great distance downstream the misaligned structures, the deflections from the wake fields have filamented and cannot be matched by the effect from the bumps anymore. It follows that the correction must be carried out as locally as possible, i.e. at as many locations as possible. The emittance correction obtained with 8 pairs of non-dispersive bump-sets and emittance measurement after each sector is highly satisfactory. On the other hand, since it is customary to demand emittance dilutions from individual effects to be smaller than 6%, the results obtained with 2 and 4 stations must be considered insufficient.

For the case of the SBLC we conclude that for successful machine tuning it is necessary to utilize 8 stations for emittance measurement. In the course of chapter 4 we will exclusively assume that the emittance is corrected with 8 pairs of bump-sets and 8 stations for emittance measurement. Scenarios involving the use of a smaller number of stations will not be pursued

	emittance growth after correction with	
stations	D-Bumps	ND-Bumps
2	-	$77\% \pm 27\%$
4	-	$10\% \pm 7\%$
8	$47\% \pm 22\%$	$2\% \pm 1\%$

Table 2.2 Single-bunch emittances from structure misalignment after correction with dispersive bumps and non-dispersive bumps. The mean values of the emittances were calculated with 10 different random seeds each for correction using 2,4 and 8 measurement stations.

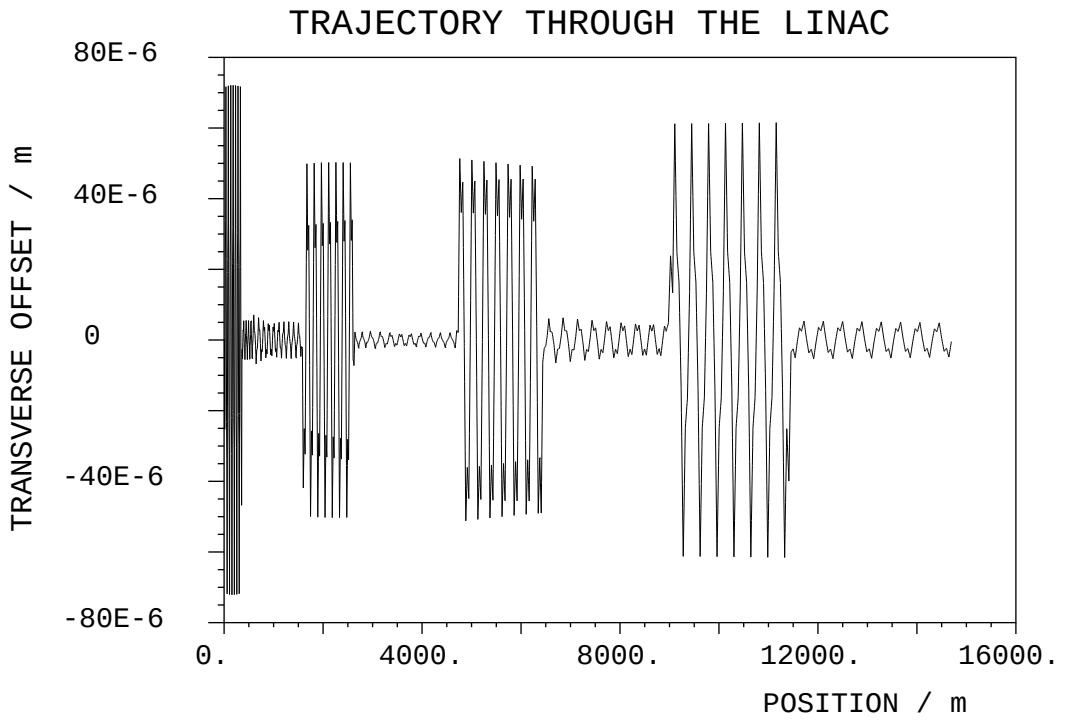

Fig. 2.19 Trajectory with optimum ND-bumps, leading to the emittance (2) of Fig. 2.18.

any further.

2.5 Minor Effects

2.5.1 Longitudinal Dipole Wake

The effect of the longitudinal dipole wake is very small. In order to demonstrate this, we looked at the voltage induced in a bunch traversing an accelerating structure with an offset of 100μm. The induced voltage versus the position within the bunch is shown in Fig. 2.20. The highest voltage induced in the bunch is -250V, the mean induced voltage -193V.

The induced voltage may in principle contribute to the filamentation of the beam. The magnitude of this additional filamentation is described by the induced rms energy spread, which evaluates to 58V. In comparison with the accelerating voltage along one structure of 102MV, this is an effect of less than $6 \cdot 10^{-7}$. Thus for practical applications the longitudinal dipole wake will have only a very small effect. Specifically, for realistic magnitudes of misalignments, the effect of this energy spread on the particle motion cannot be resolved in a computation with 23 bit mantissa.

2.5.2 Quadrupole Wake

As with the longitudinal dipole wake, the effect of the transverse quadrupole wake is tiny. In order to produce a reasonably large effect, we calculated the emittance growth caused by a misalignment of the accelerating structures of 500μm. In this simulation, the effect from the dipole wake was excluded, since it would have obscured the effect from the quadrupole wake. The monopole wake was included and the phases in the accelerating structures were set as suggested in section 2.2. For a bunch with vanishing self emittance, the mean relative centroid

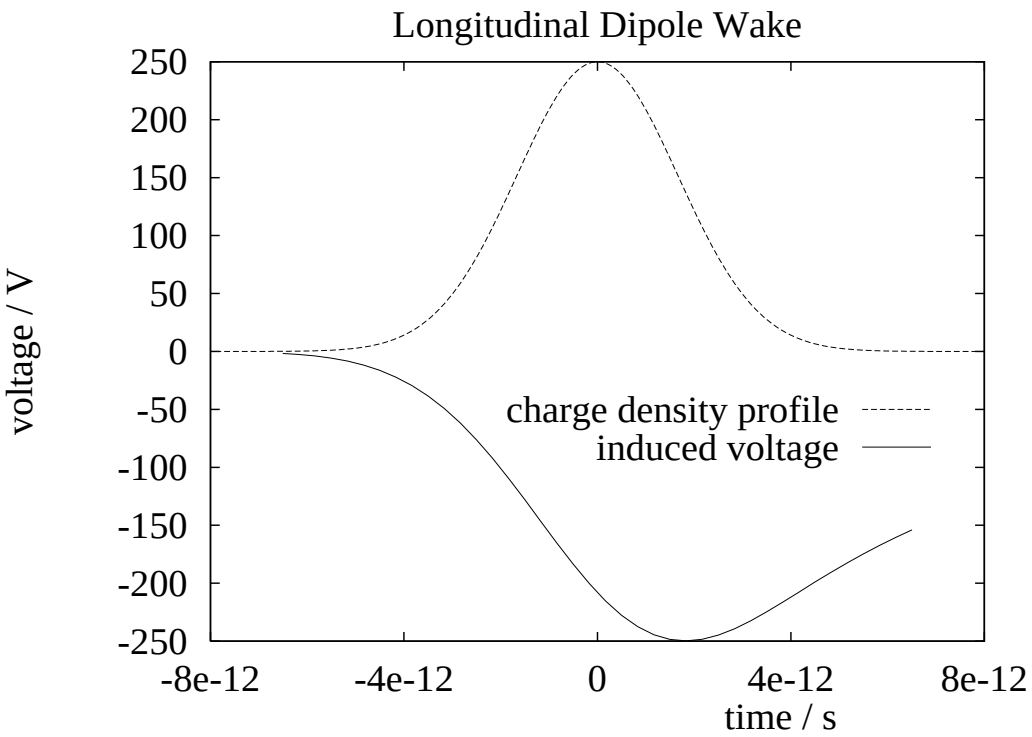

Fig. 2.20 Voltage induced by the longitudinal dipole wake in a bunch in a single structure at 100μm cavity offset (solid line). The dashed line indicates the profile of the longitudinal charge distribution.

emittance from the quadrupole wake found in a calculation using 10 different random seeds becomes $(1.4 \pm 1.6)\%$.

For a bunch injected with the nominal vertical and horizontal emittances, the increase of the relative vertical emittance at 500μm rms structure misalignment is found to be 0.4%. For comparison: the dipole wake would have caused an emittance growth of a factor greater than 30 at this value for the structure misalignment. When we reduce the structure misalignment to realistic values, the emittance contribution from the quadrupole wake falls off with the 6-th power of the rms structure misalignment. Therefore, the quadrupole wake may be ignored for realistic applications.

Chapter 3

Multi-Bunch Dynamics

In the previous chapter we investigated the effects of longitudinal and transverse wake fields and dispersion from injection offset and dipole-like kicks on a bunch of particles. It was observed that the transverse forces involved can cause a significant deformation of the bunch, resulting in an increase of the projected emittance. Similar effects are encountered on a complete bunch train: transverse wakes excited by bunches traversing an accelerating structure off axis deflect subsequent bunches. Furthermore, each bunch traversing the structure draws energy from the accelerating mode, resulting in a decrease of the available accelerating voltage for trailing bunches and thus generating an energy spread along the bunch train. Finally, the transverse kick from the accelerating mode in tilted structures gains importance.

The nonuniformity of the energy gain of the bunches must be corrected as a prerequisite for any successful beam transport as well as for successful orbit correction. This will be accomplished with the technique of "staggered timing." The transverse effects cause an increase of the projected emittance of the bunch train as a whole and must therefore be avoided by both careful alignment of the machine elements and application of correction techniques.

At several places in this chapter we shall derive machine tolerances from the contributions to the emittance due to individual effects. These tolerances will be derived from the aim of keeping the emittance contribution from individual effects below a limit of 6% of the beam emittance at injection. In doing so, we follow a practice already pursued in [29].

Throughout all our simulations we will assume that the machine lattice is of the type outlined in appendix D, with a betatron phase advance of 90° per FODO cell and a scaling of the beta function with the square root of the beam energy.

3.1 Introduction

In this section we give a brief account of how the bunch train and the wake field will be modeled.

3.1.1 Modeling the Bunch Train

In contrast to the previous chapter, we are interested now in the behavior and interaction of a large number of bunches. On the other hand, in the scope of the pure multi-bunch simulations we are not interested in the processes taking place within the bunches. The present design of the SBLC envisions using a bunch train consisting of 125 bunches separated by a distance of 4.8m (48 RF buckets).

In the course of our multi-bunch simulations we will utilize the rigid bunch approximation. In this approximation, the bunches in a bunch train are assumed to be pointlike charges of infinitesimal longitudinal extent. Furthermore, if not stated otherwise, the transverse extent of

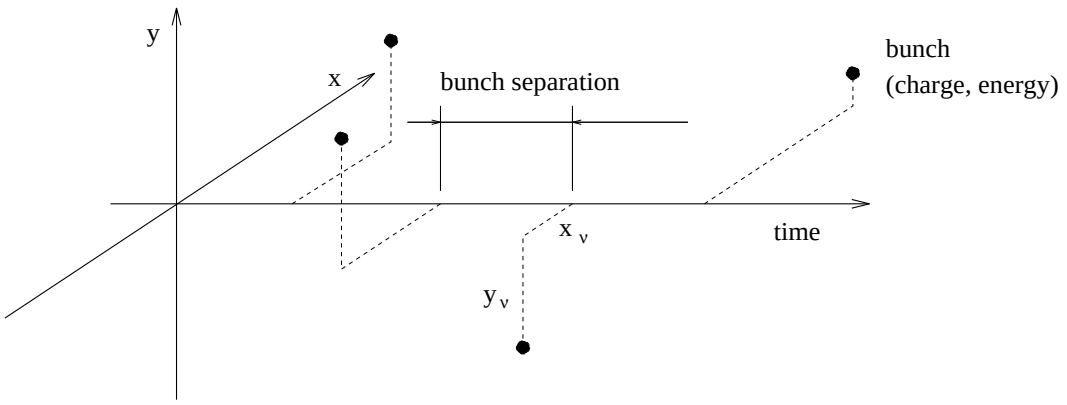

Fig. 3.1 Rigid bunch model of the bunch train for multi-bunch studies. In these simulations it is assumed that the bunches are of vanishing longitudinal and transverse extent.

the bunches is assumed to be vanishing. As a consequence, the values given for the emittances are centroid emittances, which must be combined with the self emittance to yield the total emittance of the bunch train. This way of proceeding is advantageous with respect to the interpretation of our results. In a realistic machine design one will choose the element tolerances such that the emittance contributions from the individual effects will be small in comparison with the self emittance. Thus, the behavior of the machine in a parameter regime, where this condition is met, will be of particular interest for our investigations. Therefore, the changes in the total projected emittance of the bunch train caused by individual effects would in many cases hardly be visible if the self emittance were included in the results.

Hence, for the purpose of simulating multi-bunch dynamics of a bunch train, the bunch train is described by the transverse offsets x_ν, y_ν of the bunches, the slopes x'_ν, y'_ν of their offsets, the longitudinal distances between the bunches, the bunch charges and the bunch energies as indicated in Fig. 3.1.

In all simulations it will be assumed that the bunch train consists of 125 bunches. Furthermore, we will always assume that the bunches are spaced with a distance of 4.8m and have a population of $2.9 \cdot 10^{10}$. In a few cases the two latter parameters will be subject to random errors and fluctuations. For the injection energy we will always use a value of 3.15GeV.

3.1.2 Wake Fields and Modes

For calculating the short range wake potential within a bunch we have convolved the wake potential of a short bunch with the charge distribution of the bunch. This description of the wake field was adequate since the short range wake field has large contributions of a very large number of modes extending to very high frequencies. The lower frequency components contribute significantly, but not necessarily dominantly to the short range wake field. In addition, the short range wake function of a structure is insensitive to small changes of several geometric parameters of the cells of the accelerating structure, especially the cell radius and the curvature between the cell wall and the cell iris (R_{curve} in Fig. D.2). As a consequence, the short range wake functions in two structures are in practice virtually identical despite the inevitable small machining and manufacturing errors.

These issues are entirely different for the long range wake fields encountered at large distances behind the exciting particle. The damping times for modes with very high frequencies are smaller than those for modes with lower frequencies. Moreover, the contributions to the wake from the high frequency modes cancel to some extent due to decoherence of the different

frequencies. It follows that the long range wake field is dominated by a comparatively small number of modes with low frequencies and large damping times. The behavior of the wake potential over different distances s from the bunch center is shown in Fig. 3.2, illustrating these considerations. In a first approximation, one can consider the SBLC accelerating structure as a system of 180 weakly coupled resonators, since the structure consists of 180 cells coupled by small iris apertures. It is known that a system of N coupled resonators with one resonant mode for each of the uncoupled resonators will have N different coupled modes. If we assume now that, despite the small geometry changes between adjacent cells, the resonant modes in the cells over the structure are similar and that the modes of each cell couple most strongly to the modes of the same type in adjacent cells, we will likewise get 180 coupled resonant modes of each mode type for the coupled structure. In particular, we expect to find 180 TM-like HEM_{11} modes, which, as will be outlined later, have a very strong effect on the beam.

For these reasons we will express the long range dipole wake function of the accelerating structure at distances $s > 0$ from the bunch center as a sum of modes

$$\mathcal{W}_{\parallel}(x, \tilde{x}, s) = -2\tilde{x} \sum_n x k_n \cos \frac{\omega_n s}{c_0} \exp\left(-\frac{\omega_n s}{2Q_n c_0}\right),$$

where ω_n denotes the resonant angular frequency of a mode, Q_n its quality factor, and k_n the "loss parameter", which describes the coupling strength of the mode to a beam. x is the offset of the particle exciting the wake fields and $\tilde{x}$ the offset at which the wake potential is observed. A more elaborate discussion of behavior and properties of the modes in a structure will be given in section 3.3.

This decomposition of the wake potential into a small number of discrete modes will also be convenient for another reason. As we are directing our attention now to the behavior of the wake field on large time scales, even small changes of the frequencies of the involved modes have a significant impact on the magnitude of the wake potential experienced by a trailing bunch. Hence, small machining and manufacturing errors of the structures will have a visible influence on the multi-bunch dynamics of a machine. (For the SBLC, machining precisions of $\sim 10\mu$m are expected for the cells of the accelerating structures.) As we will see later, this fact can even be exploited to obtain a partial cancellation of the wake fields of a large number of structures and thus improve the multi-bunch emittance growth significantly.

A very strong influence is exerted by the first set of dipole modes, i.e. the HEM_{11} modes. Fig. 3.3 shows the loss parameters of the (TM-like) HEM_{11} modes versus their frequencies. The modes were calculated by [36] and [37] with the mode matching method.

In cases where knowledge of the dipole modes of a complete accelerating structure is incomplete, one can resort to a qualitative description of the wake potential with the "transient approximation." This approximation exploits the fact that the small iris apertures establish only a weak coupling between adjacent cells. In this approach it is simply assumed that the wake potential is the sum of the wake potentials of the individual **uncoupled** modes of the cells of the structure. In other words: the modes of the uncoupled cells of the structure are used instead of the eigenmodes of the full structure.

The dipole modes generating the long range transverse wake field will also be referred to as higher order modes (HOM). The emittance growth caused by these modes will be called HOM-induced emittance growth.

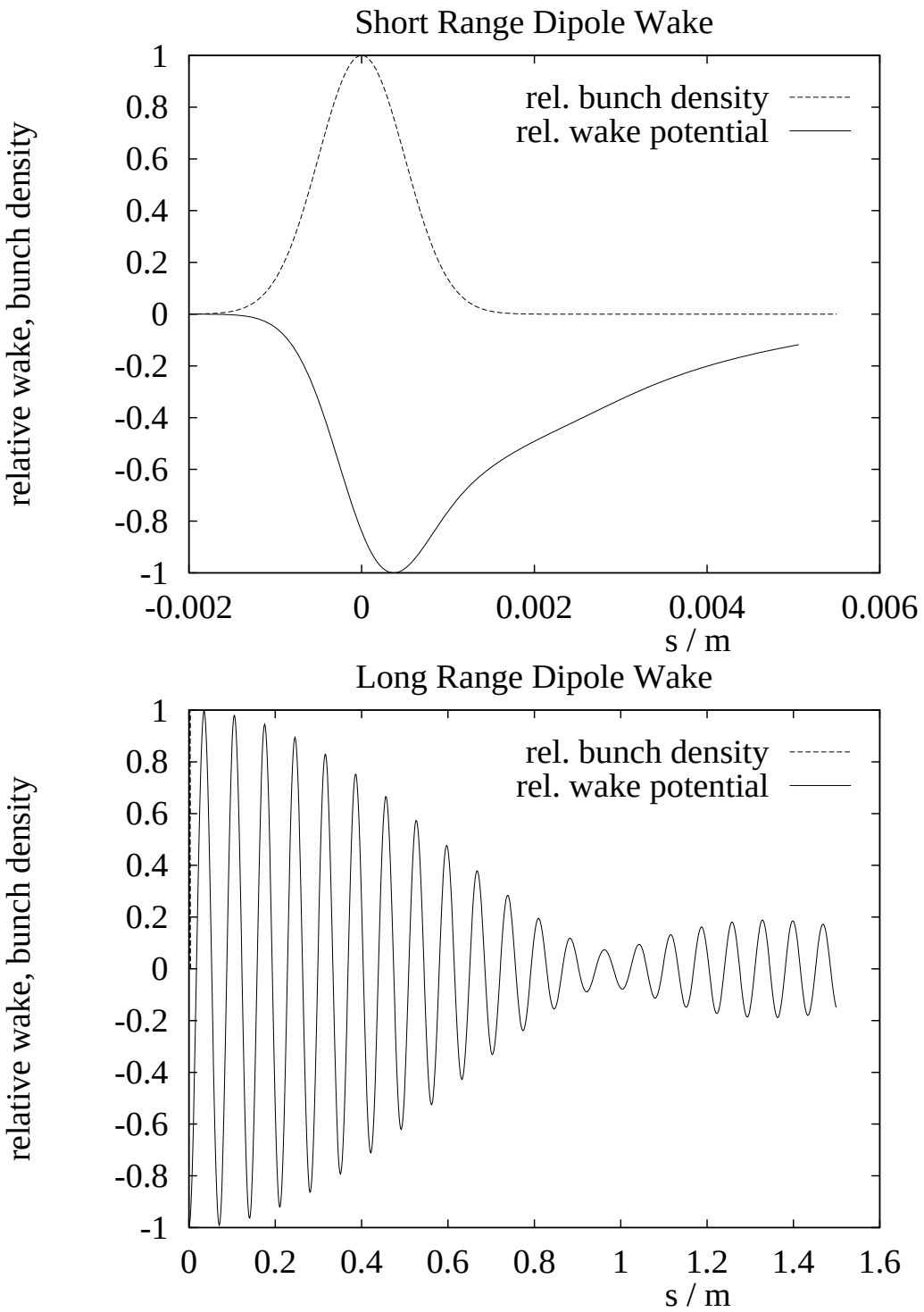

Fig. 3.2 Relative values of the longitudinal dipole wake potential on different longitudinal scales. The upper picture shows the wake in a range up to 6mm from the center of the bunch. In the lower picture the wake for distances up to 1.5m is depicted. The upper picture shows that immediately upon excitation the wake is composed of contributions extending to very high frequencies. In the lower picture, it can be seen how, at larger distances from the bunch, the wake potential becomes dominated by comparatively few resonances with high quality factor.

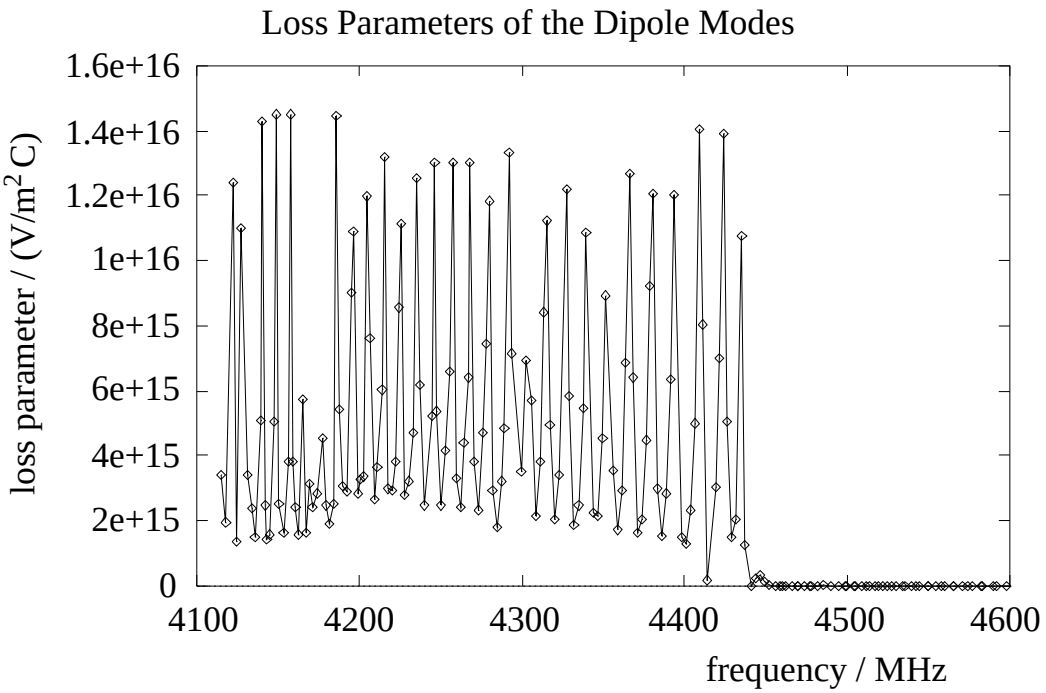

Fig. 3.3 Loss parameters of the TM-like branch of the HEM_{11} modes versus their frequencies.

3.2 Beam Loading and Staggered Timing

The current studies for a linear collider intend to achieve acceleration of the particles with an electromagnetic wave, the "accelerating mode". A particle traversing an accelerating structure draws energy from the accelerating mode, leading to a reduction of the accelerating voltage available for trailing particles. This phenomenon is known by the name "beam loading" and brings about an energy spread between the bunches in a bunch train. It is by far the dominant longitudinal long range wake effect in the SBLC.

The SBLC uses a traveling wave structure, where the voltage drop from beam loading is eased by two factors. First, the negative perturbation imposed on the field of the accelerating mode slowly propagates out of the structure. Second, energy is - for the duration of the pulse length- continuously replenished to the accelerating mode from the RF source (klystron) feeding the structure. Both processes have a typical time scale which is characterized by the filling time (to be explained below) of the structure. In the case of the SBLC, this time scale is shorter than the length of the bunch train.

For a quantitative treatment of beam loading in a traveling wave structure we essentially follow the approach given in [38]. It has been modified to model the beam not as a continuous current but as consisting of individual discrete bunches, thus allowing for variations in the bunch populations and bunch spacings and to account for the RF phase of the bunches.

To begin with, we look at the power $P(z,t)$ of the accelerating mode propagating through some cross section at the longitudinal coordinate z of the structure at the time t in absence of any beam current. As this power is subject to continuous dissipation from wall losses, we describe its evolution with the differential equation

$$\frac{\mathrm{d}P(z)}{\mathrm{d}z} = -2\alpha(z)P(z). \tag{3.1}$$

$\alpha(z)$ is an attenuation coefficient relating the ohmic power dissipation per structure length to the power flow and is obtained by

$$\alpha(z) = \frac{\omega_0}{2v_g(z)Q} \tag{3.2}$$

from the angular frequency ω_0, the quality factor Q and the group velocity $v_g(z)$ of the accelerating mode.

The SBLC study envisions the use of a so-called "constant gradient structure". These structures are commonly designed to have a constant density of (ohmic) power dissipation along z. This is achieved by varying the group velocity $v_g(z)$ of the accelerating mode linearly along the structure according to $v_g(z) = v_{g0} + zv_g'$, with v_{g0} denoting the group velocity at the beginning of the structure and v_g' the derivative of the group velocity.

Rewriting 3.1 as

$$-P(z) = \frac{v_g(z)Q}{\omega_0}P'(z) \tag{3.3}$$

and taking the derivative of 3.3 with respect to z we get

$$-P'(z) = \frac{v_g'Q}{\omega_0}P'(z) + \frac{v_g(z)Q}{\omega_0}P''(z).$$

By requiring $P''(z) = 0$ we obtain the condition for constant gradient:

$$\frac{v_g'Q}{\omega_0} = -1 \quad \Rightarrow \quad \frac{\omega_0}{Q} = -v_g'. \tag{3.4}$$

We will assume throughout all simulations that include beam loading that condition 3.4 holds.

We proceed by decomposing the total derivative of the power flow into the partial derivatives with respect to time and z and write

$$\frac{\mathrm{d}}{\mathrm{d}z}P(z,t) = \frac{\partial}{\partial z}P(z,t) + \frac{1}{v_g(z)}\frac{\partial}{\partial t}P(z,t) = -2\alpha(z)P(z,t). \tag{3.5}$$

We want to find the complex amplitude $\hat{E}(z,t)$ of the accelerating field along the structure. The field strength $E(z,t)$ is related to this complex amplitude as

$$E(z,t) = \Re e\left\{\hat{E}(z,t)\exp(j\omega_0 t)\exp\left(-\frac{j\omega_0 z}{c_0}\right)\right\}. \tag{3.6}$$

The complex amplitude $\hat{E}(z,t)$ of the accelerating field is connected with the power flow via

$$P(z,t) = \frac{|\hat{E}(z,t)|^2}{2\alpha(z)r}, \tag{3.7}$$

where r is called the shunt impedance per structure length. We will express the shunt impedance by means of a different parameter, the so-called loss parameter k of the accelerating mode as

$$r = \frac{4kQ}{\omega_0 L}, \tag{3.8}$$

where L denotes the structure length. The loss parameter relates the amplitude of the accelerating voltage $\hat{U}$ along the structure to the energy $\mathcal{U}$ stored in the accelerating mode as

$$k = \frac{|\hat{U}|^2}{4\mathcal{U}}. \tag{3.9}$$

At this point we introduce an approximation by assuming the shunt impedance to be constant along the structure. In practice, one observes a certain increase of the shunt impedance for structures in which $v_g(z)$ decreases with z.

After eliminating the power flow P with $\hat{E}$ (using 3.7) and using the fact that the accelerating wave is synchronous with the particles of the beam we recast equation 3.5 in the Laplace domain:

$$2\frac{\partial}{\partial z}\hat{E}(z,\wp)\cdot\frac{Qv_g(z)}{\omega_0} + \hat{E}(z,\wp)\frac{Qv_g'}{\omega_0} + 2\wp\hat{E}(z,\wp)\frac{Q}{\omega_0} = -\hat{E}(z,\wp), \tag{3.10}$$

or more compactly, using 3.4:

$$v_g(z)\frac{\partial}{\partial z}\hat{E}(z,\wp) + \wp\hat{E}(z,\wp) = 0, \tag{3.11}$$

where $\wp = j\omega + \sigma$ is the parameter of the Laplace transform. If the structure is traversed by a beam current $i(t)$, an additional contribution to the electric field is induced which modifies 3.11 into

$$v_g(z)\frac{\partial}{\partial z}\hat{E}(z,\wp) + \wp\hat{E}(z,\wp) = -\frac{2k}{L}i(\wp + j\omega_0). \tag{3.12}$$

Integrating this differential equation leads us to an expression for the electric field amplitude along the structure in the Laplace domain:

$$\hat{E}(z,\wp) = i(\wp+j\omega_0)\cdot\frac{2k}{L}\frac{1}{\wp}\left[\left(\frac{v_{g0}+zv_g'}{v_{g0}}\right)^{-\wp/v_g'} - 1\right] + \hat{E}(0,\wp)\cdot\left(\frac{v_{g0}+zv_g'}{v_{g0}}\right)^{-\wp/v_g'}. \tag{3.13}$$

Integrating the electric field over z then yields the amplitude of the accelerating voltage in the Laplace domain:

$$\begin{aligned}\hat{U}(\wp) &= i(\wp + j\omega_0) \cdot \frac{2k}{L}\frac{1}{\wp}\left[\frac{v_{g0}}{\omega_0/Q + \wp}\left(1 - \exp\left\{-\left(\frac{\omega_0}{Q} + \wp\right)t_{fill}\right\}\right) - L\right] + \\ &\quad \hat{E}(0,\wp) \cdot \frac{v_{g0}}{\omega_0/Q + \wp}\left(1 - \exp\left\{-\left(\frac{\omega_0}{Q} + \wp\right)t_{fill}\right\}\right). \qquad (3.14)\end{aligned}$$

Here, we have introduced a new parameter called filling time:

$$t_{fill} = \int_0^L \frac{1}{v_g(z)}\mathrm{d}z = \frac{1}{v_g'}\ln\frac{v_{g0} + Lv_g'}{v_{g0}}. \qquad (3.15)$$

The filling time is the time required by the accelerating mode to propagate to the end of the accelerating structure after turning on the RF source, i.e. the time needed to fill the entire structure with the accelerating field. It is one of the most important parameters for describing the filling and beam loading behavior of a structure.

In the following, we will use the abbreviation

$$M = \omega_0/Q.$$

We assume that the amplitude of the electric field $\hat{E}(0,t)$ at the beginning of the structure is a step function

$$\hat{E}(0,t) = E_0\exp(j\varphi_0)\vartheta(t) = E_0\exp(j\varphi_0) \cdot \begin{cases} 0 & t < 0 \\ 1/2 & t = 0 \\ 1 & t > 0 \end{cases}.$$

Furthermore, we assume that the beam current is a sum of distributions

$$i(t) = \sum_{\nu=1}^{N_b} q_\nu \cdot \delta(t - T_\nu)$$

characterized by the bunch charges q_ν and their times of arrival T_ν. N_b is the number of bunches in the bunch train. With these assumptions we write the accelerating voltage for a particle entering the structure at the time t in the time domain as

$$\begin{aligned}U(t) &= \Re e\left\{\hat{U}(t)\exp(j\omega_0 t)\right\} \\ &= E_0\frac{v_{g0}}{M}\left[\left(1 - \mathrm{e}^{-Mt}\right)\vartheta(t) - \mathrm{e}^{-Mt_{fill}}\left(1 - \mathrm{e}^{-M(t-t_{fill})}\right)\vartheta(t - t_{fill})\right] \cdot \cos\left(\omega_0 t + \varphi_0\right) \\ &+ \sum_{\nu=1}^{N_b} q_\nu\frac{2k}{L}\left[\frac{v_{g0}}{M}\left\{\left(1 - \mathrm{e}^{-M(t-T_\nu)}\right)\vartheta(t - T_\nu) - \right.\right. \\ &\qquad \left.\mathrm{e}^{-Mt_{fill}}\left(1 - \mathrm{e}^{-M(t-T_\nu-t_{fill})}\right)\vartheta(t - T_\nu - t_{fill})\right\} \\ &\qquad \left.-L\vartheta(t - T_\nu)\right] \cdot \cos(\omega_0(t - T_\nu)). \qquad (3.16)\end{aligned}$$

The cosine factors in this expression account for the phase of the RF power with respect to the bunches and of the bunches with respect to each other.

If it is assumed that the shunt impedance per structure length $r(z)$ is constant it follows from the uniformity of the power dissipation along the structure that in the absence of a beam

current the accelerating gradient $\hat{E}(z,t)$ is also constant for $t > t_{fill}$ (equation 3.7). In this case we have $|\hat{E}(z,t)| = E_0$ for the unloaded structure. Therefore, we will refer to E_0 as the "unloaded gradient" of the structure.

Finally, another important parameter of an accelerating structure is the attenuation τ, which is given by

$$\tau = \int_0^L \alpha(z)\mathrm{d}z = \frac{\omega_0}{2Q} t_{fill}. \tag{3.17}$$

It relates the power coming out of the unloaded structure to the input power as

$$P(L) = P(0)\mathrm{e}^{-2\tau}. \tag{3.18}$$

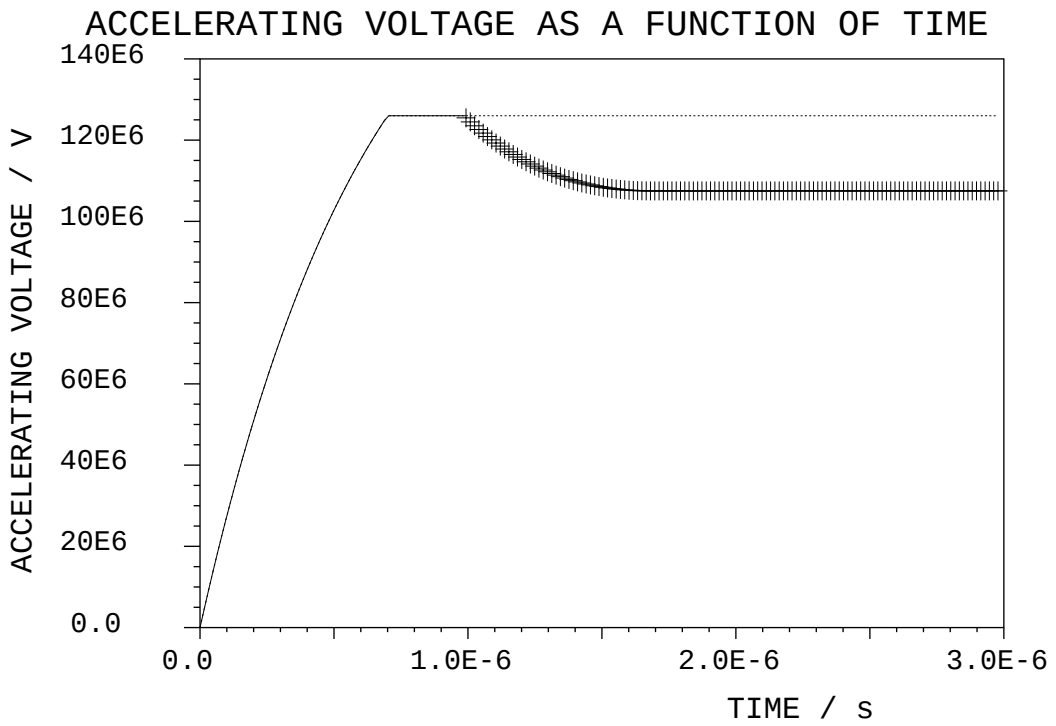

Fig. 3.4 Accelerating voltage with and without beam loading. The time is given relative to klystron turn-on. The solid line shows the voltage across the structure before injection of the beam current. The dotted line gives the voltage expected in case of no beam accelerated. The crosses show the voltages imparted on the bunches of a 300mA beam.

Fig. 3.4 and Fig. 3.5 show the beam loading for realistic parameters in a realistic constant gradient S-band structure. The assumptions are:

- structure length $L = 6\mathrm{m}$,
- $\omega_0 = 2\pi \cdot 2998\mathrm{MHz}$, $Q = 12000$, $t_{fill} = 0.7\mu\mathrm{s}$,
- loss parameter of the accelerating mode $k = 111 \cdot 10^{12}\mathrm{V/C}$,
- 125 bunches with 4.8m bunch spacing,
- unloaded gradient $E_0 = 21\mathrm{MV/m}$.

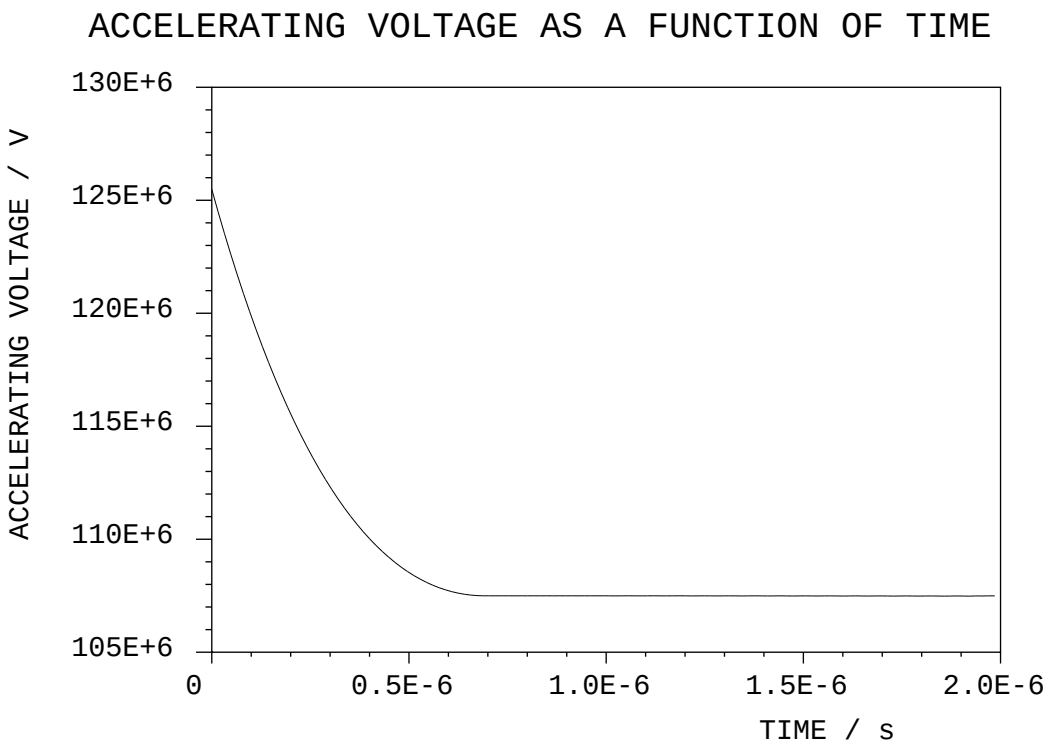

Fig. 3.5 Accelerating voltage with beam loading in detail. The time is given relative to the arrival of the first bunch at the structure.

The bunch charge was 4.65nC. Fig 3.4 shows the evolution of the accelerating voltage without beam loading (solid and dotted curve) and the voltages in the presence of beam loading (crosses). The solid curve ranging from $t = 0$ to $t = 1\mu$s shows the build-up of the available accelerating voltage in the structure. The dotted line shows the voltage in case of no beam accelerated. We see that one filling time (0.7μs) after klystron ignition the build-up of the accelerating voltage is finished and the voltage goes into a steady state. Now we assume that 1μs after klystron turn-on a beam current of 300mA is injected into the structure. As a consequence, the accelerating voltage is reduced according to the previously derived formulae. The accelerating voltages seen by the individual bunches are drawn as crosses. Again, the voltage seen by the bunches reach a steady state one filling time after injection of the beam. The reduction of the accelerating voltage is roughly 17% for our assumptions. Fig. 3.5 shows the accelerating voltages for a bunch train that has been injected after the structure has been filled completely. The voltages seen by the bunches have been joined to a continuous curve. The times here are relative to the injection time.

An energy spread on the bunch train of this magnitude is not acceptable for many reasons. In particular, the dispersive and chromatic effects would make an emittance preserving beam transport along the machine very difficult. Also, the final focus system of a linear collider can only accept a small energy spread of 3.6% (peak to peak). Particles with greater energy deviations will, due to the large chromaticity of the final focus system, be distributed over a larger spot size at the interaction point. Consequently, these particles will contribute little to the luminosity.

Therefore it is necessary to find a way to compensate the differences of the accelerating voltages between the bunches. To this end, we look at the behavior of the voltages seen at various locations in the bunch train with respect to the klystron ignition time. Fig. 3.6 shows the accelerating voltage along the bunch train for delays between klystron ignition and entry of

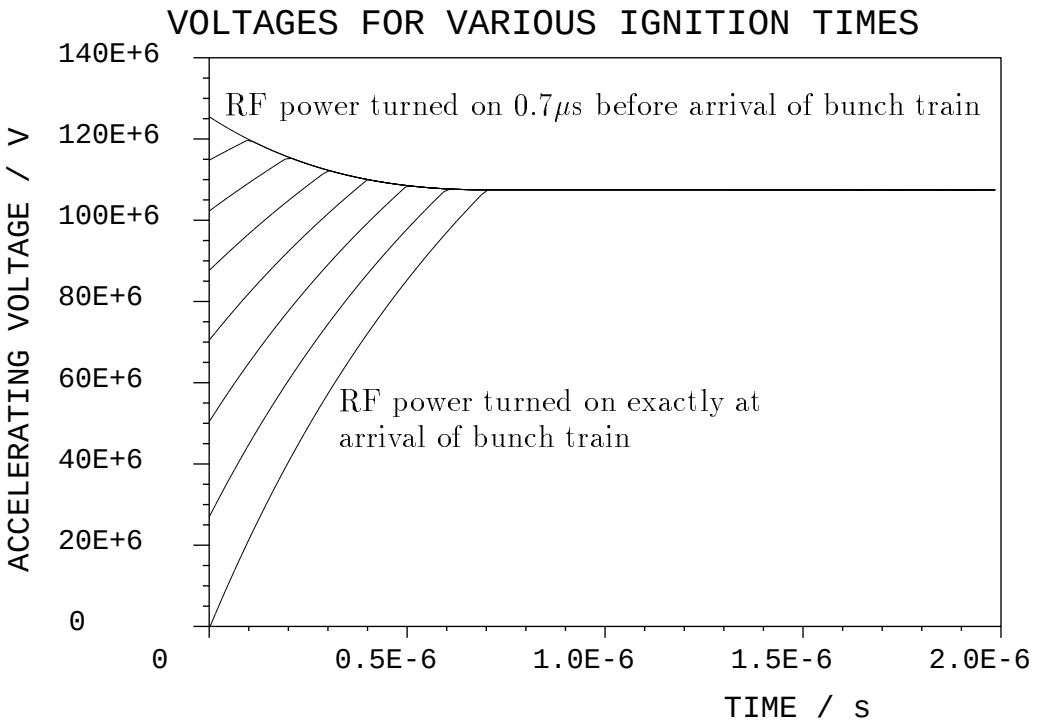

Fig. 3.6 Accelerating voltage seen along the bunch train for different delays between klystron ignition and entry of the bunch train into the structure. The time is given relative to the arrival of the first bunch at the accelerating structure.

the bunch train into the structure ranging from 0.0μs to 0.7μs. For injection of the bunch train one filling time (or more) after klystron ignition, we see the familiar drop of the voltage from its peak value by 17% to its steady state level. However, if the bunch train enters the structure earlier, the accelerating wave has not yet propagated fully to the end of the structure and hence the voltage for the first bunches is reduced. Then the voltage rises to a maximum until the filling process is completed. Thereafter it goes down again to its steady state value. If the bunch train enters the structure exactly upon klystron ignition, the voltage rises monotonically within one filling time from zero to the steady state value. It is seen thus, that by varying the ignition times of the individual klystrons one can produce very different profiles of accelerating voltages along a bunch train.

This dependence of the accelerating voltages on the time between turn-on of the RF power and arrival of the bunch train at the structure is exploited by a technique called "staggered timing". The idea there is to set the klystron ignition times of the structures to different values such that the energy spreads from different structures cancel ([39], [40]), or more specifically:

The ignition time of each klystron is adjusted to minimize the peak to peak energy spread across the bunch train behind the structure(s) fed by that klystron.

The algorithm starts by generating a vector containing the bunch energies, which all are assigned the injection energy (3.15GeV for the SBLC) as initial values. Then, the energy gains over the number of structures fed by one klystron are calculated for a number of possible klystron ignition times. The vector sums from the particle energies and the different energy gain vectors are evaluated, and of the resulting new energy vectors the one with the smallest

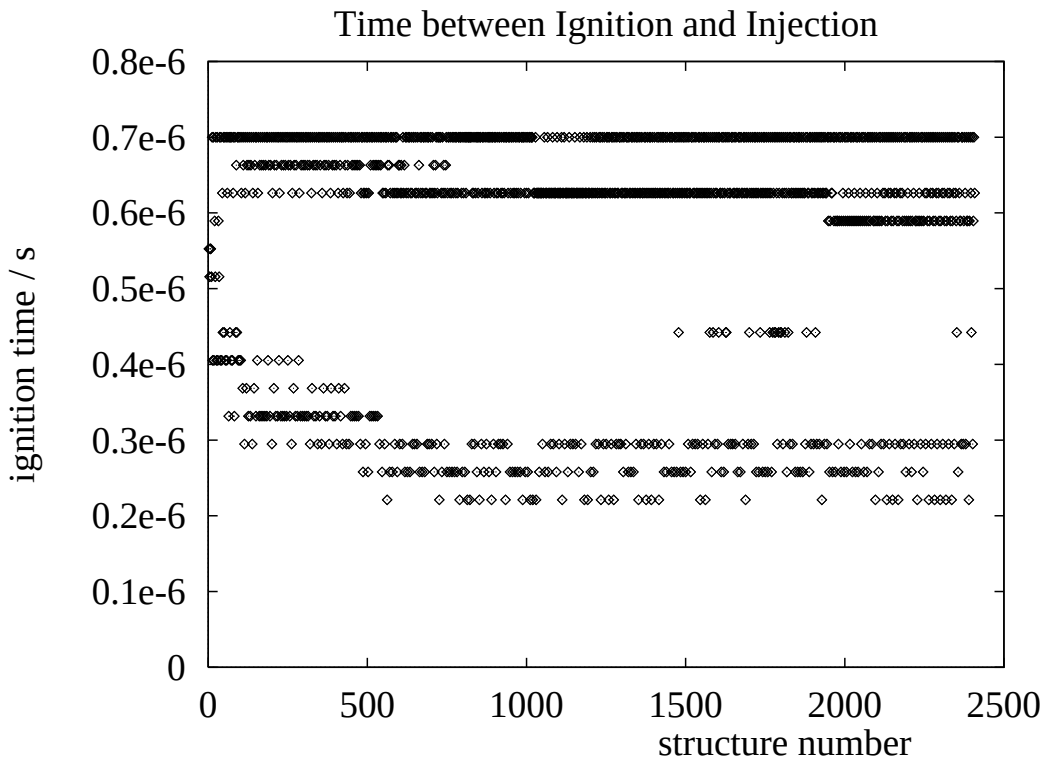

Fig. 3.7 Klystron ignition times for staggered timing. The ignition time is the interval between turn-on of the RF power at the structure and the arrival of the first bunch of the bunch train at that structure.

peak to peak energy spread is selected. The ignition time of the corresponding klystron is set to the ignition time that produces the smallest energy spread and then the procedure is repeated at the next klystron with the new energy vector.

From this algorithm one obtains a pattern of the ignition times as depicted in Fig. 3.7. Here the ignition time was allowed to assume 20 different values, which were evenly spaced between 0.0μs and 0.7μs before injection of the bunch train. It was taken into account that each klystron feeds two successive accelerating structures.

This pattern of ignition times leads to an evolution of the maximum energy spread across the bunch train as shown in Fig. 3.8. It shows the maximum and the minimum bunch energy occurring in the bunch train normalized to the mean energy. It turns out that the peak to peak energy spread in the bunch train is reduced to less than 1% at the end of the machine. Including the single bunch energy spread of $\sim 1\%$ this gives a total peak to peak energy spread across the bunch train of $\sim 2\%$, which is well acceptable for the final focus system.

Fig. 3.9 shows the energies of the individual bunches in the bunch train at the end of the linac. The energy profile displays two small peaks in the interval from 0 to 0.7μs and then becomes constant.

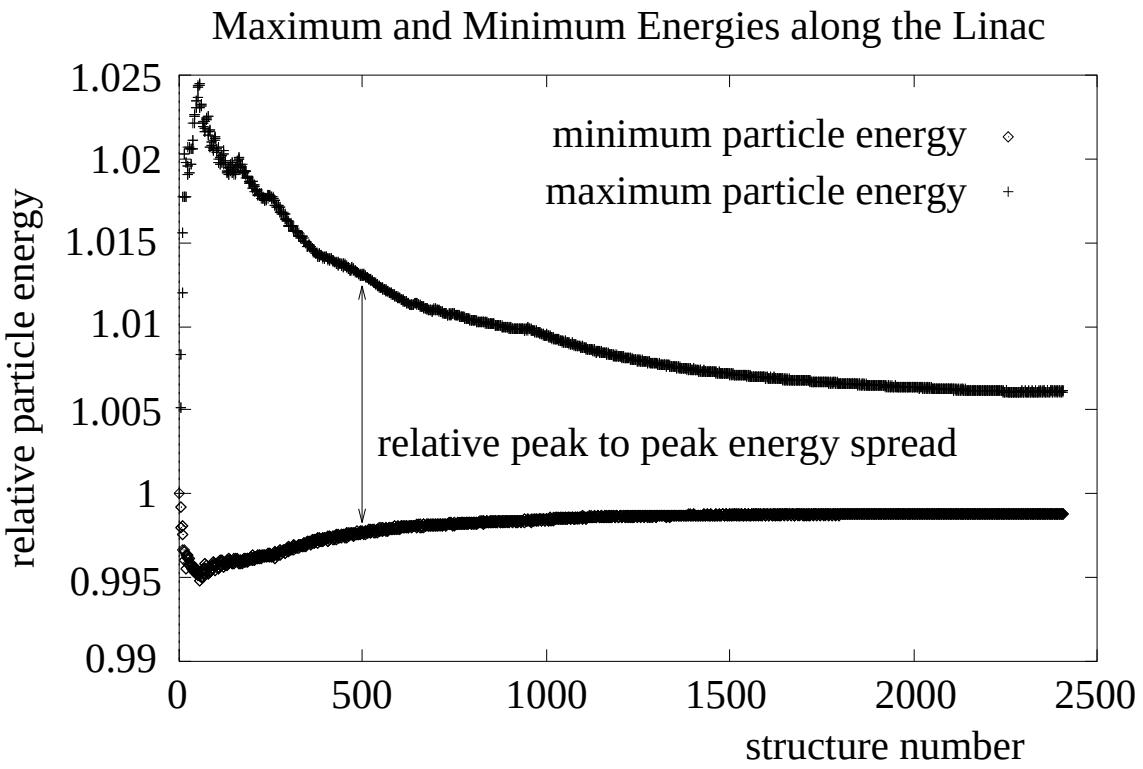

Fig. 3.8 Evolution of the relative peak to peak energy spread across the bunch train along the linac. The dots show the maximum and the minimum bunch energy in the bunch train normalized to the mean energy.

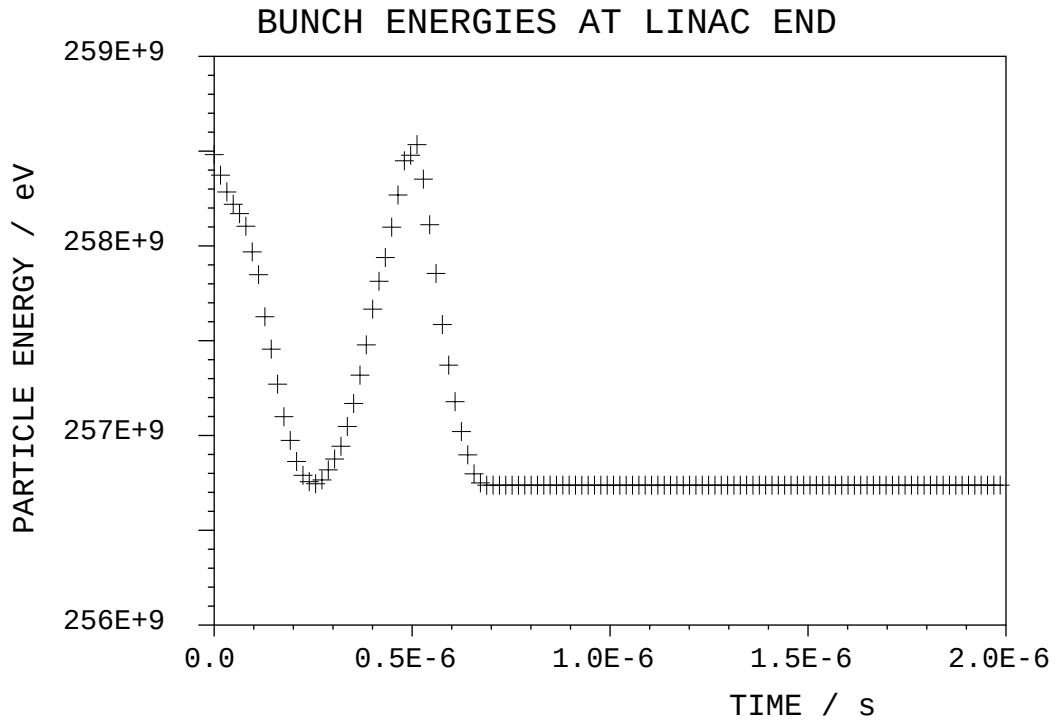

Fig. 3.9 Energies of the individual bunches at machine end with beam loading and correction of the energy spread with staggered timing.

3.3 Interaction with Dipole Modes

In chapter 2 we saw that the transverse dipole wake is a prominent source of emittance dilution for individual bunches. Long range transverse dipole wakes will affect a train of bunches comparably by imparting transverse kicks of differing magnitudes and directions on the individual bunches. In this section we will therefore give an investigation of the influence of these wakes on the multi-bunch dynamics.

The oscillatory component of the electric field in a cavity can be expressed as a sum of eigenmodes. The electric fields $\vec{\mathcal{E}}_n(\vec{x})$ of these modes are solutions of the equation

$$\text{curl curl } \vec{\mathcal{E}}_n(\vec{x}) = \omega_n^2 \mu_0 \varepsilon_0 \vec{\mathcal{E}}_n(\vec{x}), \tag{3.19}$$

where ω_n is the angular eigenfrequency of the mode n. In the case of vanishing losses ($Q_n \to \infty$) the $\vec{\mathcal{E}}_n$ are real valued. For the modes with non-vanishing azimuthal dependence there are two orthogonal polarizations of $\vec{\mathcal{E}}_n(\vec{x})$ with identical mode properties but different azimuthal orientation of the field pattern. For the dipole modes one can choose these polarizations to have the extrema of their electric field on the x- and on the y-axis. The stored energy associated with the field pattern $\vec{\mathcal{E}}_n(\vec{x})$ reads

$$\mathcal{U}_n = \frac{\varepsilon_0}{2} \int_V \vec{\mathcal{E}}_n^2 \mathrm{d}V. \tag{3.20}$$

Firstly, we will investigate in detail the effect of the TM-like branch of the HEM_{11}-modes for a variety of conditions. In addition to this, we will touch the issue of emittance growth caused by the TE-like branch of the HEM_{11}-modes.

The classification of the dipole modes into TE-like and TM-like modes originates in the analysis of resonant modes of a perfect pill-box cavity. There one finds two distinct classes of modes, namely the TE-modes, which have a vanishing longitudinal electric field, and the TM-modes, which have a vanishing longitudinal magnetic field [41]. Because the geometry of the cells of the accelerating structure resembles a pill-box, the lowest dipole modes in these cells have field configurations resembling the fields of the lowest pill-box modes. The dipole modes in an accelerating structure are commonly called TE-like and TM-like accordingly. It will turn out that the TM-like branch of the dipole modes has the potential for causing considerable growth of the projected emittance and that resolute measures will have to be taken to keep this emittance growth at a tolerable level.

3.3.1 Interaction with TM-like Modes

We consider now the special case of the interaction of the beam with the TM-like dipole modes. For simplicity, we start with the assumption that the structure is traversed by a leading charge q exciting the fields and a test charge $\tilde{q}$ at the constant offsets $\vec{x}_\perp$ and $\tilde{\vec{x}}_\perp$ from the structure axis respectively. This approximation is justified if the betatron wavelength (appendix C) is large in comparison with the structure length and hence the transverse particle offsets change little over one structure length. Further, we assume that the particles move along the z-axis at the velocity of light c_0.

The mode voltage is the synchronously integrated electric field of the field pattern $\vec{\mathcal{E}}_n(\vec{x})$ at the offset $\vec{x}_\perp$. It reads

$$V_n(\vec{x}_\perp) = \int_{-\infty}^{\infty} \mathcal{E}_{nz}(\vec{x}_\perp, z) \exp\left(\frac{j\omega_n z}{c_0}\right) \mathrm{d}z. \tag{3.21}$$

In formula 2.23 of section 2.1.3 [20] it was pointed out that the dipole component of the longitudinal wake potential scales linearly with the offsets of the leading and trailing particles. The fields of the modes can be thought of as being composed of waves of equal wave number

and frequency traveling in positive and negative direction of the z-axis. While the component traveling in the negative direction does not contribute to the interaction with the beam, the mode voltage of the component traveling in the positive direction scales linearly with the particle offset when the phase velocity is equal to the velocity of light. On the other hand, if the phase velocity deviates from c_0 the wave practically does not contribute to the interaction with the beam. For this reason, we can express the mode voltage obtained at an offset x by the voltage seen at any other offset a as:

$$V_n(x) = \frac{x}{a}\int_{-\infty}^{\infty} \mathcal{E}_{nz}(x=a, y=0, z)\exp\frac{j\omega_n z}{c_0}\mathrm{d}z. \tag{3.22}$$

The relation between the mode voltage in the plane of maximum electric field and the energy stored the mode is expressed by the "loss parameter" of the dipole mode n (see also [16], [18], [19]), [42], which is defined as:

$$k_n = \frac{V_n^*(x=a)V_n(x=a)}{4a^2\mathcal{U}_n}, \tag{3.23}$$

with the extrema of $\mathcal{E}_{nz}(\vec{x})$ lying in the x-plane. If the losses are small, then it can be shown that the longitudinal wake potential of a point charge q seen by a test charge trailing with the distance s can be expressed with this loss parameter as

$$\mathcal{W}_{\parallel}(\vec{x}_\perp, \tilde{\vec{x}}_\perp, s) = -\sum_n 2\Re e\left\{k_n\vec{x}_\perp\cdot\tilde{\vec{x}}_\perp\exp\frac{j\omega_n s}{c_0}\right\}\exp\left(-\frac{\omega_n s}{2Q_n c_0}\right)\vartheta(s). \tag{3.24}$$

The summation in this expression extends over all modes of the cavity. $\vartheta(s)$ is the step function

$$\vartheta(s) = \begin{cases} 0 & s<0 \\ 1/2 & s=0 \\ 1 & s>0 \end{cases}.$$

From the longitudinal wake potential we can obtain the transverse wake using relation 2.35. Differentiating 3.24 with respect to $\tilde{\vec{x}}_\perp$ and integrating along s we get

$$\vec{\mathcal{W}}_\perp(\vec{x}_\perp, \tilde{\vec{x}}_\perp, s) = \sum_n 2k_n\vec{x}_\perp\int_{-\infty}^{s}\Re e\left\{\exp\frac{j\omega_n\varsigma}{c_0}\right\}\exp\left(-\frac{\omega_n\varsigma}{2Q_n c_0}\right)\vartheta(\varsigma)\mathrm{d}\varsigma \tag{3.25}$$

$$\approx \sum_n 2k_n\vec{x}_\perp\Im m\left\{\frac{c_0}{\omega_n}\exp\frac{j\omega_n s}{c_0}\right\}\exp\left(-\frac{\omega_n s}{2Q_n c_0}\right)\vartheta(s). \tag{3.26}$$

The transverse wake given by equation 3.26 will impart a deflection

$$\Delta\tilde{\vec{x}}'_\perp(s) = 2q\tilde{q}\sum_n\frac{c_0}{\tilde{W}\omega_n}\vec{x}_\perp k_n\sin\frac{\omega_n s}{c_0}\exp\left(-\frac{\omega_n s}{2Q_n c_0}\right)\cdot\vartheta(s). \tag{3.27}$$

on a test charge $\tilde{q}$ with the energy $\tilde{W}$.

The transverse deflection of the particles by the dipole modes will also create an additional offset of the particles at the structure end. If a particle is deflected at the position z in an accelerating structure, the offset $\Delta\tilde{\vec{x}}_\perp$ at the structure end will depend on the deflection and on the element T_{12} of the transfer matrix $\mathbf{T}$ (see appendix C) as $\Delta\tilde{\vec{x}}_\perp(L) = T_{12}(z,L)\Delta\tilde{\vec{x}}'_\perp(z)$, where L denotes the structure length. Putting in the explicit coefficient of the transfer matrix for an accelerating structure, this becomes

$$\Delta\tilde{\vec{x}}_\perp = T_{12}(z_{kick}, L)\Delta\tilde{\vec{x}}'_\perp = \frac{\tilde{W}(z_{kick})}{\tilde{g}}\ln\frac{\tilde{W}(L)}{\tilde{W}(z_{kick})}\Delta\tilde{\vec{x}}'_\perp(z_{kick}), \tag{3.28}$$

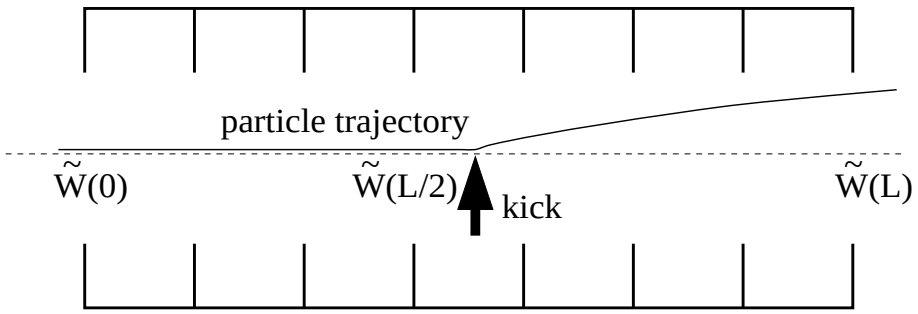

Fig. 3.10 In the central kick approximation for the calculation of the particle offset caused by deflection by dipole modes it is assumed that the particles get a concentrated transverse kick at the cavity center. $\tilde{W}(z)$ denotes the particle energy along the structure and L is the structure length.

where $\tilde{W}(z)$ denotes the energy of the kicked particle at the position z and $\tilde{g}$ is the accelerating gradient $\tilde{g} = \mathrm{d}\tilde{W}(z)/\mathrm{d}z$. The gradient is assumed to be constant along the structure. Frequently we will assume that the particles get one concentrated kick at the center of the accelerating structure. This assumption is illustrated in Fig. 3.10. Substituting the deflection $\Delta\tilde{x}'$ in 3.28 with 3.27 and using $z_{kick} = L/2$ we finally express the offset resulting at the structure end as:

$$\Delta\tilde{\vec{x}}_\perp(s) = 2q\tilde{q}\sum_n \frac{c_0}{\omega_n}\vec{x}_\perp k_n \sin\frac{\omega_n s}{c_0}\exp\left(-\frac{\omega_n s}{2Q_n c_0}\right)\cdot\vartheta(s)\cdot\frac{1}{\tilde{g}}\ln\frac{\tilde{W}(L)}{\tilde{W}(L/2)}. \tag{3.29}$$

This approximation, which assumes the kick from the dipole modes to be concentrated at the structure center, will be called the "central kick approximation." Approximations 3.27 and 3.29 will be used in most of our tracking calculations. In a few exceptional cases that will be announced explicitly we will demonstrate the application of a more refined approach to be outlined next.

Refinement

The formalism described above only accounts for the offset of the bunch with respect to the cavity. However, it is also possible to account for the slope of the particle trajectory, tilt misalignment of the structure, and structure sag.

For simplicity, we confine our considerations to the x-coordinate in the transverse plane. We assume that the leading and the trailing particle q and $\tilde{q}$ traverse the structure along the paths $x(z)$ and $\tilde{x}(z)$. Again, the longitudinal velocity is approximated to be equal to the vacuum speed of light c_0. Now we express the mode voltage introduced in 3.21 more generally as the synchronously integrated product of the relative particle offsets times the transverse derivative of the longitudinal electric field on the axis:

$$V_n^{(t)} = \int_{-\infty}^{\infty}\nabla_x\mathcal{E}_{nz}(z)x(z)\exp\frac{j\omega z}{c_0}\mathrm{d}z, \qquad \tilde{V}_n^{(t)} = \int_{-\infty}^{\infty}\nabla_x\mathcal{E}_{nz}(z)\tilde{x}(z)\exp\frac{j\omega z}{c_0}\mathrm{d}z. \tag{3.30}$$

The voltage induced on the trailing particle under the assumption of constant particle offsets was described by equation 3.24. Expanding the loss parameter in this formula into the mode voltages we can rewrite the voltage induced by one individual mode as

$$U_n(x,\tilde{x},s) = -2q\Re e\left\{\frac{1}{4\mathcal{U}_n}\frac{xV_n^*(x=a)}{a}\frac{\tilde{x}V_n(x=a)}{a}\exp\frac{j\omega_n s}{c_0}\right\}\exp\left(-\frac{\omega_n s}{2Q_n c_0}\right)\vartheta(s). \tag{3.31}$$

Here, the term $xV_n^*(x=a)/a$ pertains to the excitation of the mode by the leading particle, and $\tilde{x}V_n(x=a)/a$ to the change of energy of the trailing particle by the excited fields. Replacing these mode voltages with the voltages from 3.30, the voltage induced on the trailing charge by one mode can be expressed more generally as

$$U_n(s) = -2q\Re e\left\{\frac{V_n^{(t)*}\cdot\tilde{V}_n^{(t)}}{4\mathcal{U}_n}\exp\frac{j\omega_n s}{c_0}\right\}\exp\left(-\frac{\omega_n s}{2Q_n c_0}\right). \tag{3.32}$$

Next, we expand the particle trajectories relative to the structure axis into the polynomials P_0, P_1 and P_2 of orders 0, 1 and 2. These polynomials are defined as

$$P_0(z) = 1, \quad P_1(z) = \frac{z-\Lambda}{\Lambda}, \quad P_2(z) = \frac{z\,(L-z)}{\Lambda^2}, \tag{3.33}$$

$$\Lambda = \frac{L}{2}.$$

With the expansion coefficients p_0, p_1, p_2 and $\tilde{p_0}$, $\tilde{p_1}$, $\tilde{p_2}$ we approximate the relative trajectory of the leading and of the trailing particle through the structure as

$$x(z) = p_0P_0(z) + p_1P_1(z) + p_2P_2(z)\ , \quad \tilde{x}(z) = \tilde{p}_0P_0(z) + \tilde{p}_1P_1(z) + \tilde{p}_2P_2(z).$$

Using this approximation of the particle trajectories relative to the structure axis we write the mode voltages $V_n^{(t)}$ in the form

$$V_n^{(t)} \approx \int_0^L \nabla_x\mathcal{E}_{nz}(z)\,(p_0P_0\,(z) + p_1P_1(z) + p_2P_2(z))\exp\frac{j\omega_n z}{c_0}\mathrm{d}z.$$

Here the integration extends over the structure length L, neglecting the field outside the cavity. The physical relevance of this expansion is indicated in Fig. 3.11. The expansion coefficients

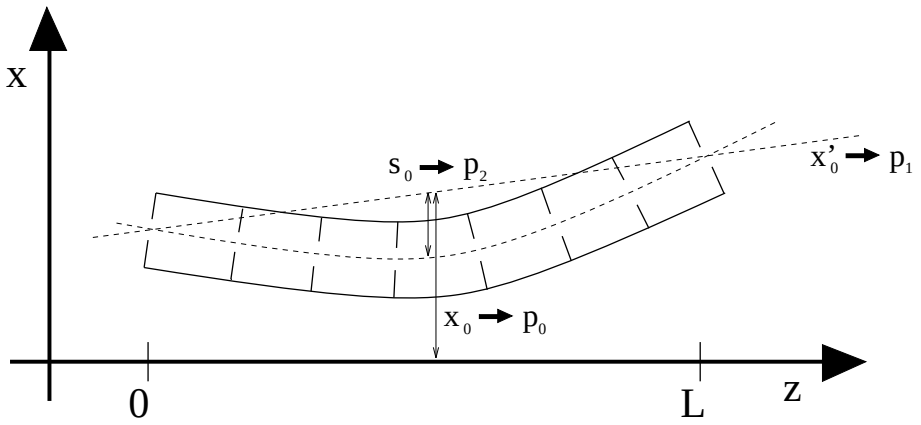

Fig. 3.11 General misaligned cavity with offset x_0, tilt x_0' and sag s_0. The particle trajectory relative to the structure axis is described by the coefficients $p_0 \ldots p_2$ of a parabola. The cavity offset, tilt and sag contribute to the coefficients p_0, p_1 and p_2 respectively.

describe the offset, the tilt and the sag of the structure and equivalent errors of the particle trajectory relative to the structure axis.

For brevity we introduce the derivative of the mode voltage with respect to the expansion coefficients p_ν of the particle trajectory

$$\mathcal{V}_{\nu n} = \int_0^L \nabla_x\mathcal{E}_{nz}(z)P_\nu(z)\exp\frac{j\omega_n z}{c_0}\mathrm{d}z. \tag{3.34}$$

With these quantities the mode voltages can be expressed as

$$V_n^{(t)} = p_0 \mathcal{V}_{0n} + p_1 \mathcal{V}_{1n} + p_2 \mathcal{V}_{2n}. \tag{3.35}$$

Now we replace these expressions for $V_n^{(t)*}$ and $V_n^{(t)}$ in equation 3.32. The voltage induced on the next bunch then becomes

$$\tilde{U}_n(s) = -q \frac{\Re e \left\{ \left(p_0 \mathcal{V}_{0n}^* + p_1 \mathcal{V}_{1n}^* + p_2 \mathcal{V}_{2n}^*\right) \left(\tilde{p}_0 \mathcal{V}_{0n} + \tilde{p}_1 \mathcal{V}_{1n} + \tilde{p}_2 \mathcal{V}_{2n}\right) \exp \frac{j\omega_n s}{c_0} \right\}}{2\mathcal{U}_n} \cdot \exp\left(-\frac{\omega_n s}{2Q_n c_0}\right) \vartheta(s).$$

Extracting the voltage seen at constant offset $\mathcal{V}_{0n}$ and $\mathcal{V}_{0n}^*$ we write

$$\tilde{U}_n(s) = -q \frac{\Re e \left\{ \left(p_0 + p_1 \frac{\mathcal{V}_{1n}^*}{\mathcal{V}_{0n}^*} + p_2 \frac{\mathcal{V}_{2n}^*}{\mathcal{V}_{0n}^*}\right) \mathcal{V}_{0n}^* \mathcal{V}_{0n} \left(\tilde{p}_0 + \tilde{p}_1 \frac{\mathcal{V}_{1n}}{\mathcal{V}_{0n}} + \tilde{p}_2 \frac{\mathcal{V}_{2n}}{\mathcal{V}_{0n}}\right) \exp \frac{j\omega_n s}{c_0} \right\}}{2\mathcal{U}_n} \cdot \exp\left(-\frac{\omega_n s}{2Q_n c_0}\right) \vartheta(s).$$

Now we introduce two additional complex parameters d_1 and d_2 ("displacement parameters of first and second order"):

$$d_{1n} = \frac{\int_0^L \nabla_x \mathcal{E}_{nz}(z) P_1(z) \exp(j\omega_n z/c_0) \mathrm{d}z}{\int_0^L \nabla_x \mathcal{E}_{nz}(z) \exp(j\omega_n z/c_0) \mathrm{d}z}, \quad d_{2n} = \frac{\int_0^L \nabla_x \mathcal{E}_{nz}(z) P_2(z) \exp(j\omega_n z/c_0) \mathrm{d}z}{\int_0^L \nabla_x \mathcal{E}_{nz}(z) \exp(j\omega_n z/c_0) \mathrm{d}z}. \tag{3.36}$$

Further, we will use the quotient

$$k_n = \frac{\mathcal{V}_{0n} \mathcal{V}_{0n}^*}{4\mathcal{U}_n} \tag{3.37}$$

as loss parameter. It differs from 3.23 only in that the integration of the voltage has been confined to the structure length. This approximation is justified by the fact that the field of the low frequency modes decays rapidly in the beam pipes.

With these parameters we finally express the voltage induced on the trailing bunch as

$$\tilde{U}_n(s) = -2qk_n \Re e \left\{ \left(p_0 + p_1 d_{1n}^* + p_2 d_{2n}^*\right) \left(\tilde{p}_0 + \tilde{p}_1 d_{1n} + \tilde{p}_2 d_{2n}\right) \exp \frac{j\omega_n s}{c_0} \right\} \exp\left(-\frac{\omega_n s}{2Q_n c_0}\right) \cdot \vartheta(s). \tag{3.38}$$

The voltage induced from particle offsets in the y-direction is calculated equivalently and is superimposed linearly on the voltage induced from the motion in the x-direction. Finally, the contributions from all modes have to be summed.

Next, we want to calculate the deflection imparted by the dipole mode n. For this purpose, we apply the Panofsky-Wenzel theorem 2.34 to equation 3.38 and obtain

$$\begin{aligned} \Delta\tilde{x}_n'(s) &= -\tilde{q} \frac{1}{\tilde{W}} \nabla_x \int_{-\infty}^{s} U(\varsigma) \mathrm{d}\varsigma = -\tilde{q} \frac{1}{\tilde{W}} \frac{\mathrm{d}}{\mathrm{d}\tilde{p}_0} \int_{-\infty}^{s} U(\varsigma) \mathrm{d}\varsigma \\ &\approx 2q\tilde{q}k_n \frac{1}{\tilde{W}} \Im m \left\{ \frac{c_0}{\omega_n} \left(p_0 + p_1 d_{1n}^* + p_2 d_{2n}^*\right) \exp \frac{j\omega_n s}{c_0} \right\} \exp\left(-\frac{\omega_n s}{2Q_n c_0}\right) \cdot \vartheta(s). \end{aligned} \tag{3.39}$$

Apart from providing a more accurate picture of the mode excitations, the displacement parameters can also be used to calculate the additional offset of the bunch caused by the

particular mode. Usually, it is assumed that the bunch is kicked by the modes at the center $z = L/2$ of the cavity, as illustrated in Fig. 3.10. Instead of using a concentrated kick to calculate the particle offset at the end of the structure, we can also assume that this offset is the superposition of infinitesimal offsets generated at various locations along the accelerating structure. Multiplying the infinitesimal deflection

$$\mathrm{d}(\Delta\tilde{x}'_n(s)) = 2q\tilde{q}\Im m\left\{\frac{c_0}{\omega_n\tilde{W}(z)}\frac{V_n^{(t)*}}{4\mathcal{U}_n}\nabla_x\mathcal{E}_{nz}(z)\exp\frac{j\omega_n z}{c_0}\exp\frac{j\omega_n s}{c_0}\right\}\exp\left(-\frac{\omega_n s}{2Q_n c_0}\right)\mathrm{d}z\cdot\vartheta(s)$$

with the transport coefficient $T_{12}(z,L)$ (see also formula 3.28) and integrating over z leads to an integral expression for the resulting offset at the end of the structure:

$$\begin{aligned}
\Delta\tilde{x}_n(s) &= 2q\tilde{q}\Im m\left\{\frac{V_n^{(t)*}\int_0^L\nabla_x\mathcal{E}_{nz}(z)\exp\frac{j\omega_n z}{c_0}\frac{c_0}{\omega_n\tilde{W}(z)}\cdot\frac{\tilde{W}(z)}{\tilde{g}}\ln\frac{\tilde{W}(L)}{\tilde{W}(z)}\mathrm{d}z}{4\mathcal{U}_n}\exp\frac{j\omega_n s}{c_0}\right\}\\
&\qquad\cdot\exp\left(-\frac{\omega_n s}{2Q_n c_0}\right)\vartheta(s)\\
&= 2q\tilde{q}\frac{c_0}{\tilde{g}\omega_n}\Im m\left\{\frac{V_n^{(t)*}\int_0^L\nabla_x\mathcal{E}_{nz}(z)\exp\frac{j\omega_n z}{c_0}\ln\frac{\tilde{W}(L)}{\tilde{W}(z)}\mathrm{d}z}{4\mathcal{U}_n}\exp\frac{j\omega_n s}{c_0}\right\}\\
&\qquad\cdot\exp\left(-\frac{\omega_n s}{2Q_n c_0}\right)\vartheta(s).
\end{aligned}\tag{3.40}$$

We can expand the logarithmic term in 3.40 into the polynomials $P_0\ldots P_2$ from 3.33 and obtain

$$\begin{aligned}
\Delta\tilde{x}_n(s) &\approx 2q\tilde{q}\frac{c_0}{\tilde{g}\omega_n}\Im m\left\{\frac{V_n^{(t)*}\int_0^L\nabla_x\mathcal{E}_{nz}(z)\left(\tilde{\ell}_0P_0+\tilde{\ell}_1P_1+\tilde{\ell}_2P_2\right)\exp\frac{j\omega_n z}{c_0}\mathrm{d}z}{4\mathcal{U}_n}\exp\frac{j\omega_n s}{c_0}\right\}\\
&\qquad\cdot\exp\left(-\frac{\omega_n s}{2Q_n c_0}\right)\vartheta(s)\\
&= 2q\tilde{q}\frac{c_0}{\tilde{g}\omega_n}\Im m\left\{\frac{(p_0\mathcal{V}_{0n}^*+p_1\mathcal{V}_{1n}^*+p_2\mathcal{V}_{2n}^*)\left(\tilde{\ell}_0\mathcal{V}_{0n}+\tilde{\ell}_1\mathcal{V}_{1n}+\tilde{\ell}_2\mathcal{V}_{2n}\right)}{4\mathcal{U}_n}\exp\frac{j\omega_n s}{c_0}\right\}\\
&\qquad\cdot\exp\left(-\frac{\omega_n s}{2Q_n c_0}\right)\vartheta(s).
\end{aligned}\tag{3.41}$$

The expansion coefficients $\tilde{\ell}_0\ldots\tilde{\ell}_2$ in equation 3.41 for the logarithmic term in 3.40 are

$$\tilde{\ell}_0=\frac{1}{2}\ln\frac{\tilde{W}(L)}{\tilde{W}(0)},\qquad\tilde{\ell}_1=-\frac{1}{2}\ln\frac{\tilde{W}(L)}{\tilde{W}(0)},\qquad\tilde{\ell}_2=\frac{(\tilde{g}L)^2}{8\tilde{W}(0)\tilde{W}(L)}.$$

Here, $\tilde{\ell}_0$ and $\tilde{\ell}_1$ are chosen to match the values of $\ln(\tilde{W}(L)/\tilde{W}(z))$ at the beginning and at the end of the structure. $\tilde{\ell}_2$ is chosen to approximate the slopes of the logarithm at the structure ends by least squares. It is very small.

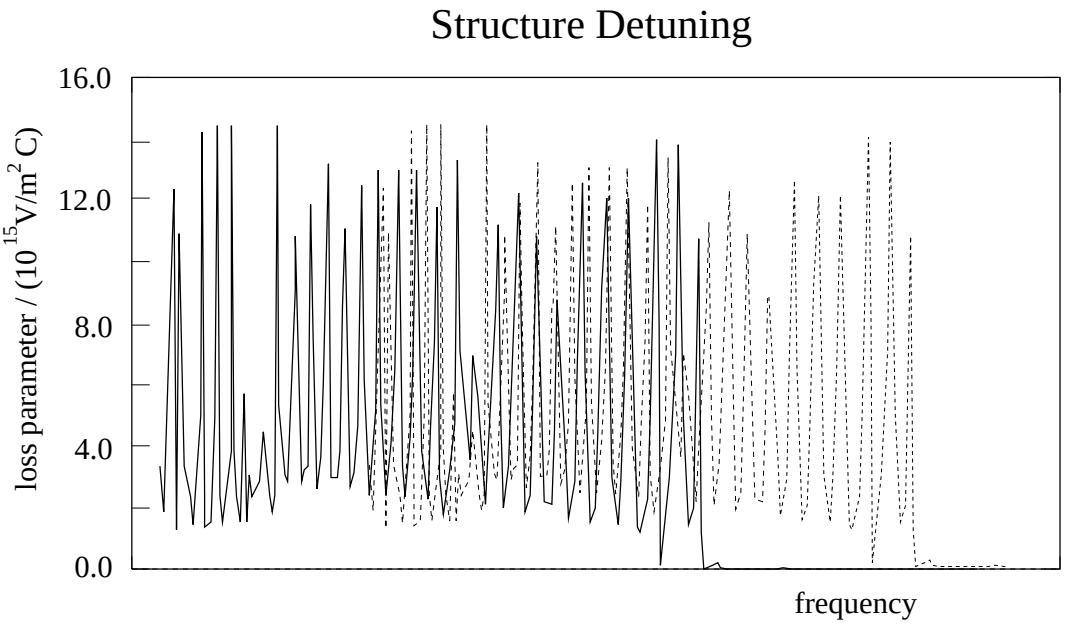

Fig. 3.12 Detuning of the frequencies of the dipole modes in different structures. The frequencies of the dipole modes are shifted deliberately, while the frequency of the accelerating mode is kept unchanged.

Extracting again the loss parameter as defined in 3.37 and putting in the displacement parameters 3.36 we finally arrive at an expression for the particle offset $\Delta\tilde{x}_n$ of the kicked particle at the end of the structure:

$$\Delta\tilde{x}_n(s) = q\tilde{q}\frac{2k_n c_0}{\omega_n \tilde{g}} \Im m\left\{(p_0 + p_1 d_{1n}^* + p_2 d_{2n}^*)\left(\tilde{\ell}_0 + \tilde{\ell}_1 d_{1n} + \tilde{\ell}_2 d_{2n}\right)\exp\frac{j\omega_n s}{c_0}\right\} \cdot \exp\left(-\frac{\omega_n s}{2Q_n c_0}\right)\vartheta(s). \quad (3.42)$$

A demonstration of this refined formalism for the treatment of the TM-like dipole modes will be given later in section 3.3.4. In particular, we will utilize the displacement parameters in order to compare the magnitude of the effects from structure sag and tilt with the effect from structure offsets. In addition, the impact of the improved calculation of the particle offsets resulting from the deflection by the modes will be considered.

3.3.2 Detuning the Dipole Modes

The transverse wake from the TM-like dipole modes is one of the most prominent causes of emittance growth in linear colliders operating in the multi-bunch mode. Therefore, we now present a detailed discussion of the properties of the multi-bunch emittance growth induced by these modes and an examination of the measures that may be undertaken to prevent this emittance growth.

By far the easiest and cheapest means to counteract emittance growth induced by the dipole modes is to detune the dipole modes of different accelerating structures. This means, we introduce different classes of structures differing slightly in some geometrical properties and hence displaying small differences of the frequencies of their dipole modes while still sharing the same properties of the accelerating mode. This detuning is illustrated in Fig. 3.12. It shows two sets of dipole modes that are almost identical except for a slight shift of the frequencies of

the modes in one passband. In practice, this is achieved by varying the curvature radius R_{curve} in the corner of the cells (see Fig. D.2). A more detailed discussion of the attainable detuning range is given in appendix D.2.

The effect of this detuning will be a decoherence of the wakes of different cells. Due to the frequency difference, the oscillatory phase advance of the modes in the structures will be different and as a consequence, we can get a partial cancellation of the wakes of these structures.

The efficiency of this method was investigated with tracking calculations. We introduced $m = 10$ different classes of accelerating structures with identical accelerating properties but different frequencies of the dipole modes. If $f_n^{(0)}$ is the frequency of the n-th mode in the undetuned structure, the frequency of the same mode in a structure belonging to the class μ was generated by a multiplication

$$f_n^{(\mu)} = (1 + \alpha\mu) f_n^{(0)}, \quad \mu = 0 \ldots m-1. \tag{3.43}$$

α is called the detuning index and μ is the class index. It is instructive to express the detuning index α by the maximum detuning Δf_{range} of an individual mode with the reference frequency f_{ref} according to

$$\Delta f_{range} = f_{ref}^{(m-1)} - f_{ref}^{(0)} = \alpha(m-1) f_{ref}. \tag{3.44}$$

Δf_{range} is called the "detuning range." Throughout this document, we will express the detuning index α by the equivalent detuning range at a mean frequency of $f_{ref} = 4300$MHz.

This detuning is not to be confused with the detuning of the profile of dipole modes in a single structure with respect to each other as discussed for instance in [43]. There, the taper profile of the structure is chosen in such a manner that the frequencies of the uncoupled dipole modes of the cells acquire a Gaussian density distribution. In a conventional, linearly tapered constant gradient structure, the uncoupled frequencies of the dipole modes are distributed rather uniformly. With this technique it is possible to get an improvement of the amplitude of the **wake potential of a single structure** at the locations occupied by the first few trailing bunches.

In order to investigate the merit of structure detuning with respect to the multi-bunch dynamics, we simulated the emittance growth from injection offset of the beam for different values of the detuning range. In this simulation we assumed for the machine:

- TM-like dipole modes as calculated by [36],
- quality factor of all dipole modes $Q = 2000$,
- accelerating gradient 17MV/m, no beam loading.

In addition to the deliberate frequency shifts for different structure classes, the dipole modes were assumed to have a relative random scatter of $2.3 \cdot 10^{-5}$. The class indices μ of the individual structures were found from random numbers. For the beam we assumed a bunch train of 125 bunches with 4.8m bunch spacing and $2.9 \cdot 10^{10}$ electrons per bunch. The beam was assumed to be injected with an offset of 10μm at a beta function of $\beta = 20.8$m.

Fig. 3.13 shows the emittance growth versus the detuning range Δf_{range}. The simulation was carried out with 14 random seeds for class indices and misalignments at each value of the detuning range. It is found that already at small detuning ranges the emittances start to diminish strongly. Generally, the emittances are improved by several orders of magnitude for all detuning ranges exceeding a few MHz. In particular, we find a minimum of the average emittances at detuning ranges of $35 \ldots 40$MHz.

A similar investigation was carried out for the emittance growth caused by machine misalignments. Here, we assumed that the accelerating structures were misaligned randomly with

beam parameters	
bunches	125
slices	
subslices	
alignment parameters	
σ_{struc}	
σ_{quad}	
σ_{BPM}	
σ_{res}	
σ_{tilt}	
inj. offs.	10μm
***HOM* parameters**	
Q	2000
Δf_{range}	
acceleration	
bl/st	no
varied	Δf_{range}

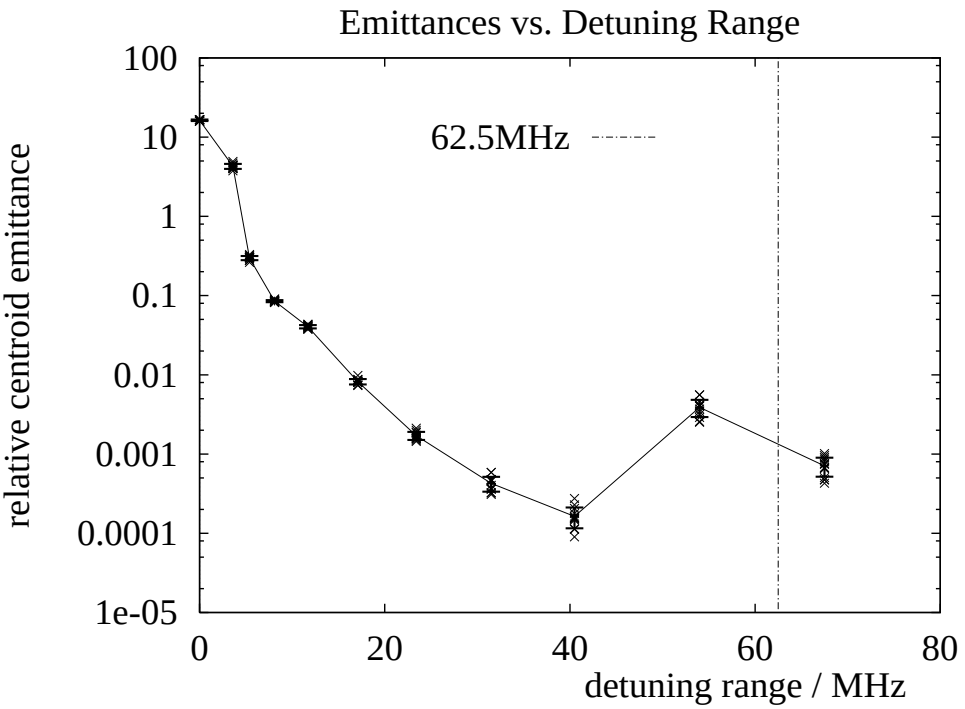

Fig. 3.13 Centroid emittances after injection offset for different detuning ranges of the TM-like dipole modes. The vertical line at 62.5MHz indicates the bunch repetition frequency. The parameter panel on the left hand side of the scatter plot is explained in appendix B.

beam parameters	
bunches	125
slices	
subslices	
alignment parameters	
σ_{struc}	100μm
σ_{quad}	
σ_{BPM}	
σ_{res}	
σ_{tilt}	
inj. offs.	
***HOM* parameters**	
Q	2000
Δf_{range}	
acceleration	
bl/st	no
varied	Δf_{range}

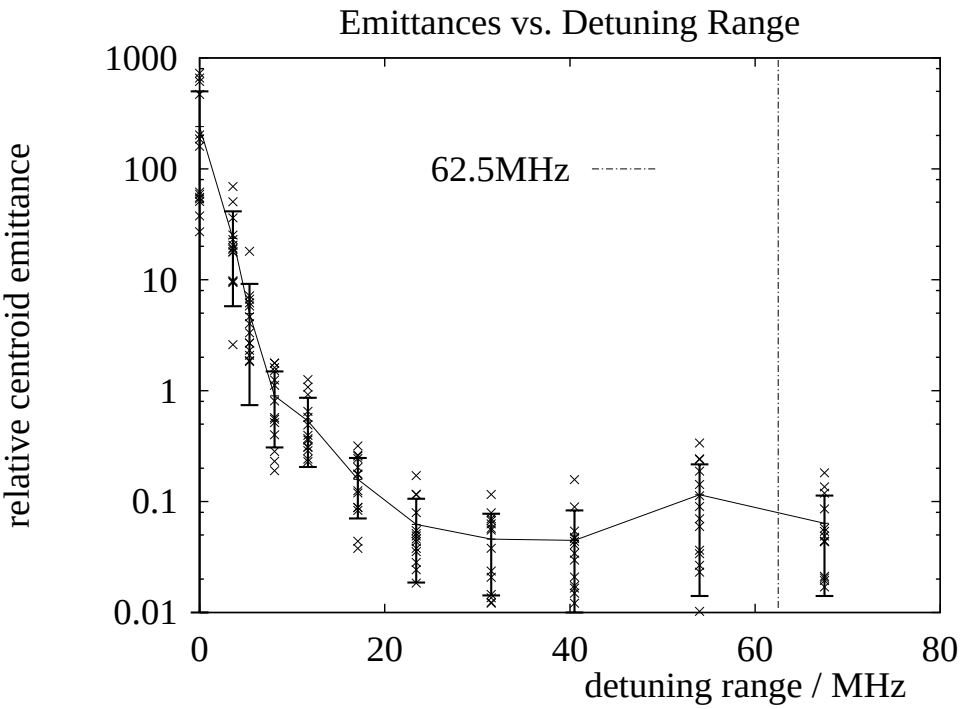

Fig. 3.14 Centroid emittances for structure misalignment with different detuning ranges of the TM-like dipole modes. The vertical line at 62.5MHz indicates the bunch repetition frequency.

respect to an ideal axis with an rms of $\sigma_{struc} = 100\mu$m, while the beam was injected perfectly on axis. The class indices μ of the structures for detuning of the dipole modes were again fond from random numbers.

Fig. 3.14 shows the emittances caused by structure misalignment versus the detuning range. A minimum for the emittance growth is again found at $\Delta f_{range} = 35 \ldots 40$MHz, confirming the result found in the case of the emittance growth from injection offset.

The detuning range that is required for effective suppression of the beam break-up driven by the long range dipole wake relates to the bunch repetition frequency. In the SBLC, the bunches are separated by a distance of 4.8m, which corresponds to a bunch repetition frequency of $f_b = 62.5$MHz. This repetition frequency is marked with a vertical line in Fig. 3.13 and Fig. 3.14. The long range wake potential is "sampled" by the beam with the bunch repetition frequency f_b, that is, the dipole modes are excited at regular intervals given by the time interval $T_b = 1/f_b$ between subsequent bunches and they also exert their influence on the beam only at these intervals. It follows, that, with respect to the effect on the beam, any change of frequency Δf of a mode is equivalent to that change plus an integer multiple of the bunch repetition frequency $\Delta f + n f_b$. When a bunch excites a mode at any of these frequencies, the phases of that mode experienced by a trailing bunch will be the same for all n. This implies that at a detuning range of the order of the bunch repetition frequency the potential for improvement of the emittances will be exhausted. This expectation is in good agreement with the actual simulation results. There it is found that for large detuning ranges ($\Delta f_{range} \approx 20$MHz) up to values approaching the bunch repetition frequency, the emittances remain at comparatively small levels.

We conclude that the current detuning technique using 10 classes of structures with an detuning range of 36MHz is an appropriate assumption for carrying out our further investigation of multi-bunch beam dynamics, and we will use this choice of detuning parameters in all simulations involving the TM-like dipole modes.

3.3.3 Influence of the Dipole Mode Quality Factors

A second very powerful method to suppress the long range wake field is damping the dipole modes. If a mode n is damped to a quality factor Q_n, the contribution to the wake potential from this mode will decay proportionally with the exponential factor

$$\vec{\mathcal{W}}_n^{damped}(s) = \vec{\mathcal{W}}_n(s) \exp\left(-\frac{\omega_n s}{2 Q_n c_0}\right). \tag{3.45}$$

As a consequence, the magnitude of the influence of a bunch on a trailing particle will decrease with its distance behind that bunch. A damping of the dipole modes was already assumed in the previous section, where the quality factors of the dipole modes were chosen to have the uniform value $Q = 2000$. The natural quality factors of these modes are in the order of $10 \cdot 10^3$.

Now we will carry out a detailed investigation of the behavior of the emittance growth with respect to the damping strength. To start with, we look at the dependence of the emittance dilution caused by structure misalignment on the quality factors. We assume that the structures are offset randomly from the machine axis with an rms of 100μm. Injection of the beam is exactly on axis. We assume 125 bunches with $2.9 \cdot 10^{10}$ electrons per bunch and 4.8m bunch spacing for the bunch train. For the machine we assume

- TM-like dipole modes as calculated by [36],
- accelerating gradient 17.0MV/m, no beam loading,
- detuning range 36MHz.

The beam was tracked through the machine for values of the quality factor ranging from $Q = 2000$ to $Q = 10000$. At each value of the quality factors, the simulation was repeated for 10 different random seeds for machine misalignment and mode detuning. Fig. 3.15 shows the bunch centers of some typical bunch trains emerging from the linac and the corresponding evolutions of the relative centroid emittance along the machine. We observe that for small values of Q the bunches at the beginning of the bunch train are subject to an irregular deflection that after a damping time of the order of $T_{damp} \approx Q/f_{dipole}$ levels off to a steady state, i.e. for bunches trailing with a distance greater than T_{damp} after the beginning of the bunch train the transverse deflections converge to a constant value. We note that this value need not vanish. This behavior is very advantageous, since a uniform transverse offset of a large number of bunches does not contribute to the emittance of the bunch train. During luminosity operation of the accelerator this offset can simply be corrected with an ordinary dipole magnet, provided that the structure vibrations are small in comparison with the structure misalignments (or slow in comparison with the pulse repetition frequency). When the quality factor of the modes is increased, the time required by the deflections to reach the steady state grows and the emittance deteriorates considerably. Finally, for large values of Q corresponding to damping times much longer than the length of the bunch train, the emittance approaches a saturation value. Fig. 3.16 shows the relative centroid emittances from structure misalignment versus the quality factor of the dipole modes. From our previous considerations it is clear that for the mode damping to produce a significant improvement of the final beam emittances, the time constant Q/f_{dipole} must be smaller than the length of the bunch train. This condition gives us $Q \ll T_{pulse} \cdot f_{dipole} \approx 2\mu\text{s} \cdot 4300\text{MHz} = 8600$. Indeed, in Fig. 3.16 we see that it is only for quality factors smaller than 8000 that the emittance starts to show any significant improvement. The relative centroid emittances found at $Q = 10000$ have a mean value of 4.8 ± 3.0, which reduces to $(2.5 \pm 0.7)\%$ at $Q = 2000$.

The same investigation was carried out concerning the emittance growth associated with injection offset of the beam. Here it was assumed that the machine elements were aligned ideally, while the beam was injected with an offset of 10μm at a beta function of $\beta = 20.8$m. Fig. 3.17 shows the relative centroid emittances found with these assumptions. The observations made during the simulation of the emittance growth from structure misalignment are confirmed. Significant reduction of the emittance can only be achieved if the quality factors are well below Q=8000. Specifically, we find a mean relative centroid emittance of $(3.3 \pm 1.1) \cdot 10^{-4}$ at $Q = 2000$, increasing by two orders of magnitude to $(3.2 \pm 0.7) \cdot 10^{-2}$ at $Q = 10000$.

3.3.4 Simulations Using the Displacement Parameters

In section 3.3.1 we had shown how by means of the displacement parameters and using expressions 3.39 and 3.42, the analysis of the mode excitation can be extended to account for structure sag and tilt as well as for the shape of the trajectory of the particles through the structure. However, the displacement parameters for the TM-like dipole modes as calculated in [36] are not known for the time being.

Nevertheless, we are interested in getting a qualitative picture of how the effect of these issues on the emittance growth compares with the emittances found in a conventional simulation according to expressions 3.27 and 3.29. Therefore, we will utilize the transient approximation of

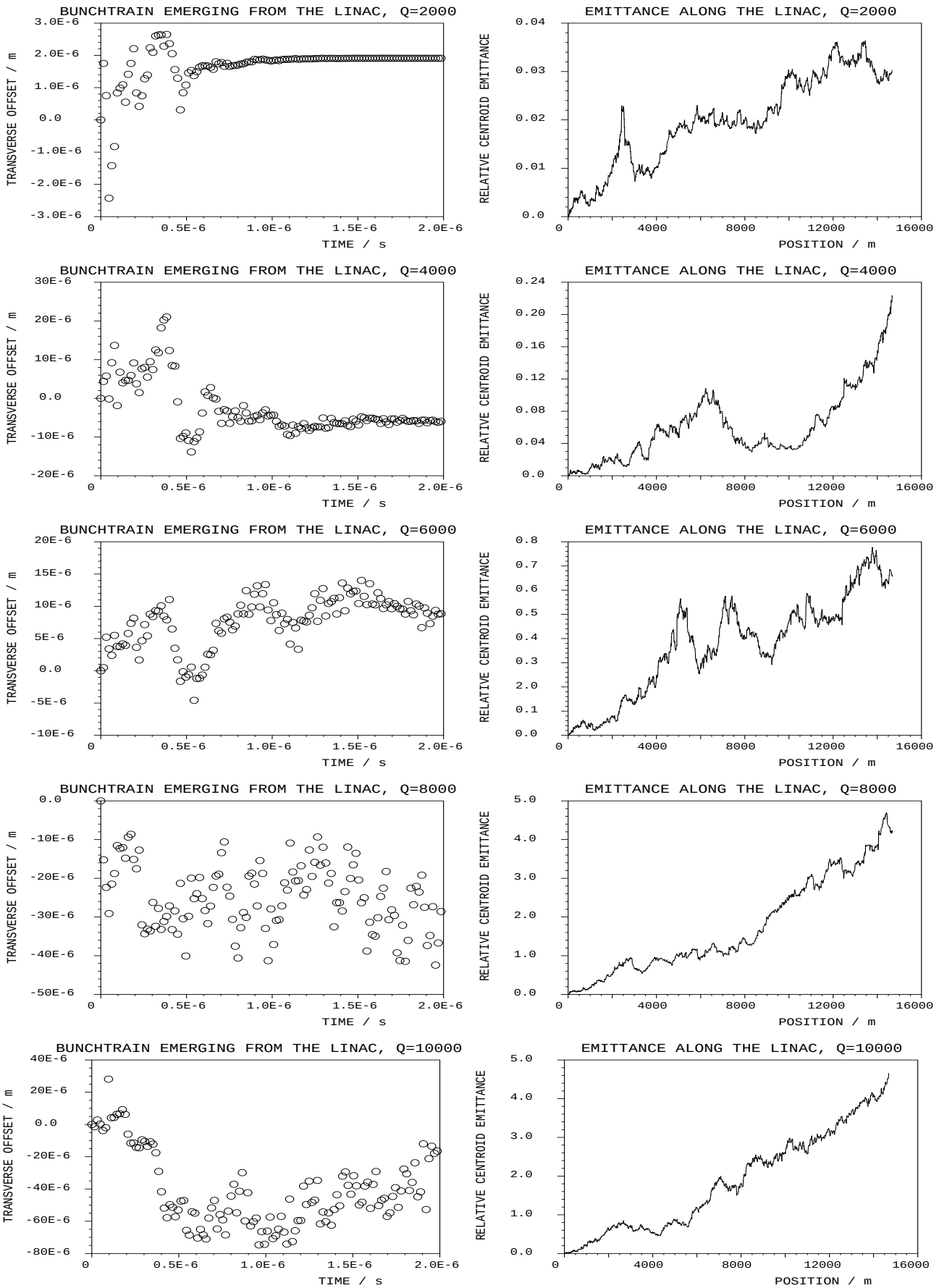

Fig. 3.15 Emittance growth for quality factors $Q = 2000,4000,6000,8000$ and 10000. In the figures showing the bunch trains, each circle denotes the center of a bunch. Bunches located at smaller values of the abscissa are ahead of the bunches at larger times.

beam parameters	
bunches	125
slices	
subslices	
alignment parameters	
σ_{struc}	100μm
σ_{quad}	
σ_{BPM}	
σ_{res}	
σ_{tilt}	
inj. offs.	
***HOM* parameters**	
Q	
Δf_{range}	36MHz
acceleration	
bl/st	no
varied	Q

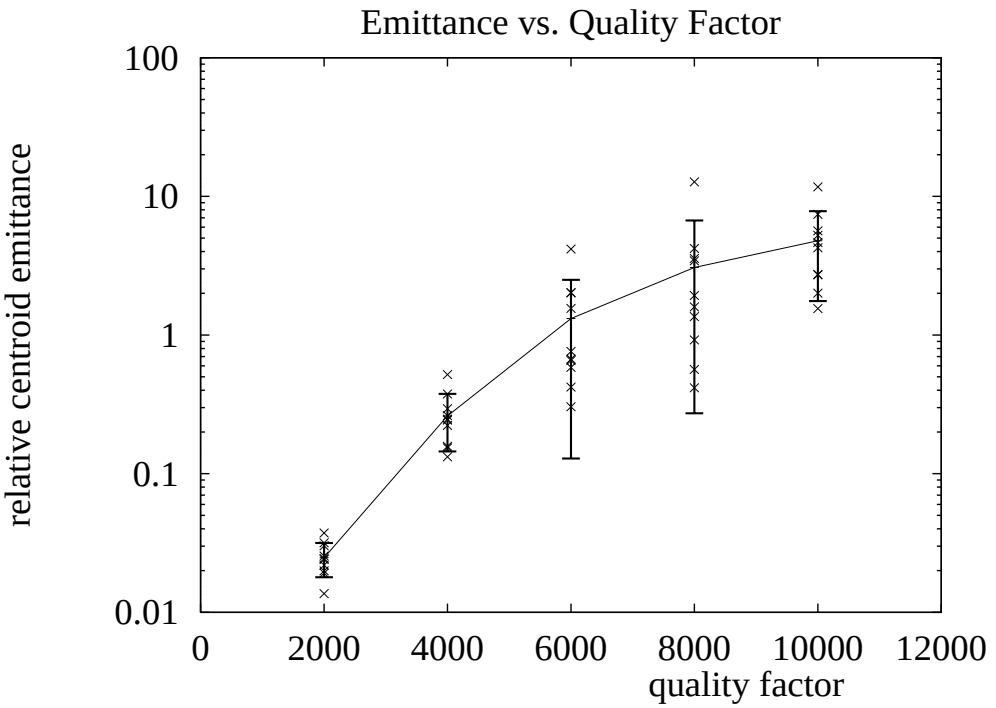

Fig. 3.16 Relative centroid emittances from 100μm rms structure misalignment at the end of the linac for quality factors of the dipole modes ranging from $Q = 2000$ to $Q = 10000$.

beam parameters	
bunches	125
slices	
subslices	
alignment parameters	
σ_{struc}	
σ_{quad}	
σ_{BPM}	
σ_{res}	
σ_{tilt}	
inj. offs.	10μm
***HOM* parameters**	
Q	
Δf_{range}	36MHz
acceleration	
bl/st	no
varied	Q

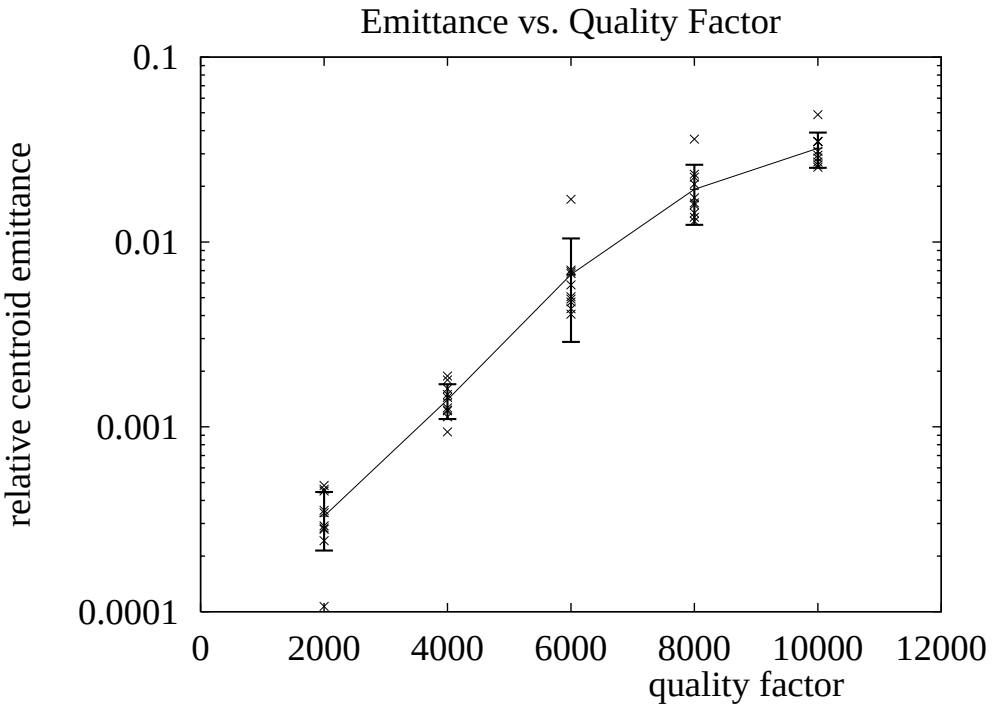

Fig. 3.17 Relative centroid emittances at the end of the linac with injection offset for quality factors of the dipole modes ranging from $Q = 2000$ to $Q = 10000$.

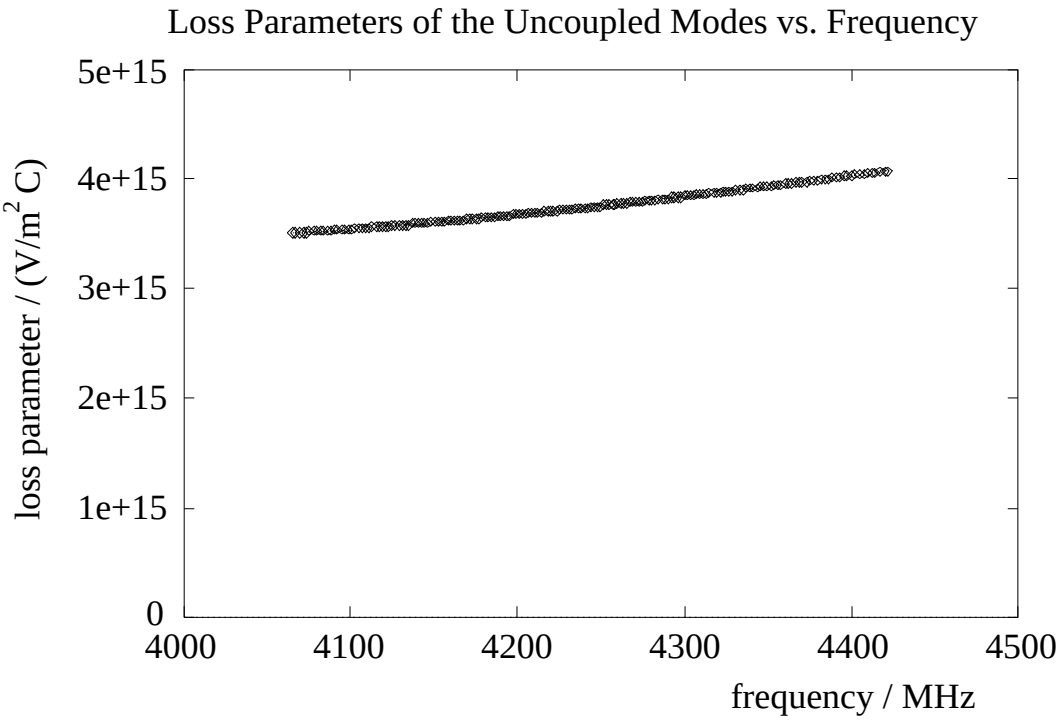

Fig. 3.18 Loss parameters versus the frequencies of the uncoupled dipole modes. In contrast to the modes shown in Fig. 3.3, which are the coupled modes of the complete structure, these are the resonant frequencies and loss parameters of the isolated individual cells of the structure.

the dipole modes in order to carry out a comparison between the different calculation methods, and to determine the relative magnitudes of the emittance growth created by structure tilt and structure sag compared with the emittance growth from structure offsets.

Fig. 3.18 shows the loss parameters versus the frequencies of the uncoupled cells of the structure. In the scope of our comparison between the two simulation techniques, these modes will be used both in the conventional formalism and the refined formalism using the displacement parameters. As the uncoupled modes extend only over a small region of the structure, namely the length of one cell (33.33mm), it is straightforward to approximate the displacement parameters of these modes as

$$d_{1\nu} = P_1(z_\nu) \qquad d_{2\nu} = P_2(z_\nu), \tag{3.46}$$

where z_ν is the longitudinal position of the ν-th cell in the structure. The resulting displacement parameters are depicted in Fig. 3.19 .

Throughout the following simulations it is assumed that the dipole modes are detuned as outlined in section 3.3.2 and have a uniform quality factor of $Q = 2000$. Moreover, we assume a constant accelerating gradient of 17MV/m without beam loading. All simulations are performed for 10 different random seeds for machine misalignment and mode detuning.

Structure Offset

As we want to show how the emittance growth from structure sag and structure tilt relates to the emittance growth from structure offset, we first perform a calculation of the emittance growth for a random structure offset of 100μm rms. In a conventional calculation with the kick from the dipole modes concentrated at the center of the accelerating structure we find a mean relative centroid emittance of $(3.16 \pm 1.4) \cdot 10^{-3}$ at the end of the machine. Calculation with

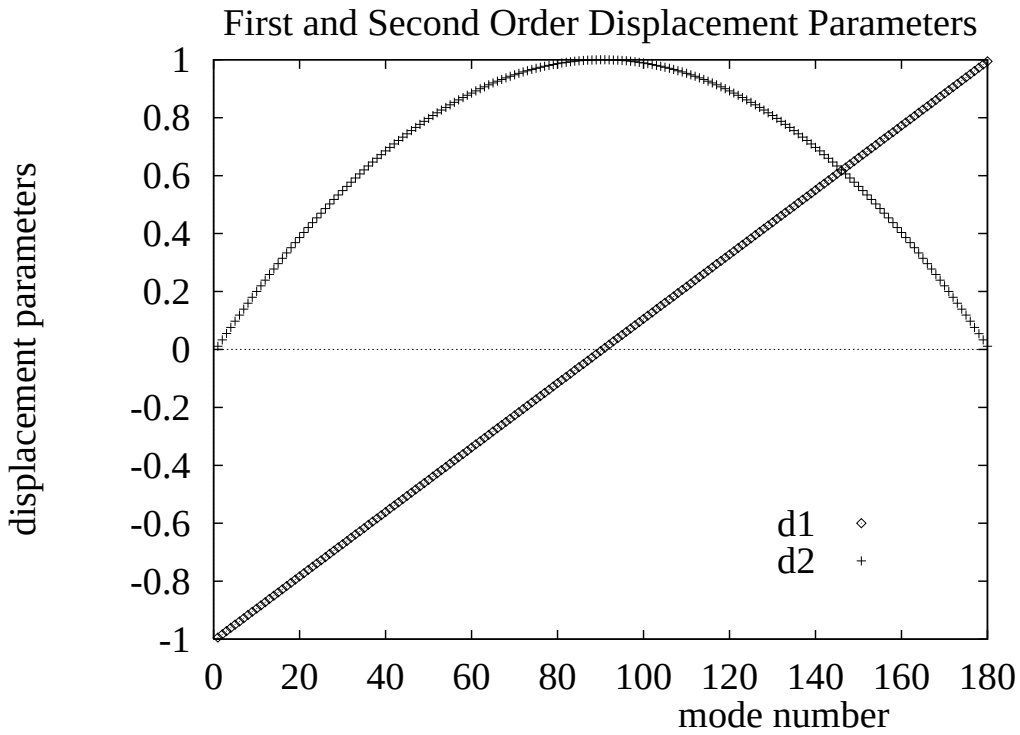

Fig. 3.19 Displacement parameters d_1 (d1) and d_2 (d2) of the uncoupled modes as shown in Fig. 3.18.

distributed kicks yields a mean relative centroid emittance of $(3.32 \pm 1.4) \cdot 10^{-3}$. As the 1σ-areas of these values have a large overlap, the observed differences between the two calculation methods must be considered statistically inconclusive. Moreover, because the difference is small by itself, it can be considered irrelevant for design and layout of an accelerating machine. The good agreement between the two calculation methods lends great justification to our use of the central kick approximation outlined in section 3.3.1.

Structure Tilt

Next, we use the formalism of the displacement parameters to calculate the emittance growth caused by structure tilts. With respect to the machine we will make the same assumptions as before, however with no structure offsets and a random tilt of the structure axes of 23.6μrad rms instead. This value is equal to the rms structure tilt that would be caused by an uncorrelated misalignment of the structure ends of 100μm each. The mean relative centroid emittance at the end of the linac with these assumptions is $(1.2 \pm 1.4) \cdot 10^{-3}$. This corresponds to 38% of the emittance caused by a random structure offset of 100μm rms. The conventional tracking algorithm does not take into account the tilt misalignment of the structures. Therefore alignment tolerances derived from these simulations should be given an appropriate safety margin that can accommodate for the extra emittance contribution from the structure tilts.

Structure Sag

Now we use our formalism to calculate the emittance contribution both from random and systematic sag of the accelerating structures, since both types of misalignment must be expected in an accelerator. First, we assume a random sag of the structures of 100μm rms. The distribution of the structure sags is Gaussian, thus allowing also for negative values of the individual

structure sags. The mean relative centroid emittance found in this case is $(7.8 \pm 4.4) \cdot 10^{-4}$, which is 25% of the emittance for a random structure offset of the same magnitude. For a systematic sag of the structures of 100μm the mean emittance growth becomes $(6.8 \pm 3.0) \cdot 10^{-4}$ or 22% of our reference value obtained from the 100μm rms structure offset.

Injection Offset / Trajectory Slopes

Finally, we compare the results obtained with the two algorithms concerning the emittance growth from injection offset. The conventional algorithm only accounts for the offsets of the particles in the structures. Using the formalism of the displacement parameters, the emittance growth may be modified by contributions from the non-vanishing trajectory slopes and by different transverse displacements found in the computation using the distributed kicks.

We assume perfect alignment of the machine and an injection offset of 10μm at $\beta = 20.8$m. In a calculation with the conventional algorithm we find a mean relative centroid emittance of $(2.6 \pm 0.2) \cdot 10^{-4}$. Using the displacement parameters this value changes to $(2.5 \pm 0.26) \cdot 10^{-4}$. Again, due to the overlap of the 1σ-regions, the difference observed in the results of the two calculation methods must be viewed as statistically insignificant.

Conclusion

There are essentially three ways in which the computation of the emittance growth caused by the dipole modes may be modified by the inclusion of the displacement parameters. First, structure sags and structure tilts can be accounted for, which otherwise would have to be neglected. Second, the offset of a particle resulting from kicks by the dipole modes can be calculated with better precision. Third, the slope of the particle trajectories can be accounted for in the excitation of the dipole modes. The simulation results concerning pure structure offset and free betatron motion from injection offset are only affected by the last two factors. In these cases, no significant differences between the two computation methods could be observed. This is explained by the fact that the trajectory slope is small in the sense that the betatron wavelength is large in comparison with one structure length. Therefore the particle offsets change little over this length. Moreover, the particle offsets resulting from deflection by the dipole modes at the end of a structure are small. On the other hand, the emittances caused by structure sag and structure tilt are found to be in an order of magnitude comparable to the emittances caused by random structure offsets. It follows that these types of misalignment can cause an additional excitation of the dipole modes with significant magnitude. The displacement parameters are an appropriate tool to account for these effects.

3.3.5 Longitudinal Dipole Wakes

As outlined in section 3.3.1, the TM-like dipole modes in principle have both a transverse and a longitudinal effect. In section 2.5.1 has been shown that the short range longitudinal dipole wake is insignificantly small. It is expected that the energy spread induced by the long range longitudinal dipole wake is even smaller, since due to the detuning of the dipole modes in the different structures the energy spreads induced in the individual structures will add up incoherently along the machine, instead of the coherent summation in the case of the short range wake. In order to verify this assumption, we carried out a tracking calculation of the beam dynamics including the long range longitudinal dipole wake. In this simulation it was assumed that the beam was injected perfectly on axis into a machine in which the accelerating structures were randomly misaligned with an rms of 100μm. The remaining elements of the machine were assumed to be aligned perfectly along the machine axis. As dipole modes we

beam parameters	
bunches	125
slices	
subslices	
alignment parameters	
σ_{struc}	100μm
σ_{quad}	
σ_{BPM}	
σ_{res}	
σ_{tilt}	
inj. offs.	
***HOM* parameters**	
Q	
Δf_{range}	36MHz
acceleration	
bl/st	no
varied	Q

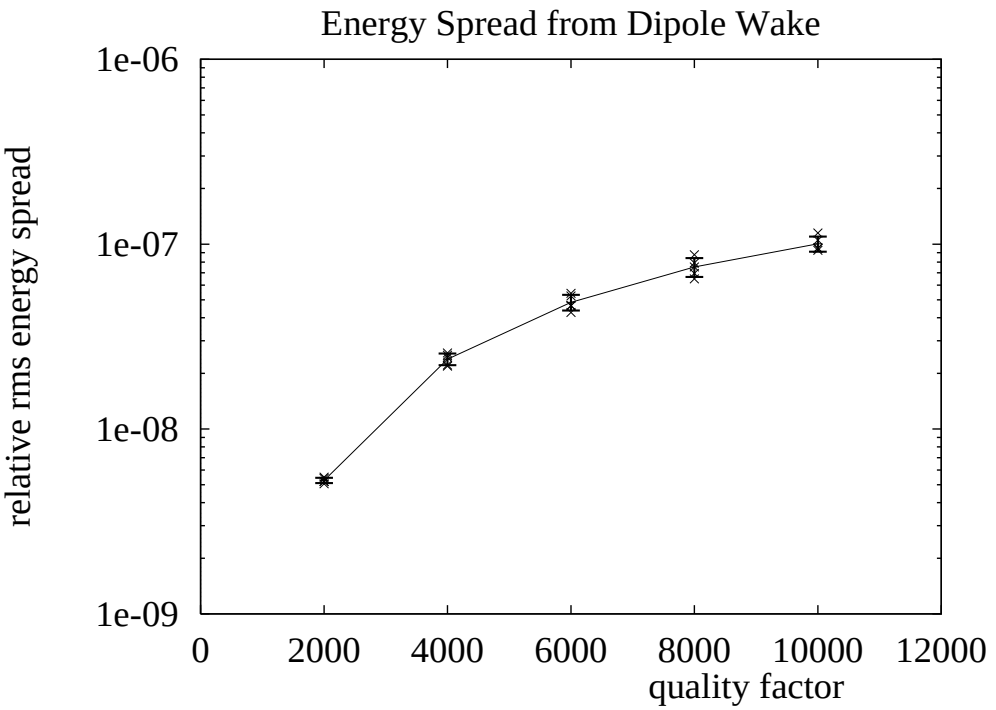

Fig. 3.20 Energy spreads induced in the bunch train by the long range dipole wake for different quality factors.

used the modes calculated by [36]. Fig. 3.20 shows the relative energy spread induced by the dipole modes under these assumptions. The calculations were done for 10 different random seeds for each value of the quality factor. The energy spreads have been normalized to the final particle energy of 250GeV. It is found that the relative energy spread induced by the dipole modes ranges from $(5.3 \pm 0.2) \cdot 10^{-9}$ rms at quality factors of the dipole modes of $Q = 2000$ to $(1.0 \pm 0.1) \cdot 10^{-7}$ rms for quality factors of $Q = 10000$. This means that even in the case of undamped dipole modes the energy spread induced from these modes is very small. Moreover, for misalignments of the structures smaller than the reference value used in our example, the energy spread decreases inversely with the square of the structure misalignment.

3.3.6 Orbit Correction

We want to investigate now the performance of the algorithms for orbit correction with respect to the suppression of emittance growth from quadrupole misalignment. As previously in section 2.3, we will again use the One-to-One, Dispersion-Free and Wake-Free algorithm to correct the particle trajectories.

In this simulation we assumed perfect alignment of the accelerating structures along an ideal machine axis, while the quadrupoles were misaligned randomly by 100μm rms with respect to that axis. Likewise, the BPM's (beam position monitors) were misaligned with respect to the quadrupoles by 100μm rms. The resolution of the BPM's was $\sigma_{res} = 5\mu$m. The simulation did not include the effect of beam loading. Instead, a constant accelerating gradient of 17MV/m was assumed. The long range dipole wake is generated from the modes calculated by [36]. Fig. 3.21 shows the relative centroid emittances after the various correction schemes for quality factors of the dipole modes ranging from $Q = 2000$ to $Q = 10000$. The calculation was done for 10 random seeds at each value of the quality factor. With the One-to-One correction we obtain a mean value of the relative centroid emittances ranging from $(3.8 \pm 2.2) \cdot 10^{-2}$ at $Q = 2000$

beam parameters	
bunches	125
slices	
subslices	
alignment parameters	
σ_{struc}	
σ_{quad}	100μm
σ_{BPM}	100μm
σ_{res}	5μm
σ_{tilt}	
inj. offs.	
***HOM* parameters**	
Q	
Δf_{range}	36MHz
acceleration	
bl/st	no
varied	Q

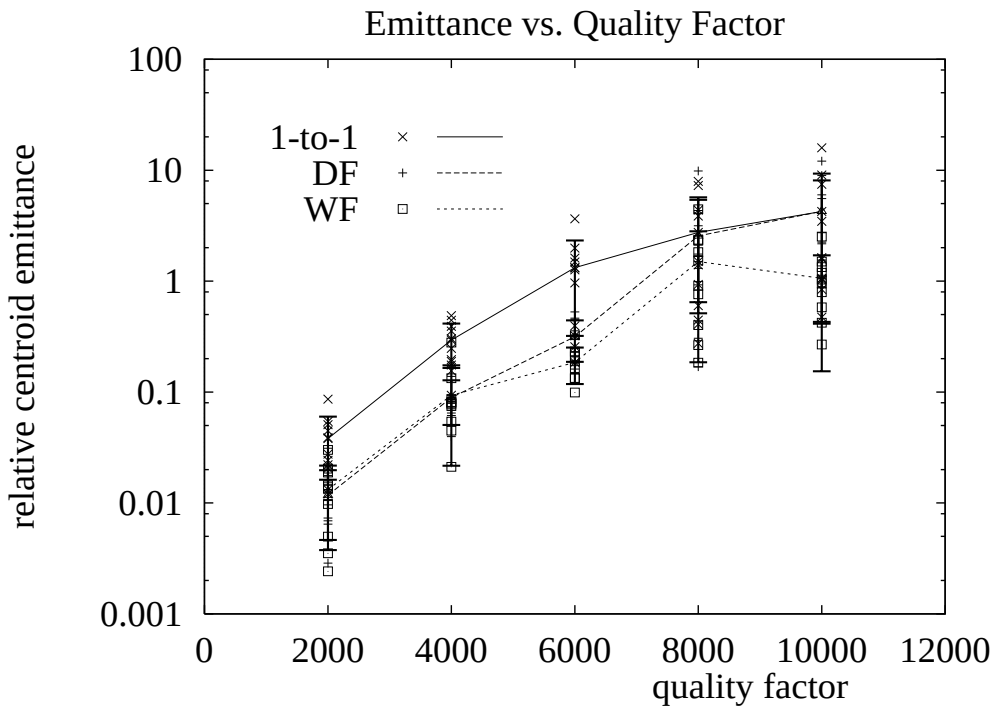

Fig. 3.21 Relative centroid emittances from quadrupole misalignment after application of orbit correction techniques (One-to-One, Dispersion-Free, Wake-Free). The quality factor of the dipole modes varies within $Q = 2000 \ldots 10000$. No beam loading is assumed.

to 4.2 ± 5.0 at $Q = 10000$. With application of the DF correction this improves slightly to values from $(1.2 \pm 0.8) \cdot 10^{-2}$ at $Q = 2000$ to 4.2 ± 3.8 at $Q = 10000$. The WF technique finally achieves $(1.3 \pm 0.9) \cdot 10^{-2}$ at $Q = 2000$, increasing to 1.1 ± 0.6 at $Q = 10000$.

This result seems to suggest that the different correction schemes perform similarly well at reducing the multi-bunch emittance growth, with only a slight advantage for the two advanced correction schemes. The dependence of the emittance growth on the quality factor of the dipole modes is confirmed.

3.3.7 Transverse Dynamics with Beam Loading

In this subsection we investigate how the results obtained in the previous sections on the character of the multi-bunch instability are modified by beam loading effects. There are essentially two ways in which beam loading influences this process. First, due to the energy spread, the bunch train will be subject to filamentation if injected off axis into the machine. In addition, trajectory distortions from quadrupole misalignments will create dispersive errors. Second, the convergence of the transverse kicks by the dipole modes to the steady state (see section 3.3.3) will be perturbed, since the deflection angle imparted by the dipole wake has a dependence on the particle energy. The first effect will exert its influence mainly on the emittance evolution connected with injection offset and quadrupole misalingment, whereas the second will also affect the emittance growth associated with structure misalignment.

Throughout our simulations of the effects induced by beam loading, we will assume that the energy spread is compensated with the technique of staggered timing. The unloaded gradient in the structures is 21MV/m and also the other assumptions concerning the beam loading behavior of the structure are as outlined in section 3.2. The RF phases of the accelerating voltage in the structures are chosen as outlined in section 2.2, with the structures in the first

beam parameters	
bunches	125
slices	
subslices	
alignment parameters	
σ_{struc}	
σ_{quad}	
σ_{BPM}	
σ_{res}	
σ_{tilt}	
inj. offs.	10μm
***HOM* parameters**	
Q	
Δf_{range}	36MHz
acceleration	
bl/st	yes
varied	Q

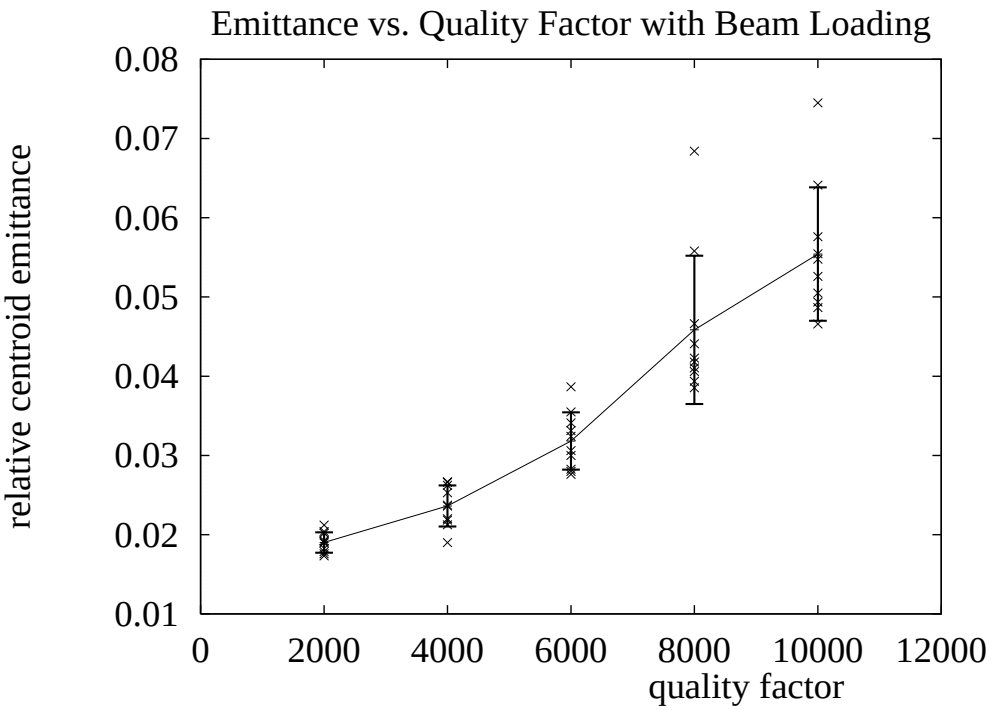

Fig. 3.22 Relative centroid emittances with injection offset for quality factors $Q = 2000 \ldots 10000$. Beam loading is corrected using staggered timing.

4 sectors running at a phase of 4° and the remaining structures set to $-12°$. For the beam we assume 125 bunches with $2.9 \cdot 10^{10}$ electrons per bunch and 4.8m bunch spacing. The long range dipole wake is generated from the dipole modes calculated by [36] (Fig. 3.3).

Following the practice already pursued in section 3.3.3, we will simulate the emittance growth at different values of the quality factors of the dipole modes. At each value of the quality factor the simulation will be repeated with 10 different random seeds for machine misalignment and mode detuning.

We look first at the case of injection offset of the beam. The machine is assumed to be perfectly aligned and the beam is assumed to be injected with an offset of 10μm at $\beta = 20.8$m. This injection offset is equivalent to a quarter beam height σ_y at injection. Fig. 3.22 shows the emittances found with these assumptions. We see that for high values of Q the emittances are similar to those found without beam loading. At $Q = 10000$ we find a mean relative centroid emittance of $(5.6 \pm 0.8) \cdot 10^{-2}$. At low values for Q, however, the emittance does not fall off indefinitely as had been observed in the case without beam loading, but approaches a lower limit that is given by the filamentation due to the multi-bunch energy spread. In this parameter regime, the worsening of the emittance growth as compared to the case without beam loading is severe. This allows us to establish an upper bound for the permissible injection offset that must not be exceeded, however strong the damping of the dipole modes may be. The mean relative centroid emittance at $Q = 2000$ is found to be $(1.9 \pm 0.14) \cdot 10^{-2}$, which sets the limit for injection offset for 6% emittance growth to 18μm. This tolerance is still looser than the tolerance given by the transverse beam size, limiting the transverse jitter to 10μm. However, deliberate systematic injection offset is occasionally suggested as a tuning parameter of a machine to optimize machine performance. The applicability of such techniques is thus found to be significantly restricted by this result.

Next, we consider the effect of the energy spread caused by beam loading on the emittance growth from quadrupole misalignment. Here, the quadrupoles and BPM's were assumed to be

beam parameters	
bunches	125
slices	
subslices	
alignment parameters	
σ_{struc}	
σ_{quad}	100μm
σ_{BPM}	100μm
σ_{res}	5μm
σ_{tilt}	
inj. offs.	
***HOM* parameters**	
Q	
Δf_{range}	36MHz
acceleration	
bl/st	yes
varied	Q

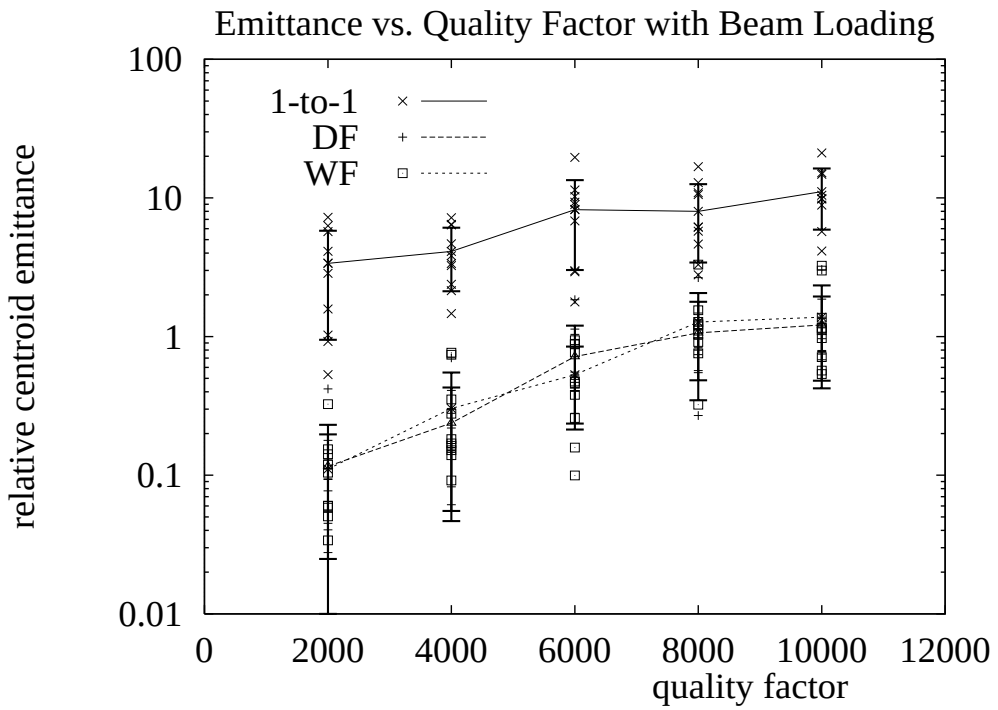

Fig. 3.23 Relative centroid emittances in a machine with misaligned quadrupoles after orbit corrections with the One-to-One (1-to-1), Dispersion-Free (DF) and Wake-Free (WF) technique. The quality factor of the dipole modes is varied from $Q = 2000$ to $Q = 10000$. Beam loading is corrected using staggered timing.

randomly misaligned with an rms of 100μm. The results of these simulations are shown in Fig. 3.23. In the case of a trajectory correction with the 1-to-1 algorithm the emittance growth is increased strongly. Moreover, the dependence of this emittance growth on the quality factor of the dipole modes is diminished. At $Q = 2000$ we find a mean relative centroid emittance of 3.4 ± 2.4, which increases to 11.1 ± 5.2 at $Q = 10000$. The reason for this behavior is that the emittance is now dominated by the dispersive errors brought about by the energy spread in connection with the orbit distortions. On the other hand, the advanced correction algorithms (Dispersion-Free and Wake-Free) remove a great deal of the dispersive errors. Hence, the worsening of the emittance growth by the introduction of beam loading is reduced and the dependence on the quality factor of the dipole modes remains strong. This implies that with use of Dispersion-Free and Wake-Free orbit correction the emittance growth is still dominated by the dipole wake. Using the DF and WF correction, the mean relative centroid emittances improve significantly to values from 0.12 ± 0.12 at $Q = 2000$ to 1.2 ± 0.7 for $Q = 10000$ for the DF algorithm and from 0.11 ± 0.8 at $Q = 2000$ to 1.4 ± 0.96 for $Q = 10000$ for the WF correction. This improvement of the emittances makes utilization of the advanced correction algorithms virtually imperative.

Finally, the effect of the multi-bunch energy spread on the emittance growth from structure misalignment is investigated. In this simulation, the quadrupoles are aligned perfectly to the ideal machine axis. The accelerating structures are misaligned with respect to that axis with an rms of 100μm. The beam is taken to be injected exactly on axis, the beam parameters being as previously. Fig. 3.24 shows the emittances found for different values of the quality factor Q. Similarly to the results for injection offset and quadrupole misalignment, we find that the emittances, as compared with the case without beam loading, are increased appreciably. This increase is again particularly strong at small quality factors ($(24 \pm 16)\%$ mean relative centroid

beam parameters	
bunches	125
slices	
subslices	
alignment parameters	
σ_{struc}	100μm
σ_{quad}	
σ_{BPM}	
σ_{res}	
σ_{tilt}	
inj. offs.	
***HOM* parameters**	
Q	
Δf_{range}	36MHz
acceleration	
bl/st	yes
varied	Q

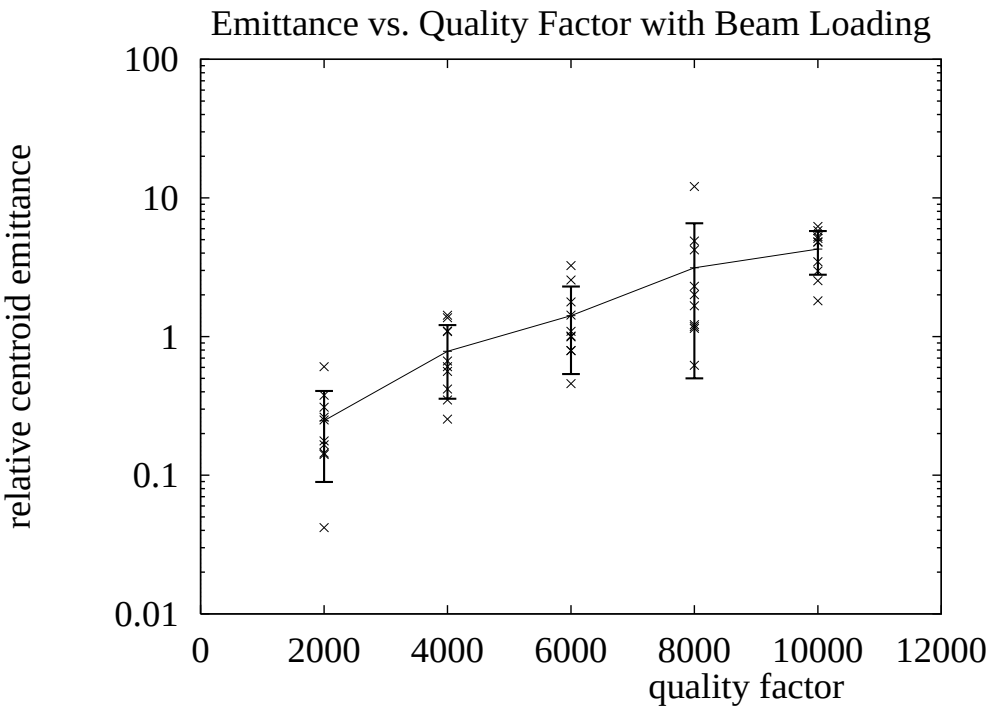

Fig. 3.24 Relative centroid emittances with structure misalignment for quality factors $Q = 2000 \ldots 10000$. Beam loading is corrected using staggered timing.

emittance at $Q = 2000$), but also the emittances obtained at high values of Q are enlarged severely ($(420 \pm 140)\%$ mean relative centroid emittance at $Q = 10000$). If one wishes to keep the emittance contribution from structure misalignment below a value of 6% of the injection emittance, then at $Q = 2000$ the accelerating structures must be aligned with a precision of 50μm.

3.3.8 Deflection by TE-like Modes

Now we investigate the interaction of charged particles with TE-like dipole modes. By the term "TE-like" we refer to modes with a field configuration which is similar to that of a TE-mode in a pill-box cavity. In a real TE-mode as encountered in a pill-box cavity, the longitudinal electric field vanishes over the entire cavity volume. It follows immediately that the longitudinal voltage vanishes, too. As the transverse momentum imparted on a particle is related to the voltage by the Panofsky-Wenzel theorem 2.34, it follows that a pure TE-mode cannot cause any deflection of a particle beam.

In reality, however, the geometry of the cells of the accelerating structure deviates distinctly from the geometry of a pill-box. For this reason the longitudinal voltages of the TE-like modes will in general not vanish and hence these modes may contribute to the particle deflections.

The potential danger of the TE-like dipole modes lies in the fact that they offer two mechanisms by which these modes can be excited. Firstly, there is the possibility of an excitation by the longitudinal electric field. The behavior of this excitation mechanism is identical with the mechanisms for the TM-like dipole modes. Again, the corresponding mode voltages will be proportional both to the transverse offsets of the leading and the trailing particle, a behavior that is invariably common to all dipole modes. Secondly, the transverse electric field for these modes is large. Therefore, a particle moving on a tilted trajectory or a particle traversing a tilted structure can excite these modes by the transverse electric field (see Fig. 3.25), since the

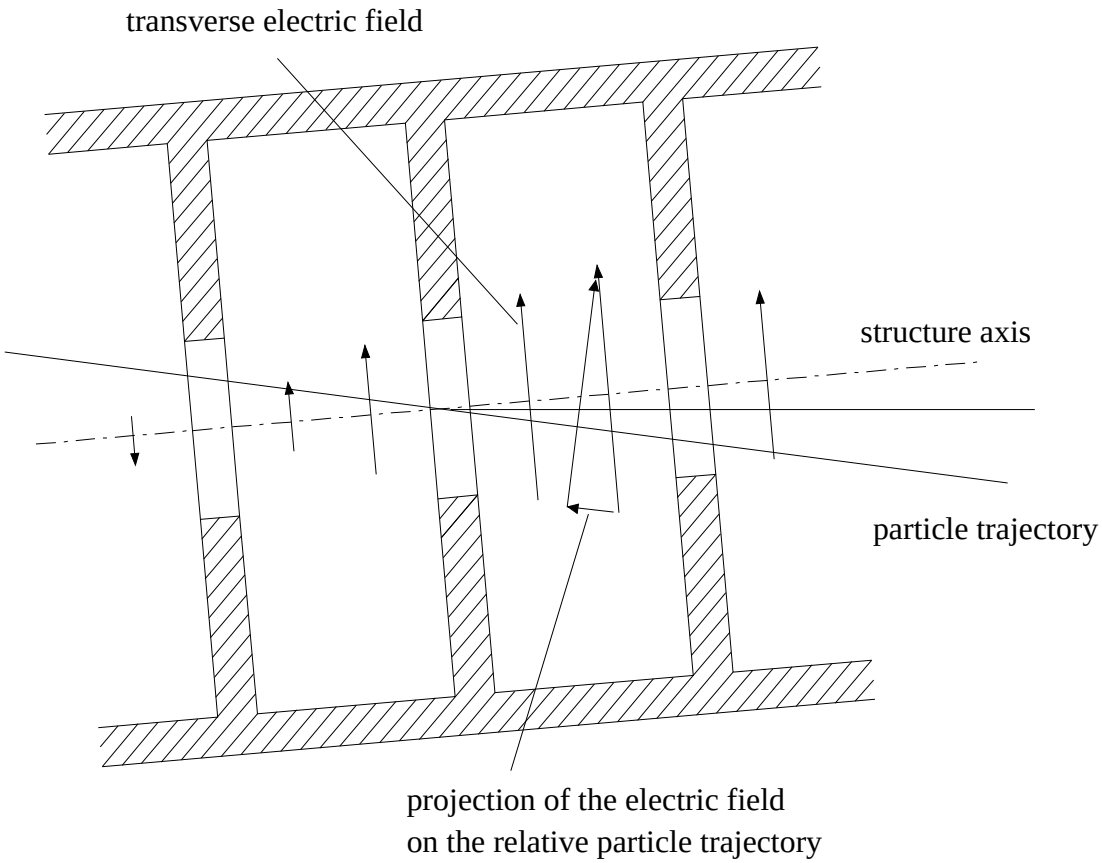

Fig. 3.25 If the particle trajectory encloses a non-vanishing angle with the structure axis, the TE-like dipole modes can be excited by the transverse E-field.

projection of the electric field on a tilted trajectory does not vanish [24].

We consider a charge q exciting the modes and a test charge $\tilde{q}$ traversing an accelerating structure with the length L on the trajectories

$$x(z) = x_{mean} + x'\left(z - \frac{L}{2}\right), \quad \tilde{x}(z) = \tilde{x}_{mean} + \tilde{x}'\left(z - \frac{L}{2}\right), \tag{3.47}$$

where x_{mean} and $\tilde{x}_{mean}$ are the mean offsets of the particles with respect to the structure and x' and $\tilde{x}'$ denote the trajectory slopes relative to the structure axis. These parameters are taken to be constant along the structure. The mode voltages of the field pattern $\vec{\mathcal{E}}_n(\vec{x})$ of the mode n along these trajectories then become:

$$V_n \approx \int_{-\infty}^{\infty} \left[\mathcal{E}_{n\perp}(z)x' + \nabla_x \mathcal{E}_{nz}(z) x_{mean}\right] \exp \frac{j\omega_n z}{c_0} \mathrm{d}z. \tag{3.48}$$

In this equation, $\mathcal{E}_{n\perp}(z)$ is the transverse electric field of the mode n on the axis and $\nabla_x \mathcal{E}_{nz}(z)$ the transverse derivative of the longitudinal electric field. In formula 3.48 it is assumed again that the longitudinal velocity of the particle is equal to the velocity of light. The mode voltage $\tilde{V}_n$ for the trajectory $\tilde{x}(z)$ calculates likewise.

Using the abbreviation

$$\mathcal{V}_{0n} = \int_{-\infty}^{\infty} \nabla_x \mathcal{E}_{nz}(z) \exp \frac{j\omega_n z}{c_0} \mathrm{d}z$$

and introducing the complex parameter

$$d_{n\perp} = \frac{\int_{-\infty}^{\infty} \mathcal{E}_{n\perp}(z) \exp(j\omega_n z/c_0) \mathrm{d}z}{\int_{\infty}^{\infty} \nabla_x \mathcal{E}_{nz}(z) \exp(j\omega_n z/c_0) \mathrm{d}z}, \tag{3.49}$$

we can rewrite the complex conjugate V_n^* of the mode voltage on the trajectory of the leading particle, and the mode voltage $\tilde{V}_n$ on the trajectory of the trailing charge as

$$V_n^* = \mathcal{V}_{0n}^* \left(x_{mean} + d_{n\perp}^* x'\right), \quad \tilde{V}_n = \mathcal{V}_{0n} \left(\tilde{x}_{mean} + d_{n\perp} \tilde{x}'\right). \tag{3.50}$$

According to our considerations in section 3.3.1, the voltage induced by one mode on the trailing particle can be expressed with these mode voltages like

$$\tilde{U}_n(s) = -2q\Re e \left\{ \frac{\left(x_{mean} + d_{n\perp}^* x'\right) \mathcal{V}_{0n}^* \mathcal{V}_{0n} \left(\tilde{x}_{mean} + d_{n\perp} \tilde{x}'\right)}{4\mathcal{U}_n} \exp \frac{j\omega_n s}{c_0} \right\} \exp\left(-\frac{\omega_n s}{2Q_n c_0}\right) \vartheta(s) \tag{3.51}$$

and replacing $\mathcal{V}_{0n}^* \mathcal{V}_{0n}/4\mathcal{U}_n$ with the conventional loss parameter k_n of the dipole modes from 3.23:

$$\tilde{U}_n(s) = -2k_n q\Re e \left\{ \left(x_{mean} + d_{n\perp}^* x'\right) \left(\tilde{x}_{mean} + d_{n\perp} \tilde{x}'\right) \exp \frac{j\omega_n s}{c_0} \right\} \exp\left(-\frac{\omega_n s}{2Q_n c_0}\right) \vartheta(s). \tag{3.52}$$

Applying the Panofsky-Wenzel theorem 2.34 to this expression for the induced voltage we obtain the transverse deflection of a particle with the energy $\tilde{W}$ by the mode n as

$$\begin{aligned}
\Delta\tilde{x}_n'(s) &= -2\tilde{q}\frac{1}{\tilde{W}} \frac{\mathrm{d}}{\mathrm{d}\tilde{x}_{mean}} \int_{-\infty}^{s} U(\varsigma)\mathrm{d}\varsigma \\
&= 2q\tilde{q}k_n \frac{1}{\tilde{W}} \int_{-\infty}^{s} \Re e \left\{ \exp \frac{j\omega_n \varsigma}{c_0} \left(x_{mean} + d_{n\perp}^* x'\right) \right\} \exp\left(-\frac{\omega_n \varsigma}{2Q_n c_0}\right) \vartheta(\varsigma)\mathrm{d}\varsigma \\
&\approx 2q\tilde{q}k_n \frac{c_0}{\omega_n \tilde{W}} \Im m \left\{ \exp \frac{j\omega_n s}{c_0} \left(x_{mean} + d_{n\perp}^* x'\right) \right\} \exp\left(-\frac{\omega_n s}{2Q_n c_0}\right) \vartheta(s).
\end{aligned} \tag{3.53}$$

Finally, in order to get the full kick on the particle, the contributions from the different modes must be summed.

In order to get a quantitative picture of the emittance growth caused by the TE-like dipole modes, we calculate the emittance growth generated by the TE-like branch of the HEM_{11} modes. As the field parameters and frequencies of the coupled TE-like modes for the SBLC structure are not known presently, we utilize the transient approximation to obtain the wake. The frequencies of the uncoupled modes range from 4206MHz in the first cell to 5117MHz in the last one. For the longitudinal loss parameter k_n we use a value of $1.18 \cdot 10^{14}\mathrm{V/m^2C}$ for the first cell, increasing to $4.8 \cdot 10^{14}\mathrm{V/m^2C}$ at the last cell of the structure, and the parameter $d_{n\perp}$ is assumed to vary between 0.144m at the beginning and 0.064m at the end of the structure. These parameters are assumed to vary linearly along the structure. Further, a uniform quality factor of the modes of $Q = 14000$ is used. As for quality factors of this magnitude the time constants Q/f_n are larger than the length of the bunch train, the resulting emittances cannot get much worse for even larger quality factors. The frequencies are given a relative random scatter of $2.3 \cdot 10^{-5}$ around their mean values, the distribution being Gaussian. Deliberate detuning, as introduced in section 3.3.2, is not assumed. The assumptions on the frequency spread is a pessimistic one, the ones on the mode qualities and detuning are almost the worst case. Finally, we assume a uniform accelerating gradient of 17MV/m without beam loading.

We first carry out a simulation in which the accelerating structures are taken to be offset randomly with respect to the machine axis with an rms of 100μm. The structure axes are parallel to the machine axis and the beam is injected exactly on axis. This means that in this simulation the interaction of the beam with the modes is dominated by excitation via the longitudinal electric field as described by the longitudinal loss parameter. In a calculation with 10 different random seeds for machine misalignment and frequency deviations we find a mean relative centroid emittance of $(6.9 \pm 2.5) \cdot 10^{-4}$, which is negligible in comparison with the effect from the TM-like dipole modes.

The next simulation is made using essentially the same assumptions; however, the structure axes are assumed to be tilted randomly with an rms of 23.6μrad. This value is equal to the rms structure tilt that would be caused by an uncorrelated misalignment of the structure ends of 100μm each. At the same time, the overall structure offsets are assumed to vanish. With this simulation we expect to observe the effect from the excitation of the TE-like modes by the transverse electric field as described by the parameter $d_{n\perp}$. The mean relative centroid emittance found under these conditions is $(4.0 \pm 1.6) \cdot 10^{-5}$.

Both emittance contributions, from the interaction with the longitudinal and the transverse electric field, are very small compared with the emittance of the beam at injection and they also are entirely negligible in comparison with the effect from the TM-like dipole modes. Therefore, the TE-like dipole modes will be ignored for the remainder of this document.

3.4 Deflection by the Accelerating Mode

We again consider the general misaligned accelerating structure as illustrated in Fig. 3.11 with an offset x_0, a tilt x_0' and a sag s_0. The structure tilt is the difference of the offsets of the structure ends divided by the structure length L, and the sag is the deviation of the structure center from the straight line between the structure ends. In such a misaligned structure, the longitudinal electric field of the accelerating mode is nonparallel to the machine axis, and the resulting transverse electric field gives a transverse kick on particles traversing the structure. For realistic magnitudes of the structure tilts, the magnitude of this kick is small in comparison with the kicks associated with misaligned quadrupole magnets for instance. Therefore, if the kicks on all bunches were identical, the orbit distortions created by the accelerating mode would be corrected almost completely in the scope of the orbit corrections. However, from

the considerations in section 3.2 the accelerating mode is known to be subject to a strong beam loading effect. As a consequence of this beam loading, the bunches of the bunch train are kicked with different strength, leading to a direct effect on the beam emittance [44]. In addition, the net betatron motion imparted on the bunch train will filament. It follows that an orbit correction will not be able to fully prevent an increase of the normalized emittance.

For a quantitative examination of this effect we describe the axis of the accelerating structure with the polynomial

$$x_{struc}(z) = C_0 + C_1 \cdot z + C_2 \cdot z^2, \tag{3.54}$$

where the coefficients $C_0 \ldots C_2$ are determined by the offset x_0, the tilt x_0' and the sag s_0 of the structure as

$$C_1 = x_0' - \frac{4}{L} s_0, \quad C_2 = \frac{4}{L^2} s_0. \tag{3.55}$$

Using 3.55, we may rewrite 3.54 as

$$x_{struc}(z) = \left(x_0 - x_0' \frac{L}{2}\right) + z \underbrace{\left(x_0' - s_0 \frac{4}{L}\right)}_{C_1} + z^2 \underbrace{s_0 \frac{4}{L^2}}_{C_2}. \tag{3.56}$$

The derivative of $x_{struc}(z)$ with respect to z is

$$x'_{struc}(z) = C_1 + 2C_2 z. \tag{3.57}$$

Assuming that the longitudinal electric field $E_{\|}$ of the accelerating mode remains parallel to the distorted structure axis and assuming $E_{\|}$ to be constant along z, we calculate the perpendicular electric field as $E_{\perp}(z) = E_{\|} x'_{struc}(z)$. This gives us the derivative of the transverse momentum of a charge q with respect to time

$$\dot{p}_{\perp}(z) = qE_{\perp}(z) = qE_{\|} x'_{struc}(z)$$

and its derivative with respect to z

$$p'_{\perp}(z) = \frac{qE_{\|}}{c_0} x'_{struc}(z).$$

By integration we get the trajectory slope of the particle along the structure:

$$x'_{particle}(z) = \frac{qE_{\|}}{W(z)} \left(C_1 z + C_2 z^2\right).$$

Here, $W(z)$ denotes the particle energy at the position z within the structure. For brevity we introduce the energy gradient of the particle $g = qE_{\|}$. The energy gradient is uniform along the structure, since the accelerating field is assumed to be uniform. A second integration finally leads us to the displacement of the particle along the structure:

$$\begin{aligned} x_{particle}(z) &= C_2 \left(\frac{z^2}{2} + \frac{W(0)^2}{g^2} \ln \frac{W(L)}{W(0)} - \frac{W(0)}{g} z\right) \\ &+ C_1 \left(z - \frac{W(0)}{g} \ln \frac{W(L)}{W(0)}\right). \end{aligned} \tag{3.58}$$

In practice, only the terms relating to the structure tilt x_0' in expression 3.58 will be relevant. The contributions arising from the structure sag can be neglected, since the transverse electric field in a sagging structure is antisymmetric with respect to the middle of the structure. Thus,

beam parameters	
bunches	125
slices	
subslices	
alignment parameters	
σ_{struc}	
σ_{quad}	
σ_{BPM}	
σ_{res}	5μm
σ_{tilt}	23.6μrad
inj. offs.	
***HOM* parameters**	
Q	
Δf_{range}	36MHz
acceleration	
bl/st	yes
varied	Q

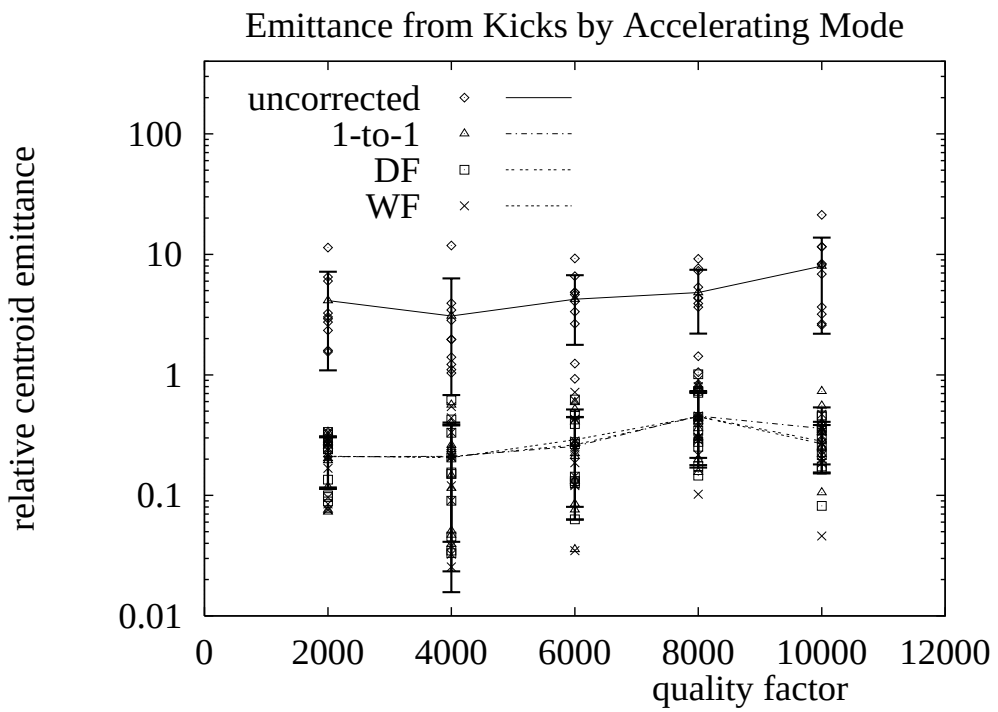

Fig. 3.26 Emittances generated by transverse kicks from the accelerating mode for quality factors of the dipole modes $Q = 2000 \ldots 10000$. Shown are the emittance values before and after orbit correction using the One-to-One, Dispersion-Free and Wake-Free algorithm. It can be seen that the emittances after orbit correction are practically independent of the correction algorithm.

the kicks in the first and in the second half of the structure cancel and hence the overall momentum transfer from a sagging structure vanishes. Nevertheless, a small displacement of the particle will be produced. This is a higher order effect caused by the fact that the kick in the first half of the structure takes place at a lower particle energy and so the deflection angle is a little higher at the beginning.

We look now at the impact of this effect on the multi-bunch dynamics. To this end we assume a machine with perfect alignment of the quadrupoles along an ideal machine axis. The structure centers have no offsets with respect to this axis, but the structure axes are tilted randomly with an angle of 23.6μrad rms. With a structure length of 6m this is the tilt angle that would be generated by an uncorrelated misalignment of the two structure ends of 100μm rms each. Beam injection is exactly on axis. The accelerating gradient is subject to beam loading and the energy spread is compensated with staggered timing as outlined in section 3.2. Moreover, the effect of the dipole modes is included and the influence of their quality factors examined. The value for Q is varied from $Q = 2000$ to $Q = 10000$ and the simulations are carried out for 10 different random seeds at each value of the quality factor. Fig. 3.26 shows both the resulting emittances without orbit correction and with orbit correction, using the One-to-One, Dispersion-Free and Wake-Free algorithms. The emittances obtained without orbit correction are very high. At a quality factor of $Q = 2000$, for instance, we find a mean relative centroid emittance of $(420 \pm 300)\%$. Moreover, we find that there is no conclusive dependence of the emittance growth on the quality factors of the dipole modes. This implies that the emittance is dominated by the instant emittance generation from the different kick magnitudes and the contributions from the filamentation of the imparted net betatron motion. The same behavior is observed after removal of the net betatron motion with the orbit corrections. In addition, it

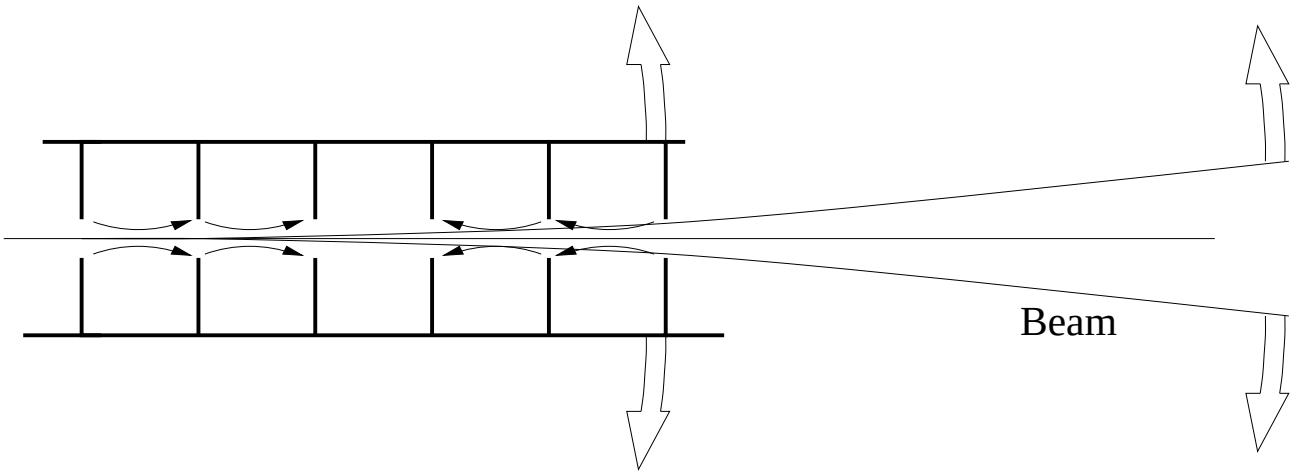

Fig. 3.27 Change of beam deflection induced by structure adjustment. The transverse kick imparted by the accelerating mode is proportional to the tilt angle of the structure and changes when the structure is moved.

is found that the type of correction is not relevant for the final emittance. The mean relative centroid emittance for the case of a One-to-One correction at $Q = 2000$ is found to be $(21 \pm 9)\%$. As for given beam parameters the emittance growth from transverse kicks from the accelerating mode is only sensitive to the alignment precision of the structures, we can establish an upper bound for the tolerable random structure tilt with respect to the machine axis at $\sigma_{tilt} = 13\mu$rad. Assuming that this angle results from an uncorrelated misalignment of the structure ends, this will correspond to an alignment precision of the structure ends of 55μm, independently of other actions taken against emittance growth.

Active Structure Adjustment

The deflection of particles by the accelerating mode has an important implication in connection with an adjustment of the accelerating structures. In several of the current schemes for a linac it is intended to sense the excitation of dipole modes by the beam and use this signal as a reference for an active movement of the structure. The aim of this procedure is to eventually align the structure axes to the beam with high precision and thus prevent wake field induced beam break-up. However, any change of a structure tilt will result in a change of beam deflection, as indicated in Fig. 3.27. From this complication it follows immediately that it is not possible to carry out a structure adjustment in a single step, because the beam orbit changes when the structure tilts are changed. Instead, it will be necessary to reiterate the adjustment procedure several times. In addition, also small changes of the structure tilts in the order of the achieved alignment precision at the beginning of the machine will accumulate to a sizeable beam motion at its end, making a successful structure alignment in that area impossible. Therefore it is also necessary to divide the adjustment procedure into several stages dedicated to different fractions of the machine. A more detailed discussion of the resulting tuning and alignment procedure for the machine will be given in section 4.2.

3.5 Perturbing Effects

Throughout the previous sections of this chapter we have been dealing with an ideal beam passing through an imperfect machine. Accelerating sections were misaligned and orbits were

distorted due to quadrupole misalignments, and beams were injected into the machine with offsets, whereas the beam itself used to be free of any imperfections. The bunch charges generally were uniform and the bunch separation always used to be exactly 4.8m.

In practice, of course, these assumptions are not true. The bunch charges within a bunch train will deviate randomly from their desired mean values. This phenomenon will be referred to as charge fluctuations. Furthermore, the bunches will have random deviations from their appointed longitudinal positions within the bunch train. This longitudinal position error will be called longitudinal jitter. These perturbations of the beam properties are bound to have an influence both on the energy spread in the beam as well as the emittance growth.

In section 3.3.3 we had seen that at low quality factors the transverse deflections of the bunches converge to a steady state at the end of the bunch train. This occurs when the relative offsets between the bunches in the bunch train are small in comparison with the magnitude of the structure misalignment and the length of the bunch train is larger than the damping time of the deflecting modes. Then, a bunch n will get practically the same transverse kicks from the bunches $n-1, n-2$, etc. as the bunch $n+1$ from the bunches $n, n-1$, etc.. If the kicks from the first bunches become small due to the mode damping, then it follows that also the sums of these kicks become practically identical for the different bunches. The convergence of the bunch deflections to the steady state is advantageous with respect to the emittance of the beam, since the emittance is a measure for the spread of the particles in the transverse degrees of freedom. However, if the bunches are not spaced equidistantly, the phases of the wakes from the bunches $n-1$, $n-2$, etc. experienced by the bunch n are different from the phases of the wakes from bunches n, $n-1$, etc. seen by bunch $n+1$. Similarly, when the bunch populations vary from bunch to bunch, the kicks imparted on the trailing bunches will vary proportionally. In either case, the imparted deflections will become different for each bunch and as a consequence, the convergence of the deflections to the steady state is perturbed.

Likewise, the accelerating voltages imparted on the bunch by the structure are influenced. In the case of longitudinal jitter this influence essentially arises from the different RF phases assumed by the bunches. Due to these phase differences, the bunches see a wrong RF phase of the accelerating mode and hence experience different energy gains. Also, the voltages induced by these bunches on trailing bunches in the context of beam loading acquire different phases. In the case of charge fluctuations, the voltage induced by a leading bunch on a trailing bunch in the scope of beam loading changes proportionally to the charge of the leading bunch.

Both consequences of these perturbations, emittance growth and growth of the energy spread, will lead to a loss of luminosity. A significantly increased energy spread will also restrict the energy resolution of the experiments.

In addition, we consider the impact of random fluctuations of the klystron phases on the final beam emittance and the beam energies. These fluctuations act primarily on the energy gains experienced by a particle traversing an accelerating structure. Effects on the emittance may arise as a byproduct from these errors of the energy gain, since machine adjustments may become suboptimal for the deviating particle energies.

Throughout all these simulations, we assume that the accelerating voltage is subject to beam loading. The unloaded accelerating gradient is taken to be 21MV/m and the multi-bunch energy spread is corrected by staggered timing. The properties of the accelerating mode are assumed to be as outlined in section 3.2. In addition, we set the RF phases of the accelerating mode to the values suggested in section 2.2, with the structures in the first 4 sectors running at an RF phase of 4° and the remaining structures set to -12°. The first 4 structures of the machine are again set to a phase of 90°. The kicks from the accelerating mode in tilted structures will be included in all simulations. Furthermore, we will use the lattice as described in appendix D and Fig. 2.6. The long range dipole wake is generated from the dipole modes calculated by [36]

beam parameters	
bunches	125
slices	
subslices	
alignment parameters	
σ_{struc}	
σ_{quad}	
σ_{BPM}	
σ_{res}	
σ_{tilt}	
inj. offs.	10μm
***HOM* parameters**	
Q	2000
Δf_{range}	36MHz
acceleration	
bl/st	yes
varied	σ_s

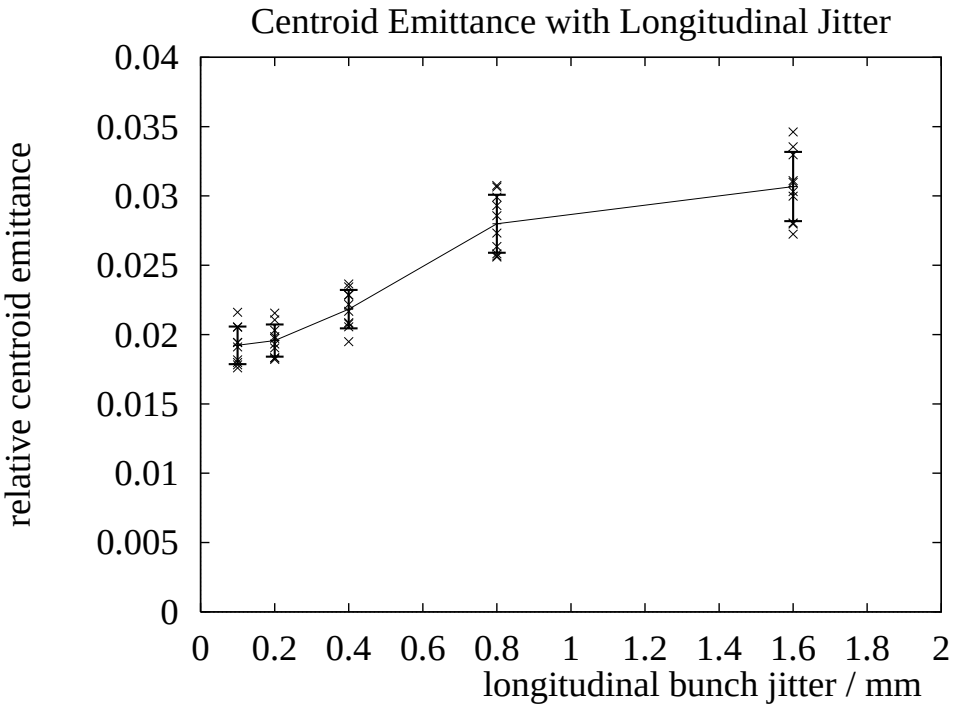

Fig. 3.28 Relative centroid emittance growth from injection offset with longitudinal bunch jitter.

(Fig. 3.3). The modes are detuned over a range of 36MHz in 10 structure classes as outlined in section 3.3.2. For the quality factors of the dipole modes we will always use a uniform value of $Q = 2000$. The beam will consist of 125 bunches with a nominal bunch population of $2.9 \cdot 10^{10}$ and a nominal bunch spacing of 4.8m.

In our investigation of the impact of machine and beam parameters on the emittance and on the energy spread we will conduct simulations of the beam dynamics for different values of these parameters. For each of these different parameter values the results from 10 different random seeds for machine misalignment, dipole mode detuning, BPM errors, and fluctuations of beam and machine parameters are taken.

3.5.1 Longitudinal Jitter

We first look at the impact of jitter of the longitudinal bunch positions on the beam dynamics. For this investigation, we assume that the bunches deviate randomly and in an uncorrelated fashion from the longitudinal bunch positions for an ideal bunch train, which are spaced by a distance of 4.8m. Furthermore, it is assumed that this longitudinal jitter has a Gaussian density distribution characterized by the standard deviation σ_s.

To begin with, we consider a perfectly aligned machine in which the beam is injected with an offset of 10μm at a beta function of $\beta = 20.8$m. Fig. 3.28 shows the emittances resulting from this injection offset for different magnitudes of the longitudinal jitter. The rms jitter magnitude σ_s ranges from 0.1mm up to 1.6mm. In this figure we see an increase of the mean relative centroid emittance from $(1.9 \pm 0.1)\%$ at $\sigma_s = 0.1$mm (this value is practically identical with the unperturbed case) to an average of $(3.1 \pm 0.2)\%$ for longitudinal jitter magnitudes of $\sigma_s = 1.6$mm.

Next, Fig. 3.29 shows the behavior of the emittance caused by a full misalignment of all accelerator elements. In this simulation, we assume perfect injection of the beam, whereas

beam parameters	
bunches	125
slices	
subslices	
alignment parameters	
σ_{struc}	100μm
σ_{quad}	100μm
σ_{BPM}	100μm
σ_{res}	5μm
σ_{tilt}	23.6μrad
inj. offs.	
HOM parameters	
Q	2000
Δf_{range}	36MHz
acceleration	
bl/st	yes
varied	σ_s

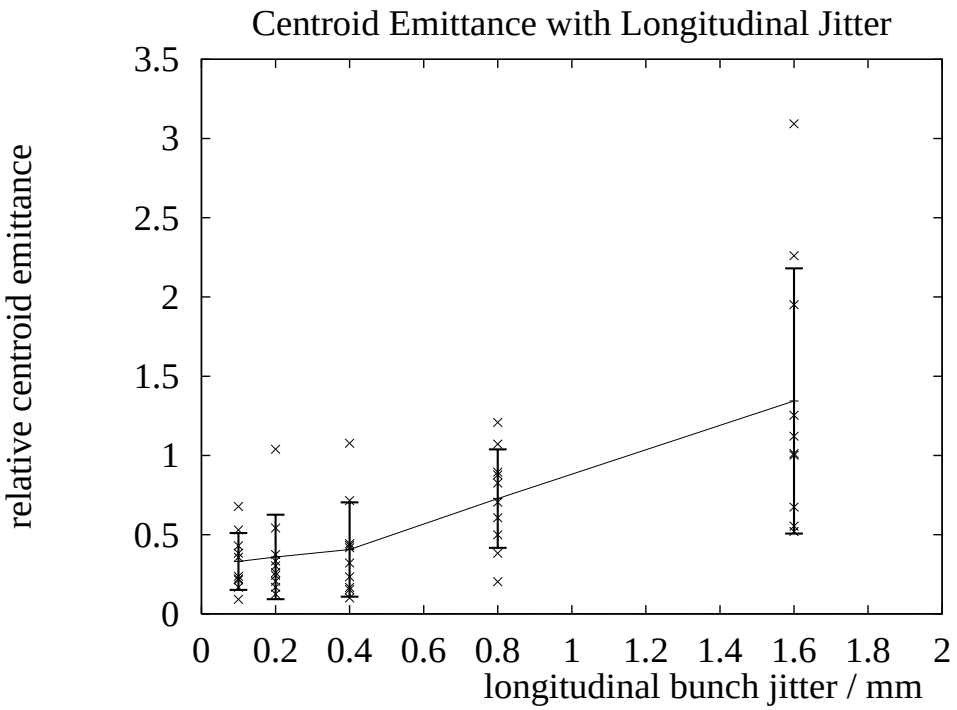

Fig. 3.29 Relative centroid emittance at full machine misalignment with longitudinal bunch jitter.

the accelerating structures, quadrupoles and BPM's are misaligned randomly with an rms of 100μm. The rms structure tilt is 23.6μrad. The orbit is corrected with the Wake-Free correction scheme assuming 5μm BPM resolution and a reduction of quadrupole strengths of 10%. We find that the mean beam emittance changes little for rms jitter magnitudes smaller than 0.4mm. At $\sigma_s = 0.1$mm we find a mean relative centroid emittance of $(33 \pm 18)\%$, which increases strongly to $(134 \pm 84)\%$ for $\sigma_s = 1.6$mm.

Finally, we look at the behavior of the multi-bunch energy spread with respect to longitudinal bunch jitter. The result of this calculation is shown in Fig. 3.30. It turns out that for large magnitudes of the longitudinal jitter the energy spread increases strongly, up to to 1.6% rms for $\sigma_s = 1.6$mm. For small values of the jitter magnitude, the energy spread approaches a finite lower value of 0.2% rms which results from the unperturbed compensation of beam loading with staggered timing as investigated in section 3.2.

From these results we conclude that by keeping the rms value of the longitudinal jitter below ~ 0.4mm...0.2mm the adverse effects on the beam quality can be kept reasonably small. The emittances do not increase significantly for jitter magnitudes up to 0.4mm and the increase of the multi-bunch energy spread is roughly a factor 2. If the jitter magnitude is kept smaller than 0.2mm, the energy spread, too, is virtually unchanged.

A tolerance on the longitudinal bunch jitter of 0.4mm...0.2mm is not unreasonably tight, since the restrictions imposed by the requirements of the final focus system are similarly stringent. At this place there is a region of minimal beta function with a length of the same order as the bunch length. If the bunches were to have a longitudinal jitter which is in the same order as the bunch length, the bunches would collide outside the central region and experience a higher beta function, leading to a direct loss of luminosity [45]. Therefore, the longitudinal jitter of the bunch positions must already of necessity be small in comparison with the bunch length.

beam parameters	
bunches	125
slices	
subslices	
alignment parameters	
σ_{struc}	
σ_{quad}	
σ_{BPM}	
σ_{res}	
σ_{tilt}	
inj. offs.	
***HOM* parameters**	
Q	2000
Δf_{range}	36MHz
acceleration	
bl/st	yes
varied	σ_s

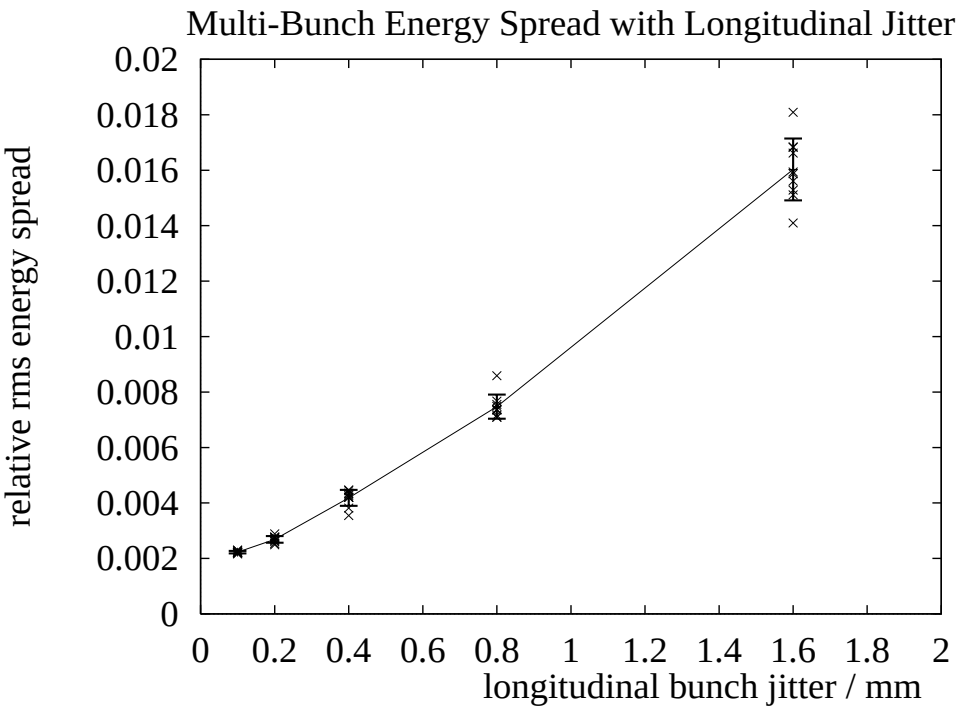

Fig. 3.30 Multi-bunch energy spread with longitudinal jitter of the bunches.

3.5.2 Charge Fluctuation

Next, we look at the behavior of the beam dynamics in the presence of fluctuations of the bunch populations. For this investigation, we assume that the charges of the individual bunches deviate randomly and in an uncorrelated manner from the nominal bunch population. Furthermore, we assume that the charge deviations have a Gaussian density distribution characterized by the mean charge deviation σ_q. In the following we will express σ_q normalized to the nominal bunch charge of 4.65nC.

To begin with, we consider a perfectly aligned machine in which the beam is injected with an offset of 10μm at a beta function of $\beta = 20.8$m. Fig. 3.31 shows the result obtained for random fluctuations of the bunch populations ranging from 2% to 16%. We find that the resulting relative centroid emittance increases only moderately and stays well within the acceptable limit of 6% even for large magnitudes of the charge fluctuation.

Next, we consider again the case of a machine in which the accelerating structures, the quadrupoles and the BPM's are misaligned randomly with an rms of 100μm each. The structures are tilted randomly with an rms of 23.6μrad. It is assumed that the trajectory is corrected with the Wake-Free algorithm. The result of this simulation is shown in Fig. 3.32. The mean final centroid emittance changes little for fluctuations of the bunch charge smaller than 8%. For larger values of the charge fluctuation, however, we get a stronger increase of the emittance. At a fluctuation magnitude of 16% the mean relative centroid emittance has increased to a value of $(71 \pm 32)\%$.

Finally, we investigate the impact of charge fluctuations on the multi-bunch energy spread. For a charge fluctuation magnitude below 8% the mean energy spread increases only little. At larger values of the fluctuation, however, the increase of the energy spread becomes very strong, reaching a mean value of 0.53% rms at a fluctuation magnitude of 16%.

Overall, we find that the character the impact of charge fluctuation on the beam behavior is fairly similar to the effect of longitudinal jitter. In view of the impact of charge fluctuation on the multi-bunch energy spread, we conclude that one should try to keep the fluctuation

beam parameters	
bunches	125
slices	
subslices	
alignment parameters	
σ_{struc}	
σ_{quad}	
σ_{BPM}	
σ_{res}	
σ_{tilt}	
inj. offs.	10μm
***HOM* parameters**	
Q	2000
Δf_{range}	36MHz
acceleration	
bl/st	yes
varied	σ_q

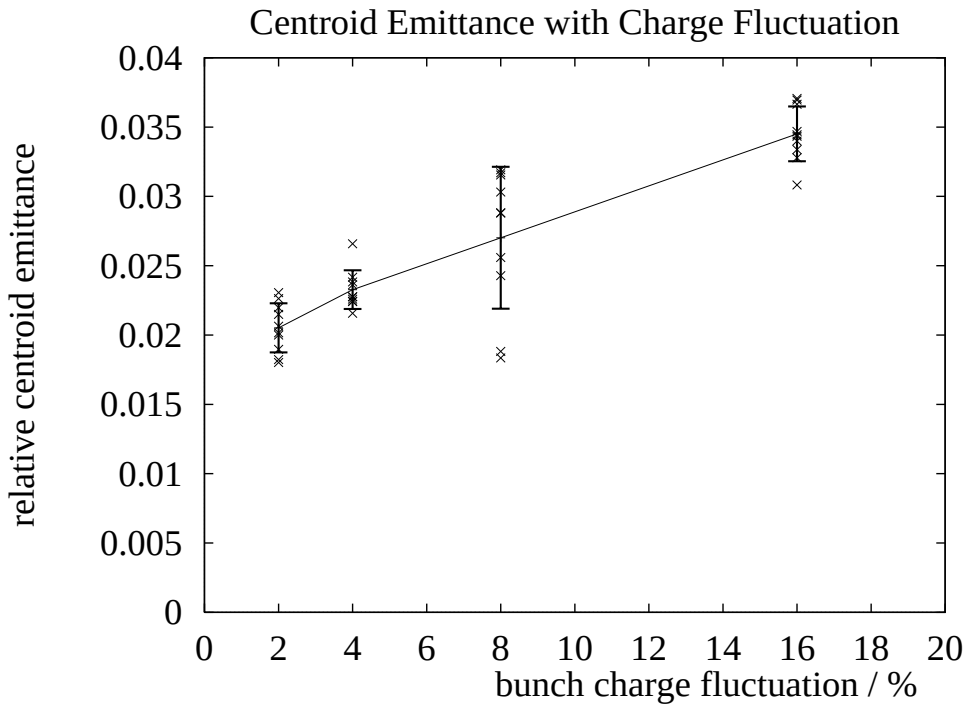

Fig. 3.31 Relative centroid emittance after injection offset with fluctuation of the bunch populations.

beam parameters	
bunches	125
slices	
subslices	
alignment parameters	
σ_{struc}	100μm
σ_{quad}	100μm
σ_{BPM}	100μm
σ_{res}	5μm
σ_{tilt}	23.6μrad
inj. offs.	
***HOM* parameters**	
Q	2000
Δf_{range}	36MHz
acceleration	
bl/st	yes
varied	σ_q

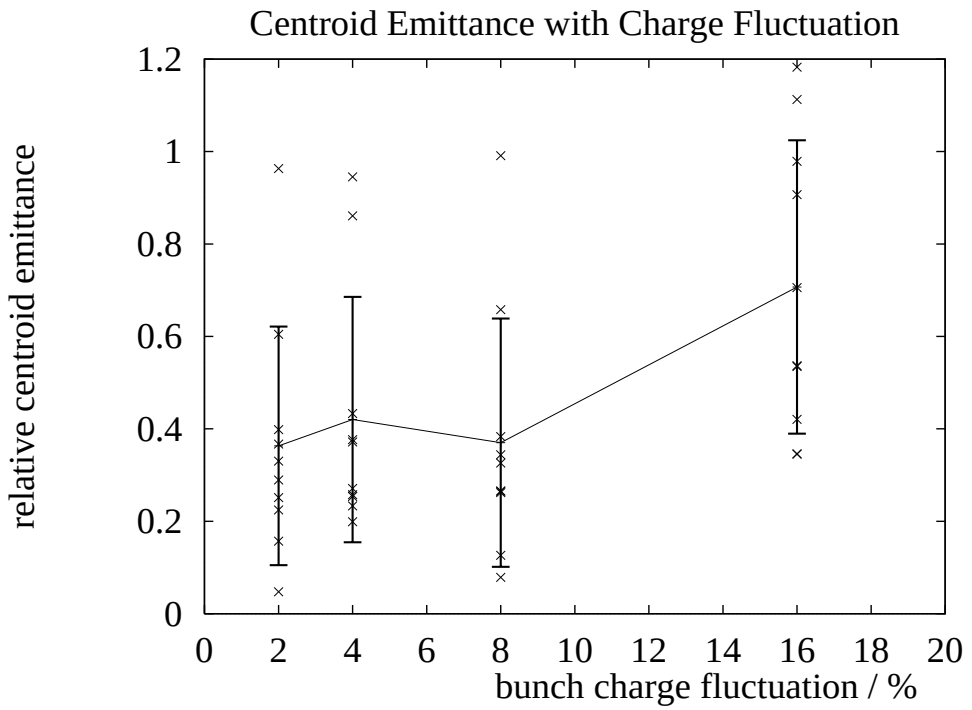

Fig. 3.32 Relative centroid emittance at misalignment of all machine elements with fluctuation of the bunch populations.

beam parameters	
bunches	125
slices	
subslices	

alignment parameters	
σ_{struc}	
σ_{quad}	
σ_{BPM}	
σ_{res}	
σ_{tilt}	
inj. offs.	

HOM parameters	
Q	2000
Δf_{range}	36MHz

acceleration	
bl/st	yes

varied	σ_q

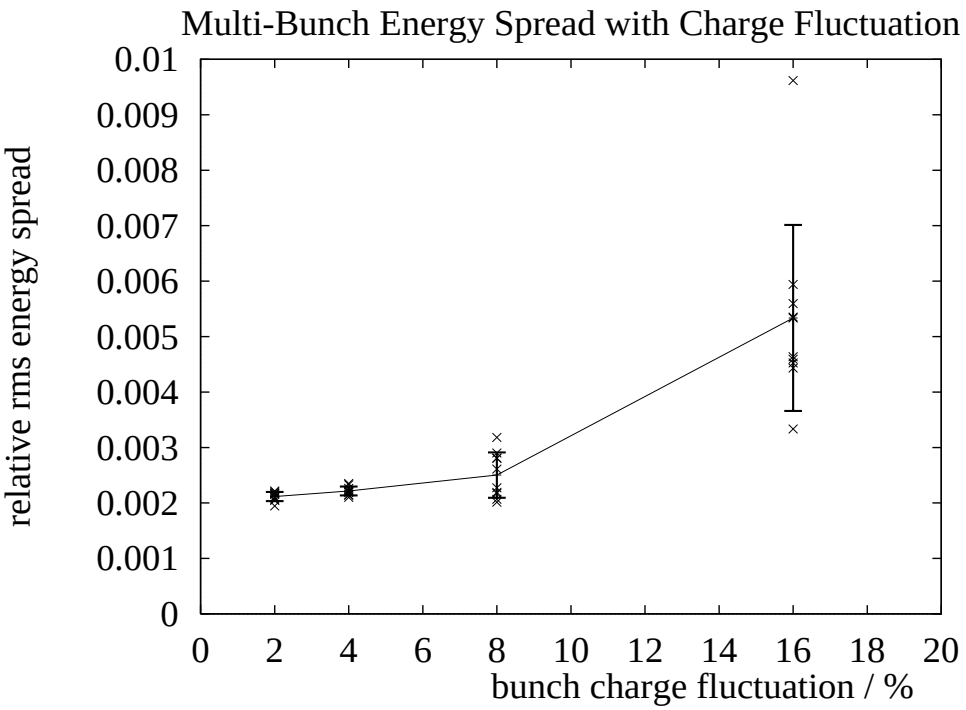

Fig. 3.33 Multi-bunch energy spread with fluctuation of the bunch populations.

below an rms value of 8%. If this tolerance is fulfilled, then one will have almost no additional multi-bunch energy spread degrading the energy resolution available to the experiments. The effect on the emittance growth would be insignificant at this level of charge fluctuation.

3.5.3 RF Phase Errors

The last effect that we examine in this chapter is the impact of phase errors on the behavior of the beam in the machine. This investigation is motivated by the anticipation that it will not be possible to adjust the phases of the accelerating voltage in the structures exactly to the desired values as referenced by some master clock. Instead, the RF phases in the individual structures are expected to have a small random error which may vary from shot to shot, i.e. from bunch train to bunch train. This phenomenon will be referred to as phasing errors. During the following simulations we assume that the individual RF phases deviate randomly and uncorrelatedly from their appointed values. The density distribution of the phase errors is assumed to be Gaussian with the mean phase error σ_φ.

In order to learn about the consequences of this effect on the multi-bunch dynamics in the SBLC, we proceed as in the previous section and start with the simulation of a beam that is injected with an offset of 10μm at a beta function of $\beta = 20.8$m. The elements of the accelerator are aligned ideally. Fig. 3.34 shows the centroid emittances found under these assumptions for magnitudes of the phasing error σ_φ ranging from $\sigma_\varphi = 1°$ to $\sigma_\varphi = 8°$. We find that even for large values of the phasing error the multi-bunch centroid emittances do not deteriorate in any conclusive fashion.

Next, we simulate the influence of phasing errors on a misaligned machine. For this purpose, we assume a machine in which the accelerating structures and quadrupoles are misaligned with an rms of 100μm with respect to an ideal axis and the BPM's, likewise, are misaligned randomly with an rms of 100μm with respect to the quadrupole centers. In addition, the accelerating structures are given a random tilt with an rms of 23.6μrad. The beam trajectory through this

beam parameters	
bunches	125
slices	
subslices	
alignment parameters	
σ_{struc}	
σ_{quad}	
σ_{BPM}	
σ_{res}	
σ_{tilt}	
inj. offs.	10μm
***HOM* parameters**	
Q	2000
Δf_{range}	36MHz
acceleration	
bl/st	yes
varied	σ_φ

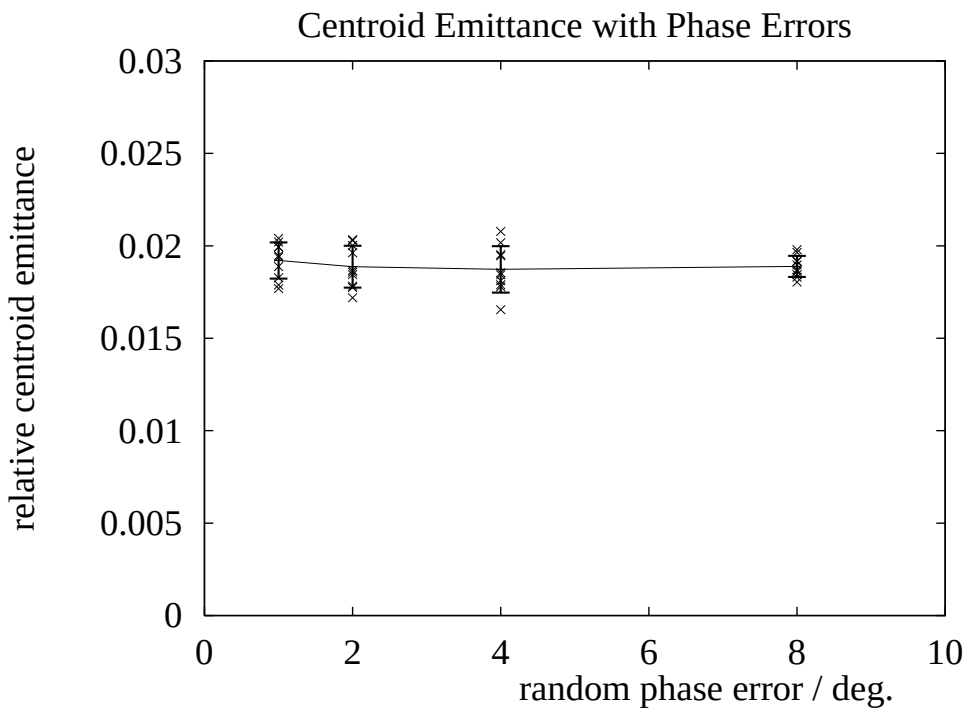

Fig. 3.34 Relative centroid emittance from injection offset with errors of the RF phase.

beam parameters	
bunches	125
slices	
subslices	
alignment parameters	
σ_{struc}	100μm
σ_{quad}	100μm
σ_{BPM}	100μm
σ_{res}	5μm
σ_{tilt}	23.6μrad
inj. offs.	
***HOM* parameters**	
Q	2000
Δf_{range}	36MHz
acceleration	
bl/st	yes
varied	σ_φ

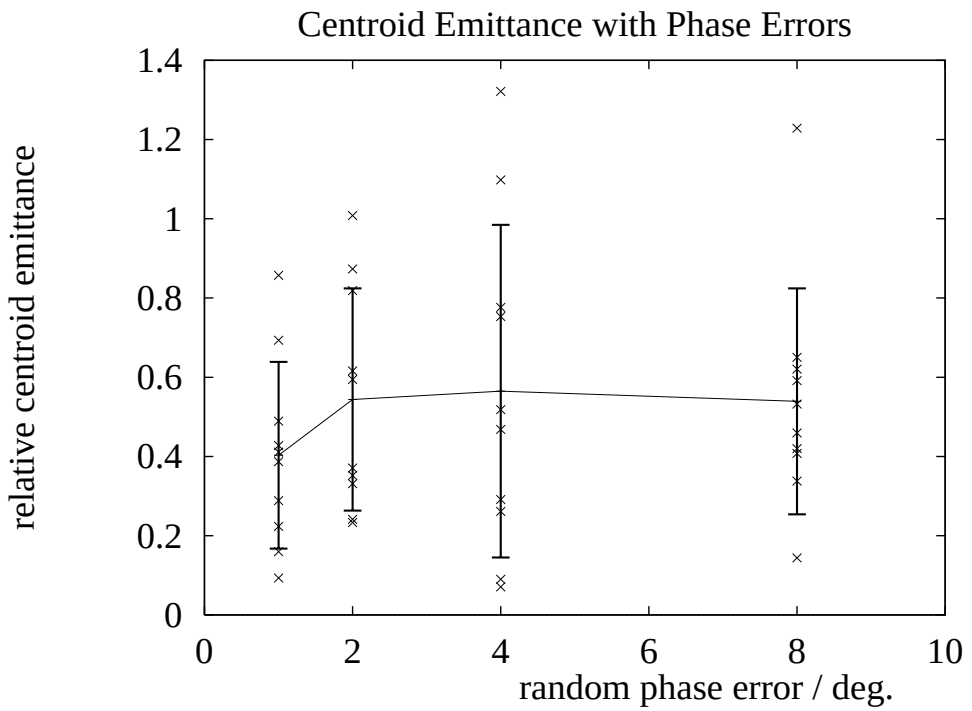

Fig. 3.35 Relative centroid emittance in a misaligned machine with errors of the RF phase.

beam parameters	
bunches	125
slices	
subslices	
alignment parameters	
σ_{struc}	
σ_{quad}	
σ_{BPM}	
σ_{res}	
σ_{tilt}	
inj. offs.	
***HOM* parameters**	
Q	2000
Δf_{range}	36MHz
acceleration	
bl/st	yes
varied	σ_φ

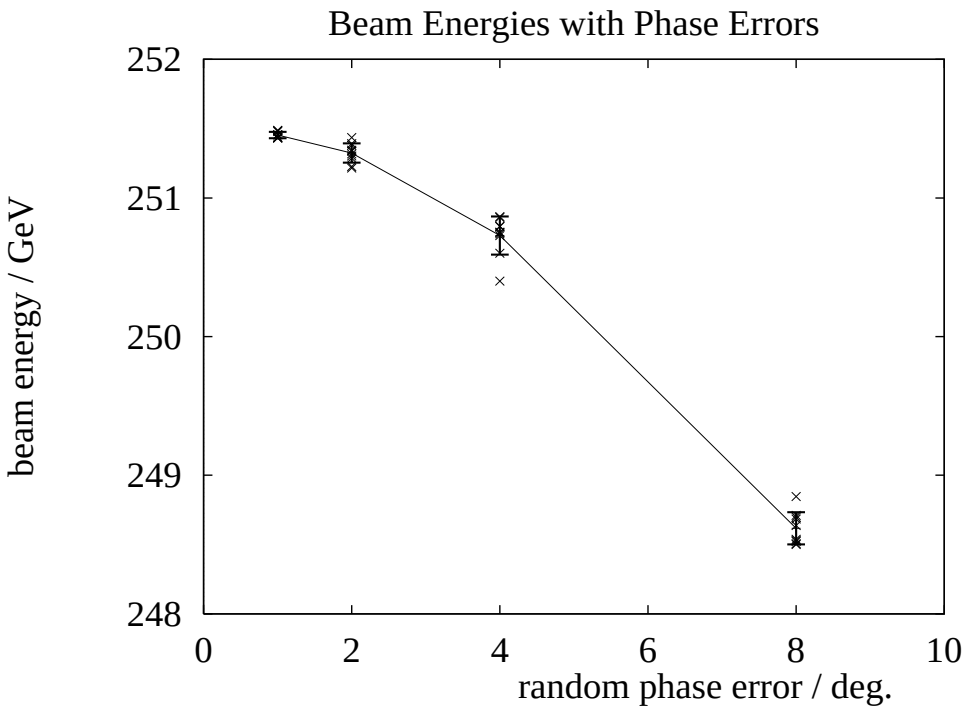

Fig. 3.36 Final beam energies for different magnitudes of the phasing error.

machine is corrected with the Wake-Free algorithm and finally the emittance growth of the complete bunch train is simulated. Fig. 3.35 shows the multi-bunch centroid emittances found with this procedure, again for magnitudes of the rms phase error ranging from 1° to 8°. The phase errors do not change the final emittances significantly. At a phase error of 1° we obtain an average of the relative centroid emittance of $(40 \pm 24)\%$, which increases to $(54 \pm 29)\%$ for a phase error of 8° rms.

From these considerations we conclude that, at least as far as the multi-bunch effects are involved, phasing errors have little influence in the emittance evolution in a linear accelerator. However, these phasing errors do have an implication for the total beam energy, since any change of the RF phase in an accelerating structure will bring about a change of the accelerating voltage seen by the beam. Although the energy spread within one individual bunch train is practically unaffected by these phasing errors, we get an energy spread between subsequent bunch trains if we assume that the phasing errors for different bunch trains are not correlated. In this case, the beam energy will vary slightly from shot to shot. This can be seen in Fig. 3.36, where we plotted the final beam energies found at different magnitudes for the rms phasing error. We see that the mean beam energy decreases for growing values of the phasing error and in addition we observe a growing spread between the beam energies of different shots. For a large phasing error of 8° we get a reduction of the mean beam energy of 1.1%. Moreover, an energy spread between different bunch trains of 0.05% rms is generated. Since this energy spread is smaller than the other major contributions to the energy spread within a bunch train, we believe that it is not critical for the beam quality.

Chapter 4

Combined Single- and Multi-Bunch Effects

In this chapter we will finally address the issues related to the complete beam dynamics, including both the single- and multi-bunch effects. Firstly, we will look at the impact of several multi-bunch effects as treated in chapter 3 on the single-bunch behavior. Then we will outline a possible complete machine tuning procedure that is required until the linear accelerator can resume luminosity operation with full beam current, using complete multi-bunch trains. Finally we will investigate the response of the full beam emittance to variations of a number of design parameters of the machine as well as to perturbing effects. This investigation will be carried out for a machine which has been adjusted according to the previously mentioned tuning procedure.

4.1 Impact of Multi-Bunch Effects on Single-Bunch Dynamics

We will turn now to the investigation of implications of multi-bunch effects on the single-bunch behavior. Some of these cross effects will bring about a serious deterioration of the beam emittance from the values that would have been expected from our experience in chapters 2 and 3.

4.1.1 Machine Tuning and Staggered Timing

In section 2.4 we had demonstrated how the single-bunch emittance at a set of measurement stations along the machine and at the machine end could be optimized by deliberately introducing non-dispersive bumps to the trajectory. However, from section 3.2 it is known that the bunches in the bunch train have different energies due to the effect of beam loading of the accelerating mode. The suggested cure for this beam loading effect cannot remove the energy spread completely and hence there remains an inter-bunch energy spread, which reaches a peak to peak value of $\approx 3\%$ at some locations in the machine. It follows that the deformations imposed on the bunches from the wakes in displaced structures acquire slightly different filamentation histories. As a consequence, the bump magnitudes, which are adjusted to minimize the emittance of the first bunch, might be suboptimal for the remaining bunches of the bunch train. Therefore, it might be conceivable that the multi-bunch energy spread brings about an additional deterioration of the single-bunch emittances in some bunches in the train.

In order to examine this point, we simulated the single-bunch emittance growth caused by structure misalignment as described in section 2.4 for a random structure misalignment of 100μm rms. In this simulation, the effect of beam loading was included and the multi-bunch energy spread was compensated by staggered timing. All other multi-bunch effects were excluded. The bunches were partitioned into 30 slices. We applied an emittance correction with non-dispersive bumps and compared the emittance achieved for a single bunch, for which the emittance was optimized, with the emittance of a complete bunch train. In a simulation with 10 random seeds we find a relative single-bunch emittance of 1.044 ± 0.04 after correction with 8 pairs of bump-sets. For the full bunch train consisting of 125 bunches this value increases to 1.054 ± 0.06. As the difference of these values is very small in comparison with the standard deviation, the deterioration of the emittance can be considered statistically insignificant. Therefore, we conclude that among the multi-bunch effects perturbing the single-bunch behavior of the beam, the multi-bunch energy spread is of secondary importance. Nevertheless, the reader should be reminded that the enhancement of the multi-bunch emittance growth by the energy spread (section 3.3.7) is considerable.

4.1.2 Kicks from the Accelerating Mode

A much more important implication of multi-bunch effects for single-bunch dynamics comes from the transverse kick imparted by the accelerating mode in a tilted structure on the accelerated particles. In section 3.4 it has already been shown how this effect can affect the multi-bunch emittance. In the scope of those simulations we had made two important observations, namely that the resulting emittance dilution had depended neither on the choice of orbit correction nor on the quality factors of the dipole modes.

We now want to look at the impact of the kick from the accelerating mode on the combined single- and multi-bunch emittance of a beam. It is expected that with the inclusion of single-bunch effects the emittance growth increases essentially for two reasons:

1. the betatron motion imparted by the kicks filaments to some extent and

2. we also get different kick magnitudes within the bunches due to the intra-bunch energy spread.

These circumstances call for a simulation of the emittance growth caused by the kicks in tilted structures in the presence of both single- and multi-bunch dynamics. Specifically, we looked at the growth of the centroid emittance for a bunch train consisting of 125 bunches partitioned into 30 slices each. It was assumed that the accelerating structures were tilted randomly with an rms of 23.6μrad. The energy spread from beam loading was assumed to be compensated with staggered timing as demonstrated in section 3.2 and the trajectory was corrected using the One-to-One algorithm. This simulation was carried out with 10 different random seeds for the machine misalignment. The relative centroid emittance found for the complete bunch train with these assumptions had a mean value of $(66 \pm 56)\%$.

If we require the emittance growth caused by this effect to be smaller than 6% of the nominal emittance, the random tilt must not exceed 7.1μrad rms. Such an rms structure tilt would be obtained by an uncorrelated misalignment of the structure ends of 30μm rms each.

4.1.3 Transverse Long Range Wake and Finite Bunch Length

One effect which might give rise to an influence of the long range wake on the emittances of the single bunches is the differential kick imparted by the long range wake on different fractions of

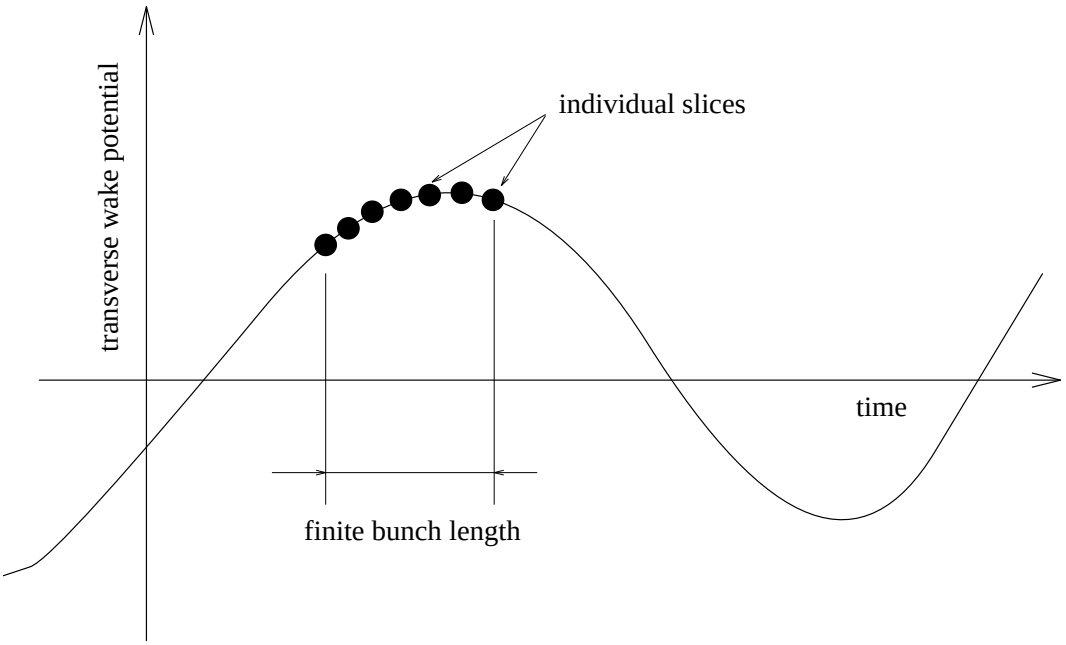

Fig. 4.1 Differential kicks by long range transverse wake due to finite bunch length. Different longitudinal regions of the bunch are kicked at different phases of the deflecting modes and deflected at different angles.

the bunch. Fig. 4.1 gives a schematic idea of this process. The oscillatory phase advance of the long range wake over the temporal length of the bunch would lead to different strong kicks at different regions of the bunch. However, since the bunch length is small in comparison with the wavelength of the deflecting modes, it is expected that the associated differential kick will bring about only a small deterioration of the beam emittance.

In order to find out how large the impact from the differential kick by the long range wake on the beam emittance is, we simulated the multi-bunch emittance growth caused by the long range wake for a random misalignment of the accelerating structures with 100μm rms. The long range dipole wake in this simulation was generated from the dipole modes calculated by [36], the modes being detuned as outlined in section 3.3.2. Then we repeated the simulation with finite bunches, consisting of 30 slices each, with the same misalignment. In this second calculation, intrabunch effects like energy spread from monopole short range wakes and from the RF phase as well as transverse short range wakes were excluded in order to isolate the pure effect of the differential kicks.

This comparison was repeated for different values of the quality factor of the dipole modes with 10 different random seeds for machine misalignment and mode detuning at each value of the quality factors. Beam loading of the accelerating mode was not included. Fig. 4.2 shows the centroid emittances found with both the rigid bunch calculation and the calculation with finite bunches. We find that the emittance values after calculation with rigid bunches and calculation with distributed bunches are practically indiscernible over the whole range of quality factors of the dipole modes. It is our conclusion that the differential kick from the long range wake has, thanks to the short bunch length, no part in the interaction between single- and multi-bunch dynamics.

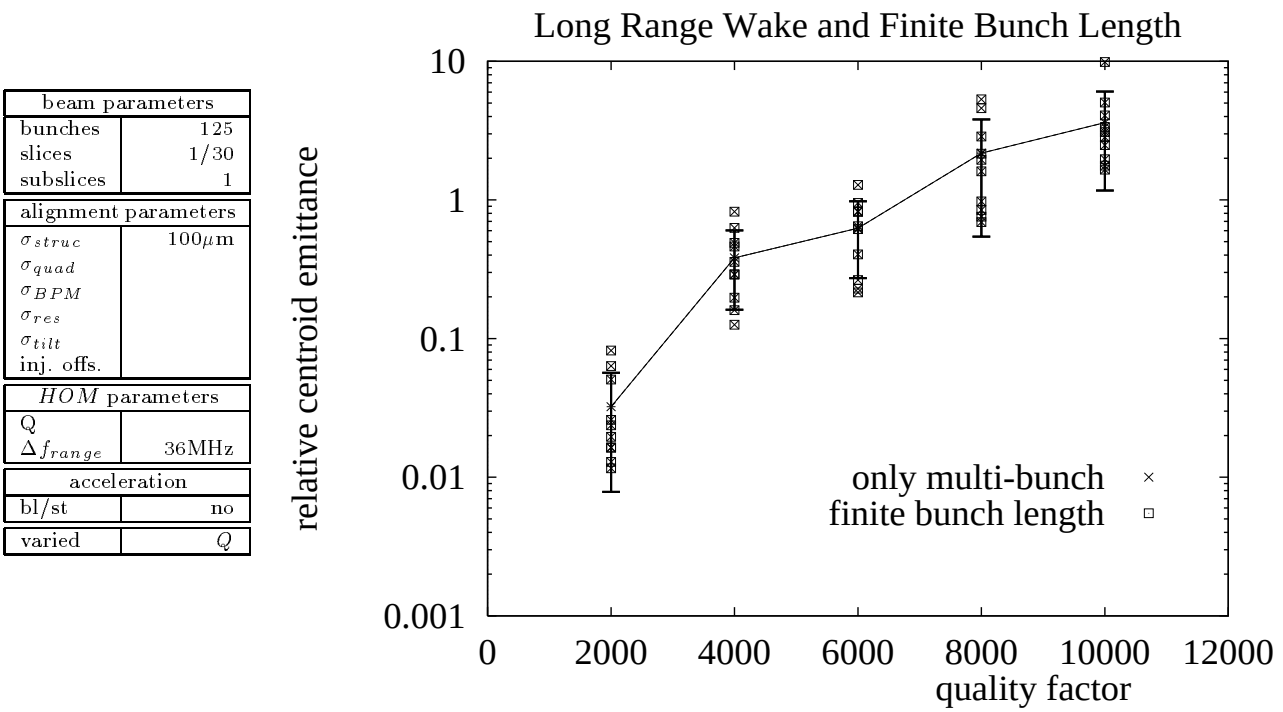

Fig. 4.2 Relative centroid emittances from long range transverse wake for pointlike and extended bunches. The emittances found in the rigid bunch calculation and with division of the bunches into slices are practically indiscernible. The marks indicating the emittance values from the two calculations overlap almost perfectly. The parameter panel on the left hand side of the scatter plot is explained in appendix B.

4.1.4 Transverse Long Range Wake and Filamentation

The second major field of interaction of the multi-bunch dynamics with the single-bunch dynamics is the filamentation of the transverse bunch motion caused by long range transverse wakes.

During our simulations of the beam break-up induced by dipole modes in chapter 3 we had capitalized on the incoherence of the kicks on the different bunches in the train in different structures. In particular, we had introduced a number of different structure classes that were deliberately detuned with respect to the frequencies of their dipole modes. Due to this detuning, the long range wake potentials of different structures experienced by a trailing bunch acquired different values. As a result, the wake contributions from different structures on one particular bunch canceled to a certain extent, leading to a suppression of the multi-bunch emittance growth.

These matters become more difficult when the single-bunch dynamics are included in this process. Although long range wake fields of a large number of structures cancel to a large extent, the wake fields and the associated transverse deflections of the bunches by a single structure have appreciable magnitudes. When a bunch is deflected by the long range wake in a structure, it starts performing a betatron oscillation around the machine axis. To a certain extent, growth of the single-bunch emittances from this betatron oscillation is suppressed by the the application of BNS damping. However, since we only used the RF phase for adjusting the energy spread in the bunch and since the beta function is varied stepwise along the machine, emittance growth cannot be avoided completely (see section 2.2). Therefore, this betatron motion of the bunch is subject to some residual filamentation, leading to an increase of the single-bunch emittance, which also pertains if later a cancellation of the net betatron motion of the bunch by a different

beam parameters	
bunches	125
slices	30/1
subslices	1
alignment parameters	
σ_{struc}	100μm
σ_{quad}	
σ_{BPM}	
σ_{res}	
σ_{tilt}	
inj. offs.	
***HOM* parameters**	
Q	
Δf_{range}	36MHz
acceleration	
bl/st	no
varied	Q

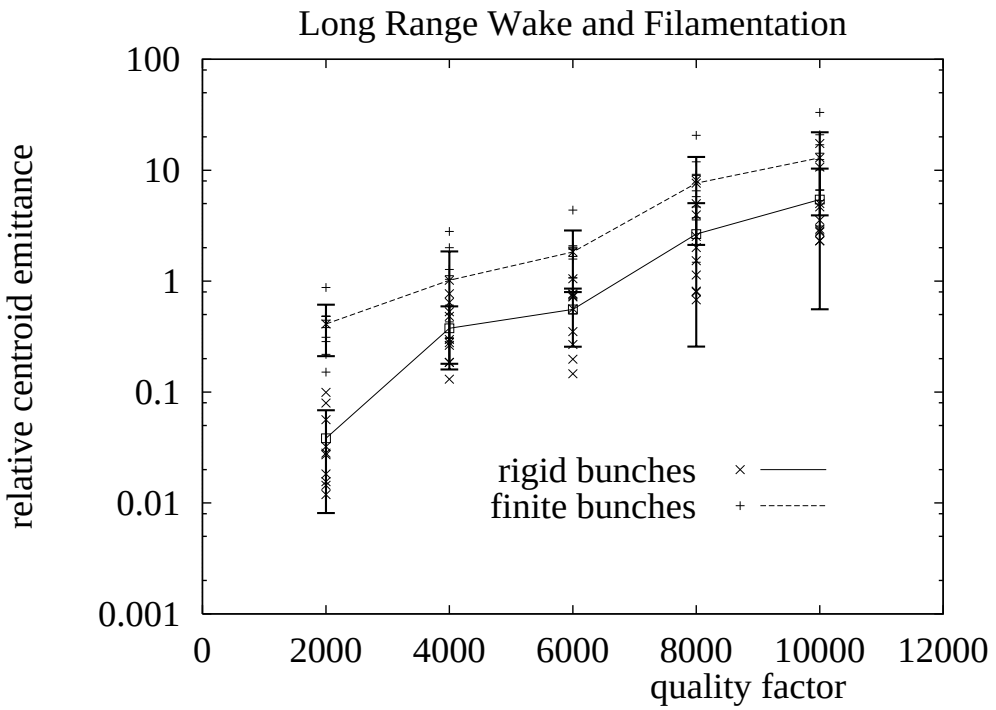

Fig. 4.3 Comparison of emittance growths from structure misalignment in the rigid bunch case and with single-bunch dynamics included (finite bunches). The primary single-bunch emittance growth had been removed by bump adjustment first.

long range wake in a structure downstream the machine occurs. Furthermore, the sequence of deflections and cancellations of deflections by the long range wake is different for each bunch in the bunch train, so the bunches in the bunch train will be subject to individually different deformations. Thus, the single-bunch emittance growth resulting from this process cannot be corrected by emittance correction techniques. We conclude that, when we include the single-bunch dynamics into the simulation of the *HOM*-induced emittance growth, we will get an additional contribution to the total emittance growth from the dilution of the single-bunch emittances.

In order to show the practical relevance of these considerations, we conducted a simulation of the emittance growth from structure misalignment. This simulation was performed for different values of the quality factor of the dipole modes, with 10 different random seeds at each value of the quality factors. We assumed that the structures were misaligned randomly with an rms of 100μm with respect to the machine axis, while the remaining machine elements were aligned perfectly. We first simulated the single bunch dynamics, including in particular the wake field effects, with a division of the bunches into 30 slices. In this simulation, the single-bunch emittance growth was corrected by adjusting 8 pairs of bump-sets as outlined in section 2.4.2. The relative single-bunch centroid emittance remaining after this procedure had a mean value of $(3 \pm 2)\%$ of the injection emittance. Then the pure multi-bunch emittance growth for the corrected machine was calculated using the rigid bunch approximation, i.e. ignoring the single-bunch effects. Afterwards, the same calculation was done for a bunch train consisting of finite bunches that were divided into 30 slices, again for the same machine. In order to isolate the pure combined effect of the long range wake on the single bunches, we excluded the beam loading effect in both simulations. The long range dipole wake was again generated from the modes calculated by [36] with a detuning range of 36MHz in 10 classes.

Fig. 4.3 shows the beam emittances that were found with these two simulations. We observe

that with single-bunch dynamics the emittances increase by roughly a factor 10.7 as compared with the case of the rigid bunch calculation for a quality factor of $Q = 2000$ for the dipole modes. At $Q = 10000$ the increase is still a factor 2.3 .

A glance at a typical bunch train emerging at the end of the machine confirms the description of the effect of the long range wake on the individual bunches. Fig. 4.4 shows a bunch train obtained in a calculation using finite bunches, thus including the complete single-bunch dynamics. The quality factor of the dipole modes in the underlying example was $Q = 10000$. We see immediately that the bunches are not only displaced from the machine axis as a whole but also the different slices within the bunches are scattered over a considerable range of offsets.

We now take a closer look at this result by comparing the first bunch of the bunch train with the 71st bunch in the train. The centers of the slices in these two bunches are depicted in Fig. 4.5. The first bunch in the bunch train is the bunch for which the emittance correction with the ND-bumps had originally been carried out. For this bunch we observe only a slight distortion, which is due to a slight imperfection of the emittance correction. In contrast, bunch number 71 is distorted considerably over a range of almost 70μm. We recall now that the simulation did not include the effect of beam loading. This means that all bunches in the bunch train have the same energy profile over the entire length of the machine. It follows that the emittance correction with the ND-bumps is optimum for all bunches in the bunch train, as long there is no interaction between the different bunches. Therefore, any differences between individual bunches in the bunch train must be due to the long range dipole wake.

4.2 Complete Machine Tuning Procedure

In the previous chapters we had investigated the application of numerous schemes for orbit and emittance correction. In several cases these schemes had been introduced as cures against individual effects. In any case, however, the applicability and merit of these schemes had been demonstrated with respect to isolated effects. Now we shall turn to devising a machine tuning procedure, which will take a misaligned machine over several stages up to full luminosity operation.

The nature of this tuning procedure is governed by several boundary conditions. First, we had learnt in section 3.2 that the accelerating voltages seen by the bunches of the bunch train are subject to a strong beam loading effect and that as a consequence correction of the energy spread was imperative. In order to achieve this we had opted for using the technique of staggered timing, which utilizes different turn-on times at the different klystrons along the machine in order to generate a set of different beam loading histories. Since we do not wish to modify these klystron turn-on times during the course of our tuning procedure, we choose to apply this measure at the very beginning of machine start-up.

Next we will carry out the beam based alignment procedure. Since we had seen in section 2.3 that the quadrupole misalignment leads to both very large particle trajectories and emittance growths, it is preferred to carry out the orbit correction as early as possible in order to achieve any transport of the beam to the end of the machine at all. Furthermore, if one wishes to actively adjust the accelerating structures to the beam, a smooth beam trajectory as reference for this adjustment procedure is first required. As it was found in sections 2.3 and 3.3.7 that only the Wake-Free correction technique holds the prospect of providing a sufficiently good trajectory, we will assume that the beam based alignment is carried out with this algorithm. As in the previous investigations we will assume a resolution of the BPM's of 5μm rms.

In section 3.4 it was found that keeping the emittance growth from differential kicks by the accelerating mode in tilted structures small imposes a fairly tight upper bound on the

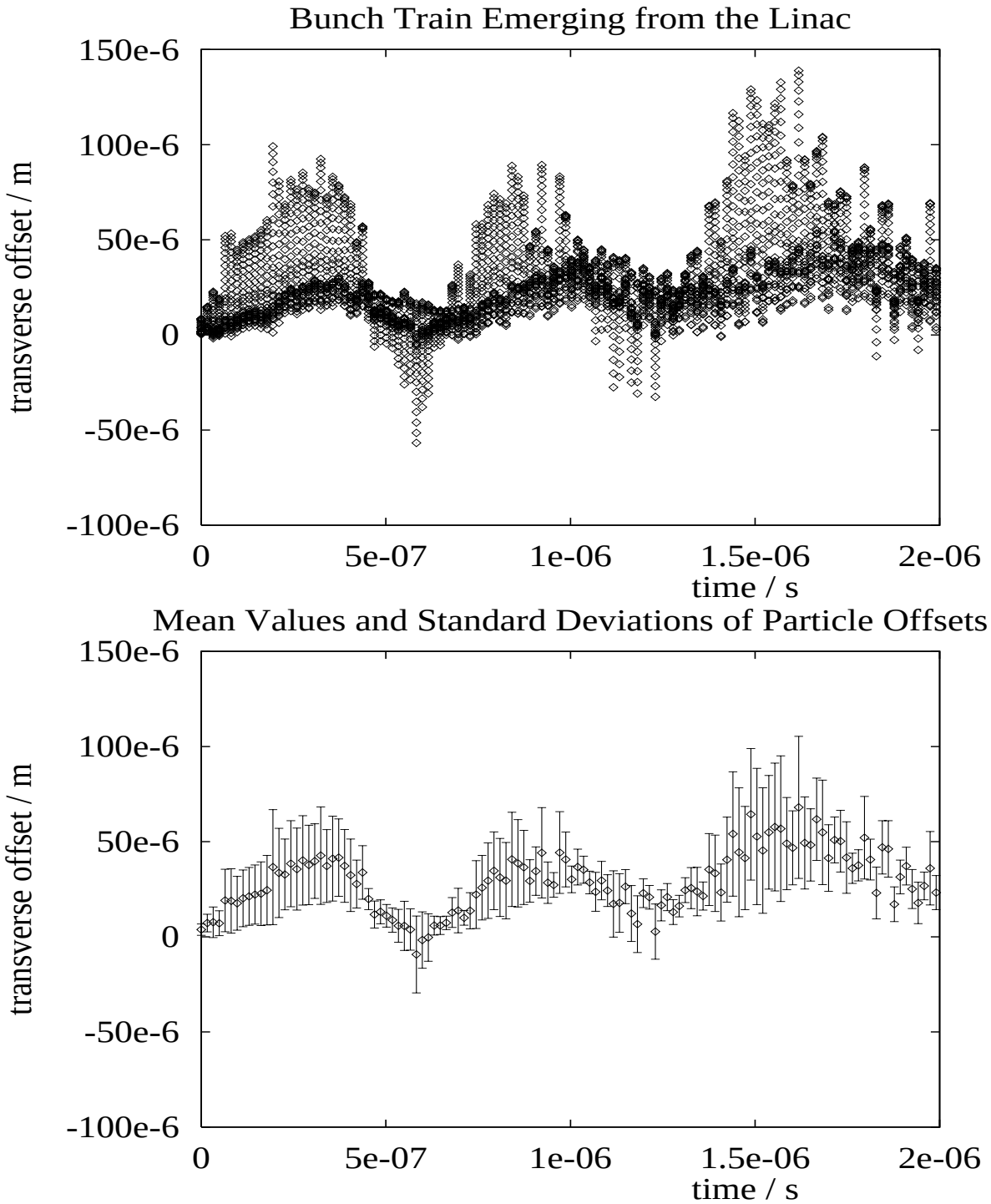

Fig. 4.4 Bunch train emerging from the linac as obtained in a calculation with finite bunches, including the single-bunch effects. The upper figure shows the transverse offsets of all slices, where each marker corresponds to the center of a slice in a bunch. In the lower figure the mean offsets of the entire bunches (markers) and the standard deviations of the particle offsets (error bars) are shown. The time is given relative to the arrival of the first bunch at the machine end. Particles at higher values of the abscissa are trailing.

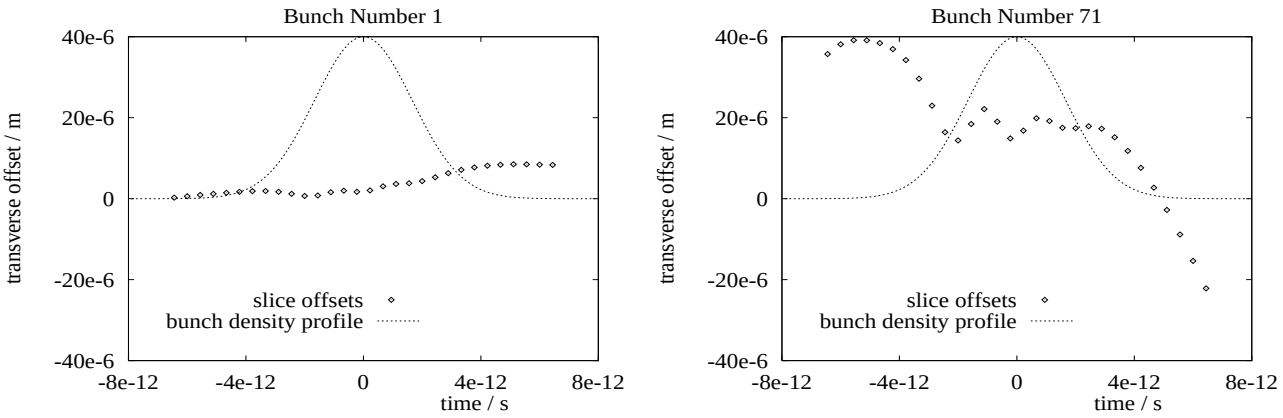

Fig. 4.5 Bunches number 1 and 71 ($Q = 10000$). Each marker represents the center of a slice. The times are given relative to the center of the bunch. Particles at smaller values of the abscissa are ahead while trailing particles are located at higher values of the abscissa. The dashed curves indicate the charge density along the bunch.

permissible random tilt of the accelerating structures. Our considerations in section 4.1 had tightened this tolerance further to an rms value of $\approx 7\mu$rad. It would be very difficult to achieve such an alignment precision by careful and precise machine assembly. Besides, ambient vibrations and slow inelastic ground deformations ([46], [47]) would destroy such an alignment within a time scale of several months. For this reason, we include an active adjustment of the position of the accelerating structures with respect to the beam trajectory to the tuning procedure. The general idea behind these active adjustment schemes is to detect the signal of the dipole modes excited by particles traversing the accelerating structures off axis and displace the structures in a fashion to minimize this HOM-signal.

At this point, it seems appropriate to make a few explanatory remarks about how such an active adjustment procedure should be carried out. In modeling the adjustment procedure for a single accelerating structure, we will generally assume that the trajectory of the beam relative to the structure is measured at the ends of the structure. On this measurement we superimpose a random measurement error which is uncorrelated for the two structure ends. Finally, the structure ends are moved independently to the modified measurements of the beam offsets. Because of the results in section 4.1.2, we will always assume a measurement error for the relative beam trajectory of 30μm rms with Gaussian distribution. In practice, the adjustment error will of course be a composite effect of measurement errors and mechanical adjustment errors from the mover system. However, the origin and composition of the total adjustment error will not be of relevance for the result of the adjustment procedure. Concerning the design of the real machine we will instead require that the combined error from trajectory measurement and mechanical adjustment errors is smaller than 30μm rms.

The total structure displacement applied in the scope of the outlined active adjustment procedure can be decomposed into a transverse translation of the complete structure and a change of the structure tilt. In section 3.4 it was seen that a tilt misalignment of an accelerating structure (or a change of its tilt) imparts a deflection of the particle beam. As a consequence, any change of a structure tilt will result in a change of beam deflection, as indicated in Fig. 3.27. From this complication it follows immediately that it is not possible to carry out a structure adjustment in a single step. Instead, it will be necessary to resort to a sequence of alternating structure adjustments and One-to-One corrections of the beam trajectory back to the orbit found with the beam based alignment procedure.

In addition, the structures will only be adjusted with a finite accuracy. Hence, in the

scope of a realistic alignment procedure the structure axes at the beginning of the machine will approach the beam trajectory until they are aligned with the precision given by the HOM sensors and actuators. Once this accuracy has been reached, consecutive adjustment steps will merely move the structures in a random manner within a boundary defined by that alignment precision. At positions more downstream of the machine these random movements accumulate to considerable fluctuations of the beam position, making a successful structure alignment impossible. Therefore it is also necessary to divide the adjustment procedure into several stages dedicated to different fractions of the machine.

The resulting full adjustment procedure is depicted in Fig. 4.6. The machine is divided into $N_{section}$ sections of roughly equal length. In the beginning, structure adjustments are carried out over the whole length of the machine, the sequence of structure adjustments and subsequent orbit corrections being repeated N_{repeat} times. Then, in the next stage, the region in which the structures are moved is confined to the remaining $N_{section} - 1$ sections of the machine and again N_{repeat} sequences of structure adjustment and orbit correction are carried out. The procedure is completed after the adjustment sequence for the last machine section is finished. For simulation of the structure adjustment in the SBLC we will divide the machine into $N_{section} = 4$ sections and use $N_{repeat} = 3$ repetitions of the adjustment sequence for each section. These parameters were found empirically to yield satisfactory results in the adjustment procedure.

The adjustment of the accelerating structures to the beam trajectory does not fully remove the emittance growth from transverse wakes, especially since we are assuming that this adjustment is only carried out with a limited precision. Therefore we include as the final step of the tuning procedure a correction of the single-bunch emittance using non-dispersive bumps. Drawing on our experience from section 2.4, we will assume correction of the emittance using emittance measurement stations at 8 locations along the machine. These stations will be located at the transitions between the sectors of the lattice and at the end of the accelerator. It must be mentioned, though, that the adjustment of the accelerating structures is the measure which removes by far the largest fraction of the emittance dilution remaining after beam based alignment. With the adjustment of the ND-bumps, we rather apply a final touch to the emittance.

We summarize that the individual steps of the tuning procedure will be carried out in the following order:

1. set klystron turn-on times (staggered timing)

2. beam based alignment

3. active structure adjustment

4. emittance correction with ND-bumps

Fig. 4.7 shows the complete tuning procedure together with the beam current chosen for each step of the procedure. During the first steps of the machine adjustment, the beam current is kept at a small value both in order to avoid damage to machine elements due to beam loss (7.5MW average beam power at the end of the accelerator) and to ensure convergence of the trajectory correction. In our simulations we will assume that during beam based alignment the bunch train consists of a single bunch with a population of $2 \cdot 10^9$. For emittance correction with ND-bumps, the bunch population is then raised to its nominal value of $2.9 \cdot 10^{10}$, the bunch train still consisting of a single bunch. After completion of the emittance correction the number of bunches in a train, too, is raised to its nominal value of 125 and the accelerator is ready for producing luminosity.

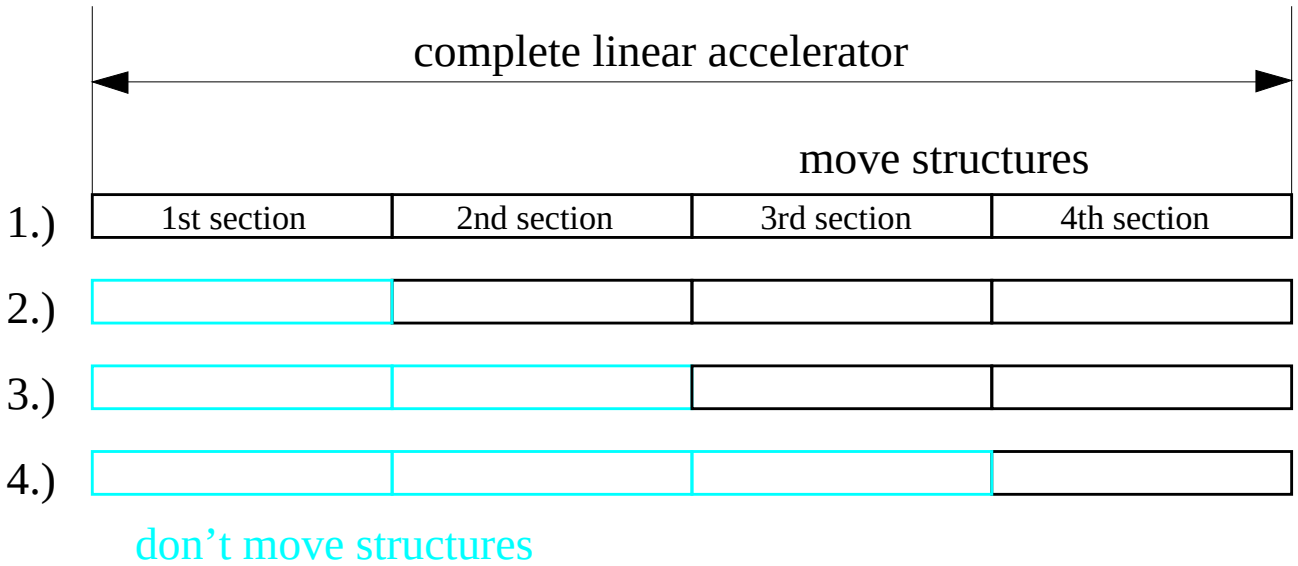

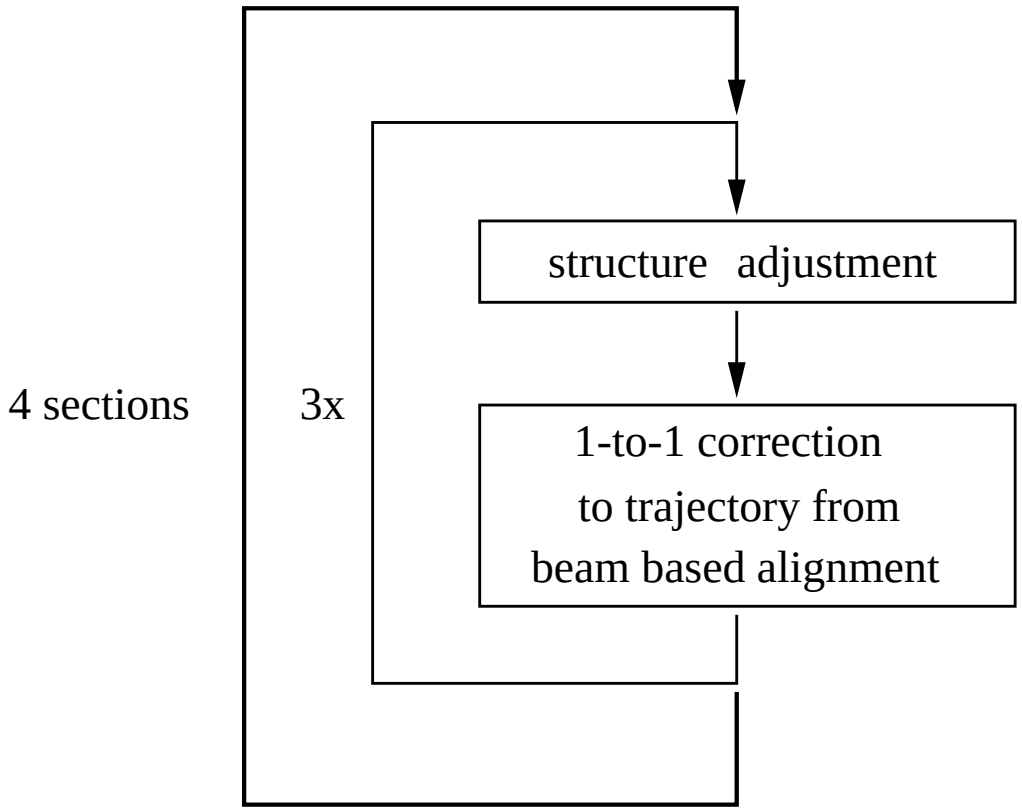

Fig. 4.6 Procedure for active structure adjustment. The accelerator is divided into several sections in order to confine manipulation of the structure positions to the regions of the machine where adjustment is still necessary. The structure adjustments alternate with reiterations of the trajectory to the trajectory found with the beam based alignment.

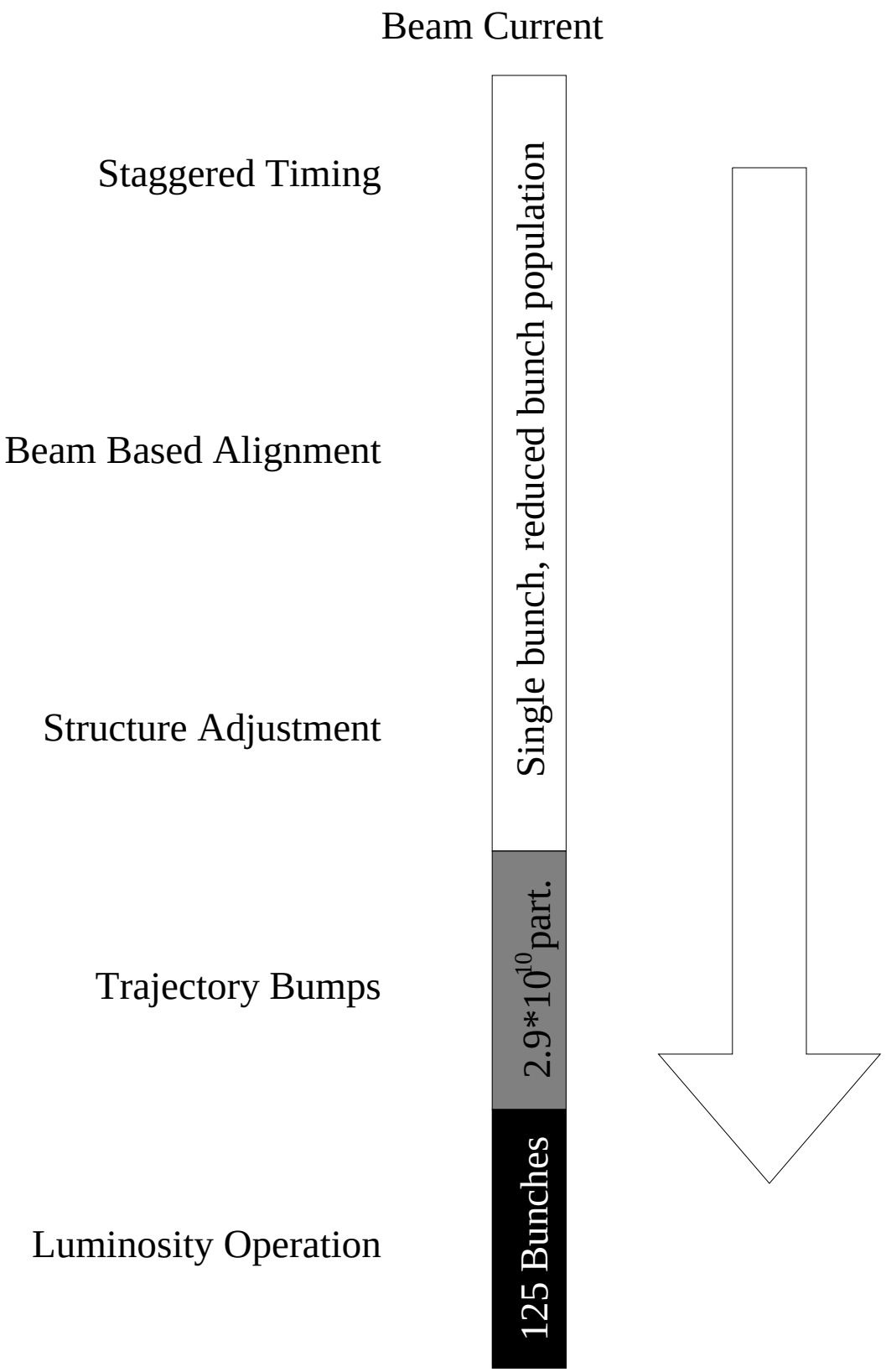

Fig. 4.7 Chronological order of the different stages of accelerator operation together with the corresponding beam current.

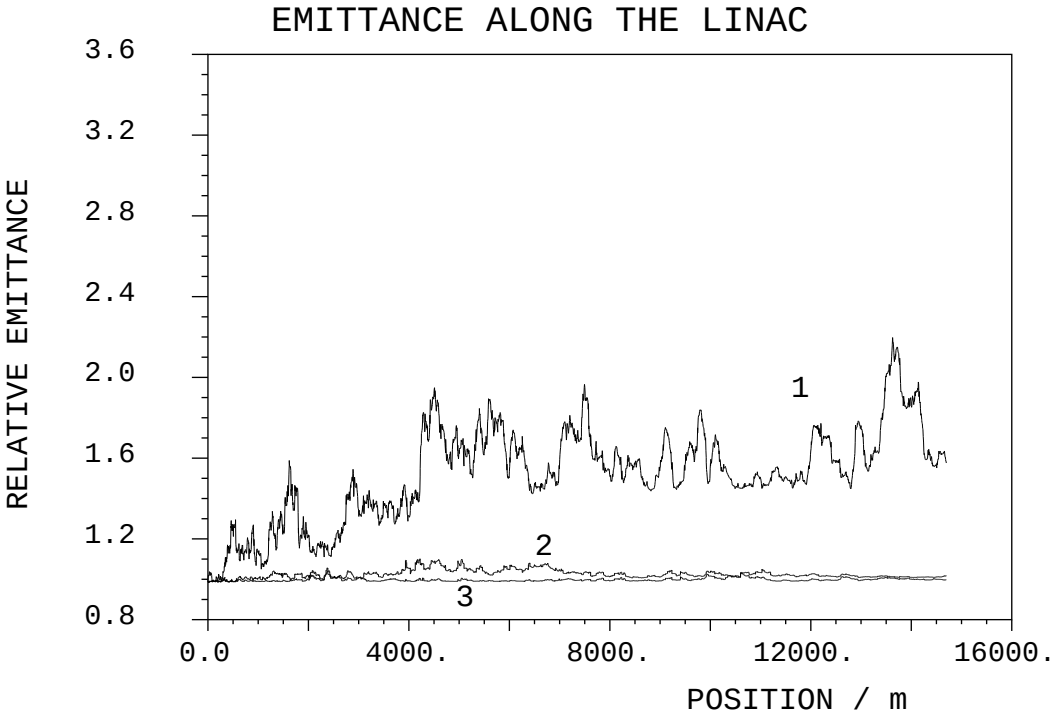

Fig. 4.8 Emittances for single-bunch operation with full bunch charge (1 bunch, 30 slices, $2.9 \cdot 10^{10}$ particles per bunch) after beam based alignment (1), structure adjustment(2) and bump adjustment(3).

Finally, one change had to be applied to the machine settings as compared with the assumptions made in chapter 2. There it had been assumed that the first 4 sectors of the machine were operated at an RF phase suitable for BNS-damping while the remainder of the machine was set to $-12°$ in order to reduce the single-bunch peak to peak energy spread. As emittance preservation considerations become more pressing with the inclusion of all single- and multi-bunch effects, we must raise the number of sectors operated with BNS-damping to 6 while the remaining 2 sectors are set to an RF phase of $-24°$ in order to reduce the energy spread. This change is modest and does not lead to any modifications of the emittance and trajectory correction methods described in chapter 2. It must be mentioned, though, that operating a sizeable fraction of this machine off the crest of the accelerating voltage constitutes a serious penalty in terms of machine efficiency. In comparison with a machine operated at the crest of the accelerating voltage, setting the last 2 sectors to $-24°$ brings about a reduction of the energy gain of 8.9GeV, corresponding to 490m of accelerating structure at an accelerating gradient of 17MV/m.

Fig. 4.8 and Fig. 4.9 are to give an example of the complete machine tuning procedure, showing the beam emittances obtained after several stages of the correction procedure. Compensation of the multi-bunch energy spread from beam loading with staggered timing was carried out beforehand. Fig. 4.8 shows the emittances for single-bunch operation along the linac after beam based alignment, after active structure adjustment and finally after adjustment of the ND-bumps. For the purpose of generating this comparison, the bunch charge was raised to its nominal value of $2.9 \cdot 10^{10}$ prior to calculating the emittance corresponding to each stage of the tuning procedure.

Likewise, Fig. 4.9 shows the emittances that would be found with operation at full beam current after the individual correction steps. A comparison of the two figures immediately

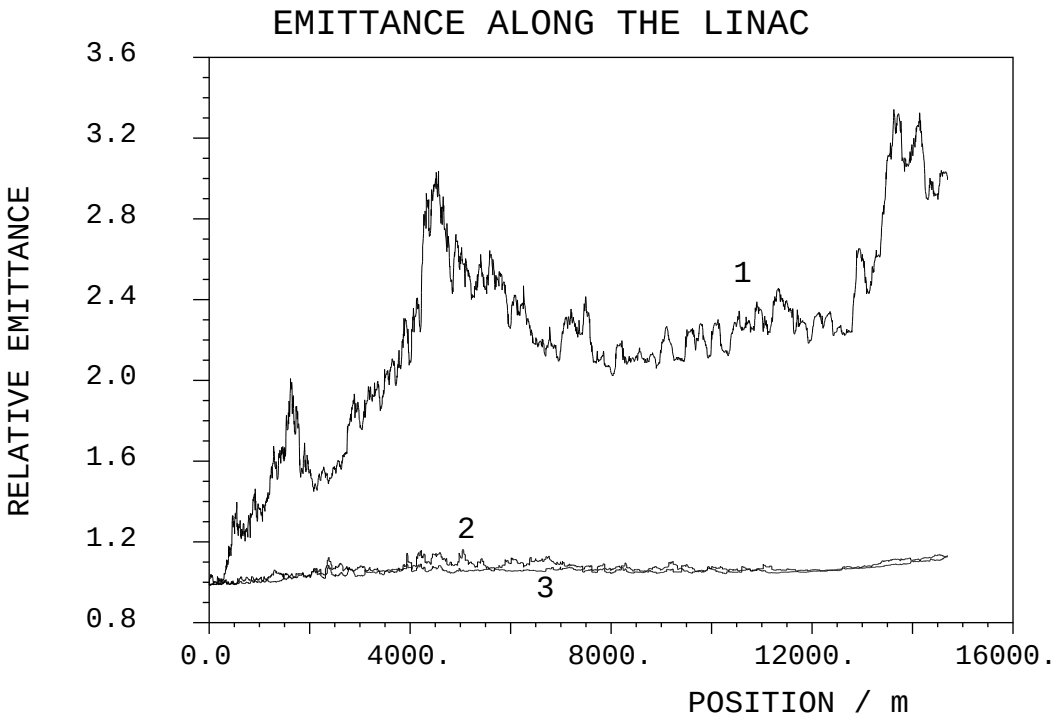

Fig. 4.9 Emittances of the full beam (125 bunches, 30 slices, $2.9 \cdot 10^{10}$ particles per bunch) after beam based alignment (1), structure adjustment(2) and bump adjustment(3).

reveals a large difference between the single-bunch emittance and the emittance of the full beam after orbit correction. This difference is caused by the superposition of the multi-bunch effects on the single-bunch dynamics of the beam, especially the long range transverse wake, beam loading and transverse kicks from the accelerating mode. As these effects act differently on each bunch in the bunch train, this additional contribution to the total emittance will not yield to emittance correction schemes (bumps), which confirms our previous assertion that satisfactory emittances cannot be achieved without active structure adjustment. Secondly, we find that the structure adjustment removes an overwhelming fraction of the emittance remaining after beam based alignment, leaving only modest opportunities for the bump optimization to achieve an emittance improvement.

As a final remark, it should be mentioned that this choice of tuning procedure is arbitrary in two points. The first arbitrary supposition lies in the assumption that the beam loading is not compensated locally. From this assumption it followed that the multi-bunch energy spread had to be compensated globally, and the accelerating voltages seen by the bunches over one structure assumed different patterns as shown in section 3.2. This assumption results in a comparatively large multi-bunch energy spread at some locations in the machine, bringing about a serious enhancement of the HOM-induced emittance growth. In addition, the differential transverse kicks from the accelerating mode in tilted structures contribute to the multi-bunch emittance. As an alternative, one might resort to removing the energy spread locally by ramping the output power of the RF sources and thus reducing the unloaded gradient for the first bunches in the train. Such a procedure has been suggested for instance in [40]. In several of the test accelerators for the collider studies being constructed currently, it is an aim to explore the feasibility of such a control of the klystron power. If in the near future experience from the test facilities should prove that a local compensation of the energy spread is practical, this would both hold the potential of providing a smaller multi-bunch energy spread with reduced implications for the

HOM-induced beam break-up, and of almost totally removing the differential kicks from the accelerating mode. As a consequence, emittance preservation in such a machine would become significantly easier. The assumption concerning generation and compensation of multi-bunch energy spread underlying our investigation must therefore be viewed as a worst case.

A second arbitrary assumption is the utilization of the non-dispersive bumps in order to achieve a final optimization of the emittance. Instead of adjusting the particle trajectory we might equally have moved the accelerating structures empirically, optimizing the emittance at several measurement stations along the machine with the same strategy that has been pursued for the ND-bumps. As with our assumptions the accelerating structures must be furnished with mover elements anyway, this alternative would not lead to any additional hardware requirements. Since the two methods hold the same potential in terms of emittance reduction, the choice can be made at a later time depending on which method turns out to be more convenient or practical.

4.3 Dependence on Machine and Beam Parameters

In chapters 2 and 3 we gave an account of the individual isolated effects relevant for the beam dynamics in a linear accelerator. Cures against emittance growth and energy spread were introduced and demonstrated, again as applied to individual effects. In section 4.1, then, we looked at the interaction of the multi-bunch effects with the single-bunch behavior of the beam. Finally, a complete procedure for machine tuning from turn-on to luminosity operation was devised in section 4.2. This enables us now to investigate the combined single- and multi-bunch beam dynamics and assess the effectiveness of the tuning procedure.

In addition, we will give a survey of how the most important design parameters influence the machine performance with regard to emittance preservation and discuss the response of the machine to perturbing effects. The goal of our investigation of the machine parameters will be to keep the growth of the normalized beam emittance within a range of 30%.

There are several assumptions that will be used throughout all of these investigations. First, we will always assume the lattice described in appendix D with a scaling of the beta function with the square root of the beam energy and 90° betatron phase advance per FODO cell. Moreover, we will always include the effect of beam loading in our simulations. In this context, we assume an unloaded accelerating gradient of 21MV/m and a compensation of the multi-bunch energy spread by staggered timing. The structure parameters describing the beam loading behavior are the same as in section 3.2. For the RF phases in the accelerating structures we always use the value of 4°, giving optimum BNS damping, in the first 6 sectors of the machine and $-24°$ in the remaining two sectors. The RF phases in the first 4 structures are again set to a value of 90°. The kicks from the accelerating mode in tilted structures will always be included in the simulations. As Greens functions for the convolution of the short range wake potentials we use the monopole and dipole wake described in appendix D.3. The long range dipole wake is generated from the dipole modes as calculated by [36] and [37] (Fig. 3.3), and the modes are detuned over a range of 36MHz in 10 classes as outlined in section 3.3.2. For the beam we will generally assume a bunch train consisting of

- 125 bunches with
- $2.9 \cdot 10^{10}$ electrons per bunch and a
- bunch spacing of 4.8m.

beam parameters	
bunches	125
slices	30
subslices	1
alignment parameters	
σ_{struc}	
σ_{quad}	
σ_{BPM}	
σ_{res}	
σ_{tilt}	
inj. offs.	10μm
***HOM* parameters**	
Q	
Δf_{range}	36MHz
acceleration	
bl/st	yes
varied	Q

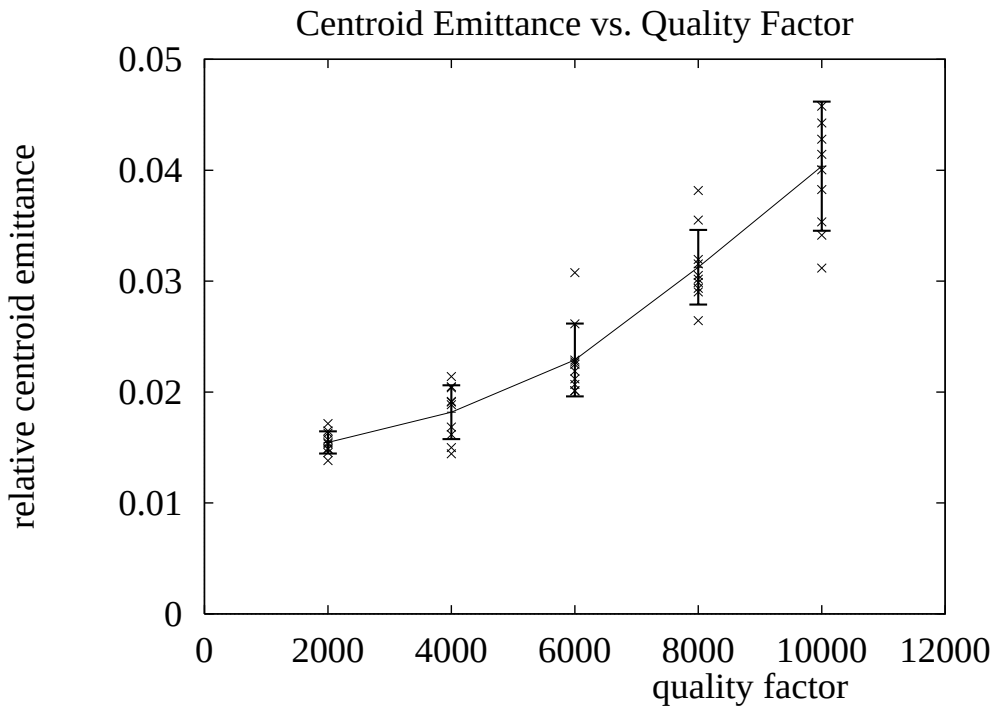

Fig. 4.10 Relative centroid emittances from injection offset for different quality factors of the dipole modes.

The bunches of the bunch train are modeled with 30 slices and there is no further division of the slices into subslices. Finally, the BPM resolution, unless stated otherwise, will always have a value of $\sigma_{res} = 5\mu$m.

In our investigation of the impact of machine and beam parameters on the emittance and on the energy spread we will conduct simulations of the beam dynamics for different values of these parameters. For each of these different parameter values the results obtained from 10 different random seeds for machine misalignment, dipole mode detuning and fluctuations of beam and machine parameters are given.

4.3.1 Quality Factor of the Deflecting Modes

The first and most important design parameter to be looked at is the quality factor of the dipole modes, which had already been discussed in chapter 3, especially in sections 3.3.3 and 3.3.7. In section 4.1.4 we had seen that apart from the conventional multi-bunch emittance growth discussed in chapter 3 the deflecting modes will also bring about an additional dilution of the single-bunch emittances, which will make the *HOM*-induced emittance growth still worse than anticipated from our multi-bunch simulations. Hence, it will become even more important to damp the quality factors of the dipole modes. We now want to see how the beam emittance depends on the quality factors if both single- and multi-bunch effects are included in the simulation.

First, we considered the emittance growth after injection of the beam with an offset of 10μm at a beta function of $\beta = 20.8$m. The machine elements were assumed to be aligned ideally along the machine axis. Fig. 4.10 shows the centroid emittances found with the above assumptions for quality factors of the dipole modes ranging from $Q = 2000$ to $Q = 10000$. The observed emittances are hardly different from the ones found in section 3.3.7. Indeed, for exhaustive use of BNS damping the emittances found in the multi-bunch case with beam

beam parameters	
bunches	125
slices	30
subslices	1
alignment parameters	
σ_{struc}	(i) 100μm
σ_{quad}	100μm
σ_{BPM}	100μm
σ_{res}	5μm
σ_{tilt}	(i) 23.6μrad
inj. offs.	
***HOM* parameters**	
Q	
Δf_{range}	36MHz
acceleration	
bl/st	yes
varied	Q

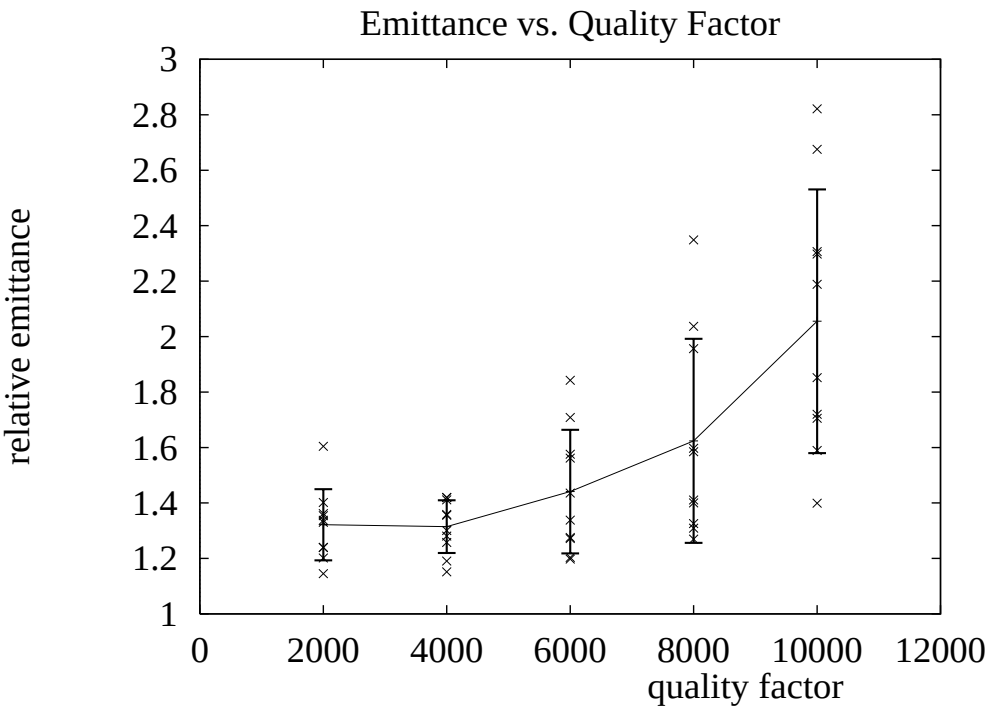

Fig. 4.11 Relative emittances in a misaligned machine after tuning procedure for different quality factors of the dipole modes.

loading had been considerably larger than the single-bunch emittances found in section 2.2. We conclude that in presence of BNS damping the growth of the beam emittance is dominated by the filamentation due to the multi-bunch energy spread or, at large quality factors of the higher order modes, by the effect of the long range wake.

Next we looked at the emittance growth caused by misalignments of the machine elements. It was assumed that the accelerating structures and quadrupoles were misaligned with an rms of 100μm with respect to the machine axis. In addition, the structures were given a random tilt of 23.6μrad rms. The BPM's were assumed to be misaligned with respect to the quadrupoles with an rms of 100μm. This machine was adjusted using the tuning procedure described in section 4.2. The beam emittances obtained for the full bunch train after machine tuning for different values of the quality factor are shown in Fig. 4.11. For quality factors exceeding $Q = 4000$ we notice a substantial increase of the emittance, caused by the long range wake field. The mean relative emittance growth found at $Q = 2000$ is $(32 \pm 13)\%$. At $Q = 10000$ this emittance growth has reached a magnitude of $(106 \pm 48)\%$. It should be mentioned that the random seeds for $Q = 2000$ have produced one exceptional relative emittance value of 1.6. However, the mean values of the emittances at $Q = 2000$ and $Q = 4000$ show no conclusive difference.

The results obtained from the simulation of a misaligned machine support the conclusion that, with the assumptions made, the quality factors of the dipole modes must not exceed a value of $Q = 4000$.

4.3.2 BPM Resolution

In section 2.3 we had looked at a variety of orbit correction techniques in order to establish a smooth beam trajectory eliminating the emittance growth induced by quadrupole misalignments and the resulting orbit distortions. Apart from the trajectory distortions from quadrupole misalignments, the necessity for orbit correction also arose from the transverse kicks in tilted

beam parameters	
bunches	1/125
slices	30
subslices	1
alignment parameters	
σ_{struc}	(i) 100μm
σ_{quad}	100μm
σ_{BPM}	100μm
σ_{res}	
σ_{tilt}	(i) 23.6μrad
inj. offs.	
HOM parameters	
Q	2000
Δf_{range}	36MHz
acceleration	
bl/st	yes
varied	σ_{res}

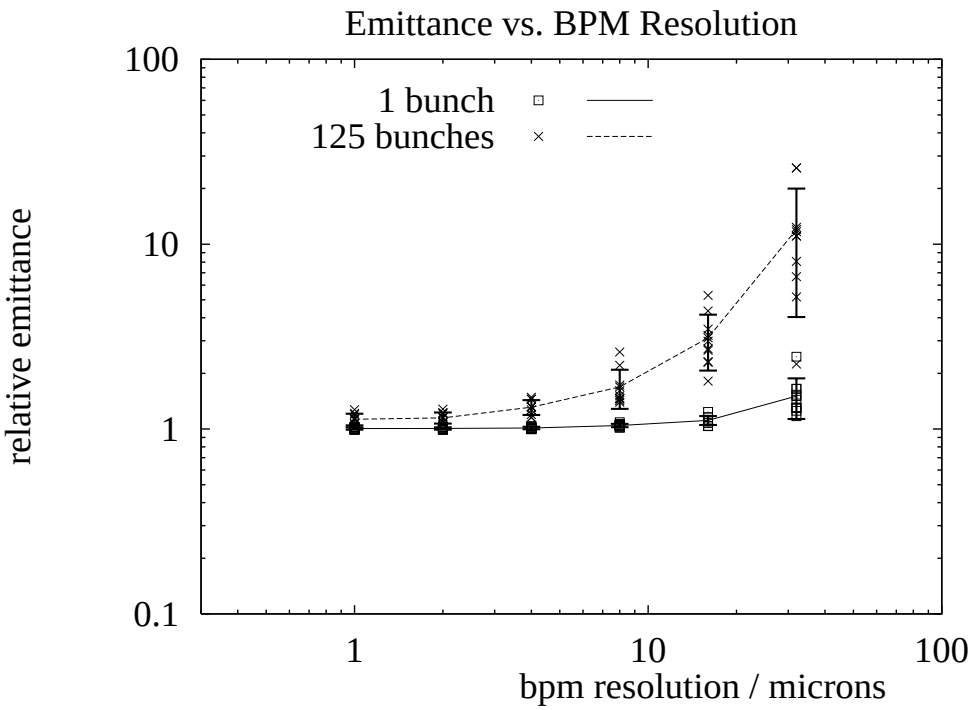

Fig. 4.12 Beam emittances in a misaligned machine after correction procedure for different values of the BPM resolution. Shown are both the emittances that would be obtained at single-bunch operation and the emittances found for operation with trains of 125 bunches.

accelerating structures. In the course of the simulations of sections 2.3.2 and 3.3.7 we had found that the Wake-Free correction technique [29] is capable of finding a sufficiently smooth orbit and eliminating a large fraction of the single- and multi-bunch emittance growth associated with orbit distortions of all origins. As a consequence, the machine tuning procedure suggested in section 4.2 necessarily included the Wake-Free orbit correction in order to generate a smooth particle trajectory and provide a reference for the following correction steps. As this correction technique primarily removes the variation of the trajectory with changes of individual quadrupole strengths, the performance of this method is largely determined by the available BPM resolution. It follows that by influencing the resulting smoothness of the trajectory this parameter also affects the result of the following correction steps and finally exerts a decisive influence on the overall quality of the complete tuning procedure. Moreover, the BPM resolution directly affects the performance of the active structure adjustment. There, the adjustment of structure axes to the observed beam trajectory alternates with a One-to-One correction of the beam to the BPM readouts determined during the beam based alignment. This reiteration of the beam trajectory is performed with an error which is given by the BPM resolution. It follows that between successive adjustment steps the beam trajectory will move randomly with an rms amplitude roughly equal to this BPM resolution. These considerations make clear that the resolution of the BPM's is one of the most decisive parameters of the overall machine design in that it will have a most crucial influence on the effectiveness of the whole tuning procedure and the resulting beam quality.

In order to judge the effect of the BPM resolution on the achievable final beam emittance we carried out an investigation that is remotely similar to the one in section 2.3.2. Here we assumed a machine in which the accelerating structures and quadrupoles were misaligned with an rms of 100μm from an ideal machine axis. The BPM centers were misaligned with respect to the quadrupole centers with an rms of 100μm and the accelerating structures were given a

random tilt of 23.6μrad. For the dipole modes we assumed a uniform quality factor of $Q = 2000$. This machine was subjected to the full tuning procedure outlined in section 4.2 for values of the BPM resolution ranging from 1μm to 32μm rms. Finally, the beam emittances for a single bunch and for a beam consisting of 125 bunches were calculated for the tuned machine.

In contrast to the investigation carried out in section 2.3.2, the BPM resolution will manifest its influence at several stages of the tuning procedure. The most obvious effect will be the smoothness of the beam trajectory as determined by the beam based alignment procedure. Next, as this orbit will be the reference for the active structure adjustment, the remaining structure tilts after adjustment will depend on the trajectory slopes remaining after beam based alignment. Furthermore, the orbit fluctuations generated by the orbit corrections between structure adjustments will reduce the alignment precision.

Fig. 4.12 shows the emittances at single-bunch operation and at operation using a complete bunch train consisting of 125 bunches after completion of the correction procedure versus the BPM resolution. We find that the single-bunch emittance is affected rather modestly by the resolution. Even for a BPM resolution of 32μm, the correction steps following the orbit correction - active structure alignment and adjustment of the ND-bumps - manage to keep the emittance growth at a mean value of $(51 \pm 37)\%$. A BPM resolution of 16μm, yielding a mean growth of the single-bunch emittance of $(11 \pm 6)\%$ might appear sufficient. For a complete bunch train consisting of 125 bunches, however, we observe a very clear increase of the emittances with larger values of the resolution. There we find that for a BPM resolution of 4μm the total emittance increases by $(29 \pm 13)\%$ on average, which is just about the emittance growth we want to allow for. The relative emittances found for larger values of the BPM resolution are not satisfactory, reaching a mean value of $(1200 \pm 800)\%$ for a BPM resolution of 32μm. From this consideration it follows that to enable a satisfactory machine adjustment the accelerator should be equipped with beam position monitors with a resolution of 4μm at each quadrupole.

A very similar, though slightly stronger requirement can be deduced from a different consideration. It is known that slow inelastic ground motions [46] and elastic vibrations in the tunnel continuously generate small new displacements of the machine elements. In particular, the displacement of quadrupoles will bring about a distortion of the actual beam orbit from the desired trajectory, leading both to a transverse jitter of the beam spot at the interaction point and to an additional emittance growth along the linac. As both effects tend to reduce the available luminosity, this vibration induced beam motion must be counteracted. For the high frequency component of the vibrations this may be achieved by active stabilization of the quadrupoles [48]. The low frequency component of the transverse beam motion, however, will have to be eliminated by continuously steering the beam back to the orbit as determined in the course of the tuning procedure. This trajectory maintenance is done with a limited accuracy, which is determined by the resolution of the beam position monitors. As a consequence, trajectory maintenance causes an additional contribution to the emittance growth.

In order to get a picture of the magnitude of this effect, we considered an ideally aligned machine on which we carried out a One-to-One trajectory correction on all quadrupoles, thus including also the defocusing ones. For this correction we assumed a BPM resolution of 5μm.

Fig. 4.13 shows the centroid emittances of a full beam of 125 bunches per pulse for a simulation including both single- and multi-bunch effects after this correction versus the quality factor of the dipole modes. For a quality factor of $Q = 2000$ for the dipole modes we get a mean relative centroid emittance of $(11.6 \pm 5.9)\%$, increasing to a mean value of $(14.4 \pm 9.4)\%$ at $Q = 10000$. If we want to confine this additional emittance contribution to a value below 6% this restricts the required BPM resolution to 3.6μm and 3.2μm respectively. These values get along well with the requirements derived from the simulations of the tuning procedure.

It is our conclusion that, depending on the quality factors of the dipole modes, a BPM

beam parameters	
bunches	125
slices	30
subslices	1
alignment parameters	
σ_{struc}	
σ_{quad}	
σ_{BPM}	
σ_{res}	5μm
σ_{tilt}	
inj. offs.	
***HOM* parameters**	
Q	
Δf_{range}	36MHz
acceleration	
bl/st	yes
varied	Q

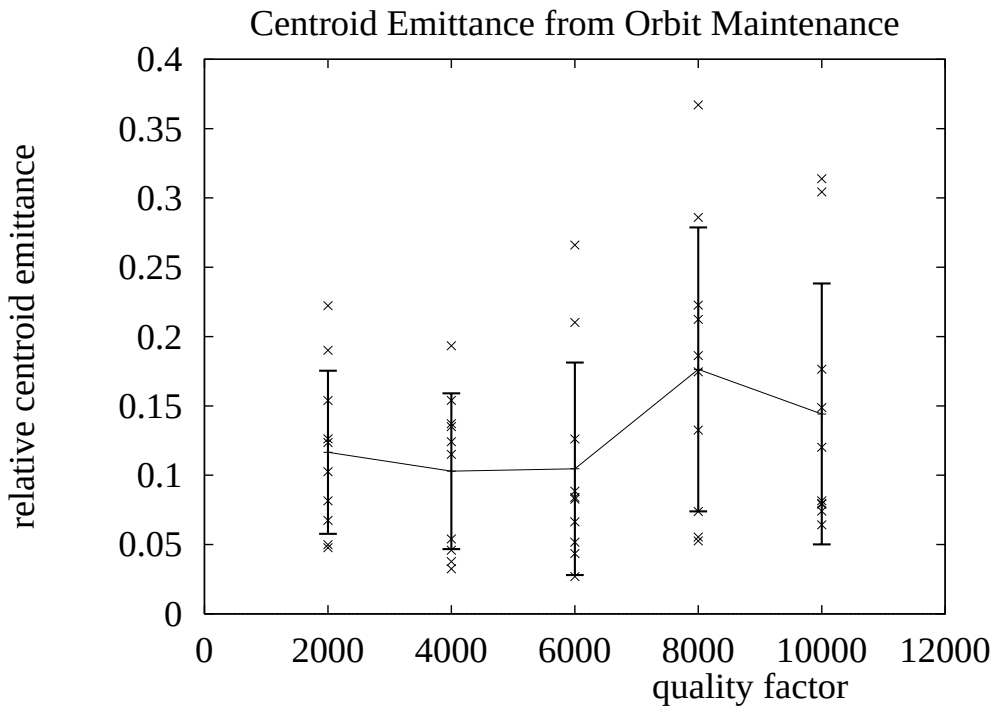

Fig. 4.13 Additional emittance contribution from finite BPM resolution after orbit reiteration for different quality factors of the dipole modes.

resolution between 3μm and 4μm will be appropriate for both establishing a machine condition capable of preserving a sufficiently small emittance and then maintaining the beam trajectory over a longer period.

4.3.3 Charge Fluctuation

In this section we shall look at the influence of fluctuations of the bunch populations on the emittance and the energy spread in the beam. A similar investigation was already carried out in section 3.5.2, where we simulated the aggravation of the multi-bunch emittance growth and the increase of the multi-bunch energy spread as a consequence of charge fluctuation. Here we will essentially address the same issue, this time however with regard to the combined single- and multi-bunch dynamics in the machine.

There are several mechanisms by which fluctuations of the bunch population will affect the beam emittance. The first mechanism acts through the single-bunch behavior: the deflection of particles in the bunch by transverse wake fields scales proportionally with the bunch charge, as does the energy spread induced by the short range monopole wake. The contribution to the energy spread generated by the phase of the accelerating mode along the bunch remains constant. It follows that the balance between chromatic and wake field effects established by BNS damping is perturbed, and hence transverse kicks on the bunches acquire a greater tendency to filament. Secondly, at low quality factors of the deflecting modes, the steady state of the particle deflections encountered at the end of the bunch train is disturbed by the nonuniformity of the mode excitations from the different bunches, leading to an enhancement of the *HOM*-induced multi-bunch emittance growth. Furthermore, the different bunch charges lead to an additional contribution to the multi-bunch energy spread, which in turn brings about a perturbation of the previously mentioned steady state. At the same time, the additional spread of the accelerating voltages affects the deflection strengths by the accelerating mode in

beam parameters	
bunches	125
slices	30
subslices	1
alignment parameters	
σ_{struc}	(i) 100μm
σ_{quad}	100μm
σ_{BPM}	100μm
σ_{res}	5μm
σ_{tilt}	(i) 23.6μrad
inj. offs.	
***HOM* parameters**	
Q	2000
Δf_{range}	36MHz
acceleration	
bl/st	yes
varied	σ_q

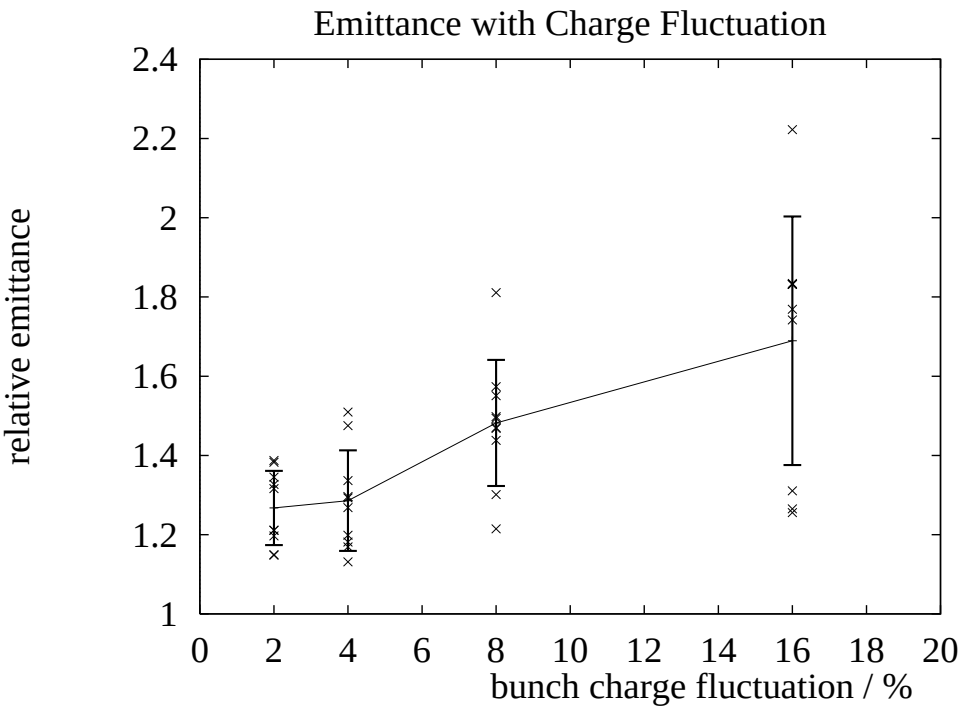

Fig. 4.14 Impact of population fluctuations on the emittance in a misaligned machine after tuning procedure.

a tilted cavity. Again, in absence of charge fluctuations this effect would reach a steady state after one filling time of the structure. This steady state will now be perturbed. All of these effects will cause an additional increase of the emittance growth over what would have been expected in the ideal case. Apart from that, the energy spread in the beam becomes larger.

First, we investigated the effect of charge fluctuations on the emittance growth from misalignment of the machine elements. Specifically, we assumed a random misalignment of 100μm rms for the structures and quadrupoles with respect to the machine axis and for the BPM's with respect to the centers of the quadrupoles. Furthermore, we assumed a random tilt of the accelerating structures of 23.6μrad. The machine was subjected to the full machine tuning procedure as described in section 4.2, comprising staggered timing of the klystrons, orbit correction, active structure adjustment and non-dispersive bumps. Then, the motion of a bunch train through the machine was tracked. The mean bunch population was $2.9 \cdot 10^{10}$ particles per bunch and the deviations of the bunch charges were assumed to have a Gaussian distribution with the standard deviation σ_q. The charge deviations of the different bunches were not correlated. Finally, for the dipole modes a uniform quality factor of $Q = 2000$ was used for simulation of the *HOM*-induced particle deflections. The result of this simulation can be seen in Fig. 4.14, which shows the full beam emittances, comprising both self emittance and centroid emittance, for random charge fluctuations of the bunches ranging from 2% rms to 16% rms. In contrast to what had been observed in section 3.5.2, we now find that also smaller charge fluctuations can result in a visible deterioration of the beam emittance by the end of the machine. At a fluctuation magnitude of 4% we find a mean growth of the total emittance of $(28.6 \pm 12.7)\%$, which increases to a value of $(68.9 \pm 31.3)\%$ for 16% charge fluctuation.

An equivalent examination was conducted for the case of emittance growth from injection offset. Here we assumed an ideally aligned machine in which the beam was injected with an offset of 10μm at a beta function of $\beta = 20.8$m. The only correction which had to be applied was to eliminate the multi-bunch energy spread from beam loading by staggered timing of the

beam parameters	
bunches	125
slices	30
subslices	1
alignment parameters	
σ_{struc}	
σ_{quad}	
σ_{BPM}	
σ_{res}	
σ_{tilt}	
inj. offs.	10μm
***HOM* parameters**	
Q	2000
Δf_{range}	36MHz
acceleration	
bl/st	yes
varied	σ_q

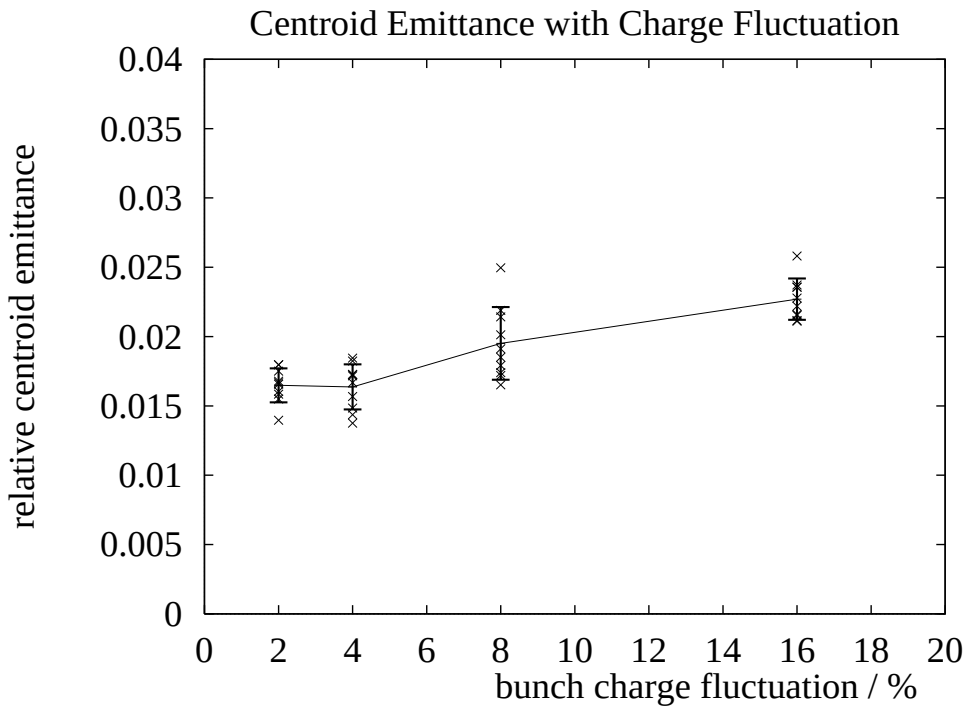

Fig. 4.15 Relative centroid emittances from injection offset for different magnitudes of the fluctuation of the bunch charges.

klystrons. The assumptions on the beam current were as before for the case of the misaligned machine. The outcome of this simulation differs only little from what had been found in the multi-bunch case. Fig. 4.15 shows that the mean centroid emittance increases only little even for large magnitudes of charge fluctuations. It follows that in any case the emittance growth from injection jitter is not a limiting effect as long as the injection jitter does not exceed its maximum allowable magnitude of 10μm.

Fig. 4.16 finally shows us the total energy spread encountered for different magnitudes of charge fluctuations. This energy spread contains both the intra-bunch energy spread from short range wakes and different RF phases of the accelerating mode and the multi-bunch energy spread from beam loading. For charge fluctuations of $\sigma_q = 16\%$ it reaches a magnitude of 0.6% rms. Similarly to what had been observed in the pure multi-bunch case, the energy spread increases only modestly as long as the charge fluctuation does not exceed 4%.

These observations drive us to express the requirements on the stability of the bunch charge in a more pressing manner than previously. The increase of emittance dilution from machine misalignments by charge fluctuations leads us to the requirement that the rms charge fluctuation does not exceed 4% instead of the 8% that would have been allowable judging from the pure multi-bunch calculations. If the tolerance of 4% can be met, the increase of the total energy spread of the beam also remains at a moderate level.

4.3.4 Longitudinal Jitter

Another perturbation of the beam dynamics that needs to be investigated is the longitudinal jitter of the bunches in the bunch train. Again, a similar investigation had been carried out earlier in section 3.5.1, where we considered the impact of the longitudinal position error on the multi-bunch emittance growth. We wish to reiterate this investigation, focusing now on the reaction of the full beam dynamics on longitudinal jitter.

beam parameters	
bunches	125
slices	30
subslices	1
alignment parameters	
σ_{struc}	
σ_{quad}	
σ_{BPM}	
σ_{res}	
σ_{tilt}	
inj. offs.	
***HOM* parameters**	
Q	2000
Δf_{range}	36MHz
acceleration	
bl/st	yes
varied	σ_q

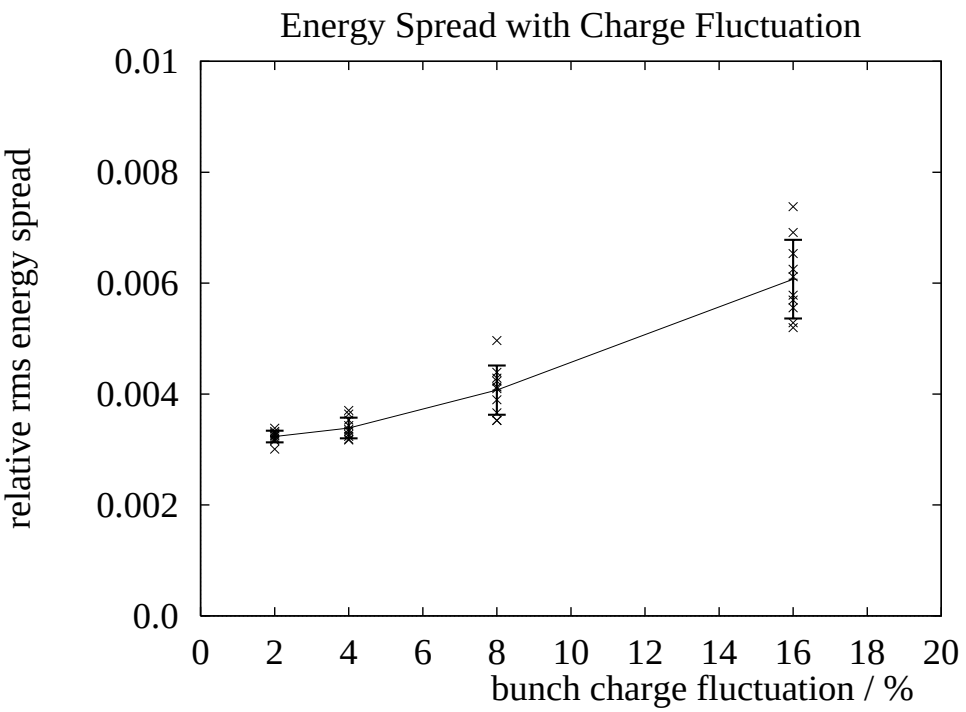

Fig. 4.16 Total rms energy spread of the beam for different magnitudes of charge fluctuations.

Very similar to fluctuations of the bunch populations, longitudinal jitter will affect the beam behavior by mechanisms relating both to single- and multi-bunch effects. As far as the pure single-bunch behavior is concerned, the longitudinal jitter will place the individual bunches on different phases of the accelerating voltage, where the efficiency of BNS damping is reduced. As a consequence, the tendency of transverse bunch motions to filament will be enhanced. Concerning the multi-bunch effects, we will obtain both a perturbation of the steady state of the *HOM*-induced particle deflections found at low quality factors of the dipole modes and an additional multi-bunch energy spread. This additional energy spread will in turn perturb the steady state of the *HOM*-induced particle deflections. It follows that longitudinal jitter has the potential of aggravating both the beam emittance and the energy spread.

Proceeding similarly as in the investigation of charge fluctuations, we considered the impact of longitudinal jitter on the emittance growth from injection offset in a perfectly aligned machine, on the emittance growth in a misaligned machine after correction and on the energy spread of the beam.

First, we simulated the influence of longitudinal jitter on the emittance growth from element misalignments in the accelerator. We assumed that the quadrupoles and accelerating structures were misaligned randomly with an rms of 100μm with respect to an ideal machine axis and the BPM's were misaligned with an rms of 100μm with respect to the quadrupole centers. In addition, the accelerating structures were given a random tilt of 23.6μrad rms. Then we carried out the machine tuning procedure as outlined in section 4.2, assuming a BPM resolution of 5μm. The quality factors of the dipole modes causing the long range dipole wake are assumed to have a uniform value of $Q = 2000$.

After completion of the correction procedure we simulated the emittance growth in the machine. Now the bunches were allowed to deviate randomly from their appointed longitudinal positions, which were separated by a distance of 4.8m. The longitudinal jitter was assumed to have a Gaussian density distribution with the standard deviation σ_s. The position errors of the different bunches were uncorrelated. Fig. 4.17 shows the full beam emittances, containing

beam parameters	
bunches	125
slices	30
subslices	1
alignment parameters	
σ_{struc}	(i) 100μm
σ_{quad}	100μm
σ_{BPM}	100μm
σ_{res}	5μm
σ_{tilt}	(i) 23.6μm
inj. offs.	
***HOM* parameters**	
Q	2000
Δf_{range}	36MHz
acceleration	
bl/st	yes
varied	σ_s

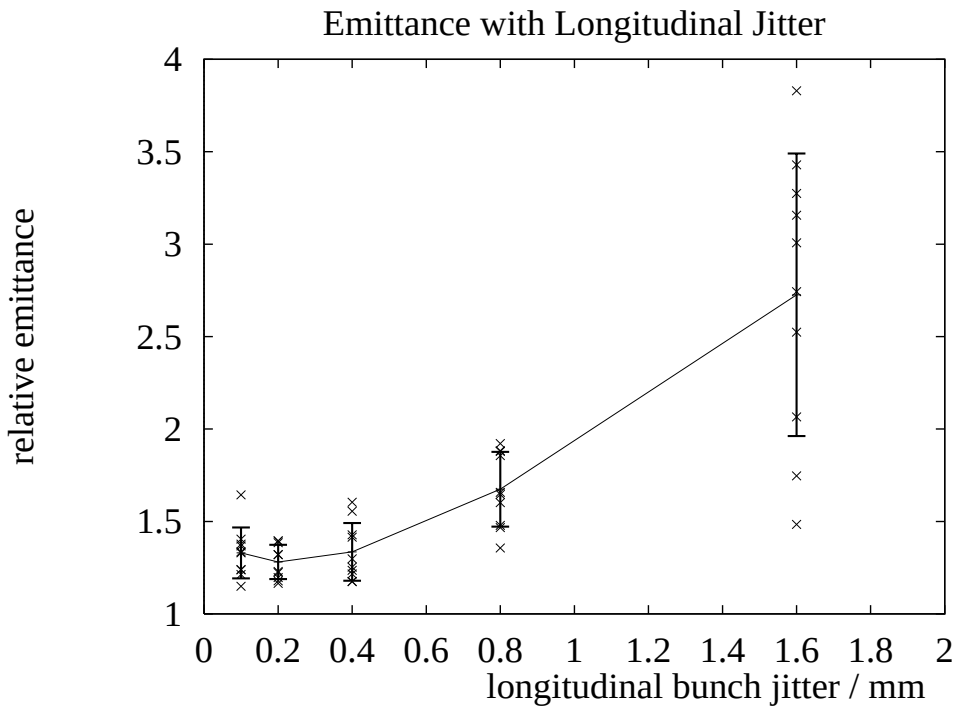

Fig. 4.17 Relative emittances in a misaligned machine in the presence of longitudinal jitter of the bunch positions.

both the self emittance and the centroid emittance, found with this procedure for different magnitudes of the longitudinal jitter, ranging from $\sigma_s = 0.1$mm to $\sigma_s = 1.6$mm. We see that the emittance changes little for jitter magnitudes up to $\sigma_s = 0.4$mm, where we find a mean emittance growth of $(34 \pm 16)\%$. At a jitter magnitude of 0.8mm we begin to see a decisive increase of the emittance growth to $(67 \pm 20)\%$ and at 1.6mm jitter magnitude, finally, the emittances have increased severely by $(173 \pm 76)\%$. We must point out that, although the random seeds produce an exceptional relative emittance value of 1.64 at a jitter of 0.1mm, the mean values of the emittances at 0.1mm and 0.2mm are not conclusively different.

Secondly, we turned to the emittance growth from injection offset at a perfectly aligned machine. The beam parameters were chosen as in the previous simulation. The injection offset was 10μm at a beta function of $\beta = 20.8$m. The centroid emittances resulting in this simulation are shown in Fig. 4.18. Again, the rms longitudinal jitter varies between 0.1mm and 1.6mm. Similarly to the case of the misaligned machine examined before, we find a modest increase of the emittances for jitter magnitudes up to 0.4mm, which turns into a significant aggravation for 0.8mm and finally grows strongly for a jitter magnitude of 1.6mm. Unlike the results found earlier in the scope of the multi-bunch simulations in section 3.5.1, The increase of the emittance after injection offset for large jitter magnitudes is such that it would become a limiting factor. At $\sigma_s = 1.6$mm we find a mean relative centroid emittance of $(8.5 \pm 1.6)\%$. As we want to restrict the emittance contribution from injection offset to 6% of the emittance at injection, the permissible injection offset for 1.6mm longitudinal jitter would be confined to 8.4μm. However, this limitation is hypothetical, since a longitudinal jitter of this magnitude is by no means acceptable.

The third issue that needs to be examined is the response of the energy spread in the beam to longitudinal jitter of the bunches. Fig. 4.19 shows the total rms energy spread in the beam for jitter magnitudes ranging from 0.1mm to 1.6mm. We find that already small jitter magnitudes immediately lead to a significant increase of the energy spread, reaching a mean value of 1.6%

beam parameters	
bunches	125
slices	30
subslices	1
alignment parameters	
σ_{struc}	
σ_{quad}	
σ_{BPM}	
σ_{res}	
σ_{tilt}	
inj. offs.	10μm
***HOM* parameters**	
Q	2000
Δf_{range}	36MHz
acceleration	
bl/st	yes
varied	σ_s

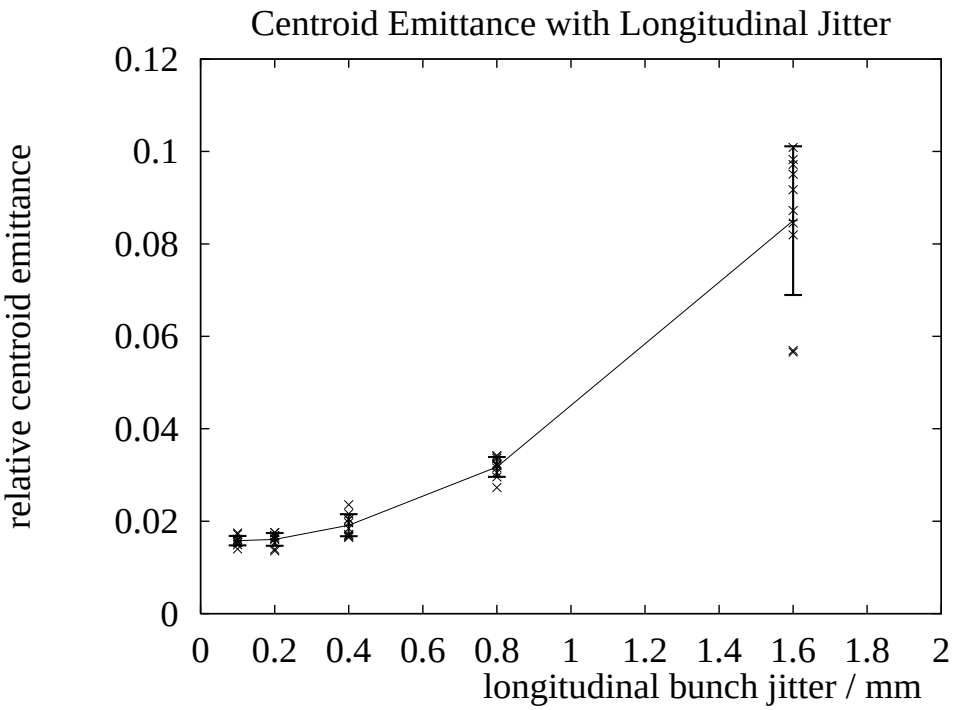

Fig. 4.18 Dependence of the relative centroid emittance from injection offset on longitudinal jitter of the bunches.

beam parameters	
bunches	125
slices	30
subslices	1
alignment parameters	
σ_{struc}	
σ_{quad}	
σ_{BPM}	
σ_{res}	
σ_{tilt}	
inj. offs.	
***HOM* parameters**	
Q	2000
Δf_{range}	36MHz
acceleration	
bl/st	yes
varied	σ_s

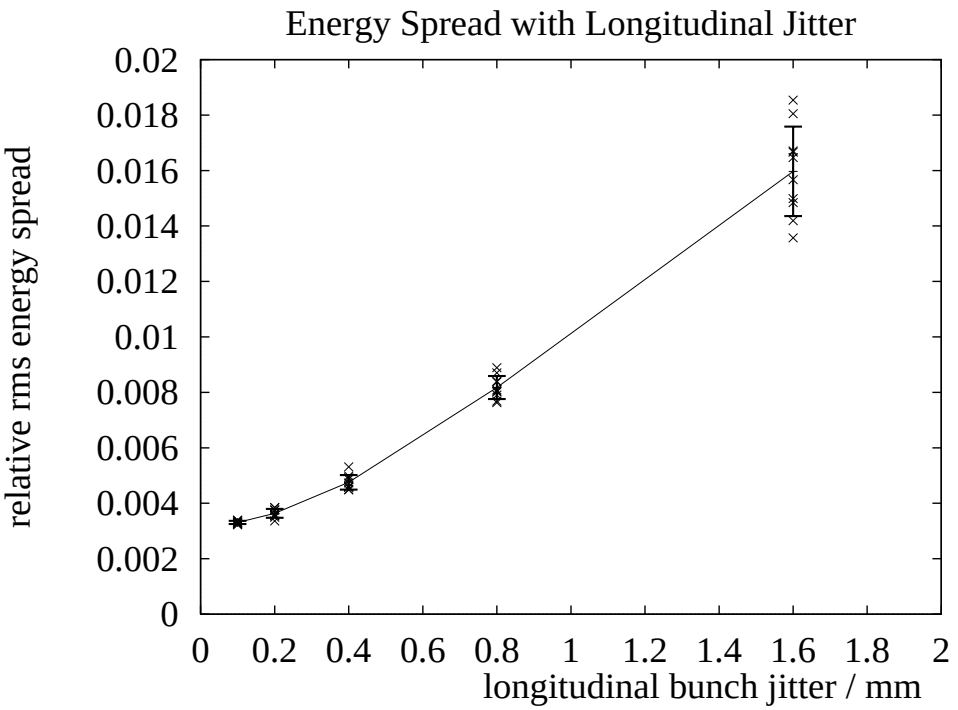

Fig. 4.19 Impact of longitudinal position jitter of the bunches on the energy spread in the beam.

rms for jitter magnitudes of $\sigma_s = 1.6$mm. Therefore, keeping the jitter as small as possible is essential to obtaining a small energy spread.

The nature of the development of the energy spread with the jitter magnitude essentially leads us to the same conclusion as earlier in section 3.5.1, that the rms longitudinal jitter must not exceed a value of 0.4mm and a jitter magnitude smaller than 0.2mm will be favorable for producing a small energy spread. The emittance dilution from machine misalignments will not change strongly as long as these requirements are met. A jitter tolerance of 0.2mm rms is not unreasonably tight, as similar requirements arise from issues relating to the interaction of the colliding beams in the final focus [45].

4.3.5 RF Phase Errors

In section 3.5.3 we had simulated the effect of errors of the RF phases in the accelerating structures on the multi-bunch dynamics. The results obtained there had suggested that this effect does not influence the multi-bunch emittance growth very strongly. Moreover, we had seen that these phasing errors are capable of generating an energy spread between different bunch trains and bring about a slight reduction of the final beam energies.

We now want to compare these results with the case of combined single- and multi-bunch simulations. While the implications of the phasing errors concerning the reduction of the final beam energy and the generation of an energy spread between different bunch trains remain the same, we may get an increase of the beam emittances. Ideally, the dilution of the single-bunch emittance would be suppressed by the application of BNS damping. There, the wake field effects are canceled to a large extent by the chromatic effect arising from an appropriate correlated energy spread along the bunch (section 2.2). This energy profile is established by setting the RF phases in the accelerating structures to suitable values. The perturbation of this state will enhance the tendency of transverse bunch motions to filament and hence lead to an increased emittance growth.

Again, we started by looking at a misaligned machine in which the accelerating structures and quadrupoles were misaligned randomly with respect to an ideal axis with an rms of 100μm. Moreover, the BPM's were misaligned with respect to the quadrupole centers by 100μm rms. The accelerating structures were tilted randomly with an rms of 23.6μrad. The misaligned machine was subjected to the full machine tuning procedure according to section 4.2. It was assumed that the dipole modes have a uniform quality factor of $Q = 2000$. Finally, the RF phases in the accelerating structures were given an uncorrelated random error with Gaussian density distribution and a standard deviation σ_φ. Fig. 4.20 shows the beam emittances found for phasing errors ranging from 1° to 8° rms. We see that for phasing errors up to 4° the emittance growth shows no conclusive response and remains at a mean value of $(30 \pm 12)\%$ even for a mean phasing error of 4°. Only at a phase error of 8° rms does the emittance growth increase to a mean value of $(54 \pm 41)\%$. As such a growth of the emittance was not observed in the pure multi-bunch calculations, this increase must be due to the single bunch effects outlined above.

Next we looked at the emittance growth caused by injection errors. Here we assumed an ideally aligned machine into which the beam was injected with a systematic offset of 10μm at a beta function of 20.8m. The centroid emittances resulting from this procedure are shown in Fig. 4.21. It turns out that the centroid emittances do not change in any conclusive fashion and remain well beneath the value of 6% of the self emittance that would have been tolerable.

We conclude that the aggravation of the emittance growth by errors of the RF phases remains tolerable if the magnitude of this error does not exceed 4° rms. This constraint originates in the response of the emittance dilution from machine misalignments to phasing errors.

beam parameters	
bunches	125
slices	30
subslices	1
alignment parameters	
σ_{struc}	(i) 100μm
σ_{quad}	100μm
σ_{BPM}	100μm
σ_{res}	5μm
σ_{tilt}	(i) 23.6μm
inj. offs.	
HOM parameters	
Q	2000
Δf_{range}	36MHz
acceleration	
bl/st	yes
varied	σ_φ

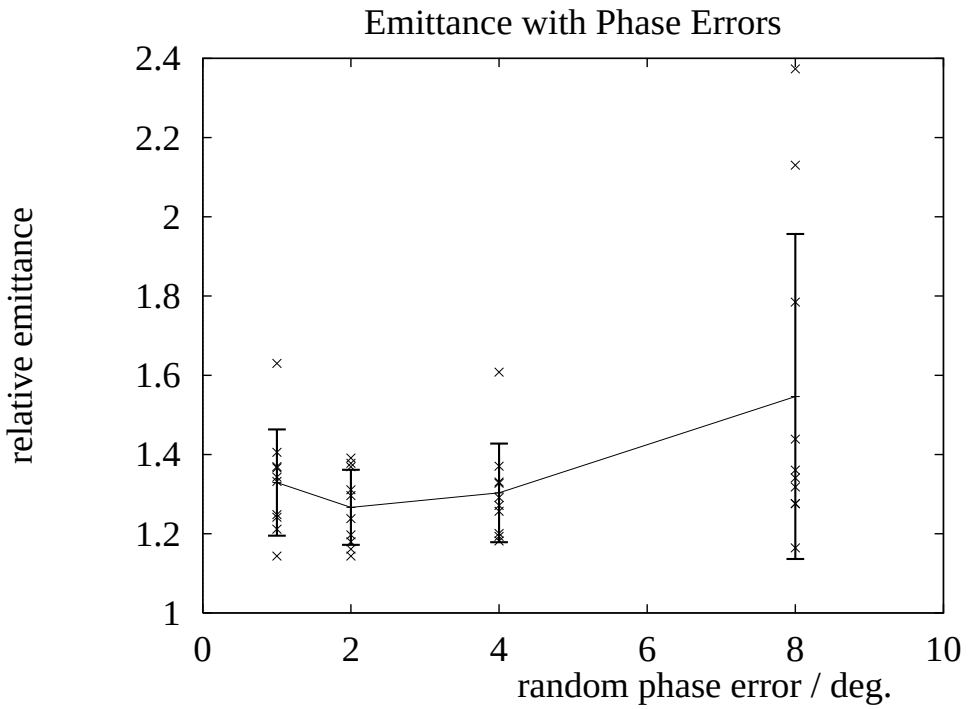

Fig. 4.20 Dependence of the relative emittance in a misaligned machine on phase errors of the accelerating voltage.

beam parameters	
bunches	125
slices	30
subslices	1
alignment parameters	
σ_{struc}	
σ_{quad}	
σ_{BPM}	
σ_{res}	
σ_{tilt}	
inj. offs.	10μm
HOM parameters	
Q	2000
Δf_{range}	36MHz
acceleration	
bl/st	yes
varied	σ_φ

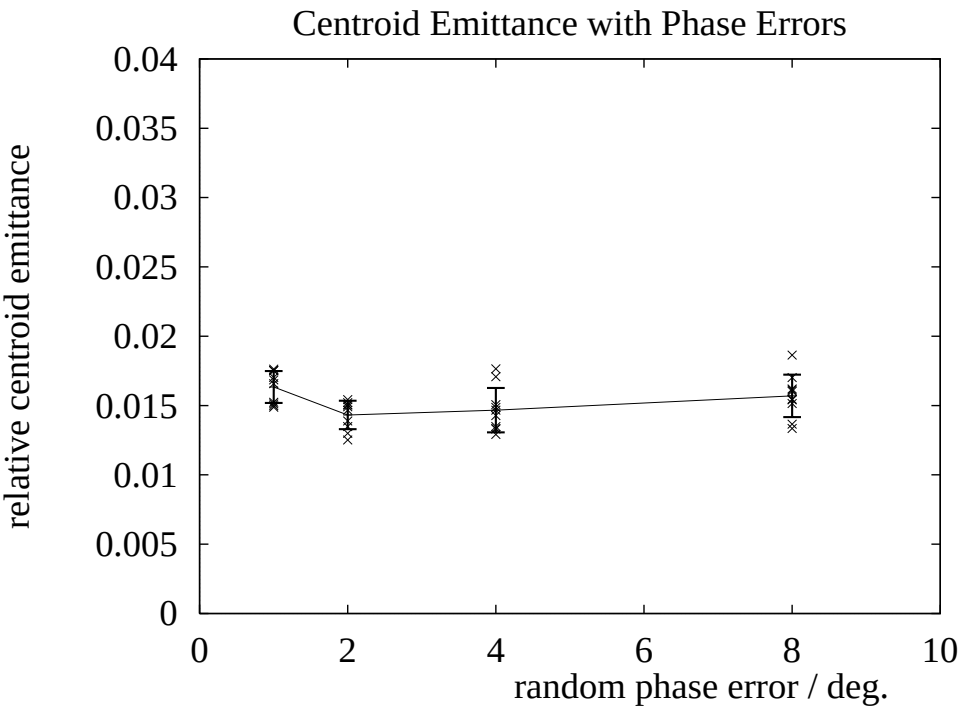

Fig. 4.21 Relative centroid emittances from injection offset with RF phase errors.

Chapter 5

Summary

In this document we have investigated a large variety of effects governing the behavior of a beam of particles in a linear accelerator. This investigation comprises both the simulation of effects affecting the beam quality and the evaluation of a number of corrective measures to ease these effects or their consequences. These examinations were first carried out separately in chapter 2 for the single-bunch dynamics and in chapter 3 for multi-bunch issues.

The essential processes driving the effects observed in section 2 were the deflection of particles by the short range transverse wake, and the filamentation due to the intra-bunch energy spread from the short range monopole wake and the RF phase of the accelerating mode with respect to the particles in the bunch. We have found an optimum operating point for BNS damping at an RF phase of 4°. Then, the emittance growth from structure and quadrupole misalignment has been studied and the merit of correction procedures as proposed in [29] (beam based alignment, trajectory bumps) was demonstrated.

In chapter 3 we looked at implications arising from the interaction of a multitude of bunches in a bunch train. During these investigations it was found that three effects have a decisive impact on the growth of the multi-bunch emittance. The first effect is the deflection of particles by TM-like dipole modes excited by bunches traversing an accelerating structure off axis. Second, there is the effect of beam loading, which by introducing an inter-bunch energy spread enhances the HOM-induced emittance dilution, causes filamentation and dispersion and in addition gives rise to a third effect, namely the emittance dilution from differential kicks by the accelerating mode in tilted structures. If the deflecting modes are suppressed by damping measures, the latter effect establishes the upper bound for the tolerable structure misalignment.

Then, in chapter 4 we have joined several correction measures to a complete tuning procedure capable of bringing a misaligned accelerator up to an operating condition enabling it to maintain a beam quality appropriate for experimental purposes. In the design of this tuning procedure, we have drawn on the experience with the individual correction measures as applied to individual effects that had been collected particularly in sections 2.2, 2.3.2, 2.4.2 and 3.2, comprising the application of BNS damping over a large fraction of the machine length, staggered timing, beam based alignment, active structure adjustment and non-dispersive bumps. The beam based alignment procedure required utilization of the Wake-Free correction scheme. During our investigation of the combined single- and multi-bunch dynamics it was our goal to restrict the growth of the normalized emittance to $\sim 30\%$ of its original value of $5.0 \cdot 10^{-7}$radm. Finally, a detailed investigation of the behavior of the combined single- and multi-bunch behavior with respect to variations of several machine and beam parameters was carried out.

In the course of the considerations made in chapters 2 to 4 we were able to establish a number of tolerances on alignment precisions of machine elements, on the allowable quality factors of deflecting modes, the performance and availability of diagnostic devices, and the

stability of beam parameters and machine settings. As these results are scattered over the range of a sizeable document, we consider it useful to give a short review of the final tolerances and design requirements and point out the effect or simulation which finally put the actual limit on a particular tolerance. The figures quoted in this context are to be understood for a machine that has been adjusted according to the tuning procedure suggested in section 4.2, which in turn is derived from the results obtained from several earlier sections.

BPM Resolution
The limitation on the allowable BPM resolution arises from simulations of the combined single- and multi-bunch behavior in section 4.3.2, where we had determined the resolution required for both establishing a sufficiently good machine state and then maintaining that state. Depending on the quality factor of the deflecting modes, we found that the BPM resolution required for trajectory maintenance ranges between 3.2μm and 3.6μm.

Active Structure Adjustment
We found two effects limiting the allowable final misalignment of the accelerating structures. At low quality factors for the deflecting modes, the emittance dilution from the transverse kick by the accelerating mode in tilted structures becomes dominant over the HOM-induced emittance dilution. Our considerations in section 3.4 restricted the maximum rms structure tilt to 13μrad, which had been tightened further to 7μrad when the single-bunch dynamics was included in section 4.1.2. A tilt of this magnitude would be generated if the ends of a 6m accelerating structure were misaligned independently with an rms of 30μm. At high values for the quality factors of the deflecting modes the allowable transverse misalignment of the structures with respect to the beam are dictated by the HOM-induced emittance dilution. At $Q = 10000$ for all dipole modes the tolerance on the mean structure offset reduces to 11μm.

Transverse Injection Jitter
Our results from section 3.3.3 suggest that the emittance growth associated with transverse injection offset of the beam is dominated by filamentation due to the multi-bunch energy spread at low quality factors of the deflecting modes and by HOM-induced beam break-up at high quality factors. Perturbing effects like charge fluctuation and longitudinal jitter were demonstrated to add a slight aggravation to this emittance growth. However, in order to limit the random motion of the beam spot at the interaction point, it is required that the injection jitter does not exceed a quarter beam height, which is 10μm at $\beta = 20.8$m. Under this restriction the growth of the centroid emittance from injection offset was found to be lower than 6% of the self emittance. This still holds when we introduced perturbing effects (charge fluctuations, longitudinal jitter) with magnitudes that would be tolerable in practical machine operation.

Qualtiy Factors of the Deflecting Modes
The quality factor of the deflecting modes is a parameter that determines the strength of the HOM-induced emittance growth decisively. The strongest manifestation of this effect is found in the emittance growth caused by misalignment of the machine elements. In theory, any emittance growth caused by machine misalignments could be removed by providing better alignment precision for the active structure adjustment. However, as only a limited precision for this adjustment seems practical, we have assumed an adjustment precision of 30μm independently for the ends of each accelerating structure during the machine tuning procedure. Under this assumption it was found that with the underlying tuning procedure a satisfactory emittance can be achieved for quality factors

of the deflecting modes of up to $Q = 4000$. The simulation leading to this result was presented in section 4.3.1.

Charge Fluctuations
Fluctuations of the bunch populations had been shown to affect the beam behavior in several ways. On one hand, the efficiency of BNS damping was reduced, as the the energy spread required for canceling the wake field effects depends on the bunch charge. This led to an increase of the single-bunch emittance growth. In addition, the steady state of the HOM-induced bunch deflections was perturbed. On the other hand, the energy spread within the bunch train was increased. The investigation of the combined single- and multi-bunch dynamics in section 4.3.3 revealed that for satisfactory emittance preservation the rms charge fluctuation must not exceed 4%. This requirement also is compatible with the production of a small energy spread.

Longitudinal Jitter
Longitudinal jitter of the bunches with respect to their nominal position affects the beam quality in a fashion that is very similar to the effects associated with charge fluctuations. The emittance dilution is enhanced by the deviation of the bunches from the optimum RF phase for BNS damping, and a perturbation of the steady state of the HOM-induced emittance growth encountered at low quality factors of the deflecting modes. The simulations from section 4.3.4 suggest that in order to keep a small energy spread the longitudinal jitter should not exceed a value of 0.2mm rms.

Phasing Errors
Similar to the effects from charge fluctuation and longitudinal jitter, phasing errors of the accelerating mode in the individual structures have the potential of enhancing the emittance growth and introducing an additional energy spread.

The simulations in sections 3.5.3 and 4.3.5 suggest that the emittance growth originates in the single-bunch dynamics and is due to the deviation from the conditions required for BNS damping. The energy spread caused by the phasing errors is not an energy spread within one bunch train, but a spread of the mean energies of different bunch trains, since we assumed that the phase errors are independent from shot to shot. The implications for the beam emittance found in section 4.3.5 lead to the recommendation that the phase errors must not be larger than 4° rms.

The alignment requirements on the machine elements are rather relaxed in comparison with designs aiming to operate at higher frequencies. Likewise, a BPM resolution of 3μm is larger than what will be needed in most other machine designs. Looser tolerances are only allowed for at TESLA, a proposal for an accelerator using superconducting accelerating structures, where the very large iris apertures lead to small wake fields and the modest focusing strength, combined with small energy spreads, cause comparatively small dispersive effects. Ways to damp the deflecting modes to low quality factors are currently being explored with great vigor. We therefore conclude that from the beam dynamics viewpoint the construction of a 2×250GeV linear collider operating in the S-band seems feasible.

Appendix A

Formula Symbols

B	magnetic induction
c_0	vacuum speed of light
D	electric displacement, dispersion
d_1, d_2	displacement parameters
$d_\perp$	field parameter (TE-like dipole modes)
E	electric field strength
e	elementary charge
f	frequency, focal length
H	magnetic field strength
H_D	pinch factor
$\mathbf{I}$	unit matrix
i	current
j	imaginary unit
$\vec{j}$	current density
K	focusing strength
k	loss parameter, focusing strength
L	length
$\mathcal{L}$	luminosity
$\ell_0 \ldots \ell_2$	expansion coefficients
$m_{xx} \ldots$	distribution moments
N_b	number of bunches in a bunch train
N_s	number of slices per bunch
N_{ss}	number of subslices per slice
N_W	relative simulation range for initial uncorrelated energy spread
N_σ	relative simulation range for longitudinal bunch coordinate
P	power
$P_0 \ldots P_2$	polynomials for trajectory expansion
p	momentum
$\wp$	$= j\omega + \sigma$, parameter of the Laplace transform
q	charge
Q	quality factor

R	radius
r	radius, shunt impedance per structure length
s	longitudinal coordinate along the bunch
t,T	times
$\mathbf{T}$	transfer matrix
t_{fill}	filling time of an accelerating structure
U	voltage
$\mathcal{U}$	field energy stored in a mode pattern
V	mode voltage, volume
$\mathcal{V}$	field integrals along $P_0 \ldots P_2$
v	velocity
v_g	group velocity
W	energy
$\mathcal{W}$	wake potential
$\mathcal{W}'_\perp$	distributed transverse wake potential
w	wake function
$\vec{\mathcal{X}}$	$= (x, x', y, y')$, four dimensional coordinate vector
x, y	transverse coordinates
z	longitudinal coordinate in the machine
α	alpha (Twiss) function, attenuation coefficient, detuning index
β	beta (Twiss) function, relativistic factor
γ	gamma (Twiss) function, relativistic factor
δ	momentum deviation
$\delta(t)$	δ-distribution:

$$\delta(t) = \lim_{T \to 0} \begin{cases} 0 & t < 0, t \geq T \\ 1/T & 0 \leq t < T \end{cases}$$

ϵ	emittance
ε_0	vacuum dielectric constant
κ	curvature
λ_β	betatron wavelength
μ_0	vacuum permeability
μ	betatron phase advance
ξ	chromaticity
θ	deflection angle
$\vartheta(t)$	step function:

$$\vartheta(t) = \begin{cases} 0 & t < 0 \\ 1/2 & t = 0 \\ 1 & t > 0 \end{cases}$$

ρ	charge density
σ_{BPM}	BPM alignment precision (rms)
σ_q	charge fluctuation (rms)

σ_{quad}	quadrupole alignment precision (rms)
σ_{res}	BPM resolution (rms)
σ_s	longitudinal jitter (rms)
σ_{struc}	alignment precision of accelerating structures (rms)
σ_x, σ_y	beam width, beam height (rms)
σ_z	bunch length (rms)
σ_φ	klystron phase error (rms)
τ	attenuation parameter
φ	RF phase
ψ	betatron phase
ω	angular frequency

General conventions:

- Matrices are written in boldface capital letters ($\mathbf{M}, \ldots$).
- Transposed matrices and vectors are indicated with a "t" ($\mathbf{M}^t, \ldots$).
- Vectors are indicated by an arrow ($\vec{v}, \ldots$).
- Mean values are denoted by a bar ($\bar{v}, \ldots$).
- The complex conjugate is indicated by an asterisk ($E^*, \ldots$).
- Derivatives with respect to time are denoted with a dot ($\frac{\mathrm{d}}{\mathrm{d}t}x = \dot{x}, \ldots$).
- Derivatives with respect to z are denoted with a prime ($\frac{\mathrm{d}}{\mathrm{d}z}x = x', \ldots$).
- At many occasions the mean values $\bar{x}$ and standard deviations σ_x of simulation results obtained from a number of different random seeds are presented in the form $\bar{x} \pm \sigma_x$.

Appendix B

The Parameter Panel

Numerous figures in this document are furnished with a panel showing the most important beam and machine parameters for the simulation. These parameter panels generally have the following appearance:

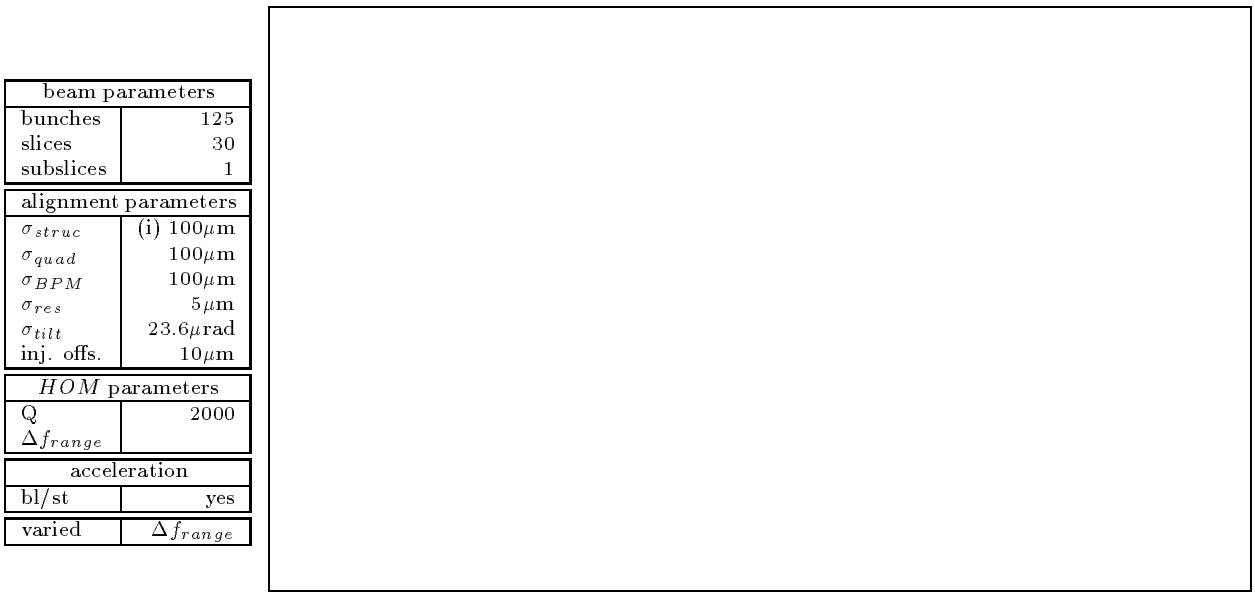

Fig. B.1 Typical appearance of the parameter panels in connection with figures showing simulation results.

This parameter panel shows information on the beam parameters, on the assumed misalignments, on the TM-like dipole modes, on the acceleration, and on the parameter that has been changed if a parameter scan has been conducted. In the field for the "beam parameters" the number of bunches per bunch train, the number of slices per bunch and the number of subslices per slice are given. The field for the "alignment parameters" contains the following entries:

σ_{struc}	rms magnitude of the random structure misalignment with respect to the machine axis.
σ_{quad}	rms magnitude of the random quadrupole misalignment with respect to the machine axis.
σ_{BPM}	rms magnitude of the random misalignment of the beam position monitors with respect to the quadrupole axes.
σ_{res}	BPM resolution, giving the rms magnitude of the random measurement errors of the beam position monitors.
σ_{tilt}	rms magnitude of the random tilt of the accelerating structures with respect to the machine axis.
inj. offs.	magnitude of the systematic injection offset.

The values in the fields σ_{struc} and σ_{tilt} may have the prefix "(i)". This prefix indicates that the quoted structure misalignment is assumed prior to an active adjustment of the structure axes to the measured beam position. The structure offsets with respect to the beam after this procedure may be considerably smaller that the quoted value.
The field for the "HOM parameters" shows the range over which the frequencies of the dipole modes are deliberately detuned and the quality factor assumed for these modes.
In the field labeled "acceleration" it is specified whether beam loading and correction of the energy spread with staggered timing are included ("bl/st yes") or a constant accelerating gradient is assumed ("bl/st no"). It is only used when trains of more than one bunch are simulated.
The field "varied" finally shows the parameter that has been changed if a parameter scan has been conducted.

Appendix C

Particle Optics

In this chapter we want to give a brief review of the fundamental concepts of linear charged particle optics. The purpose of this introduction is to acquaint the reader with the most fundamental parameters describing the properties of a beam and the machine lattice guiding its motion. For a more detailed description of the matter the reader is referred to other sources. Equally extensive and instructive accounts of the motion of charged particles in a lattice of accelerator elements can be found in [14], [49], [50] and numerous other sources on charged particle optics.

We will begin our review by a description of the transverse particle motion in the three most important elements of a linear accelerator. Then, we derive a differential equation describing the general particle motion in a linear accelerator. Finally, we will discuss the solutions to this equation for particles at design energy and the deviations of the transverse motion for particles with energies differing from the design energy.

Accelerating Structure

An accelerating structure is an element which transfers kinetic energy to charged particles by means of an electric field. The total energy gain, ΔW, of a particle after traversing the structure normalized to the elementary charge, e, is called the accelerating voltage $U = \Delta W/e$. The amplitude of the accelerating voltage divided by the structure length L is called the accelerating gradient. We investigate the transverse motion of a particle in an accelerating structure by starting from the conservation of the transverse momentum (no transverse forces present):

$$\Big(\beta^{rel}(z)\gamma^{rel}(z)x'(z)\Big)' = 0, \tag{C.1}$$

where $\beta^{rel}(z)$ and $\gamma^{rel}(z)$ denote the relativistic factors of the particle. Under the assumption that the accelerating force on the particle is constant along the structure, it can be shown that the transverse coordinates of a particle entering the structure with the transverse offset x_1 and the transverse slope x_1' are transformed into the coordinates x_2, x_2' at the end of the structure as

$$\begin{pmatrix} x_2 \\ x_2' \end{pmatrix} = \mathbf{T}_{acc} \cdot \begin{pmatrix} x_1 \\ x_1' \end{pmatrix} = \begin{pmatrix} 1 & \dfrac{\beta_1^{rel}\gamma_1^{rel}}{\gamma'} \ln \dfrac{\gamma_2^{rel}(1+\beta_2^{rel})}{\gamma_1^{rel}(1+\beta_1^{rel})} \\ 0 & \dfrac{\beta_1^{rel}\gamma_1^{rel}}{\beta_2^{rel}\gamma_2^{rel}} \end{pmatrix} \begin{pmatrix} x_1 \\ x_1' \end{pmatrix} \tag{C.2}$$

(see also [49]) where β_1^{rel}, γ_1^{rel}, β_2^{rel} and γ_2^{rel} are the relativistic factors at the beginning and at the end of the structure and $\gamma' = (\gamma_2^{rel} - \gamma_1^{rel})/L$ is the derivative of the relativistic factor. In our simulations we use the approximation $\beta^{rel} \approx 1$.

Later it will be convenient to use the normalized coordinates

$$\vec{x}_N = \begin{pmatrix} x_N \\ x_N^\dagger \end{pmatrix} = \sqrt{\beta^{rel}\gamma^{rel}} \begin{pmatrix} x \\ x' \end{pmatrix}. \tag{C.3}$$

We point out that the normalized trajectory slope $x_N^\dagger$ is not the derivative of the normalized transverse offset x_N with respect to the longitudinal coordinate z and therefore has been marked with a dagger instead of a prime. This will become relevant at a later instance. With the normalized transport matrix the normalized coordinates transform into

$$\vec{x}_{N2} = \mathbf{T}_{accN}\vec{x}_{N1} = \begin{pmatrix} \sqrt{\frac{\beta_2^{rel}\gamma_2^{rel}}{\beta_1^{rel}\gamma_1^{rel}}} & \frac{\sqrt{\beta_1^{rel}\beta_2^{rel}\gamma_1^{rel}\gamma_2^{rel}}}{\gamma'} \ln \frac{\gamma_2^{rel}(1+\beta_2^{rel})}{\gamma_1^{rel}(1+\beta_1^{rel})} \\ 0 & \sqrt{\frac{\beta_1^{rel}\gamma_1^{rel}}{\beta_2^{rel}\gamma_2^{rel}}} \end{pmatrix} \vec{x}_{N1}. \tag{C.4}$$

Thus, we have expressed the transport behavior with a transport matrix with $\det \mathbf{T}_{accN} = 1$.

Drift Space

A drift space is a region in which no external forces act on the beam. Conservation of the transverse momentum leads to

$$x''(z) = 0. \tag{C.5}$$

Therefore the transverse coordinates of a particle entering the drift space with the initial transverse offset x_1 and the transverse slope x_1' are transformed into [49]

$$\begin{pmatrix} x_2 \\ x_2' \end{pmatrix} = \mathbf{T}_{drift} \cdot \begin{pmatrix} x_1 \\ x_1' \end{pmatrix} = \begin{pmatrix} 1 & L \\ 0 & 1 \end{pmatrix} \begin{pmatrix} x_1 \\ x_1' \end{pmatrix} \tag{C.6}$$

where L is the length of the drift space.

Quadrupole Magnet

A quadrupole is a magnet in which the transverse magnetic induction varies linearly with the distance from the magnet axis as:

$$B_x = gy, \quad B_y = gx.$$

Here, $g = \partial B_x/\partial y = \partial B_y/\partial x$ is called the field gradient. The field gradient together with the particle momentum p and the particle charge q defines the quadrupole strength as

$$k = \frac{qg}{p}. \tag{C.7}$$

The trajectory in a transversely misaligned quadrupole is a solution of the differential equation

$$x''(z) + k\,(x(z) - x_{quad}) = 0, \tag{C.8}$$

where x_{quad} is a transverse offset of the quadrupole with respect to the z-axis. By integration one finds that the coordinates of a particle traversing the quadrupole are transformed according to

$$\begin{pmatrix} x_2 \\ x_2' \end{pmatrix} - \begin{pmatrix} x_{quad} \\ 0 \end{pmatrix} = \mathbf{T}_{quad} \left[\begin{pmatrix} x_1 \\ x_1' \end{pmatrix} - \begin{pmatrix} x_{quad} \\ 0 \end{pmatrix} \right] \tag{C.9}$$

or

$$\begin{pmatrix} x_2 \\ x_2' \end{pmatrix} = \mathbf{T}_{quad} \begin{pmatrix} x_1 \\ x_1' \end{pmatrix} + (\mathbf{I} - \mathbf{T}_{quad}) \begin{pmatrix} x_{quad} \\ 0 \end{pmatrix}. \tag{C.10}$$

The second term in equation C.10 constitutes a dipole-like transverse kick on the particles traversing a misaligned quadrupole. This kick acts independently of the initial particle coordinates.

The transfer matrix $\mathbf{T}_{quad}$ evaluates to:

$$\mathbf{T}_{quad} = \begin{cases} \begin{pmatrix} \cos\phi & \frac{1}{\sqrt{|k|}}\sin\phi \\ -\sqrt{|k|}\sin\phi & \cos\phi \end{pmatrix} & k > 0 \\ \\ \begin{pmatrix} \cosh\phi & \frac{1}{\sqrt{|k|}}\sinh\phi \\ \sqrt{|k|}\sinh\phi & \cosh\phi \end{pmatrix} & k < 0 \end{cases} \tag{C.11}$$

In these formulae we have introduced $\phi = \sqrt{|k|}L$, with L denoting the quadrupole length. From equation C.7 it follows that the magnitude of the focusing or defocusing effect on a particle is inversely proportional to the particle momentum, which will lead to different particle trajectories through the machine for particles of different energy.

For small values of the quadrupole length the transport matrices may be written in the thin lens approximation

$$\mathbf{T}_{quad} \approx \begin{pmatrix} 1 & 0 \\ \mp\frac{1}{f} & 1 \end{pmatrix}, \quad \frac{1}{f} = kL \tag{C.12}$$

where f is called the focal length of the quadrupole.

We finally remark that the transfer matrix between any two points in the machine can be obtained by successive multiplication of the transfer matrices belonging to the machine elements between these points.

General Equation of Motion

We introduce the focusing strength $k_0(z)$ for a particle at design momentum p_0 as a function of the longitudinal position in the machine. This focusing strength is non-vanishing only in the quadrupoles. Then equations C.1, C.5 and C.8 can then be combined to a general differential equation for a particle at design energy:

$$\left(\beta^{rel}(z)\gamma^{rel}(z)x'(z)\right)' + k_0(z)\beta^{rel}(z)\gamma^{rel}(z)x(z) = \beta^{rel}(z)\gamma^{rel}(z)\kappa_0(z), \tag{C.13}$$

where the term κ_0 contains all dipole-like deflections for a particle at the design momentum, i.e. deflections that do not depend on the transverse particle offset. It comprises especially contributions from dipole magnets or misaligned quadrupoles, but also dipole wakes excited by leading particles. The motion for a particle with a momentum p differing from the design momentum is described using the relative momentum deviation $\delta = (p - p_0)/p_0$ as:

$$\left(\beta^{rel}(z)\gamma^{rel}(z)x'(z)\right)' + (1-\delta)k_0(z)\beta^{rel}(z)\gamma^{rel}(z)x(z) = (1-\delta)\beta^{rel}(z)\gamma^{rel}(z)\kappa_0(z). \tag{C.14}$$

Using the normalized trajectory

$$x_N(z) = \sqrt{\beta^{rel}(z)\gamma^{rel}(z)}x(z) \tag{C.15}$$

from definition C.3, this equation can be rewritten as

$$x_N''(z) + \left((1-\delta)k_0(z) - \frac{\frac{\mathrm{d}^2}{\mathrm{d}z^2}\sqrt{\beta^{rel}(z)\gamma^{rel}(z)}}{\sqrt{\beta^{rel}(z)\gamma^{rel}(z)}} \right) x_N(z) = (1-\delta)\sqrt{\beta^{rel}(z)\gamma^{rel}(z)}\kappa_0(z). \quad \text{(C.16)}$$

The term $\left(\mathrm{d}^2/\mathrm{d}z^2\sqrt{\beta^{rel}(z)\gamma^{rel}(z)}\right)/\sqrt{\beta^{rel}(z)\gamma^{rel}(z)}$ can in practice be neglected.

Orbit, Betatron Motion and Twiss Parameters

We will proceed now by first discussing the motion of a particle with design energy along the machine, which means $\delta = 0$. The solution to the inhomogenous equation C.13 for such a particle is called the "orbit" $x_o(z)$. It is determined by the initial conditions $x_o(z_0) = x_o'(z_0) = 0$. On this orbit, a solution of the homogenous differential equation may be superimposed, which is called the "betatron motion." In the normalized coordinates it is described by the differential equation

$$x_{N\beta}''(z) + \left(k_0(z) - \frac{\frac{\mathrm{d}^2}{\mathrm{d}z^2}\sqrt{\beta^{rel}(z)\gamma^{rel}(z)}}{\sqrt{\beta^{rel}(z)\gamma^{rel}(z)}} \right) x_{N\beta}(z) = 0. \quad \text{(C.17)}$$

Equation C.17 is of Hill's type and describes a free transverse oscillation of the particle in the restoring force characterized by the focusing strength.

Introducing the "beta function" $\beta(z)$ and the "betatron phase" $\psi(z)$, the solution to this equation can be described with the ansatz

$$x_{N\beta}(z) = \sqrt{C\beta(z)}\cos\left(\psi(z) + \psi_0\right), \qquad \psi(z) = \int_0^z \frac{\mathrm{d}\zeta}{\beta(\zeta)}, \quad \text{(C.18)}$$

$$x_\beta(z) = \frac{1}{\sqrt{\beta^{rel}(z)\gamma^{rel}(z)}} x_{N\beta}(z). \quad \text{(C.19)}$$

C is an arbitrary constant of motion. The beta function $\beta(z)$ is the first of the three "Twiss Parameters" and must not be confused with the relativistic factor $\beta^{rel}(z)$. The spatial distance in z required by a particle to perform a full betatron oscillation or, in other words, for the betatron phase to change by an increment of 2π is called the "betatron wavelength" λ_β.

We now want to calculate the normalized trajectory slope $x_N^\dagger(z)$ from the normalized orbit $x_N(z)$. From definition C.3 we get

$$\begin{aligned}
x_{N\beta}^\dagger(z) &= \sqrt{\beta^{rel}(z)\gamma^{rel}(z)}x_\beta'(z) = \sqrt{\beta^{rel}(z)\gamma^{rel}(z)}\frac{\mathrm{d}}{\mathrm{d}z}\left(\frac{x_{N\beta}}{\sqrt{\beta^{rel}(z)\gamma^{rel}(z)}}\right) \\
&= \frac{\mathrm{d}}{\mathrm{d}z}x_{N\beta} - x_{N\beta}\frac{\frac{\mathrm{d}}{\mathrm{d}z}\left(\beta^{rel}(z)\gamma^{rel}(z)\right)}{2\beta^{rel}(z)\gamma^{rel}(z)} \\
&= \sqrt{\frac{C}{\beta(z)}}\left[\frac{1}{2}\beta'(z)\cos\left(\psi(z)+\psi_0\right) - \sin\left(\psi(z)+\psi_0\right)\right] - x_{N\beta}\frac{\frac{\mathrm{d}}{\mathrm{d}z}\left(\beta^{rel}(z)\gamma^{rel}(z)\right)}{2\beta^{rel}(z)\gamma^{rel}(z)}.
\end{aligned}$$

Introducing the "alpha function"

$$\alpha(z) = -\frac{1}{2}\left[\beta'(z) - \beta(z)\frac{\left(\beta^{rel}(z)\gamma^{rel}(z)\right)'}{\beta^{rel}(z)\gamma^{rel}(z)}\right] \quad \text{(C.20)}$$

we rewrite the normalized trajectory slope more compactly as

$$x'_{N\beta} = -\sqrt{\frac{C}{\beta(z)}}\Big[\alpha(z)\cos\left(\psi\left(z\right)+\psi_0\right)+\sin\left(\psi(z)+\psi_0\right).\Big] \tag{C.21}$$

The alpha function $\alpha(z)$ is the second of the Twiss parameters. In the case of vanishing acceleration ($\mathrm{d}\beta^{rel}/\mathrm{d}z = \mathrm{d}\gamma^{rel}/\mathrm{d}z = 0$), the alpha function reduces to

$$\alpha(z) = -\frac{1}{2}\beta'(z).$$

This form is well known from the theory of storage rings.

The set of Twiss parameters is completed by finally introducing the gamma function

$$\gamma(z) = \frac{1+\alpha^2(z)}{\beta(z)}. \tag{C.22}$$

This definition of the gamma function ensures the relation

$$\beta(z)\gamma(z) - \alpha^2(z) = 1.$$

Beam Ellipse

We can define an ellipse in the x_N-x'_N plane according to

$$\vec{x}_N^t \mathbf{E} \vec{x}_N = \vec{x}_N^t \begin{pmatrix} c & a \\ a & b \end{pmatrix} \vec{x}_N = c x_N^2 + 2a x_N x'_N + b x_N'^2 = \epsilon_N. \tag{C.23}$$

Here, a, b and c are arbitrary constants, constrained only by the requirements $b > 0$, $c > 0$ and $bc - a^2 = 1$. In this ellipse equation, we have introduced the constant ϵ_N, which is called the normalized emittance. The area enclosed by the ellipse is determined by the constant ϵ_N as $A = \pi\epsilon_N$. The ellipse matrix $\mathbf{E}$ is transformed through the lattice as

$$\mathbf{E}_2 = \left(\mathbf{T}_N^t\right)^{-1} \mathbf{E}_1 \mathbf{T}_N^{-1}, \tag{C.24}$$

where $\mathbf{T}_N$ is the normalized transfer matrix between the points z_1 and z_2 of the machine. During the transformation of the ellipse through the machine lattice, the emittance ϵ_N is conserved. This is due to the fact that $\det \mathbf{T}_N = 1$. The geometrical significance of the elements of the ellipse matrix can be seen in Fig. C.1. It is important to note that the maximum x excursion of the ellipse is given by $\sqrt{b\epsilon_N}$.

In particular, it is common practice to characterize the transverse distribution of particles in a beam by an ellipse according to

$$\begin{pmatrix} c & a \\ a & b \end{pmatrix} = \frac{1}{\epsilon_N}\begin{pmatrix} m_{x'x'\,N} & -m_{xx'\,N} \\ -m_{xx'\,N} & m_{xx\,N} \end{pmatrix}, \quad \epsilon_N = \sqrt{m_{xx\,N} m_{x'x'\,N} - m_{xx'\,N}^2}, \tag{C.25}$$

where, $m_{xx\,N}$, $m_{xx'\,N}$ and $m_{x'x'\,N}$ are the distribution moments of the particles of the beam in the normalized coordinates.

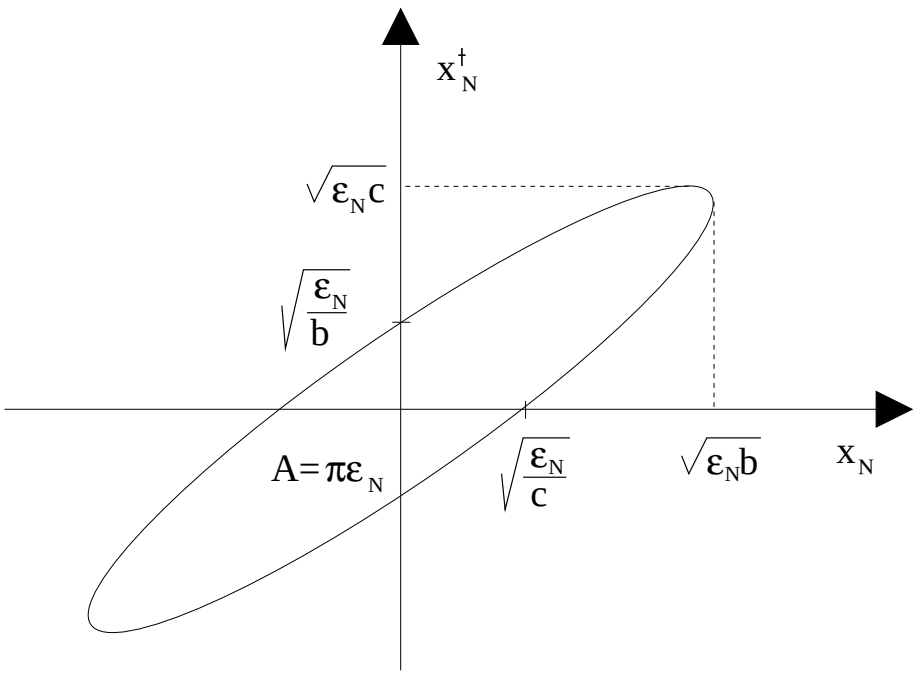

Fig. C.1 Geometrical meaning of the elements of the ellipse matrix.

Machine Ellipse and Beam Matching

The ansatz C.18 for the solution for the solution of Hill's equation C.17 is not sufficient to determine the beta function uniquely. In circular machines, the beta function of the lattice and the other Twiss functions are fixed by the requirement that they must be periodic with the machine circumference L, that is

$$\begin{aligned} \beta(z) &= \beta(z+L), \\ \alpha(z) &= \alpha(z+L), \\ \gamma(z) &= \gamma(z+L). \end{aligned} \tag{C.26}$$

Linear accelerators, of course, do not have this periodicity. However, linacs are usually composed of periodically recurring sequences of machine elements. The SBLC for instance is anticipated to obtain a FODO lattice (see appendix D.1). A FODO lattice is a sequence of identical subunits, sequences of machine elements, which are referred to as FODO cells. The Twiss functions in this case are determined by requiring that the Twiss functions of the lattice be periodic with the length L_P of a such a FODO cell.

The normalized transfer matrix over one periodically repeating subunit of the machine lattice can be expressed elegantly using the periodic machine Twiss parameters $\beta(z)$, $\alpha(z)$ and $\gamma(z)$ as fixed by C.26 as

$$\mathbf{T}_N(z, z+L_P) = \mathbf{I}\cos\mu + \mathbf{J}\sin\mu, \tag{C.27}$$

where μ is the betatron phase advance over this length and $\mathbf{I}$ is the unit matrix. The matrix $\mathbf{J}$ is defined as

$$\mathbf{J}(z) = \begin{pmatrix} \alpha(z) & \beta(z) \\ -\gamma(z) & -\alpha(z) \end{pmatrix}, \quad \mathbf{J}^2 = -\mathbf{I}. \tag{C.28}$$

A matrix $\mathbf{E}$ describing a beam ellipse at the position z_1 or containing the distribution moments according to C.25 is transformed by C.27 as (see C.24)

$$\mathbf{E}_2 = \mathbf{E}_1\cos^2\mu - \left(\mathbf{J}_1^t\mathbf{E}_1 + \mathbf{E}_1\mathbf{J}_1\right)\cos\mu\sin\mu + \mathbf{J}_1^t\mathbf{E}_1\mathbf{J}_1\sin^2\mu. \tag{C.29}$$

Since the Twiss parameters and the betatron phase advance per lattice subunit have a non-vanishing dependence on the momentum deviation δ of the particles constituting the beam ellipse, the transformation law for off-energy particles starting out with the identical initial ellipse matrix $\mathbf{E}$ over a number of n lattice cells is expressed more generally as

$$\mathbf{E}_2(\delta) = \mathbf{E}_1 \cos^2 n\mu(\delta) - \Big(\mathbf{J}_1^t(\delta)\mathbf{E}_1 + \mathbf{E}_1\mathbf{J}_1(\delta)\Big) \cos n\mu(\delta) \sin n\mu(\delta) + \mathbf{J}_1^t(\delta)\mathbf{E}_1\mathbf{J}_1(\delta) \sin^2 n\mu(\delta). \tag{C.30}$$

Expression C.30 indicates, that in general the beam ellipses for off-energy particles are transformed differently, with a dependence on δ. However, when we consider the case of a transformation of the beam over one betatron wavelength, i.e. $n\mu(\delta = 0) = 2\pi$, we find that the first derivative of the beam ellipse matrix $\mathbf{E}_2$ from C.30 with respect to the momentum deviation δ can be made to vanish by fulfilling the condition

$$\mathbf{J}_1^t(\delta = 0)\mathbf{E}_1 + \mathbf{E}_1\mathbf{J}_1(\delta = 0) = \begin{pmatrix} 2(\alpha(z_1)c_1 - \gamma(z_1)a_1) & \beta(z_1)c_1 - \gamma(z_1)b_1 \\ \beta(z_1)c_1 - \gamma(z_1)b_1 & 2(\beta(z_1)a_1 - \alpha(z_1)b_1) \end{pmatrix} = 0. \tag{C.31}$$

This leads to the requirement that the ellipse parameters ascribed to the beam are equal to the periodic Twiss parameters of the machine lattice:

$$\begin{aligned} b_1 &= \beta(z_1), \\ a_1 &= \alpha(z_1), \\ c_1 &= \gamma(z_1). \end{aligned} \tag{C.32}$$

If the beam ellipse fulfills this condition, the beam is said to be matched. In this case, the beam

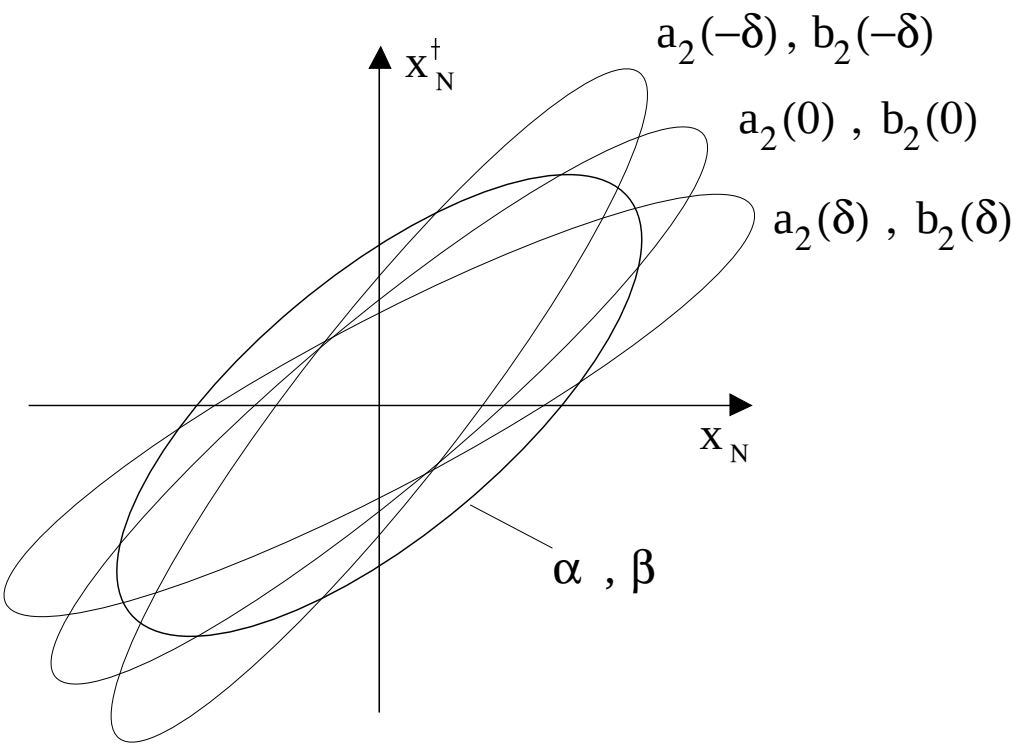

Fig. C.2 Chromatic filamentation of an unmatched beam. If the ellipse parameters of the beam are not matched to the periodic Twiss parameters of the lattice (α, β, γ) the beam ellipses for particles with energy deviation are transformed differently. As a result, the projected emittance increases.

ellipses for particles with a small momentum deviation δ are transformed **over the length of**

one betatron oscillation in the same way as the beam ellipse for particles at design energy. If the matching condition is not met, the congruence of the different beam ellipses will be destroyed in the transformation, leading to an increase of the projected emittance. This process, which is called "chromatic filamentation", is illustrated in Fig. C.2. In our simulations, we will always assume that the beam is matched at injection. This corresponds to the condition

$$m_{xx\,N} = \epsilon_N \beta(0), \quad m_{xx'\,N} = -\epsilon_N \alpha(0), \quad m_{x'x'\,N} = \epsilon_N \gamma(0) \tag{C.33}$$

for the distribution moments of the beam at injection.

Dispersion and Chromaticity

We now return from the analysis of an ensemble of particles to the modifications that are imposed on the transverse motion of a single particle that occur when its energy deviates from the design energy.

As equation C.16 contains a dependence on the deviation δ of the particle energy from the design energy, the solution for the orbit also has a dependence on this deviation. We write the orbit of a particle with momentum deviation δ as $x_o(z,\delta)$. The derivative

$$D(z) = \frac{\mathrm{d}}{\mathrm{d}\delta} x_o(z,\delta) \tag{C.34}$$

is called the "dispersion function." In the normalized coordinates it is characterized by the differential equation

$$D_N''(z) + D_N(z)\left[k_0(z) - \frac{\frac{\mathrm{d}^2}{\mathrm{d}z^2}\sqrt{\beta^{rel}(z)\gamma^{rel}(z)}}{\sqrt{\beta^{rel}(z)\gamma^{rel}(z)}}\right] = k_0(z)x_{No}(z) - \sqrt{\beta^{rel}(z)\gamma^{rel}(z)}\kappa_0(z), \tag{C.35}$$

$$D(z) = \frac{1}{\sqrt{\beta^{rel}(z)\gamma^{rel}(z)}} D_N(z). \tag{C.36}$$

Note that in contrast to circular machines, this dispersion is caused by dipole-like kicks and the resulting trajectory distortions. The contribution to the dispersion from the orbit therefore must not be neglected.

Finally, particles with an energy deviation δ from the design energy will move along the lattice with different betatron phase advance. The betatron phase at the position z in the lattice for an off-energy particle is commonly expressed with a quantity known as "chromaticity" as

$$\psi(z,\delta) = \psi(z) + 2\pi\delta\xi(z) \tag{C.37}$$

where the chromaticity $\xi(z)$ is calculated as

$$\xi(z) = -\frac{1}{4\pi}\int_0^z k_0(\zeta)\beta(\zeta)\mathrm{d}\zeta \tag{C.38}$$

If the chromaticity of a lattice does not vanish (which is generally the case), particles of different energy starting out with identical betatron oscillations get out of betatron phase and will eventually occupy different points in the transverse phase space. This process, which will lead to a dilution of the projected emittance, is referred to as "filamentation."

Appendix D

SBLC: Fundamental Design and Layout Properties

In this chapter we give a brief summary of some fundamental design and layout issues concerning the SBLC linac, as far as they are relevant for the investigation of beam dynamics. Some of the material presented here is based on preliminary assumptions and must not be viewed as a final design. The issues covered will essentially be related to the machine lattice and, in particular, the accelerating structure.

D.1 Machine Lattice

The lattice of the SBLC main linac is assumed to be a "FODO lattice." A FODO lattice consists of an alternating series of focusing and defocusing quadrupole magnets separated by a (commonly uniform) distance containing accelerating structures. In our calculations, drift spaces are omitted. A "FODO cell" is a set of one focusing and one defocusing quadrupole magnet and the corresponding accelerating structures behind them. The FODO cells at the beginning of the linac have one structure after each magnet. Proceeding from the beginning of the linac to the I.P., the machine is divided into 8 "sectors", each of which consists of a number of identical FODO cells, thus constituting a locally uniform lattice segment. The focusing strength is reduced stepwise from sector to sector of the lattice, to the effect that the beta function of the lattice scales with the square root of the beam energy (see Fig. 2.6). As it is assumed that the betatron phase advance per FODO cell remains constant over the entire length of the machine, this variation of the beta function is achieved by stretching the length of the individual FODO cell in later sectors and placing more (2,3,..., max. 8) structures between adjacent quadrupoles, as illustrated in Fig. D.1. The focal length of the quadrupoles in the different sectors is increased proportionally to keep the betatron phase advance per cell at 90°.

At the transition between two sectors the installation of matching sections in order to match the different Twiss parameters of adjacent sectors will be necessary [1]. The number of FODO cells in each sector is given in table D.1.

[1] For the tracking calculations these matching sections were represented by simple transfer matrices, thus ignoring their internal structure. The transfer matrices between adjacent sectors n and $n+1$ were

$$\mathbf{T} = \begin{pmatrix} \sqrt{\beta_{n+1}(z)/\beta_n(z)} & 0 \\ 0 & \sqrt{\beta_n(z)/\beta_{n+1}(z)} \end{pmatrix}$$

for both planes, where $\beta_n(z)$ and $\beta_{n+1}(z)$ denote the beta functions in the adjacent lattice sectors at the transition.

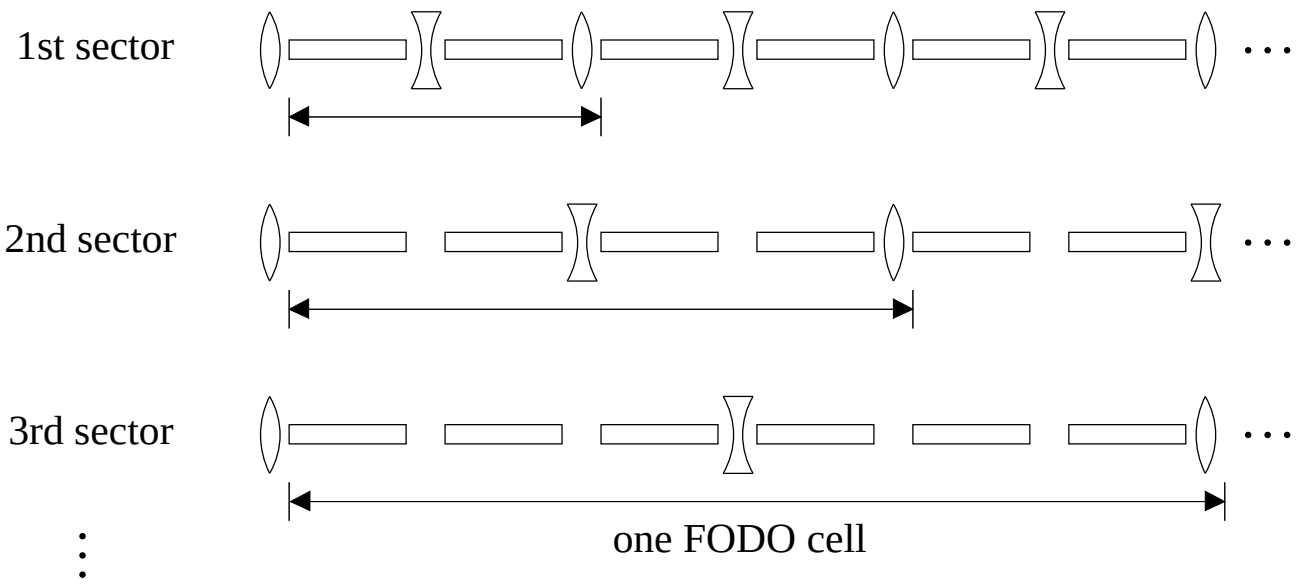

Fig. D.1 Sequence of machine elements in the different sectors of the lattice. While in the first sector there is always one accelerating structure between two adjacent quadrupoles, the length of a FODO cell in the following sectors is stretched by placing more structures between adjacent quadrupoles.

Sector	1	2	3	4	5	6	7	8
FODO cells	48	40	36	36	32	32	32	31

Table D.1 Number of FODO cells in the different sectors of the machine lattice.

D.2 Accelerating Structure

Acceleration in the main linac is to be achieved in normally conducting traveling wave structures operating in the $\frac{2\pi}{3}$-mode at a frequency of 2.998GHz, which corresponds to a wavelength of 10cm. The length of one cell of the structure must therefore be 33.33mm. Each cell of the structure is made of a so-called "cup", which is depicted in Fig. D.2 A full accelerating structure has 180 cells and hence is made of 180 cups and one end plate. Fig. 1.2 in chapter 1 showed how the individual cells are assembled into a structure. Some of the cells will be equipped with higher order mode dampers (HOM-dampers) to reduce the Q-values of the undesired dipole modes in the structure. The length of a structure is 6m.

Power Considerations

The cells and cups of a structure are not identical, since the structure is designed as a constant gradient structure. In a constant gradient structure, the group velocity of the accelerating mode is reduced along the axis in order compensate for the longitudinal decrease of the RF power and hence to obtain a uniform power dissipation per length element along the structure. Also, the accelerating gradient along the structure becomes more uniform. This variation of the group velocity is achieved by "tapering" the structure, i.e. by reducing the iris diameter with increasing cell number and simultaneously reducing the cell diameter to adjust the frequency of the accelerating mode to the desired value.

The underlying accelerating structure is defined in its geometrical properties by the require-

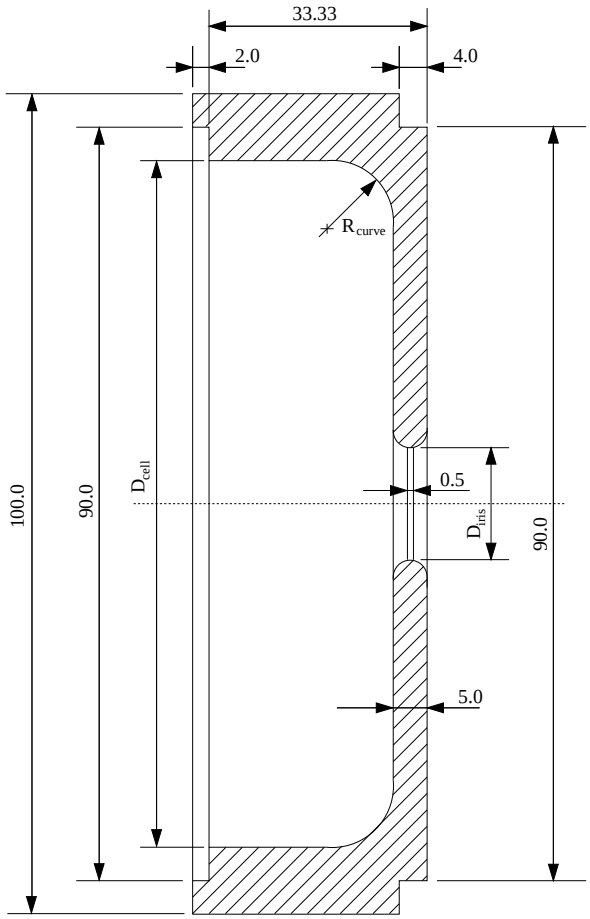

Fig. D.2 Single "cup" of the accelerating section. Lengths are given in mm.

ment that the value for the attenuation τ (formula 3.17) is $\tau = 0.57$. With the assumption that the quality of the accelerating mode is $Q = 12000$ this leads to a variation of the iris diameter from $D_{iris\,1} = 30.776$mm to $D_{iris\,180} = 21.786$mm and of the cell diameter from $D_{cell\,1} = 82.716$mm to $D_{cell\,180} = 79.984$mm.

The RF power needed to feed the structures is generated in klystrons. The SBLC study aims at using klystrons with a power of 150MW, which would allow two structures to be fed by one klystron. A block diagram of this arrangement is shown in Fig. D.3. A modulator generates a pulse of high voltage and high current driving one klystron, which in turn supplies its RF power to two accelerating structures.

HOM Detuning Range

An important measure to suppress the adverse influence of higher order modes will be to detune the HOM frequencies in different structures in order to get a partial cancellation of the combined wake fields in these structures. In practice, this detuning will be achieved by varying the curvature radius R_{curve} in the corner of the cells (see Fig. D.2). The other parameters of the cell geometry, the cell diameter D_{cell} and the iris diameter D_{iris} would then be adjusted to give the correct properties of the accelerating mode for structures with different R_{curve}. In this context, one is interested in how large a detuning one can attain by this manipulation of the cell geometry. Therefore, we looked at a cell located in the middle of the accelerating structure and calculated the frequency of the dipole π-mode for different values of R_{curve}. The result of this investigation is given in table D.2. The cell diameter D_{cell} had been adjusted for the

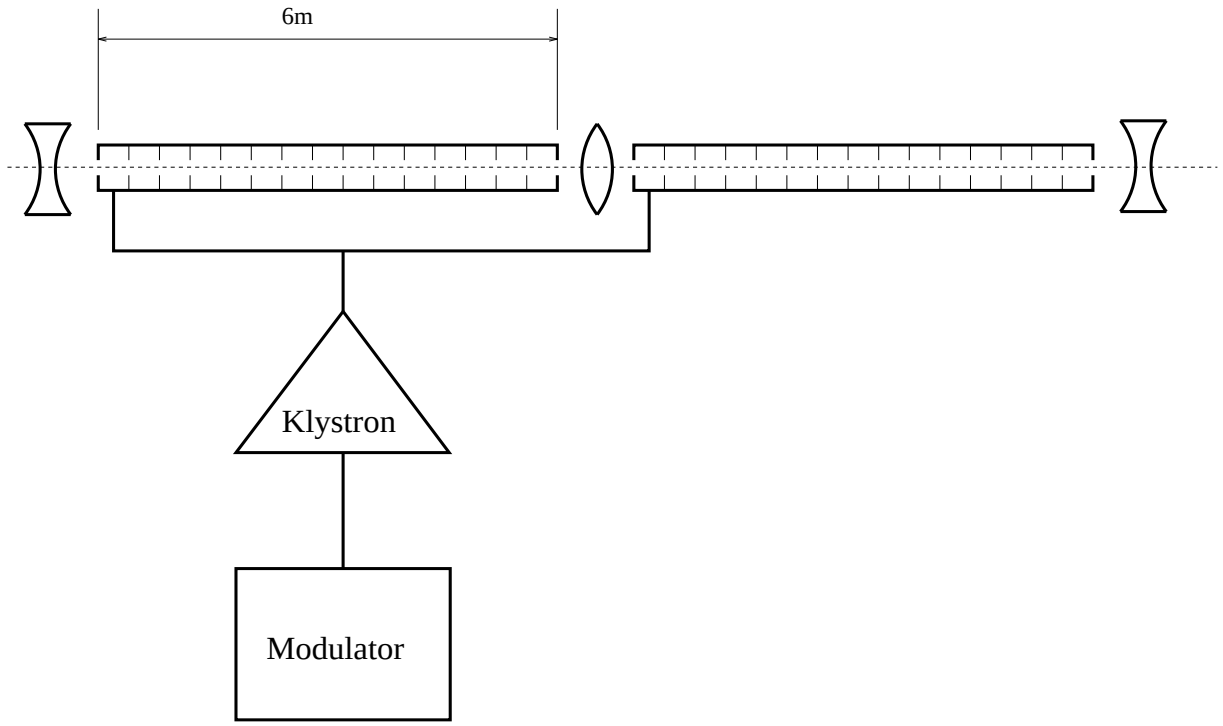

Fig. D.3 Accelerating module consisting of a modulator, a klystron and two accelerating structures.

D_{iris}	D_{cell}	R_{curve}	f_{π}^{dipole}
26.946mm	79.922mm	0.0mm	4294.82MHz
26.946mm	81.408mm	10.0mm	4287.14MHz
26.946mm	85.070mm	20.0mm	4225.41MHz

Table D.2 Frequencies of the π-mode of the TM-like HEM_{11} modes for different values of the curvature radius R_{curve} (see also Fig. D.2). The cell diameter D_{cell} is adjusted in order to keep the frequency of the accelerating mode at its design value.

different values of R_{curve} to keep the frequency of the accelerating mode at its design value. From the resulting frequencies of the dipole modes we conclude that detuning ranges in the order of $\approx$ 70MHz are feasible with variations of the curvature radius R_{curve} from 0 to 20mm.

D.3 Short Range Wakes

The wake potentials for the accelerating structure were calculated with the code MAFIA T2 ([22], [23]). At present, calculation of the wake of a bunch considerably shorter than 0.5mm (bunch length in the SBLC) in the full 6m structure is not possible for reasons of both memory and CPU time requirements. However, it is necessary to carry out this calculation on a sufficiently long structure, since the wake in an array of cells differs from the sum of the wakes of the individual cells. For a long structure where the cells are all identical, the shape of the wake potential converges to a limit function whose amplitude depends linearly on the number of cells (this can be deduced for instance from [51]). Unfortunately, this limit cannot be applied to a tapered structure.

Therefore, a compromise had to be made between structure length and bunch length. For our purposes we have chosen to calculate the wake of a 15-cell structure with the same total taper of the iris diameter as the full 180-cell structure. The bunch length in this calculation was $\sigma_z = 0.5$mm with Gaussian charge distribution. As wake potentials for the full 180-cell structure we used the wakes of the 15-cell structure scaled by a factor 12. Fig. D.4 to Fig. D.7 show the wakes of the full structure (180 cells) and the bunch density versus the longitudinal position in the bunch.

We must point out that convolving these wake potentials with the charge distribution of a 0.5mm bunch will produce a final wake potential corresponding to a larger bunch length. Substituting the value of 0.5mm for both the length of the simulated bunch and the bunch used in the numerical wake computation in formula 2.26, we find that the the resulting wake will correspond to a Gaussian charge distribution with a length of $\sigma_z = 0.707$mm.

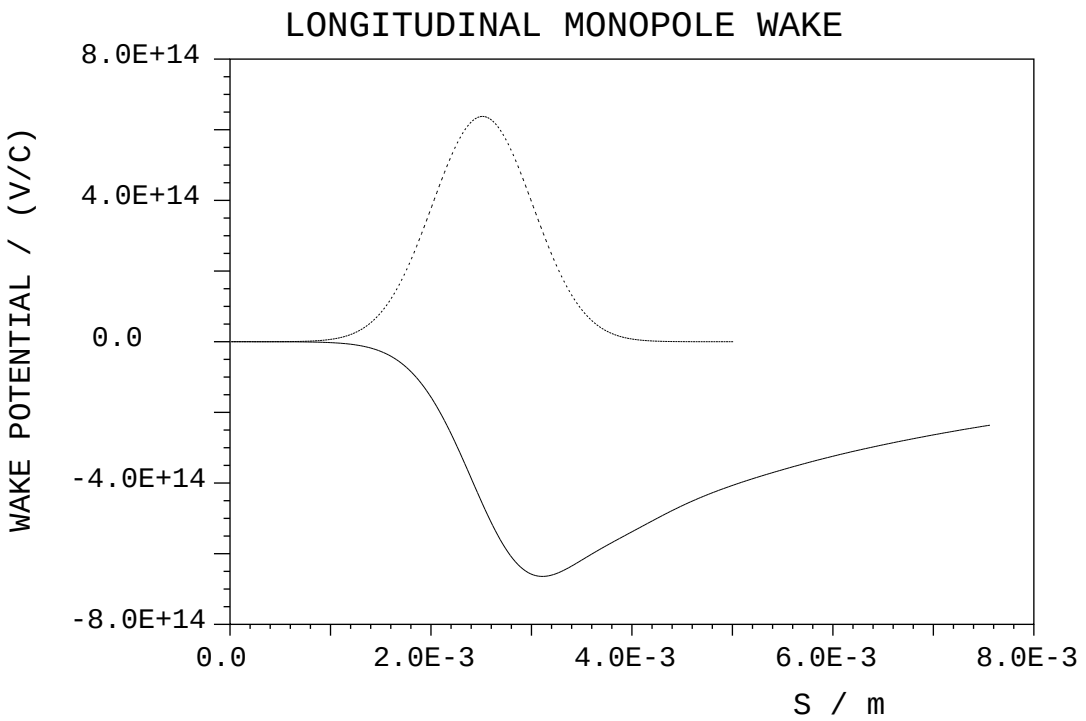

Fig. D.4 Longitudinal monopole wake potential in the SBLC structure (solid curve). The dotted curve shows the profile of the bunch generating this wake potential.

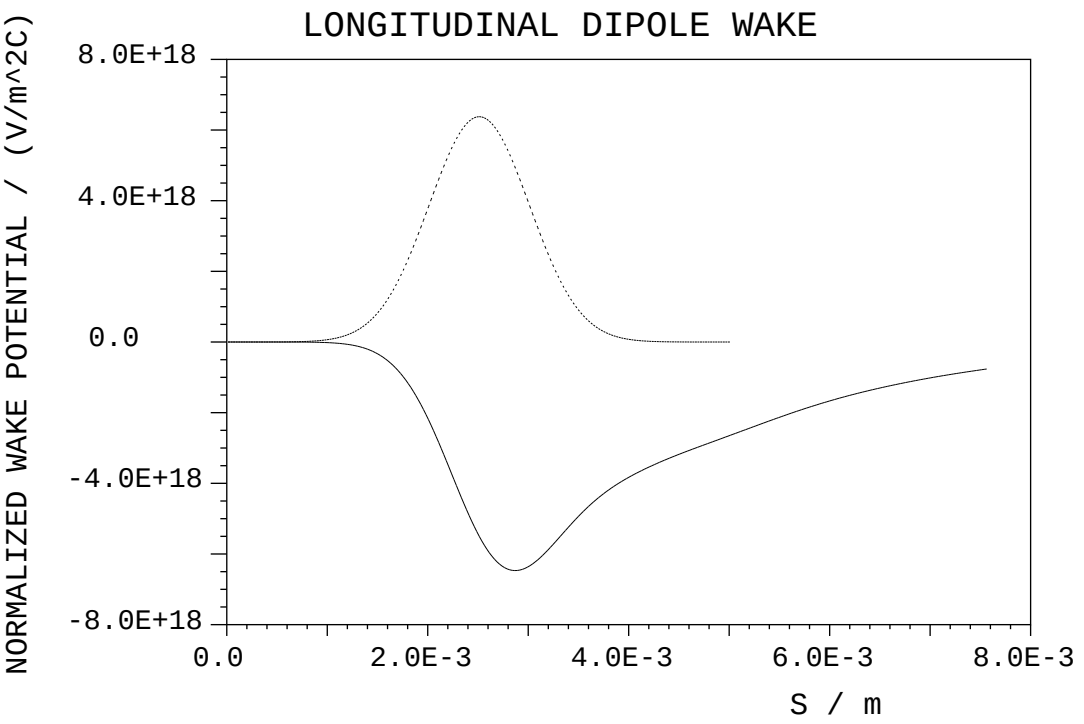

Fig. D.5 Longitudinal dipole wake potential in the SBLC structure normalized to the square of the bunch offset (solid curve). The dotted curve shows the profile of the bunch generating this wake potential.

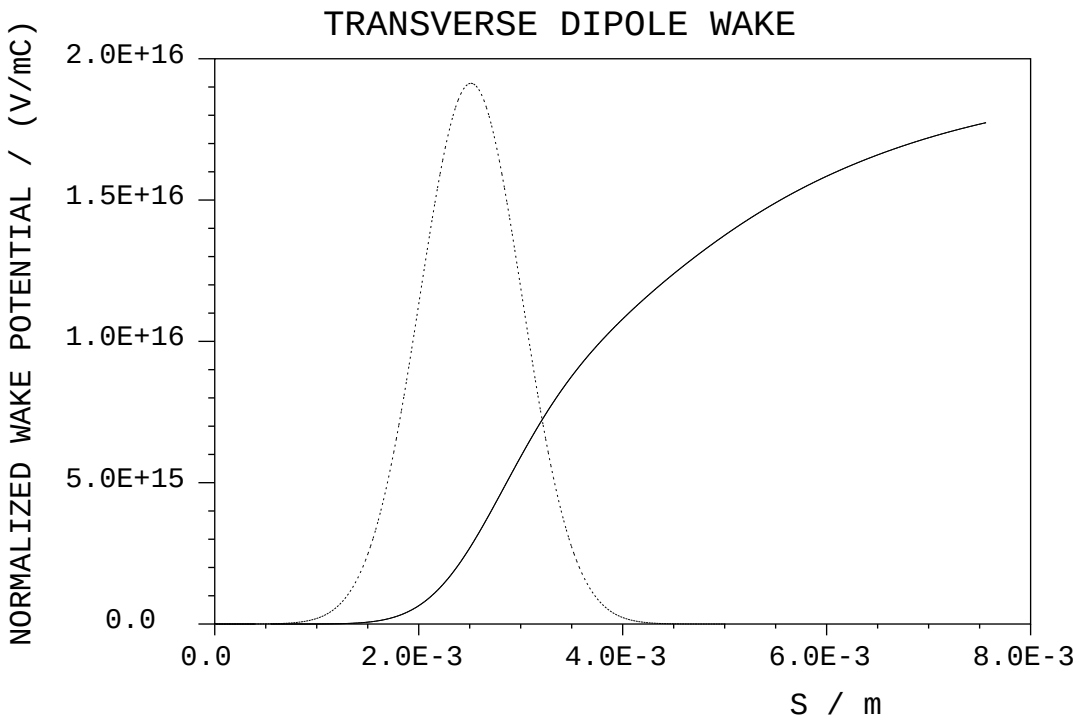

Fig. D.6 Transverse dipole wake potential in the SBLC structure normalized to the bunch offset (solid curve). The dotted curve shows the profile of the bunch generating this wake potential.

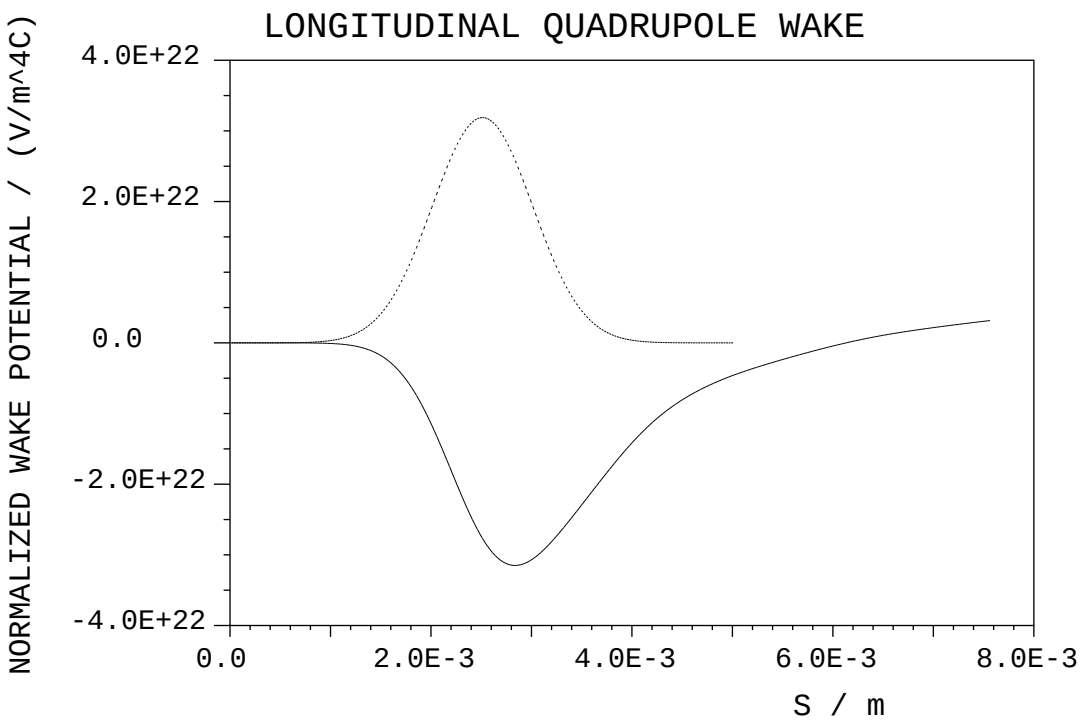

Fig. D.7 Longitudinal quadrupole wake potential in the SBLC structure normalized to the 4-th power of the bunch offset (solid curve). The dotted curve shows the profile of the bunch generating this wake potential.

Bibliography

[1] R. Brinkmann: "HERA Status and Plans", Presented at the 16th IEEE Particle Accelerator Conference (PAC 95) and International Conference on High Energy Accelerators (IUPAP), Dallas, Tx., May 1-5, 1995, SLAC-PUB-4902

[2] P. M. Zerwas: "e^+e^- Linear Colliders: Physics Prospects", ECFA Workshop on e^+e^- Linear Colliders, 25 July - 2 August 1992, Garmisch Partenkirchen, ECFA 93-154, June 1993

[3] Soo-Bong Kim for the CDF and D$\emptyset$ Collaborations: "Observation of the Top Quark", Talk given at the 15th International Conference on Physics in Collision (PHYSCOLL95), Cracow, Poland, June 8-10, 1995, FERMILAB-CONF-95-276-E, June 1995

[4] "Proceedings of the Fifth International Workshop on Next-Generation Linear Colliders", Stanford Linear Accelerator Center, Stanford University, Stanford, California 94309, October 1993, SLAC-436

[5] K. Flöttmann, J. Rossbach: "A High Intensity Positron Source for Linear Colliders", Proccedings of the High Energy Accelerator Conference, Hamburg, pp. 142-144, 1992

[6] S. A. Kheifets, R. D. Ruth, T. H. Fieguth: "Bunch Compression for the TLC", Particle Accelerators, Vol. 30, pp. 79-84, 1990

[7] T. Limberg, L. Rivkin: "Damping rings and Bunch Compression Summary", ECFA Workshop on e^+e^- Linear Colliders, 25 July - 2 August 1992, Garmisch Partenkirchen, ECFA 93-154, June 1993

[8] D. Sprehn, R. M. Phillips, G. Caryotakis: "The Design and Performance of 150-MW S-Band Klystrons", Presented at the 40th Anniversary IEEE International Electron Devices Meeting, San Francisco, Ca., December 11-14, 1994, SLAC-PUB-6677

[9] Figures provided by N. Holtkamp

[10] R. Brinkmann: "Optimization of a Final Focus System for Large Momentum Bandwidth", Deutsches Elektronen Synchrotron, November 1990, DESY M-90-14

[11] D. L. Burke: "Results from the Final Focus Test Beam", Invited talk at the 4th European Particle Accelerator Conference (EPAC 94), London, England, 27 June - 1 July 1994, SLAC-PUB-6609

[12] A. W. Chao: "Physics of Collective Beam Instabilities in High Energy Accelerators", John Wiley & Sons, 1993

[13] T. O. Raubenheimer: private communication

[14] K. L. Brown, R. V. Servanckz: "First- and Second-Order Charged Particle Optics", lectures given at 3rd Summer School on High Energy Particle Accelerators, Upton, N.Y., July 6-16, 1983, SLAC-PUB-3381, July 1984

[15] J. Buon: "Beam Phase Space and Emittance", Fifth General Accelerator Physics Course, University of Jyväskylä, Finland, 7-18 September 1992, CERN 94-01

[16] K. L. F. Bane: "Wakefield Effects in a Linear Collider", Proceedings of the U.S. Summer School on High Energy Particle Accelerators, Batavia, Illinois, Aug. 13-31, 1984

[17] K. L. F. Bane, T. Weiland, P. B. Wilson: "Wake Fields and Wake Field Acceleration", Proceedings of the 1983 Summer School on High Energy Particle Accelerators, Brookhaven National Laboratory and State University of New York at Stony Brook, July 6-16, 1983

[18] T. Weiland, R. Wanzenberg: "Wake Fields and Impedances", Joint US-CERN Accelerator Course, Hilton Head, So. Carolina, Nov. 7-14 1990, Springer Verlag Berlin, Heidelberg, 1992

[19] T. Weiland, B. Zotter: "Wake Potentials of a Relativistic Current in a Cavity", Particle Accelerators, Vol. 11, pp. 143-151, 1981

[20] T. Weiland: "Comment on Wake Field Computation in Time Domain", Nucl. Instr. Meth. 216, 1983, pp. 31-34

[21] P. Wilson, K. L. F. Bane, K. Satoh: "A Computer Simulation of Longitudinal Single-Bunch Effects in Electron-Positron Storage Rings", Proceedings of the 1981 Particle Accelerator Conference, Washington, D.C., Mar 11-13, 1981, IEEE Trans. NS-28, No.3, 1981

[22] M. Dehler: "Numerische Lösung der Maxwellschen Gleichungen auf Kreiszylindrischen Gittern", Dissertation, Technische Hochschule Darmstadt, 1993

[23] T. Weiland: "Transverse Beam Cavity Interaction", Nucl. Instr. Meth. 212, 1983, pp. 13-21

[24] T. Weiland: private communication

[25] T. Weiland: "On the Quantitative Prediction of Bunch Lengthening in High Energy Electron Storage Rings", Deutsches Elektronen Synchrotron, December 1981, DESY 81-088

[26] W. K. Panofsky, W. A. Wenzel: "Some Considerations Concerning the Transverse Deflection of Charged Particles in Radio-Frequency Fields", Rev. Sci. Instrum. 27, p. 967, 1956

[27] V. Balakin, A. Novokhatsky, V. Smirnov: "VLEPP: Transverse Beam Dynamics", Proceedings of the 12th Int. Conf. on High Energy Accelerators, Fermilab, 1983

[28] J. T. Seeman, N. Merminga: "Mutual Compensation of Wakefield and Chromatic Effects of Intense Linac Bunches", SLAC-PUB-5220, Stanford Linear Accelerator Center, Stanford University, Stanford, CA 94309, May 1990

[29] T. O. Raubenheimer: "The Generation and Acceleration of Low Emittance Flat Beams for Future Linear Colliders", Ph.D. thesis, Stanford Linear Accelerator Center, Stanford University, Stanford, California 94309, November 1991

[30] R. D. Ruth: "Emittance Preservation in Linear Colliders", Proceedings of the US-CERN School on Particle Accelerators, South Padre Island, Tx., October 23-29, 1986

[31] C. E. Adolphsen et al.: "Beam Based Alignment Technique for the SLC Linac", Presented at the IEEE Part. Acc. Conf., Chicago, Il., March 20-23, 1989, SLAC-PUB-4902

[32] T. L. Lavine et al.: "Beam Determination of Quadrupole Misalignments and Beam Position Monitor Biases in the SLC Linac", Presented at the 1988 Linear Accelerator Conference, Williamsburg, Va., October 3-7, 1988, SLAC-PUB-4720

[33] T. O. Raubenheimer, R. D. Ruth: "A New Method of Correcting the Trajectory in Linacs", Proc. of the 1989 IEEE Part. Acc. Conf., Chicago, Il., 1989

[34] T. O. Raubenheimer: "A New Technique of Correcting Emittance Dilutions in Linear Colliders", Nucl. Instr. Meth., A306, 61, 1991

[35] J. T. Seeman: "New Compensation of Transverse Wakefield Effects in a Linac by Displacing Accelerating Structures", Proceeding of the 1990 Linear Accelerator Conference, Albuquerque, New Mexico, September 10-14, 1990, LA-12004-C, p. 390

[36] U. van Rienen: "Higher Order Mode Analysis of Tapered Disc-Loaded Waveguides Using the Mode Matching Technique", Particle Accelerators, Vol. 41, pp. 173-201, 1993

[37] M. Witting: "Untersuchung elektromagnetischer Eigenschaften von Wanderwellenröhren mit der Methode der Orthogonalentwicklung", Diplomarbeit, Institut für Hochfrequenztechnik der Technischen Hochschule Darmstadt, Fachgebiet Theorie Elektromagnetischer Felder, May 1992

[38] J. W. Wang: "RF Properties of Periodic Accelerating Structures for Linear Colliders", Ph.D. thesis, Stanford Linear Accelerator Center, Stanford University, Stanford, California 94309, July 1989, SLAC-339

[39] N. Holtkamp: private communication

[40] K. A. Thompson, R. D. Ruth: "Simulation and Compensation of Multibunch Energy Variation in NLC", May 1993, SLAC-PUB-6154

[41] K. Simonyi: "Theoretische Elektrotechnik", VEB Deutscher Verlag der Wissenschaften, Berlin, 1989

[42] K. L. F. Bane, P. B. Wilson: "Longitudinal and Transverse Wake Potentials in SLAC", Proceedings of the High Energy Accelerators Conference, Geneva, pp. 592-596, 1980

[43] K. L. F. Bane, R. L. Gluckstern: "The Transverse Wakefield of a Detuned X-Band Accelerator Structure", Particle Accelerators, Vol. 42(3-4), pp. 123-169, 1993

[44] R. Wanzenberg: private communication

[45] R. Brinkmann: private communication

[46] B. A. Baklakov et al.: "Investigation of Seismic Vibrations and Relative Displacements of Linear Collider VLEPP Elements", Proc. 1991 IEEE Part. Acc. Conf., San Francisco, USA, pp. 3273, 1991

[47] R. Brinkmann, J. Rossbach: "Observation of Closed Orbit Drift at HERA Covering 8 Decades of Frequency", Deutsches Elektronen Synchrotron, April 1994, DESY HERA 94-04

[48] J. Rossbach et al.: "A Note on Ground Vibration Issues Related to the Choice of a Linear Collider Site", DESY M-94-06, internal report, September 1994

[49] J. Rossbach, P. Schmüser: "Basic Course on Accelerator Optics", Fifth General Accelerator Physics Course, University of Jyväskylä, Finland, 7-18 September 1992, CERN 94-01

[50] K. Wille: "Physik der Teilchenbeschleuniger und Synchrotronstrahlungsquellen", B. G. Teubner, Stuttgart, 1992

[51] S. A. Heifets, S. A. Kheifets: "High Frequency Limit of the Longitudinal Impedance of an Array of Cavities", May 1988, SLAC-PUB-4625

Acknowledgements

First, I want to thank Prof. Dr. Th. Weiland for making this work possible and for his scientific guidance. Furthermore, I would like to thank Dr. R. Brinkmann and Prof. Dr. A. Richter for being second examiners. Thanks are also due to Prof. Dr. G. A. Voss for continuous encouragement and support.

I am deeply indebted to my tutor Dr. R. Wanzenberg for his support of my work, numerous suggestions and discussions and finally for careful reading of this thesis.

Particular gratitude is also due to Dr. M. Dohlus for for his advice and for numerous most instructive discussions. Likewise I want to thank Dr. D. Kelly, Dr. J. Palkovic, Dr. B. Parker, Dr. T. Sen, Dr. N. Walker and S. G. Wipf most cordially for reading the manuscript and their advice concerning english usage. Moreover, I want to thank Dr. G. Hoffstätter, Dr. N. Holtkamp, Dr. A. Mosnier, Dr. T. Raubenheimer and Dr. J. Rossbach for many stimulating discussions.

Through the years I have benefited considerably from the pleasant atmosphere and constructive spirit both at the "MAFIA"-collaboration at the TH Darmstadt and at the MPY division of DESY, where I have received help and suggestions from a large number of colleagues. In this context, I want to make special mention of U. Becker, Dr. M. Böge, M. Marx, Dr. Zhang Min, Dr. U. van Rienen, B. Schumann and P. Thoma.